Design, Characterisation and Testing of Organic Semiconductors in the Production of Solar Fuels



Floriana Moruzzi

Linacre College

University of Oxford

Supervised by: Professor Iain McCulloch and Dr Ludmilla Steier

Submitted: March 2023

This thesis is submitted to the Department of Organic Chemistry, University of Oxford, in partial fulfilment of the requirements for the degree of Doctor of Philosophy

Declaration

I declare that the work outlined in this thesis was carried out in the Department of Chemistry at Oxford University and in the Departments of Chemistry and Chemical Engineering at Imperial College London between October 2018 and February 2023, under the supervision of Prof. Iain McCulloch and Dr. Ludmilla Steier. This thesis is entirely my own work, and except where otherwise stated, describes my own research.

F. Moruzzi

Copyright Declaration

The copyright of this thesis belongs to the author. Unless stated otherwise the contents of this thesis are licensed under a Creative Commons Attribution-Non-Commercial-No Derivatives 4.0 International Licence (CC BY-NC-ND), any reproductions should credit the author. Please seek permission from the copyright holder for uses of this work that are not included in this licence or permitted under UK Copyright Law

Acknowledgements

Firstly, I would like to thank my supervisor, Prof. Iain McCulloch, for taking me on as a student and for his support and supervision over the course of my PhD, for his patience and valuable discussions. It has been such an honour to work for someone I admire so much. Thank you also to my second supervisor, Dr Ludmilla Steier for her support, scientific discussion, and advice. It has been valuable to me to have such a great role model. I would like to express my thanks to the entire McCulloch group, I have loved working with and getting to know all of you. I am especially thankful to Dr Andrew Wadsworth for his training and advice at the start of my PhD, thank you also to Dr Petruta Maria, Dr Matt Bidwell, Dr Jan Kosco and Dr Max Moser for their valuable advice. I am particularly thankful to Dr Cath Aitchison for her help, I feel lucky to have worked alongside someone so knowledgeable, capable, and strong. A special thanks to Ben Willner, I am so thankful for all our discussions, your incredible baking, for your support and help, co-supervising with you was a pleasure. Thank you to Maryam for her valuable work, and chats, I have loved getting to know you. Thank you to Weimin, Balaji, and Marios, what a privilege to work with such great chemists! A big thank you to Sophie for being my companion over this PhD journey, and to the rest of the McCulloch group. Thank you also to Ben and Dikshita in the Steier group, you have both come so far and I am incredibly proud of you. I would like to thank my collaborators, working with other people and other groups has been one of the best parts of working in research. I am especially thankful to Dr Tack Ho Lee, Dr Sora Gonzalez-Carrero, and their PI Prof. James Durrant, their support and discussions have been invaluable over the last years. Thank you to the Eslava group at Imperial College, especially Ed and Yasmine, it was a pleasure working together. Thank you also to the Williams group, for their help in settling in at Oxford, for their valuable input and enthusiasm, especially Gloria, Lisa, and Brad and of course their PI Prof Charlotte Williams. I would like to thank my students Matt and Angie, supervising and training has been my favourite part of this PhD, and I am thankful for your hard work and enthusiasm. A special thanks to the CRL workshop for their patience and help in setting up the photocatalysis lab at Oxford with me, for taking my ideas seriously, for their hard work, and for always having the right tools and advice, especially Ron, Colin, Billy, and Lee. I would like to thank Swagelok for their courses and patience. Finally, thank you to my friends for their comfort, time, and advice, and a special thanks to my parents, my sister Ginny and the rest of my family, which I feel so lucky to be a part of, for their love and support, for keeping me grounded and for putting up with me. Thank you to Eugene for his encouragement and love. I don't know where I would be without you all!

Abstract

Carbon dioxide emissions from burning fossil fuels is one of the key underlying causes of global warming. The removal of carbon dioxide from the atmosphere, as well as the mitigation of the use of fossil fuels is of growing concern with carbon dioxide levels approaching non-reversible amounts, and addressing the issue is becoming imperative. Solar fuels offer an elegant solution and merit research and understanding. Solar fuels store solar energy in chemical bonds and offer a synthetic, carbon neutral and renewable alternative to fossil fuels. They directly address issues of the intermittency of solar energy and its transport and storage. Carbon dioxide photocatalysis also offers the possibility of a carbon negative process, via synthetic formation of chemicals such as methanol or higher hydrocarbons for use as feedstock or solvents in chemical industries. This thesis focuses on the use of organic semiconductors for solar fuels applications. The processability of organic materials, tuneable energetics, and functionalities as well as their inexpensive starting supplies and scalability make them an ideal candidate as materials in the formation of solar fuels. This work initially focused on photoelectrochemical water splitting. Specifically, it was found that the presence of an organic overlayer with glycol chains and anchor groups showed an increase coverage of TiO_2 ALD at low cycle numbers, and showed an increased stability compared to the same device with no overlayer. This study highlighted the potential of organic functionalities in addressing the issues of adhesion and stability in photocathodes. Principles from photoelectrochemistry were adapted when looking into photochemistry for carbon dioxide reduction. Firstly, a set up was designed, built, and optimised for gas phase photoreduction of carbon dioxide. In conjunction a series of conjugated, solution processable polymers of intrinsic microporosity were designed and adjusted for use as materials catalysing carbon dioxide photoreduction in the presence of hydrogen. The structure-performance relationship was interpreted, and it was found that increasing pore sizes and higher photoluminescence decay times were related to increased CO production. The polymers were also tested as heterojunctions and with the presence of a copper-based co-catalyst which enhanced activity significantly. Learning from the design of this iptycene based series, another series based on spirobifluorene compounds, with higher yields and fewer synthetic steps was designed to further investigate pore sizes and taking advantage of the structure's known fluorescent properties. These studies paved the way for solution processable polymers for this application. This work outlines the interdisciplinary nature of photocatalysis and emphasizes the multitude of factors to be reconsidered in this application, in an attempt to lead to intelligent material and testing design.

Contents

1. INTRODUCTION 1

1.1. Climate Change and Solar Energy 1

1.1.1. Motivation and History 1

1.1.2. Renewable Energy Focused on Solar 2

1.1.3. Hydrogen 4

1.1.4. Carbon Dioxide Reduction 4

1.1.4.1. Current methods for methane, carbon monoxide and methanol production 5

1.2. Working Principles 6

1.2.1. PV + Electrolysis 7

1.2.1.1. Photovoltaics 7

1.2.1.2. Coupling with electrochemistry 8

1.2.2. Photoelectrocatalysis 8

1.2.3. Photocatalysis 10

1.2.3.1. Light absorption 11

1.2.3.2. Charge separation 11

1.2.3.3. Transfer of charges 14

1.2.3.4. Utilisation of charges 15

1.3. Photoreduction of Carbon Dioxide 16

1.3.1. General information 16

1.3.2. Hydrogen oxidation as the co-reaction 18

1.3.2.1. Hybrid systems 19

1.3.3. Organic Semiconductors 19

1.3.3.1. Carbon Nitrides 20

1.3.3.2. Polymer Networks 21

1.4. Techniques and Concepts 32

1.4.1. Optoelectronic Properties 32

1.4.1.1. Photoelectron spectroscopy in air (PESA) 32

1.4.1.2. UV-Vis 32

1.4.1.3. Time-correlated single photon counting (TCSPC) 33

1.4.1.4. Photoluminescence quantum yield (PLQY) 35

1.4.2. Material Properties 35

1.4.2.1. Brunauer–Emmett–Teller (BET) 35

1.4.2.2. Inductively coupled plasma mass spectrometry (ICP-MS) and digestion 38

1.4.3. Techniques 38

1.4.3.1. ALD 38
1.4.3.2. Calculating parameters in photocathode chopped light curves. 40
1.4.3.3. Organic photovoltaics (OPV) basic theory 41

1.5. Project Aims and Thesis Outline 43

1.6. References 44

List of Figures

Figure 1.1: Terrestrial solar spectrum at AM 1.5 using data modelled by the SMARTS2, adapted from refs. [17,18] *Figure plotted with Matt Rosenfeld, and included also in his part II thesis.* 3

Figure 1.2: Schematic representation of solar fuel cycle. 5

Figure 1.3: Illustration of various types of technologies for the production of solar fuels.[62] Illustrating a) PV cell supplying energy for electrolysis b)PV cell in an "artificial leaf" wireless set-up, with OEC and HEC on either side of the PV cell, including electrodes c)photoanode PEC device, d)photocathode PEC device, e) tandem photocathode-photoanode device with no added bias f)photocatalysis of particles in water, g)photocatalysis in gas phase of particles on a substrate..... 7

Figure 1.4: Schematic of a typical conventional structure solar cell architecture, where ITO is indium tin oxide, an electrode, HTL is the hole transporting layer and ETL the electron transporting layer. 8

Figure 1.5: Schematic of general photocatalysis operation, showing the 4 key steps: 1) light absorption 2) charge separation 3) transfer of charges 4) utilisation of charges. 11

Figure 1.6: Typical Jablonsky diagram taken from ref[94]. S refers to a singlet state and T refers to a triplet state. 13

Figure 1.7: Schematic of three different types of heterojunctions, showing a) type I, b) type II and c) type III 14

Figure 1.8: diagram summarising factors effecting carbon dioxide photocatalyst design..... 17

Figure 1.9: possible binding modes of carbon dioxide adsorbed onto a photocatalyst, figure redrawn adapted from ref[118] 17

Figure 1.10: typical structure of g-C_3N_4 20

Figure 1.11: Chemical structures **1-16**, figure adapted from [102] 22

Figure 1.12: Chemical structures **17-27** 24

Figure 1.13: Chemical structures **28-39** 26

Figure 1.14: Chemical structures **40-48** 27

Figure 1.15: example of PESA spectra taken from ref.[176] 32

Figure 1.16: A method to obtain the bandgap of a polymer by construction from a UV-Vis spectrum, Figure adapted from Matt Rosenfeld Part II thesis. 33

Figure 1.17: Gas adsorption stages diagram, a) shows the beginning of pore filling and micropore filling, b) monolayer formation c) formation of multilayer d) fully filled pore. 36

Figure 1.18: Isotherm types, image is from ref.[192] duplicated with permission. 36
Figure 1.19: description of features of a typical Type IV isotherm, adapted from ref. [193] with permission. 37
Figure 1.20: Schematic of ALD function.....39
Figure 1.21: Figure showing the ALD growth times where (a) shows linear growth- Frank-Van der Merwe Growth, (b) shows Volmer-Weber Growth while (c) and (d) show two types of Stranski-Krastanov growth. This figure was reproduced from [206] with permission.....40
Figure 1.22: Explanation of parameters extracted from chopped light curves monitoring photocathode performance, where V_{onset} is extrapolated from tangent a, V_{dark} is the dark onset potential, obtained from the dark current, V_{photo} is calculated from the difference between the two. Crossover potential is where tangent a and b meet. 41
Figure 1.23: Typical current density vs voltage curve for a solar cell.....42

List of Tables

Table 1.1: Products and half-cell redox potentials of various half-reactions that can occur during photocatalytic water splitting or CO_2 reduction. Reproduced with permission from[102]. Reported at pH 7 rather than at standard conditions (pH 0) in order to reflect the pH that would be required in water at neutral conditions. 15
Table 1.2:Table summarising data from recent literature on carbon dioxide photoreduction 28

Abbreviations

°C = degrees Celsius

Đ = polydispersity

δ = NMR chemical shift

ε = molar extinction coefficient

λ = wavelength

μ = micro

AA = ascorbic acid

AM 1.5 = Air Mass 1.5 global spectrum

ATP = adenosine triphosphate

AQY = apparent quantum yield

BET = Brunauer-Emmett-Teller

BHJ = bulk heterojunction

Bipy = bipyridine

Bpin = pinacolato boron, $(CH_3)_4C_2O_2B$

BT = 2,1,3-benzothiadiazole

CB = conduction band

CB = chlorobenzene

CCS = carbon capture and storage

COD = cyclooctadiene

COF = covalent organic framework

CV = cyclic voltammetry

DCB = dichlorobenzene

DCM = dichloromethane

DIO = 1,4-diethylene dioxide

DMF = N,N'-Dimethylformamide

DMSO = dimethyl sulfoxide

EDTA = ethylenediaminetetraacetic acid

Ea = activation energy

EA = electron affinity

E_g = bandgap; optical gap

EI = electron ionisation

ETL = electron transport layer

eq. = mole equivalent(s)

eV = electron volt(s) = 1.602×10^{-19} J

FF= fill factor

FET = field-effect transistor

FMO = frontier molecular orbital

FTIR = fourier-transform infrared spectroscopy

g-C_3N_4 = graphitic carbon nitride

GC-FID = gas chromatography with flame ionisation detection

GPC = gel permeation chromatography

GPC (ALD) = growth per cycle

Gt = gigaton(s) = 10^{12} kg

HCP = highly cross-linked polymer

HEC = H_2 evolution catalyst

HER = hydrogen evolution reaction

HOF = hydrogen-bonded organic framework

HOMO = highest occupied molecular orbital

HPLC = high-performance liquid chromatography

HRMS = high-resolution mass spectrometry

HTL = hole transport layer

ICP-MS = inductively coupled plasma - mass spectrometry

ICP-OES = inductively coupled plasma - optical emission spectrometry

ICT = intramolecular charge transfer

IP = ionisation potential

IPCE = incident photon to converted electron

ITO = indium tin oxide

IUPAC = International Union of Pure and Applied Chemistry

J = NMR coupling constant

J_{SC} = short circuit photocurrent

K = kelvin

LED = light-emitting diode

LUMO = lowest unoccupied molecular orbital

MFC = mass flow controller

M_n = number-averaged molecular weight

M_w = weight-averaged molecular weight

n-BuLi = n-Butyllithium

NADP = nicotinamide adenine dinucleotide phosphate

NBS = N-bromosuccinimide

nm = nanometre(s) = 10^{-9} m

NMR = nuclear magnetic resonance (spectroscopy)

NP = nanoparticle

OD = outer diameter

OEC = O_2 evolution catalyst

OER = oxygen evolution reaction

OLED = organic light-emitting diode

OPV = organic photovoltaic

OSC = organic solar cell

OWS = overall water splitting

$P(o\text{-}tol)_3$ = tri(o-toyl)phosphine

P3HT = Poly(3-hexylthiophene)

PCBM = phenyl C61/71 butyric acid methyl ester

PCE = power conversion efficiency

PD = polydispersity = M_w/M_n

$Pd_2(dba)_3$ = tris(dibenzylideneacetone)dipalladium(0)

$Pd(OAc)_2$ = palladium(II) acetate PDI polydispersity index

PDINO = (N,N'-Bis(N,N-dimethylpropan-1-amine oxide)perylene-3,4,9,10-tetracarboxylic diimide)

PESA = photoelectron spectroscopy in air

PFO = poly(9,9'-dioctylfluorene), in other work represented by PF or PDF

Ph = phenyl

PIAS = photo-induced absorption spectroscopy

PIM = polymer of intrinsic microporosity

PL = photoluminescence

PLQY = photoluminescence quenching yield

ppb = parts per billion

ppm = parts per million

PTFE = polytetrafluoroethylene

PV = photovoltaic

Rpm = revolutions per minute

RT = room temperature

RWGS = reverse water gas shift reaction

SEM = scanning electron microscopy

SMARTS2 = Simple Model for Atmospheric Radiative Transmission of Sunshine

S_N2 = second-order nucleophilic substitution

S_NAr = nucleophilic aromatic substitution

SPQY = specific product quantum yield

TAS = transient-absorption spectroscopy

TDMAT= Tetrakis(dimethylamido)titanium(IV)

TEA = triethylamine

TEM = transmission electron microscopy

TGA = thermogravimetric analysis

Th = thiophene

THF = tetrahydrofuran

TMS = tetramethylsilane

TOF = turn over number

TON = turn over frequency

TOEA = triethanolamine

UV-Vis = ultra-violet visible (spectroscopy)

VB = valence band

V_{OC} = open circuit voltage

wt% = percent by weight

XPS = x-ray photoelectron spectroscopy

1. Introduction

This introduction will firstly outline the motivations for the work presented in this thesis, then will explain the basic principles of solar fuels and photocatalysis. The next section will then include a summary of the literature in the field of carbon dioxide photoreduction, followed by the techniques and principles utilised throughout the studies. The project aims and an outline of the thesis will be presented at the end of the chapter.

1.1. Climate Change and Solar Energy

1.1.1. Motivation and History

By burning fossil fuels, humans are releasing an extra 29 gigatons of carbon dioxide per year, which cannot be absorbed by oceans and land, and therefore largely remains in the atmosphere.[1] As of 2020, the level of carbon dioxide is at 416 ppm, the highest in 650 000 years.[2] The current rate of increase of CO_2 in the atmosphere is a 100 times faster than the rate of increase from when the last ice age ended. The increasing anthropogenic CO_2 concentration in the atmosphere is widely accepted as being the main factor in global warming.[3] This term refers to the phenomenon, experienced in recent decades, in which the mean temperature of the combined air and sea surface temperatures averaged over the globe are increasing.[4] Carbon dioxide, alongside methane and water vapour are present in the atmosphere and they absorb outgoing IR radiation, effectively acting as a "blanket" around the globe which results in a green-house effect, thus causing global warming.[3] Global warming has been linked to extreme weather, disruption of habitats, increased disease and pollution, and rising sea levels.[5] The earth's temperature has increased by 0.9 ^{o}C since 1880.[6] The increase in temperature due to carbon dioxide emissions, is not expected to be reversed if CO_2 emissions stopped completely. It is therefore not only imperative to address emissions, but to also begin thinking of ways to mitigate the amount of carbon dioxide present in the atmosphere.[7,8] The 2015 Paris COP21 Agreement aims to limit global warming to below 1.5 ^{o}C total temperature increase compared to pre-industrial revolution levels.[9,10] According to the International Energy Agency, emissions have to be reduced by 70 % by 2040 to keep on track with this aim.[11] One of the benefits from this has been the increased attention towards renewable energies, especially solar.[12]

1.1.2. Renewable Energy Focused on Solar

Renewable energy sources can produce energy indefinitely, without running out, unlike fossil fuels and nuclear energy, which are classified as non-renewable. Another particularly interesting property of renewable energy is that it has the potential to provide energy with net zero emissions, thus addressing the pressing concern of mitigating carbon dioxide in the atmosphere.[13]

Around 1.08×10^{14} kW of solar energy reaches the Earth's atmosphere. If 0.1% of this energy was utilised with an efficiency of 10%, energy consumption would be met four times over. If we could capture one hour's worth of all solar energy entering the atmosphere, it would be possible to meet the human energy needs for an entire year.[14] This leaves solar energy as the most abundant out of all renewable energies available.

Solar energy can be harnessed in various ways, as heat in solar thermal processes, as electricity using photovoltaics, and stored in chemical form using photocatalysis and photo electrochemistry. Solar thermal power refers to the process of harnessing solar energy to provide heat, either by passively harnessing solar light such as using lenses to concentrate the energy, or actively, making use of pumps and fans to circulate heat carrying fluids. These can directly provide heat to residential homes or industry.[15] Concentrated solar power, (CSP), concentrates solar energy using mirrors, which yields high enough temperatures to form steam and generate electricity by turning a turbine, these are more suited to larger areas with a lot of sun exposure. CSP markets now have a cumulative global capacity of around 5.5 GW, while solar thermal power has a capacity of 480 GW.[15] Photovoltaics (PV) enable the conversion of solar energy into electricity directly. These normally require a semiconducting material. Semiconductors normally have bandgaps between 1 and 3.5 eV and are characterised by their ability to become conductive when injected with a charge either at an electrode or by photo-excitation.[16]

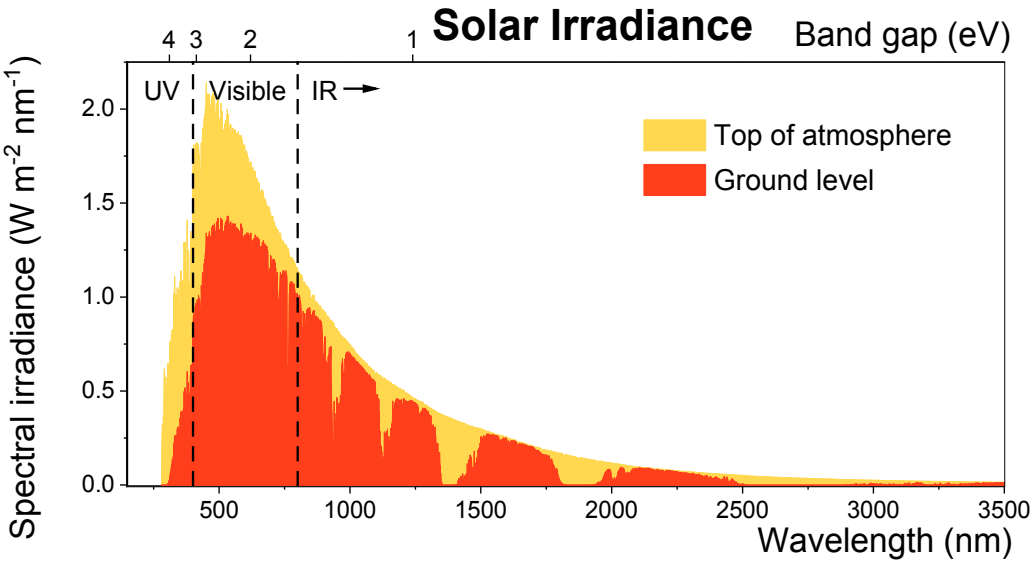


Figure 1.1: Terrestrial solar spectrum at AM 1.5 using data modelled by the SMARTS2, adapted from refs. [17,18] *Figure plotted with Matt Rosenfeld, and included also in his part II thesis.*

Semiconductors that absorb in the UV region normally have an increased driving force in photo-redox reactions, but semiconductors absorbing visible light (between 400 and 800 nm), as shown in **Figure 1.1**, are able to absorb a much larger portion of the solar spectrum.[18] PV capacity as of 2019 is over 635 GW, which supplies 2% of global electricity demand.[19] PV have the potential to fully substitute coal-fired power plants in Europe and it is the solar technology currently most likely to keep on track with the goals of the Paris Agreement.[20] Furthermore, as of 2020, due to technological advances in the last decade, PV is the cheapest source of energy globally.[21] However, an issue remains in the use of PV as the sole form of harnessing solar energy, which is the intermittent and geographically dependent supply of sunlight, and the discrepancy between demand times and highest PV efficiency times. Currently PV technologies rely on batteries and solar-grid integration to address this issue, which suffer from wasteful energy losses, and raise possible concerns in the future scalability of batteries and their disposal.[22–26] An exciting solution is the use of solar fuels, whereby solar energy can be harnessed and stored in chemical bonds, formed using photoelectrocatalysis or photocatalysis.[27] Solar fuels are a synthetic and clean alternative to fossil fuels, they have the potential of diversifying the supply of energy, by forming fuel which can be stored and transported, while retaining the sustainability, renewability and carbon neutral nature of solar energy.[28] Forming solar fuels effectively tackles the challenges associated with the intermittent nature of solar energy supply, and tackles the challenge of cost-effectively and efficiently storing energy, since it is preserved in chemical bonds.[29] This is because the fuels obtained can

be used at night, or in areas with few day-time hours, and they can be easily transported, especially if the hydrocarbon produced are in the liquid phase.

1.1.3. Hydrogen

The idea that it would be cheaper to send hydrogen through pipes rather than electricity through wires was first published in 1972.[30,31] Generally in the 1970s the idea of obtaining hydrogen from electrolysis of water and transferring it to cities began to gain interest.[32,33] Hydrogen has the highest energy per mass of fuel, but the lowest by volume. It can be utilised either in a fuel cell, or combusted to replace natural gas, with its only by-product being water.[34,35] Currently, hydrogen's uses are tied strongly to the fertiliser industry, due to its use in the Haber Bosch process and the production of ammonia, and it is also used in the production of methanol.[36] Nonetheless it is expected to play a key role in the future of fuel and electricity, as we take steps away from fossil fuels.[37]

Currently over 90% of hydrogen is formed from fossil fuels, either via steam reforming of natural gas or oil, or via gasification of coal, and about 4% is formed from water electrolysis.[38] Electrolysis is a promising method for hydrogen production, whereby water is broken down into oxygen and hydrogen using a current passing through two electrodes in water. The efficiencies reached with this method can be up to 80%.[39] However, the electrical energy required for this process is often acquired through fossil fuels consumption. Incorporating solar light into hydrogen evolution, can mitigate or minimise the use of fossil fuels partially or completely.[40,41]

1.1.4. Carbon Dioxide Reduction

Another approach consists of directly photo-reducing carbon dioxide into carbon based solar fuels. This is particularly interesting because (1) it could produce carbon-based chemicals such as methane, directly combustible into exploitable energy, releasing CO_2 for an overall carbon neutral process and (2) it has the potential of establishing an overall carbon negative process via the formation of substances such as methanol, acetic acid, or even higher hydrocarbons, which could be used in industry.[42,43] The schematic in **Figure 1.2** illustrates this in more detail. First, solar energy is used in the conversion of carbon dioxide into carbon-based chemicals, which can be stored and transported. Some of these carbon-based products can be combusted to release energy in the place of fossil fuels, releasing CO_2, in the carbon neutral process. Some of these can be utilised in the chemical industry in an overall carbon negative process. Carbon dioxide photocatalysis has the potential to simultaneously tackle the energy crisis and

environmental issues resulted from global warming. It offers the possibility of mitigating increasing carbon dioxide levels in the atmosphere, as well as providing carbon-based feedstock and a carbon neutral, direct alternative to fossil fuels.

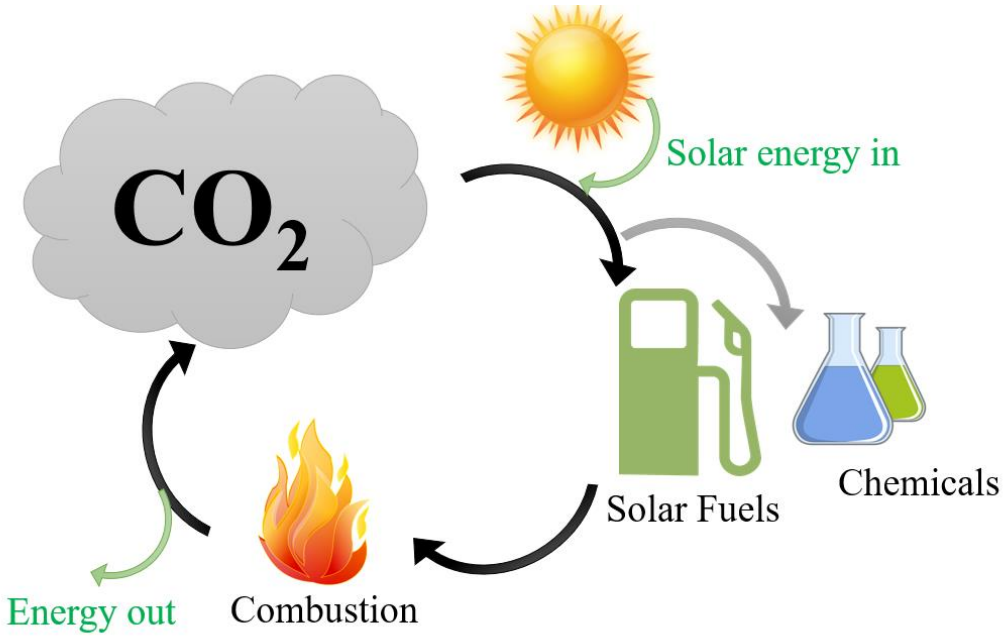


Figure 1.2: Schematic representation of solar fuel cycle.

1.1.4.1. Current methods for methane, carbon monoxide and methanol production

Methanol can be used in synthetic chemistry in making hydrocarbons, polymers, proteins and as a solvent. It is also a possible source of liquid fuel.[44] Methanol can be used in a fuel cell, bypassing the need for hydrogen, it can be blended with gasoline or diesel which has shown promise, or it can be used as a fuel by itself, having shown an efficiency of over 40% in methanol fuelled engines, which is comparable to current diesel engines.[45–48] Currently industrial production of methanol comes from the reaction of carbon monoxide and hydrogen, reacted over a copper-zing based catalyst on an alumina support at pressures of around 50-100 bar, at 270 ^{o}C.[44] Carbon monoxide has uses in manufacturing of hydrocarbons such as the aforementioned methanol and aldehydes. It is mostly formed via burning carbon dioxide in an excess of carbon, at temperatures of above 800 ^{o}C.[49] Another known process used to convert syngas (carbon monoxide and hydrogen) into methanol or liquid hydrocarbons, is the Fischer-Tropsch process, which also requires temperatures of up to 300 ^{o}C.[50–53] Methane is commonly used as a fuel, ranging from rocket launchers to camping stoves. [54,55] Methane in industry is

mainly obtained from the Sabatier reaction, by which hydrogen and carbon dioxide are converted into methane and water over a nickel catalyst at around 350 ºC and 30 bar, with a highly exothermic process requiring careful thermal control, and efficiencies of around 50%.[56] The prospect of obtaining these products using renewable energy, and utilising them as storage for solar energy would be extremely exciting in the tackling of carbon dioxide emissions from fossil fuels, and in addressing their depletion and the absolute need to find alternatives, especially since the change in infrastructure is minimal when the same products are obtained.[57,58] Photoelectrocatalysis and photocatalysis provide the opportunity to do just this. Natural photosynthesis is the basis for photocatalysis. Normally, photosynthesis describes a process that is thermodynamically uphill, while photocatalysis describes a kinetically uphill process that is sped up with the use of a photocatalyst, these terms, however, are often not separated in literature.[59] Natural photosynthesis is the process that plants use to convert light into chemical energy, which is stored in glucose molecules made from carbon dioxide and water, with oxygen as a by-product. Biological photosynthesis employs a Z-scheme (explained further in section 1.2.3.2) whereby, chlorophyll absorbs photons leading to an electron and a hole pair being formed. The hole is used to oxidise water into oxygen, while the electron undergoes an electron transport chain to provide the synthesis of ATP (adenosine triphosphate), and the reduction of NADP (nicotinamide adenine dinucleotide phosphate) to NADPH.[60,61]

1.2. Working Principles

This section will introduce some of the key concepts of photocatalysis (PC), photo electrochemistry (PEC) and will touch on photovoltaics (PV). **Figure 1.3** illustrates the types of technologies that can be utilised for solar fuels production, highlighting the differences between PC, PEC, and PV + electrolysis. To help with this discussion, a brief overview of PV will be described in Section 1.2.1 followed by PEC outlined in Section 1.2.2 and finally moving towards PC in Section 1.2.3.

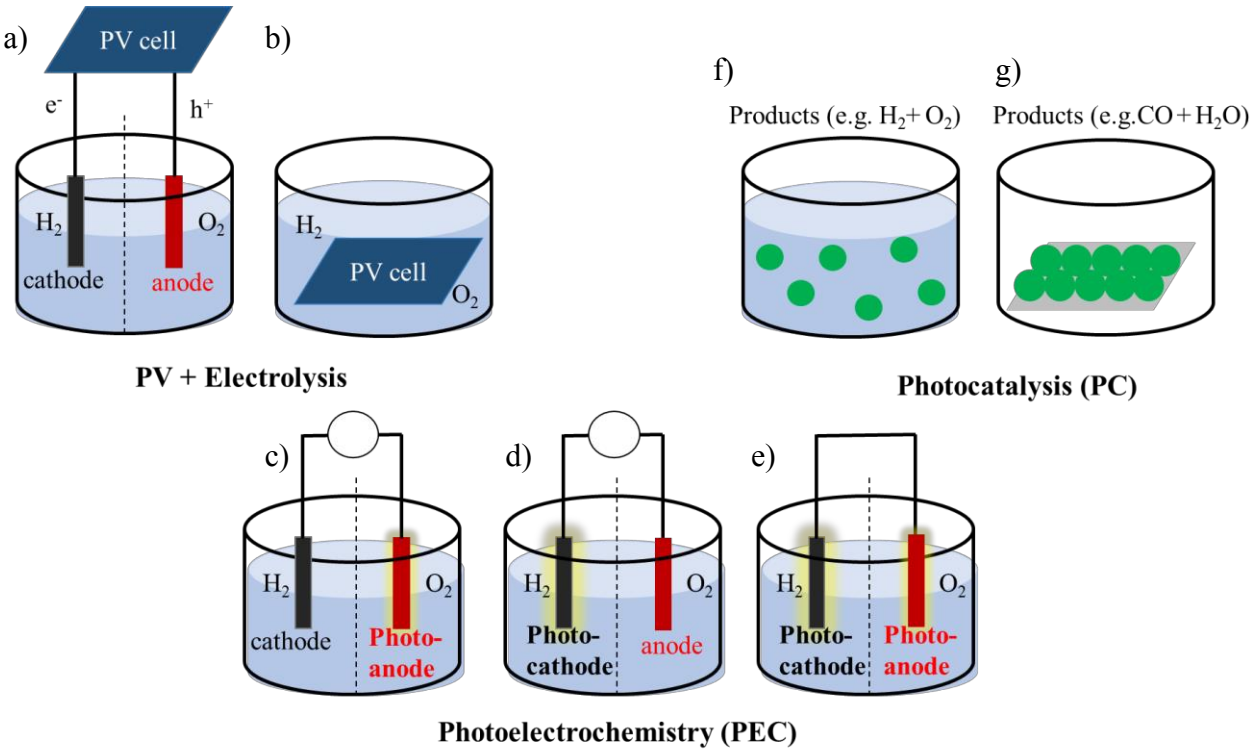


Figure 1.3: Illustration of various types of technologies for the production of solar fuels.[62] Illustrating a) PV cell supplying energy for electrolysis b)PV cell in an "artificial leaf" wireless set-up, with OEC and HEC on either side of the PV cell, including electrodes c)photoanode PEC device, d)photocathode PEC device, e) tandem photocathode-photoanode device with no added bias f)photocatalysis of particles in water, g)photocatalysis in gas phase of particles on a substrate.

1.2.1. PV + Electrolysis

One promising technique for solar fuels production is the implementation of a photovoltaic device to supply electricity to an electrolysis or electrochemistry device to produce solar fuels, illustrated in **Figure 1.3a)**. Hydrogen evolution will mostly be covered since it is a much easier and more researched reaction than carbon dioxide photoreduction. Many of the same considerations are, however, useful, since the potentials required are similar and the methodologies come from the same concepts. Firstly PV function will be explained, and then tied into its use to power electrocatalysis.

1.2.1.1. Photovoltaics

Photovoltaic devices, as mentioned, convert solar energy into electricity directly. Silicon based photovoltaic cells are the most commonly used in solar panels to date.[63,64] Photovoltaics are made up of a central photoactive material, normally absorbing in the visible region of the solar spectrum, sandwiched between two charge transporting layers, which in turn have electrodes either side, as shown by the schematic in **Figure 1.4**, which outlines the architecture of a typical conventional structure device. In the context of OPV, a conventional structure, the cathode

(Indium Tin Oxide-ITO in this case) is loaded on glass, followed by a hole transporting layer deposited on top. The electron transporting layer sits on top of the photoactive layer, which in turn is partially covered by a metal electrode. In this type of architecture, conducting glass constitutes the bottom electrode, and a low work function metal or oxide is at the top. In an inverted structure, the two metals are inverted in the device, this is commonly used with perovskite photoactive materials.[65] In a PV device, the photoactive layer absorbs a photon which causes the formation of a hole and an electron, which in turn are split up in the structure and travel to their respective electrodes, which "collect" the charge formed in the form of electric current, giving electricity.

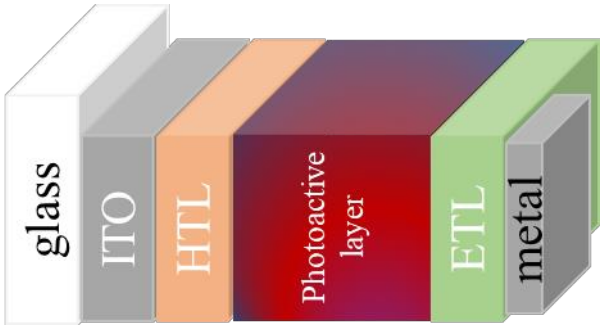


Figure 1.4: Schematic of a typical conventional structure solar cell architecture, where ITO is indium tin oxide, an electrode, HTL is the hole transporting layer and ETL the electron transporting layer.

1.2.1.2. Coupling with electrochemistry

Figure 1.3a) shows how PV can be used to provide the first type of solar fuel system, in which a photovoltaic provides electricity for the electrolysis of water into hydrogen and oxygen at each electrode respectively.[66] This method currently is the most advanced and most efficient in the field, especially since electrolysis to split water is now a commercial process, but does suffer from high costs, and requires multiple PV cells or multijunction in order to supply the high voltage.[36] Solar water splitting cells, also known as "artificial leaves" are comprised of a PV layer for light absorption, compacted with electrolysers, immersed in the water, directly carrying out reduction and oxidation reactions on either side of the solar cell, without the need for an external wire connection, as illustrated in **Figure 1.3b).**[67] Recently Andrei *et al* showed the potential of a perovskite based floating artificial leaf, for syngas or hydrogen production, showing the potential of this technology for large scale applications.[68,69] Although currently efficiencies and stabilities are low for this process, it has a lot of potential with further research.

1.2.2. Photoelectrocatalysis

Figure 1.3c-e) showcases photoelectrochemical methods for solar fuel production. **c** and **d** show the usual photoelectrode cell, with the configurations of a n-type photoanode-HEC cathode or p-type photocathode-OEC anode respectively. Whereby only one of the two components is the light absorber, but a current and voltage is also required to offset the remaining half reaction.[70] These are both assisted processes, and are often split in order to optimise each photoelectrode, however unassisted photocatalysis can be achieved by pairing an optimised photoanode with an optimised photocathode, requiring no further bias, as shown in **Figure 1.3e).**[71,72]

The formation of hydrogen via light-assisted water splitting has been of increasing interest as a solution for mitigating our dependence on fossil fuels. Hydrogen formation from sunlight is particularly attractive in tackling the intermittent nature of solar radiation, by allowing harvested photons to be stored in chemical bonds, thus facilitating usage, transport and scale up of widespread renewable solar energy usage.[73] Photoelectrochemical water splitting is a direct route into achieving renewable hydrogen production. It constitutes a semiconducting catalyst that absorbs solar energy to drive the redox processes that form hydrogen and oxygen, the equations of which are summarised below.[74]

Reduction	$2H^+(aq) + 2e^- \rightarrow H_2(g)$	Hydrogen evolution reaction (HER)	(1.1)
Oxidation	$H_2O(l) \rightarrow \frac{1}{2} O_2(g) + 2H^+(aq) + 2e^-$	Oxygen evolution reaction (OER) [75]	(1.2)
Overall	$H_2O(l) \rightarrow H_2(g) + \frac{1}{2} O_2(g)$	$\Delta G = +237$ kJ mol^{-1} [76]	

The free energy requirement of water splitting is $\Delta G = +237$ kJ mol^{-1}, which corresponds to $E°= 1.23$ V ($E° = -\Delta G°/nF$). Therefore, theoretically, semiconductor bandgap must be at least 1.23 V in order to provide sufficient potential to drive water splitting.[77] This is defined at standard conditions, of 1 M concentration, 1 atm pressure and 25 ^oC temperature. This potential is unchanged at varying pH following the Nernst equation. At high pH hydrogen and oxygen evolution require a lower reduction potential, while at low pH a lower oxidation potential is required. This should be taken into account when optimising photocathodes and photoanodes, since conditions which can aid one reaction, can disfavour the other.[78]In practice, due to losses at the electrodes and interfaces and low conductivity, water splitting often requires an overpotential, to surpass the kinetic barriers to hydrogen and oxygen evolution. This normally

requires an overall potential of around 1.5-1.8 V. A semiconductor suitable for this application should have a sufficient bandgap to drive this reaction but should also remain small enough to maximise the amount of solar light absorbed. The visible range of the spectrum (390-700 nm) accounts for around 43% of solar energy, to take advantage of this, the materials bandgap should be lower than 3 eV. Visible-light absorbing semi-conductors are ideal candidates.[79] In order for a photoelectrochemical system to work, the Frontier Molecular Orbitals (FMOs) /Conduction band (CB)/ Valence Band (VB) of the material should be aligned with that of the redox potentials required. The conduction band should be more negative than the reduction potential of H^+/H_2, and the valence band should be more positive than the oxidation potential of O_2/H_2O.

1.2.3. Photocatalysis

A schematic of the basics of photocatalysis is shown in **Figure 1.3f-g),** no external bias is required in the conversion of solar energy into chemical energy by a photocatalyst. The concept of photochemistry was firstly postulated in the 19th century, whereby the Grotthuss–Draper principle stated that only absorbed light in a system could bring about a photochemical change.[80] Over the course of the 20th century studies were carried out, especially on oxides and their photochemical properties, highlighting reactions which can occur on metal oxide surfaces upon UV-light absorption.[81] The field of photocatalysis took off following the oil crisis of the 1970s which prompted an urgent search into renewable energy alternatives.[82] Fujishima and Honda reported in 1972 on water photolysis using n-TiO_2, effectively showing water splitting into hydrogen and oxygen for the first time without using external applied potentials.[83] Following this, research blossomed into inorganic semiconducting single crystals able to carry out water splitting under visible light. Activity in this area decreased due to challenges with material stability, high costs and low efficiencies. Since the 1990s this area picked up again due to the shift from single crystal materials, to high surface area nanostructures, prompted by dye-sensitised colloidal TiO_2 films, proposed by O'Regan and Grätzel, which was pivotal and caused an increased interest in photocatalysis.[72,84]

Photocatalysis is characterised by 4 key steps, highlighted in **Figure 1.5**. The first is the absorption of light by the photocatalyst to form an exciton (bound electron-hole pair). The second is the separation of the exciton into excited charges, the third is the transfer of the electrons and holes to the active site of reaction, and the fourth is the utilisation of these charges

in reactions. Both half reactions of the redox systems must occur for the system to be sustainable and function.[85] This section will cover the four steps in more detail.

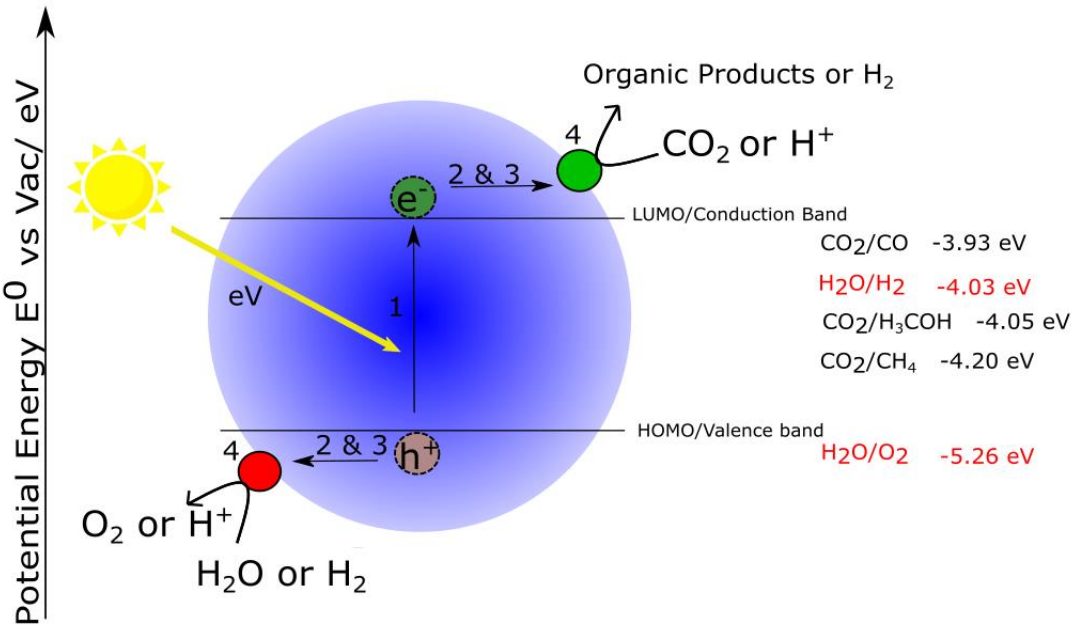


Figure 1.5: Schematic of general photocatalysis operation, showing the 4 key steps: 1) light absorption 2) charge separation 3) transfer of charges 4) utilisation of charges.

1.2.3.1. Light absorption

Light absorption in photocatalysis is very much like light absorption in photovoltaic devices. This first step of photocatalysis proceeds with the absorption of a photon of energy, from a semiconductor which has a bandgap smaller than the photon energy absorbed.[86] Bandgap refers to the difference in energy of adding or removing an electron in a system.[87] A bandgap is the energy difference between a conduction band minimum and valence band maximum in inorganic semiconductors, and between the lowest unoccupied molecular orbital (LUMO) and highest occupied molecular orbital (HOMO) in an organic semiconductor. This distinction is due to the lack of molecular orbitals in many inorganic materials, and rather a delocalisation of states across its structure.[88] Absorption of a photon excites an electron, leading to the formation of an exciton, a coulombically bound hole and electron pair.

1.2.3.2. Charge separation

Formation of an exciton needs to be followed by its dissociation into electron and hole polarons.[89] The exciton binding energy keeps the charges together. The dielectric constant of a material is defined as a measure of how easily a material can become polarised when an electric field is imposed. Inorganic semiconductors normally have high dielectric constants, the charges can more easily spread through the structure, leaving them more screened, and leading to a lower coulombic interaction. This results in a low exciton binding energy, normally around 0.01 eV, and forms what are known as a Wannier–Mott excitons. Conversely, organic polymers have a low dielectric constant, the excitons formed are known as Frenkel-type, and the charges are located very close to each other, leading to a high binding energies, normally between 0.1 and 1 eV.[89–91] Most of the excitons end up recombining, especially in organic materials, due to the high binding energies. Exciton dissociation is often spontaneous in inorganic materials, but in organic materials it often requires donor acceptor character at interfaces between domains with different packing, or at a heterojunction.[92] Fluorescence and phosphorescence are two methods of radiative decay in organic semiconductors, by which the exciton recombines; the former when the ground state and excited state are of the same spin multiplicity, the latter occurs when intersystem crossing is available in the molecule. Non-radiative decay pathways are also available, such as losing energy as heat when a molecule decays within an excited state to a lower vibrational state.

A summary of radiative and non-radiative decay pathways is shown in **Figure 1.6**: Typical Jablonsky diagram taken from ref[94]**Figure 1.6**, also including the relative lifetimes of each transition. Absorption is the fastest, at around 10^{-15} s, while phosphorescence is the slowest at magnitudes of between 10 and 10^{-6} s. For photocatalysis to occur, recombination should be minimised, and the charges require to be separated to take part in the redox reactions.[93]

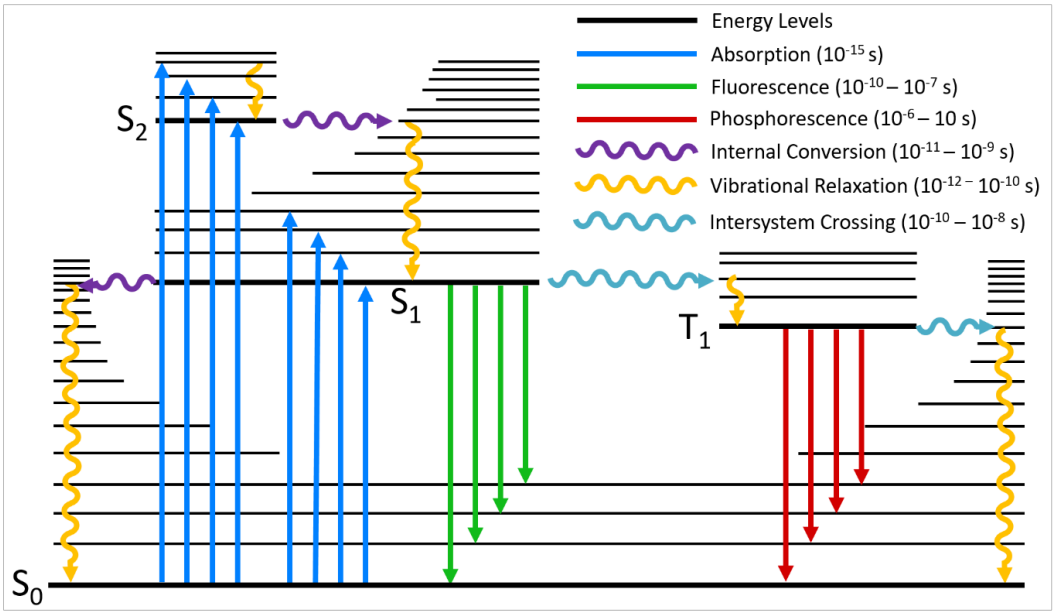


Figure 1.6: Typical Jablonsky diagram taken from ref[94]. S refers to a singlet state and T refers to a triplet state.

Since organic semiconductors suffer from significant losses due to recombination, a technique to improve efficiencies is to use heterojunctions. Heterojunctions arise from the interface of two semiconducting materials of different bandgaps and band alignments, and can be described as type I, type II or type III, which are illustrated in **Figure 1.7**. [95,96]

Type I heterojunctions, sport a straddled gap between semiconductor A and B, the bandgap of semiconductor B will be smaller than that of A, the LUMO will be shallower and the HOMO deeper than A. This means that the charges generated on A will both migrate onto B, where both the reduction and oxidation reactions can take place. This method is not as helpful in reducing recombination, since both redox reactions still occur on the same material and holes and electrons collect on the same material, but it enables the absorption of light at two different energies, due to the two different bandgaps, which can increase the light absorbed and therefore impact rate. Type II heterojunctions have a staggered gap, both the HOMO and LUMO of semiconductor B are deeper than semiconductor A. Because of this, excited electrons from either of the materials will collect onto semiconductor B, while the holes generated will migrate to semiconductor A. This splits up the redox reactions since they happen on one of each of the semiconductors and can vastly decrease recombination. Type III shows a broken gap, the splitting between the staggered gap is so high that there is no longer any overlap. This also does not necessarily aid with charge separation but allows interlayer charge transfer. Z schemes use this type III offset and make use of a charge shuttle in between the semiconductors, in a similar manner to natural photosynthesis. [96] Type I heterojunctions are particularly useful for

photoluminescence detectors, since exciton dissociation is unfavourable, Type III can be used in photocatalysis with Z-schemes, or in the use of tunnel diodes. Type II is the most used in organic photocatalysis and photoelectrocatalysis, due to the often rate determining recombination of charges and the benefits associated with exciton splitting aided by a heterojunction.[97]

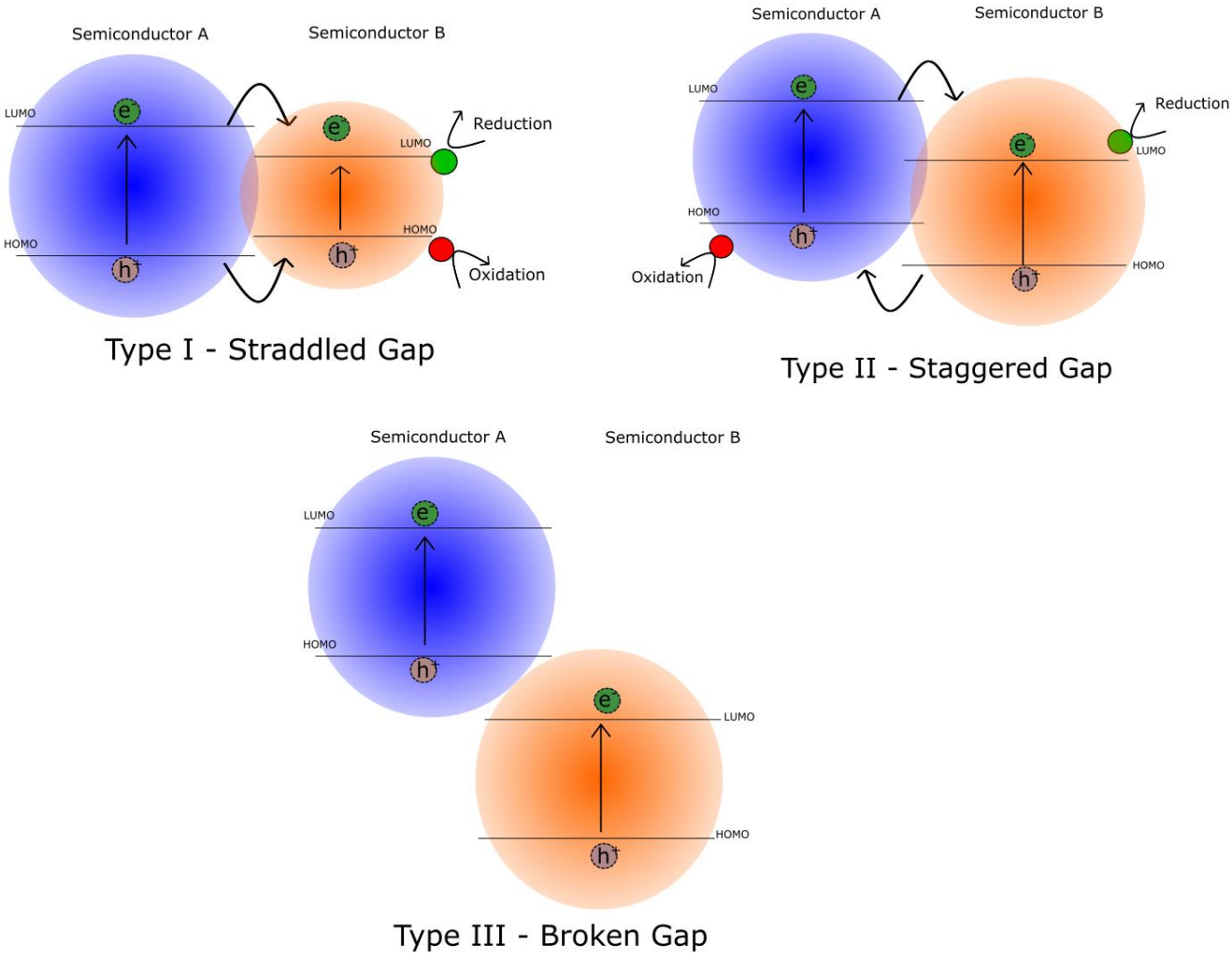


Figure 1.7: Schematic of three different types of heterojunctions, showing a) type I, b) type II and c) type III

1.2.3.3. Transfer of charges

Redox reactions normally occur at a different site to light absorption and exciton formation, so transfer of charges within a system is critical. [98–100] Charge transfer in an organic semiconductor

can occur normally as either a band regime, made up of delocalised wavefunctions of the carrier and therefore coherent transport, or via the hopping regime, whereby the wavefunctions of charges are localised and transport happens in a hopping mechanism. The band regime normally describes charges that have mobilities of more than 5 $cm^2\ V^{-1}\ s^{-1,}$ which is consistent with some regular crystal molecules. However, small molecules and semiconductors normally have much lower mobilities, orders of magnitude below inorganics, which suggest hopping mechanisms are more likely in these structures. This hopping mechanisms is described as a tunnelling of charges within localised states within the molecule. [101] Exciton migration happens on a much smaller distance of a few nm, compared to the hundreds of nanometres that light absorption can occur through.

1.2.3.4. Utilisation of charges

The process of charge utilisations refers to the charges that get to the surface or active site of the molecule and carry out the oxidation and reduction reactions required for photocatalysis. **Table 1.1** shows some of the redox potentials of possible reactions in carbon dioxide photocatalysis.

Table 1.1: Products and half-cell redox potentials of various half-reactions that can occur during photocatalytic water splitting or CO_2 reduction. Reproduced with permission from[102]. Reported at pH 7 rather than at standard conditions (pH 0) in order to reflect the pH that would be required in water at neutral conditions.

Product	**Half-reaction**	E^0 **(pH 7, V *vs.* NHE)**	E^0 **(pH 7, V *vs.* Vac.)**	**Equ^**
Superoxide	$O_2\,(g) + e^- \leftrightarrow O_2^{\bullet-}$	−0.16	-4.28	(1.3)
Methane	$CO_2\,(g) + 8H^+ + 8e^- \leftrightarrow CH_4\,(g) + 2H_2O\,(l)$	−0.24	-4.20	(1.4)
Ethane	$2CO_2\,(g) + 14H^+ + 14e^- \leftrightarrow C_2H_6\,(l) + 4H_2O\,(l)$	−0.27	-4.17	(1.5)
Ethanol	$2CO_2\,(g) + 12H^+ + 12e^- \leftrightarrow C_2H_5OH\,(l) + 3H_2O\,(l)$	−0.33	-4.11	(1.6)
Methanol	$CO_2\,(g) + 6H^+ + 6e^- \leftrightarrow CH_3OH\,(l) + H_2O\,(l)$	−0.39	-4.05	(1.7)
Hydrogen	$2H^+ + 2e^- \leftrightarrow H_2\,(g)$	−0.41	-4.03	(1.8)
Carbon monoxide	$CO_2\,(g) + 2H^+ + 2e^- \leftrightarrow CO\,(g) + H_2O\,(l)$	−0.51	-3.93	(1.9)
Formic acid	$CO_2\,(g) + 2H^+ + 2e^- \leftrightarrow HCOOH\,(l)$	−0.58	-3.86	(1.10)
Oxalic acid	$2CO_2\,(g) + 2H^+ + 2e^- \leftrightarrow H_2C_2O_4\,(l)$	−0.87	-3.57	(1.11)
Oxygen	$2H_2O\,(l) \leftrightarrow O_2\,(g) + 4H^+ + 4e^-$	+0.82	-5.26	(1.12)

The use of a co-catalyst at the material surface/active site can be very useful at this point to facilitate reactions. Co-catalyst can promote the driving and separation of charges due to the interface it forms with the light harvesting material, and can decrease the activation energy

required for photocatalysis to occur, even when charges have enough thermodynamic energy for the reaction.[103]

1.3. Photoreduction of Carbon Dioxide

1.3.1. General information

CO_2 photocatalysis is a much more challenging process than water splitting, since on top of the hurdles presented by hydrogen evolution, the following factors must also be carefully considered: (1) CO_2 photoreduction, like hydrogen evolution from water, is a thermodynamically uphill process. (2) The CO_2 molecule is symmetric and linear, resulting in a very stable and chemically inert molecule which requires activation.[104] (3) When the reaction is carried out in an aqueous solution, hydrogen evolution (HER) from water splitting is an undesired reaction pathway which directly competes with CO_2 reduction, since it requires a comparable reduction potential than HER, but requires more electrons normally.[66] The low solubility of CO_2 in aqueous solvents, and resulting low transport of the molecule to the sites of reduction, contribute to the increased amount of hydrogen, produced preferentially to CO_2 photoreduction products.[105,106] (4) CO_2 photoreduction is a multi-electron process with the potential of forming various products. This makes the process unselective and at times unpredictable which decreases its utility and efficiency. **Table 1.1** outlines some of the key reactions possible at the site of reduction and oxidation.[107,108]

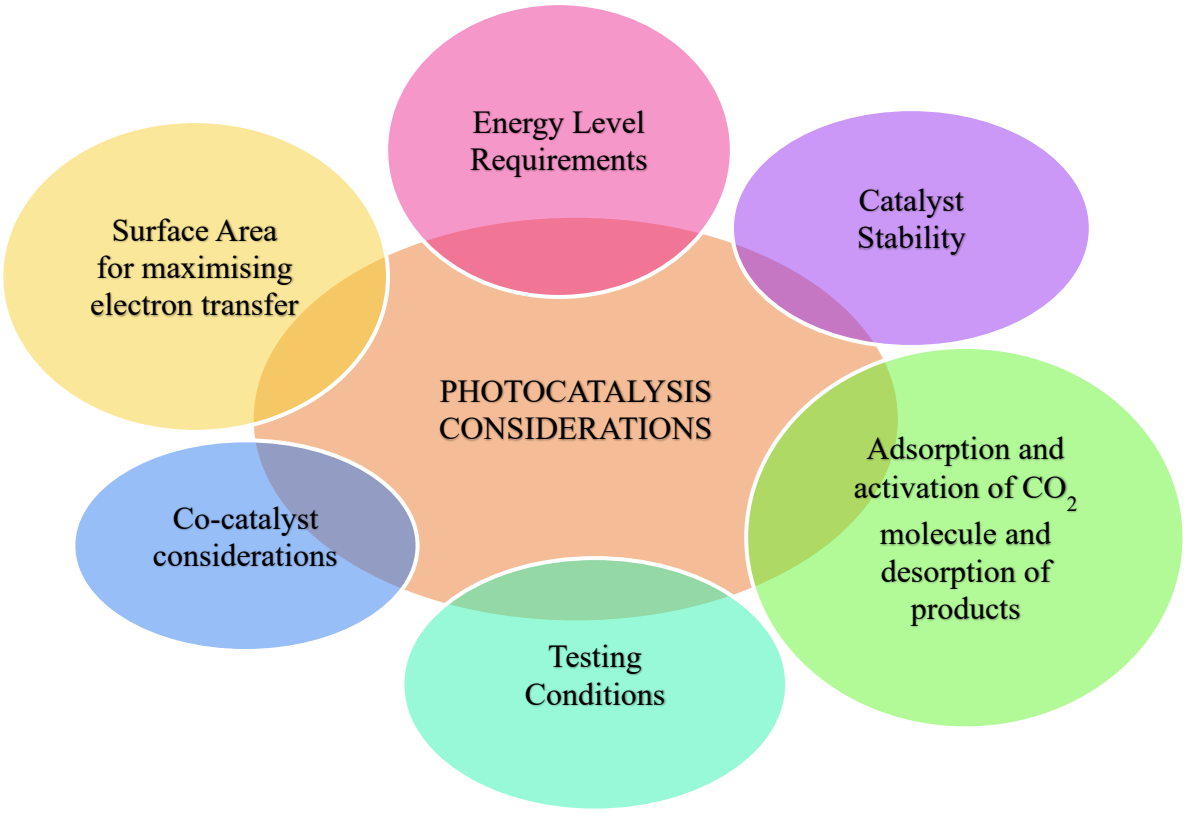


Figure 1.8: diagram summarising factors effecting carbon dioxide photocatalyst design.

Predicting which structural features will aid effective and efficient CO_2 photoreduction is challenging.[109] Many considerations required for hydrogen evolution are also important in CO_2 photocatalysis, such as the importance of band alignment, quantum efficiencies, effective charge separation and long-lived charges.[110,111] Some key factors are summarised in **Figure 1.8**. However, the unpredictability of the reaction calls for further considerations when designing or choosing a material: due to the high thermodynamic requirements for breaking the strong CO_2 bonds, activation of the molecule is a requirement for photocatalysis. To this end, molecules with functional groups that can bind and activate the CO_2 and the reaction intermediates are of great interest. A specific interaction to CO_2 might also enhance the selectivity of the reduction process since polar interactions can enhance the binding and activation of CO_2. The effective tuning of the active site using functional groups has been shown computationally and in electrochemical CO_2 conversion. An example of this was the addition of ammonium functional groups to a polymer matrix, which were found to increased production rates and affect product selectivity, compared to the polymer matrix without these functional groups.[112] **Figure 1.9** shows examples of possible binding modes of carbon dioxide onto a surface, which can help its activation. These can include coordination via the oxygen or carbon atoms, or mixed coordination over carbon and oxygen together.[113–115] A high surface area should be included in the design of such materials, to better adsorb CO_2 gas and provide the molecules with enough reaction sites for effective electron transfer processes to occur. Porosity of the catalyst is a possible way to provide this high surface area.[116] Another important factor is the requirement for a co-catalyst. These aid the overall efficiency of photocatalysis by lowering the activation energy for chemical reactions to take place, activating catalytic sites, playing a role in electron transport and decreasing charge recombination. [107,117] Overall, designing a photocatalyst for carbon dioxide photoreduction required careful consideration of all these factors.

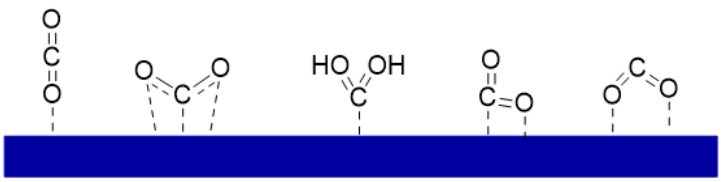


Figure 1.9: possible binding modes of carbon dioxide adsorbed onto a photocatalyst, figure redrawn adapted from ref[118]

1.3.2. Hydrogen oxidation as the co-reaction

The mimicking of nature to obtain artificial photosynthesis, converting carbon dioxide into glucose has so far been challenging to replicate. This is mainly because the complicated biological systems and electron cascades adopted in nature are currently challenging to adapt to a synthetic solar fuel set-up.[119,120] For the processes to become economically viable and competitive at a large scale, and to achieve the aim of stabilising if not reducing the amount of carbon dioxide in the atmosphere, current efficiencies of carbon dioxide photoreduction would be required to improve by several orders of magnitude. Hydrogen evolution from water splitting using renewable resources, has been more thoroughly researched and is overall a simpler process than carbon dioxide photocatalysis, and more likely to achieve economically viable efficiencies in a shorter time.[121] As highlighted in section 1.1.4.1, the reduction of carbon dioxide in hydrogen can yield CO (via RWGS), methane (via the Sabatier reaction), methanol and higher hydrocarbons (via the Fischer-Tropsch process).[122] Carrying out these processes photocatalytically instead of thermally, or at least partially photocatalytically can vastly increase their sustainability, either in the process overall, or in the raw materials supplied.[123–125] Photothermal CO_2 photocatalysis proceeds via photocatalytic mechanisms, whereby IR light is used to heat the catalyst. Using higher energy light, in the visible or UV region, lowers the energy barrier required by heat and therefore enables the reaction to occur at low temperature.[126] The presence of hydrogen has the advantage of not requiring a sacrificial agent, which increases the simplicity of the system and can attribute to keeping costs down. Currently, inorganic systems are at the forefront of carbon dioxide photo-hydrogenation, with distinct success in the production of C1 products (CO, CH_4 and CH_3OH).[126] In order for catalytic hydrogenation of CO_2 to be sustainable, the hydrogen should not come from fossil fuels but rather from biomass via photocatalysis, pyrolysis or liquefication, or from water splitting. [127]

Li *et al* have reported on Pd@H_yWO_{3-x} for carbon dioxide hydrogenation, to obtain CO in rates of 1.3 $mmolg^{-1}h^{-1}$ with 99% selectivity in a batch reactor system.[128] The group later showed the precise incorporation of copper atoms on the surface increased the rate of CO formation in the same system.[129] Titania has been at the forefront of photocatalysis for decades.[130] The Zhou group reported on nanocomposites of Ce doped TiO_2 with loaded Pd, with rates of 73 $\mu molg^{-1}h^{-1}$ of CH_4 produced and 9 $\mu molg^{-1}h^{-1}$ of CO, whereby Ce doping vastly improved carbon dioxide photocatalysis, extending the light response of the titania by adding impurity energy levels, with increased performance being attributed to the synergic effect of palladium nanoparticles on the surface promoting electron capture and CO_2 activation.[131] Inorganic

semiconductors are currently at the forefront of performance in carbon dioxide reduction photocatalysis[132–135].The highest performing materials for gas phase photocatalysis tend to exhibit high porosity, a property which has been shown to enhance properties of CO_2 adsorption and activation, increased charge separation and charge transfer, increased gas diffusion, and reaction rate.[136] Despite this, inorganic semiconductors are limited by their poor energetic tunability, which is important for the optimisation of light harvesting/conduction and valence band placement to optimise photocatalytic activity. Inorganic materials are often more precious than organic semiconductors, which decreases their abundancy and increases their price, and are more difficult to process.

1.3.2.1. Hybrid systems

Hybrid systems are essentially used in nature for photosynthesis. The cascade of electron transfer offers advantages such as decreasing charge recombination and enhancing electron transport, thus leading to an increased rate of CO_2 photoreduction.[137–139] Example of hybrid systems of sensitizer/semiconductor/molecular catalyst have been of growing interest.[139–142] Zhang *et al* recently reported on an organic-inorganic hybrid catalyst, which takes advantage of an electron transfer relay system.[143] This was achieved by using a porphyrin-based covalent triazine framework, coupled with iron oxide nanoparticles and a ruthenium-based photosensitizer. CO evolution rate of 8.0 $\mu molh^{-1}$ with 93% CO selectivity, which is superior to that of the binary system. The highest apparent quantum efficiency was also evaluated as 1.43% at 450 nm. The group explained the importance of strong CO_2 adsorption due to the porphyrin and triazine structure, along with its high porosity, combined with the electron cascade created by the other two components which formed an increased performance system.[143] Won *et al* also reported on a ternary organic-inorganic system featuring a Rhenium based catalyst on a titania support.[140] Zhang *et al* reported a Manganese complex anchored on Bi_2WO_6 nanoparticles with bisphosphonate functional groups.[137] Both for a selective photoreduction of carbon dioxide into carbon monoxide.

1.3.3. Organic Semiconductors

Organic materials have been investigated mainly for liquid phase photocatalysis, such as COFs, hyper-crosslinked polymers, and carbon nitrides.[143–152] The synthetic preparation of these materials, however, typically results in an intractable product, limiting their processability. Molecular photocatalysts have also been tested but have suffered from difficulty in preparation and scalability, low processability and low stability.[153]

1.3.3.1. Carbon Nitrides

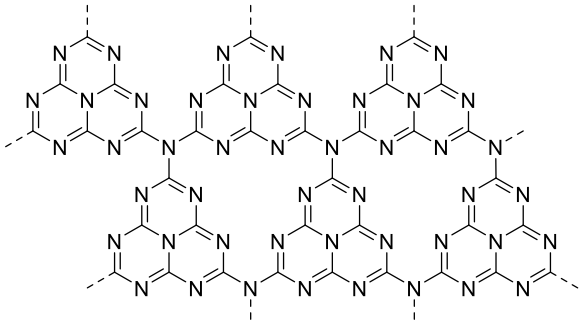


Figure 1.10: typical structure of g-C_3N_4

Carbon nitride (g-C_3N_4)-based composites are the organic systems that have been most tested both for hydrogen evolution and for carbon dioxide. Their typical structure is shown in **Figure 1.10** and consist of carbon and nitrogen atoms forming an ordered polymer. The typical LUMO and HOMOs lie at 3.4 eV and 6.8 eV respectively, with a typical bandgap between 2.7 and 3.4 eV. The bands straddle the potentials for hydrogen and oxygen evolution, making carbon nitride a good candidate for water splitting and carbon dioxide photocatalysis.[154] Due to low absorption in the visible region, modifications to the structures are often included. These materials offer high surface areas, good thermal and chemical stability, and high quantum efficiencies. They are also synthesized from abundant materials and are of low toxicity. Structure modifications of carbon nitrides have shown increased performances for photoreduction.[149,155–157] For example, Xia *et al* report an increase in performance with the addition of nitrogen vacancies in the crystal structure. At 41% humidity the group report CO_2 reduction to CO with an average production rate of 5.38 $\mu molh^{-1}g^{-1}$ and a selectivity of 78%, testing their material in the gas phase, with no sacrificial agent. [156] Shi *et al* reported that carbon vacancies within the crystal structure showed a product rate increase. The CO evolution rate was 4.18 $\mu molg^{-1}h^{-1}$, more than 3 times more that of graphitic carbon nitrides. The increase was attributed to an increase in charge carrier formation.[151] Similarly Wang *et al* have shown that elemental doping with sulphur was able to increase rate of photocatalysis 2.5 times, due to narrowing the bandgap of the material.[158] Crake *et al*, synthesised nanocomposites of titanium dioxide and carbon nitride nanosheets (CNNS), for CO_2 photoreduction in hydrogen. The materials also showed promise in CO_2 capture, with the composite showing double the adsorption of CO_2 compared to CN or TiO_2 alone. A CO production rate of 2 $\mu molg^{-1}h^{-1}$ was obtained TiO_2 P25 alone showed a rate of 1.5 $\mu molg^{-1}h^{-1}$ and CNNS 0.2 $\mu molg^{-1}h^{-1}$, g-C_3N_4 0.1

$\mu molg^{-1}h^{-1}$, using hydrogen as a sacrificial agent. The group proposed a Type II heterojunction formation, with the hydrogen oxidation occurring on the CNNS site and the reduction on the TiO_2.[159] Although carbon nitrides have shown great promise, doping is required for energetic tuning, which is less straight forward than synthetic modifications, and the systems are largely insoluble, which impacts the processibility of the systems.

1.3.3.2. Polymer Networks

Polymer networks often achieve high surface areas and can make use of the tunability offered by organic materials. Most, however, are not solution processable, due to the extended structures obtained, but have shown success in carbon dioxide photoreduction. These networks can begin paving the way for intelligent synthetic design, as well as showing that organic materials can be used in this application. [102,160,161] **Figure 1.11** highlights some of the best performing organic systems for carbon dioxide photocatalysis to date. [93]

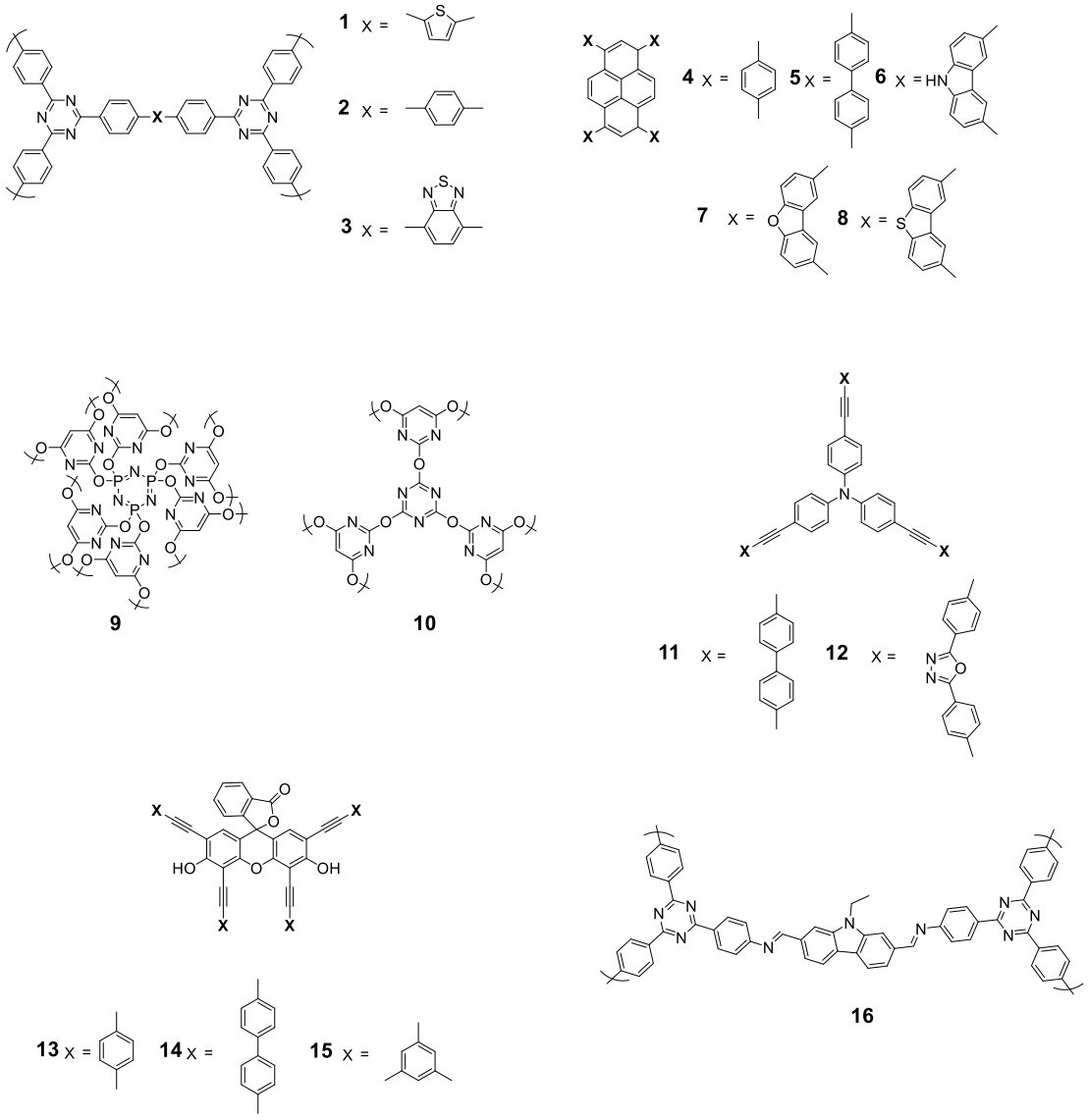


Figure 1.11: Chemical structures **1-16**, figure adapted from [102]

The triazine based polymers shown in structures **1-3** from **Figure 1.11** were presented by Yang *et al,* in this study, the co-monomer units were employed to vary the bandgap and to promote an acceptor-donor character within the structure which was deemed to improve mobility. The insoluble materials were tested as a dispersion in water, with $CoCl_2$ as a co-catalyst in solution and with TEOA as a hole scavenger. The study moreover found that acetonitrile and water in a 1:4 ratio were the best solvent combination for an increased CO production rate. Material **3**, containing the BT unit was the best performing with a rate of CO production of 18.2 μmol h^{-1} and an apparent quantum yield (AQY) of 1.75% at 405 nm. The BT unit was hypothesised to improve charge separation due to the higher donor/acceptor character afforded to the molecule by the inclusion of this electron-withdrawing co-monomer.[162] This could be partially true since if the LUMO and HOMO character on the polymer is focused on different parts of the structure,

charge separation at an interface or at a co-catalyst or sacrificial reagent could be facilitated. Structures **4-8,** based on pyrene networks were tested in an ionic liquid medium, which aided the solubility of carbon dioxide, and therefore showed a greater CO formation than H_2 evolution. In this study, a direct correlation between the overpotential supplied for photocatalysis by the materials and the rate of carbon monoxide produced was found. As the LUMO level became less negative (−3.66 eV for **4** to −2.92 eV for **8**) the higher the rate of CO produced, up to 2.4 $\mu molh^{-1}$, or 47.4 $\mu molg^{-1}h^{-1}$. Excitingly, these studies were done in air, showing the feasibility of using these materials and this system as direct carbon and water capture and photocatalysis systems.[163] The study on structure **9** and **10** by Guo *et al* showed threefold increase in production rate to 22.5 $\mu molg^{-1}h^{-1}$ with a high methane selectivity and an AQE value of NOP-COP was 0.32%, with the incorporation of phosphorous in the structure. The studies were carried out in water with TEOA as a sacrificial agent. A 3 fold increase from 5.7 to 15.9 ns was observed for structure **10,** the three-fold increase was hypothesised to indicate that structure **10** with its increased charge lifetimes could allow more opportunities for free charges to carry out redox reactions, thus explaining the increase in rate.[163] The CMPs **11** and **12** were tested in the gas phase using water vapor and carbon dioxide gas. The presence of the oxadiazole group increased the rate of CO production from 0.9 to 37.15 $\mu mol\ g^{-1}\ h^{-1}$. This was attributed to an increased uptake of CO_2, ease of charge transfer to the molecule and a decrease in optical bandgap. This study further supported the need for amine and oxygen functional groups in the design of conjugated microporous polymers for this application.[164] The structures **13-15** published by Yu *et al* were eosin-based polymers. CO was produced at a rate of 33 $\mu mol\ g^{-1}\ h^{-1}$ and a selectivity of 92 %. The structures were tested in an aqueous solution. Interestingly, the group found that the adsorption capacities for carbon dioxide were directly related to the BET surface areas in this study. Furthermore, the direct comparison by Yu *et al* between eosin and the eosin-based polymer in **13** shows the importance of conjugation and high surface area, since the eosin alone was able to produce 5 $\mu mol\ g^{-1}\ h^{-1}$ of CO only. Despite this, performance was found to not linearly depend on surface area. These suggest that although surface area is an important requirement, functional group considerations for an increased CO_2 interaction and an increased charge separation might be more important in directly affecting catalyst performance. These studies are very useful in comparing specific modifications of a system tested in the same manner, however, a lack of testing and reporting standardization in this field prevents true comparison between different materials within different studies, and a lack of controls or isotope labelling prevents from fully understanding the pathways at play.[165] The COF structure, **16,** shown in **Figure 1.11**, highlighted a donor-

acceptor framework for carbon monoxide and stoichiometric oxygen production from carbon dioxide and water. The material outperformed the benchmarking carbon nitride by a factor of nearly 70. Testing was done using gaseous CO_2 and H_2O, DFT calculations showed nitrogen atoms on the triazine rings as potentially active sites in photocatalysis. This work championed donor-acceptor character strategies for an increased charge separation and transport in the molecule.[166]

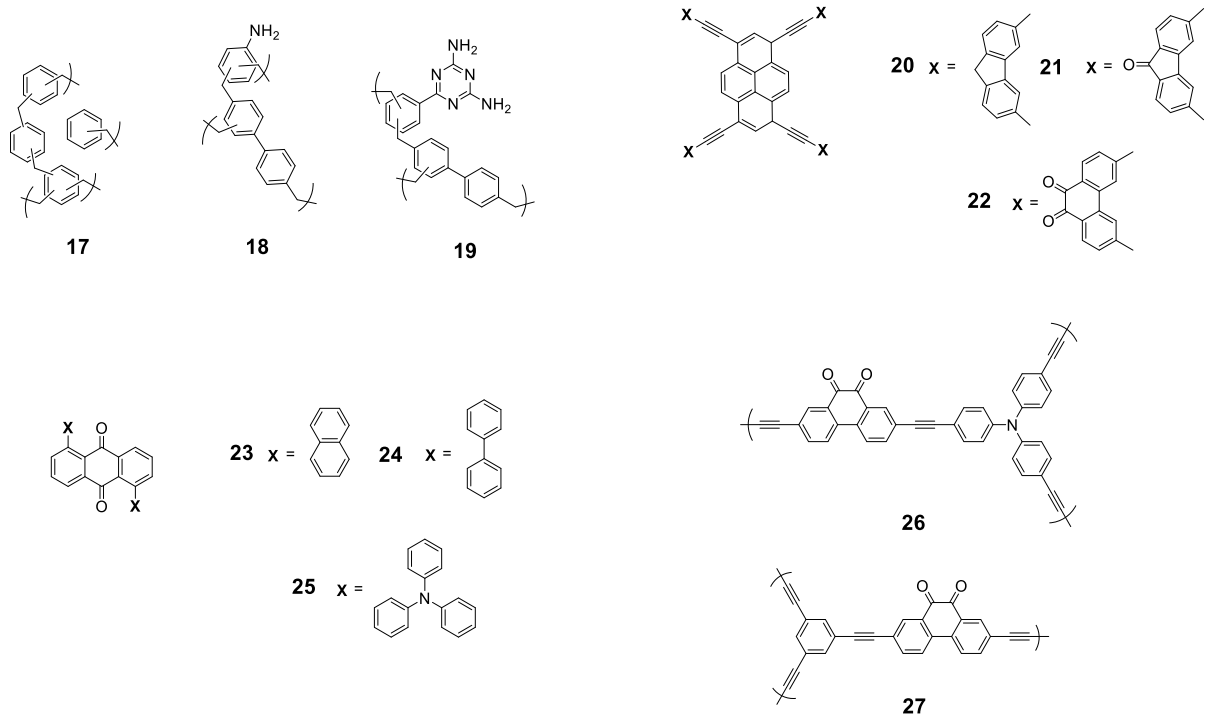


Figure 1.12: Chemical structures **17-27**

Schukraft *et al* published work on a series of hypercrosselinked polymers for hydrogen or water assisted CO_2 photoreduction. Hypercrosslinked polymers are aromatic polymers that can crosslink to form densely packed structures, as seen in structure **17-19**. Structure **19** was the best performing and showed a rate similar to that obtained for TiO_2 P25, both using hydrogen or water as a sacrificial agent. Photocatalysis was carried out in the gas phase to take advantage of both carbon dioxide capture and photocatalysis properties. The polymers were found to improve in rate in the presence of water versus hydrogen, possibly due to increased water absorption compared to hydrogen. The study was supported by isotope labelling studies and control experiments, highlighting the photocatalytic nature of the polymers, so it is an exciting proof of concept for organic materials for this application.[152] Wu *et al* recently published a series of red-light absorbing CMPs for CO and CH_4 production. The structures as shown in **Figure 1.12** as **20-22**. The materials were tested in aqueous phase with TEOA as the scavenger.

The materials obtained high rates of methane and carbon monoxide production, 293.7 and 282.6 μmol h^{-1} g^{-1} respectively and with no hydrogen production detected, for structure **22**. This was thought to be the best performing due to increased CO_2 uptake and improved charge transfer.[167] The donor-acceptor conjugated polymer motif was utilised by Wang *et al,* in their gas phase testing of structures **23-25**. In water vapour and CO_2. The selectivity for CO was almost 100% with a rate of 69.7 $\mu molg^{-1}h^{-1}$ for structure **24**. The donor acceptor systems were first modelled by DFT, the ones with the most appropriate acceptor-donor character and energy levels were chosen to be synthesised. The best performing showed the highest surface area and selectivity for carbon dioxide adsorption, with an impressive porosity of 572 m^2g^{-1} for this insoluble solid. [168] A similar set of structures were recently published by Barman *et al* and these CMPs are represented in structures **26** and **27**. Structure **26** was the best performing, yielding high amounts of CH_4, at a rate of 2.15 $mmolg^{-1}h^{-1}$, it should be noted that this rate is high, but could be inflated using very small amounts of photocatalyst in the system. The CMP's donor-acceptor character was credited with suppressing charge recombination and the structure showed long lived charges, this was not seen in the non-donor-acceptor analogue, which did not show the same long lived charges and a rate that was over 8 time lower in CH_4 production, the catalyst also showed high stability over 60 hours with no decrease in operational activity.[169]

In the last year, Naphthalene Diimide (NDI) and fluorene-based compounds have been tested for the photoreduction of carbon dioxide with some success, marking some of the first soluble organic materials to function for this application, without added co-catalysts, these structures are shown in **Figure 1.13**.

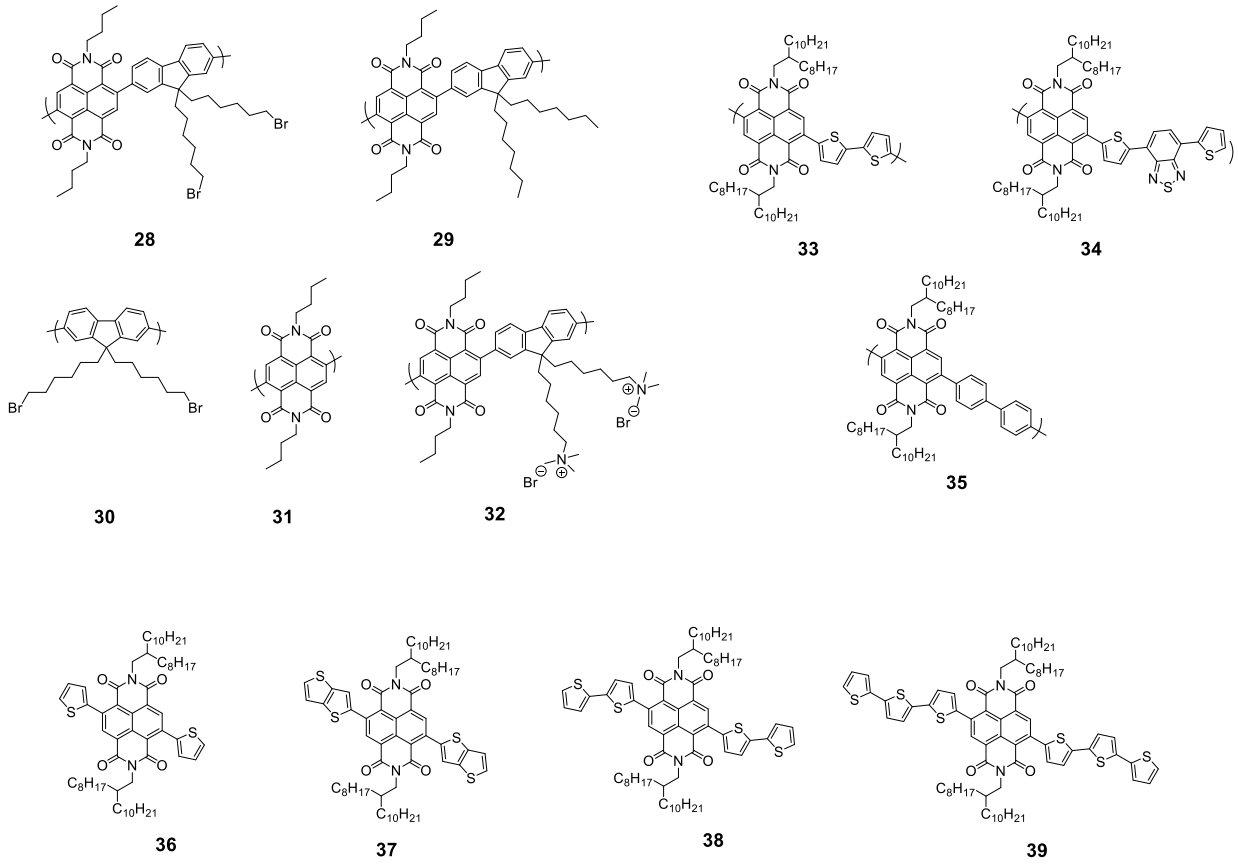


Figure 1.13: Chemical structures **28-39**

Structures **28-32** were tested by the Lai group, **30,** which did not contain an NDI molecule, had the highest LUMO and was the best performing polymer for the formation of CO, with a production rate of 10 $\mu molg^{-1}h^{-1}$. However, the study did not show any oxygen evolution studies, nor controls or isotope labelling studies, and CO could be seen without water present in the system, which does suggest some possible degradation or trapped carbonaceous species might be occurring or present.[170] More convincing evidence was provided by Wang *et al,* in the study including polymers **33-35**. **35** was shown to have the largest dihedral angles along the backbone due to the phenyl-phenyl interactions and possessed the longest electron lifetime and smallest resistance to charge transfer and was shown to be the best performing polymer of the three. Although oxygen evolution experiments were not shown, so the oxidation method is not explained, isotope labelling data was provided to show the catalytic nature of the polymers, which were also remarkably stable. Interestingly, CH_4 production began rising after 250 hours, which would be consistent with a formation mechanism stemming from CO as the intermediate.[171] The same group also reported a similar study done on NDI acceptor-donor small molecules, highlighted in structures **36-39.** Electron donating character was progressively increased going from **36** to **39**, but **38** was the best performing, the group

hypothesised a trade-off between charge separation stemming from donor-acceptor character, and appropriate energy levels to drive the redox reactions.[172]

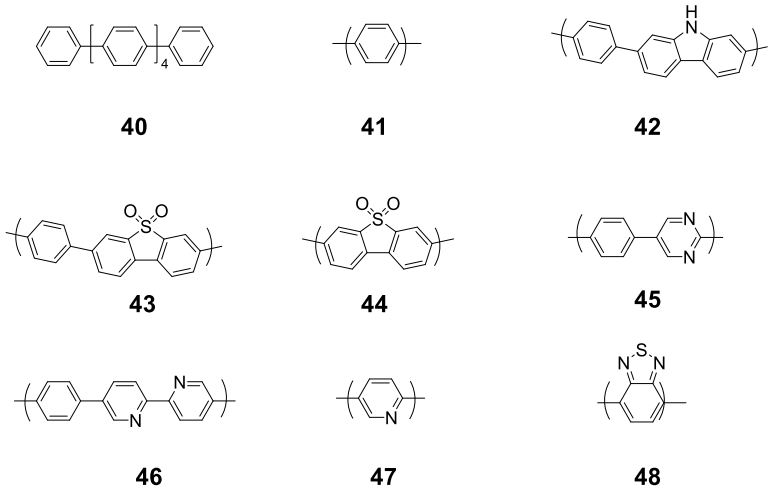


Figure 1.14: Chemical structures **40-48**

The Sprick group reported on conjugated organic polymers for the production of CO and H_2 (syngas) from water with TEOA as a sacrificial agent. The polymers tested can be seen in **Figure 1.14**, as structures **40-48**. Structure **43** was the best performing polymers for CO evolution, while also showing high evolution rates of 959.1 $\mu molg^{-1}h^{-1}$and 1523.7 $\mu molg^{-1}h^{-1}$ respectively. The group investigated the H_2/CO ratios achieved by the polymers, and the study served to show that linear conjugated polymers can be used for syngas production.[173] **Table 1.2** summarises the data presented above, relevant to recent updates in this field, comparing both testing conditions and materials.

The organic structures shown in these studies are exciting as a proof of concept that organic materials can function as photocatalysts for carbon dioxide photoreduction. However, to the author's knowledge, no solution processable, conjugated and porous material has yet been reported for this application, which leaves a gap in the field for a potentially ideal type of organic semiconductor for carbon dioxide photocatalysis. Furthermore, primary liquid phase testing has been employed or batch type systems in the gas phase, rather than a recycling system, which could be important for scalability and for reaching higher hydrocarbon products in the future.

Table 1.2:Table summarising data from recent literature on carbon dioxide photoreduction

#	**HOMO/ LUMO/eV** [eV *vs.* Vac.]	**Eg**/eV	**Conditions**	**Co-catalyst and Impurity** (loading wt. %)	**BET (N_2)** / $m^2\ g^{-1}$	**CO_2 uptake**	**Performance** / $\mu mol\ h^{-1}$	**Selectivity of Main Product.** /%	**EQE or AQY/%**	**Mass/** mg	**Irradiation source**	**Stability**/h	**Ref**
$Pd@WO_3$	-	3.2	$Pd@WO_3$ batch reactor, 1:1 H_2:CO_2 Gas phase	Inorganic system	77	-	1.3 mmol $g^{-1}\ hr^{-1}$ 1.3 $\mu mol\ h^{-1}$	99 (CO)	0.0056	1	300 W Xe arc lamp	~45	[128]
Pd/Ce-TiO_2	-	2.8	Pd/Ce-TiO_2 , CO_2 and H_2 with a ratio of 1:4, 25 bar	Inorganic system	50	50	73 $\mu molg^{-1}h^{-1}$ of CH_4 7.3 $\mu molh^{-1}$	89 (CH_4)	-	100	Xe arc lamp	15	[131]
Ti-NS/CN	-7.4/-4.5 -6.5/3.7	3.2	The photoreactor (35 cm^3 batch photoreactor, 1.25 bar, CO_2/H_2 ratio of 1.5 (vol/vol)	Hybrid system	174	0.5	2 $\mu molg^{-1}h^{-1}$ 53 $\mu mol\ m^{-2}\ h^{-1}$	(CO)	-	25	Xe arc lamp (150 W, $\lambda > 325$ nm equipped with water filter	-	[159]
P25 TiO_2	-7.4/-4.5	3.2	The photoreactor (35 cm^3 batch photoreactor, 1.25 bar, CO_2/H_2 ratio of 1.5 (vol/vol)	Inorganic system	-	-	1.5 $\mu molg^{-1}h^{-1}$ 39 $\mu mol\ m^{-2}\ h^{-1}$	(CO)	-	25	Xe arc lamp (150 W, $\lambda > 325$ nm equipped with water filter	-	[159]
g-C_3N_4	-7.0/-4.2	2.8	The photoreactor (35 cm^3 batch photoreactor, 1.25 bar, CO_2/H_2 ratio of 1.5 (vol/vol)	-	17	0.06	0.1 $\mu molg^{-1}h^{-1}$ 3 $\mu mol\ m^{-2}\ h^{-1}$	(CO)	-	25	Xe arc lamp (150 W, $\lambda > 325$ nm equipped with water filter	-	[159]

3	-5.92/-3.49^	2.43	Acetonitrile:water 4:1, TEOA as sacrificial reagent Room temperature and Atmospheric Pressure	$CoCl_2$ (0.01) **Pd traces*	37	-	18.2 μmolh^{-1}	81.6 (CO)	1.75 (405 nm)	15	> 420nm 300 W Xe lamp	24	162
8	-5.64/-2.98*	2.66	Ionic Liquid Medium treated with air TEOA as sacrificial reagent Room temperature and Atmospheric Pressure	**Ni traces*	-	-	47.37 μmol g^{-1} h^{-1} 2.37 μmol h^{-}	98.3 (CO)	-	50	> 420nm 220 W Xe lamp	50	163
10	-5.83/-3.69*	2.32	Aqueous solution, TEOA as sacrificial reagent Room temperature and Atmospheric Pressure	-	44.5	7.21 wt%	22.5 μmol g^{-1} h^{-1} 1.13 μmolh^{-1}	90.2 (CH_4)	0.32% (420 nm)	50	> 420nm 300 W Xe lamp	120	163
12	-6.47/-4.09^	2.38	Gas phase, with CO_2 passing first through a water bubbler. Room temperature and Atmospheric Pressure	**Pd and Cu traces*	512	24 cm^{3}g^{-1}	37.15 μmol g^{-1} h^{-1} 0.56 μmolh^{-1}	~100 (CO)	-	15	> 420nm 300 W Xe lamp	20	164
15	-6/-2.55*	2.45	Aqueous solution, no added sacrificial reag ent Room temperature and Atmospheric Pressure	**Pd (0.1)* **Cu (0.13)*	445	39 cm^{3}g^{-1}	33 μmol g^{-1} h^{-1} 0.33 μmolh^{-}	92 (CO)	-	10	> 420nm 300 W Xe lamp	50	165
16	−5.66/−3.62*	2.04	Water and CO_2 gas phase testing, 1 bar.	-	521	43 cm^3 g^{-1}	102.7 μmol g^{-1} h^{-1} 5.14 μmol h^{-1}	98 (CO)	0.104 (420)	50	> 420nm 300 W Xe lamp	10	166
19	-5.77/-2.58	3.19	Gas phase CO_2:H_2O mixture	**Pd (0.4)*	360	0.92 mmol/g	15.6 μmol g^{-1} h^{-1}	98 (CO)	-	10-15	> 420nm 300 W Xe lamp	15	152

				*Cu (0.015)			180 μmolm-2h-1						
19	-5.77/-258	3.19	Gas phase CO_2:H_2 mixture	*Fe traces*	360	0.92 mmol/g	6.3 $\mu mol\ g^{-1}\ h^{-1}$ 72.3 μmolm-2h-1	92 (CO)	-	10-15	> 420nm 300 W Xe lamp	15	[152]
22	-4.95/-3.27^	1.64	Aqueous phase, in MeCN, TEOA, BNAH	*Pd and Cu traces*	580	38 $cm^3\ g^{-1}$	282.6/293.7 $\mu mol\ g^{-1}\ h^{-1}$	99 (CO + CH_4)	-	5	>600 nm 300 W Xe lamp	-	[167]
24	-6.12/-3.15^	2.97	Gas phase reactor with injected H_2O, CO2 provided by balloon.	-	572	48.4 $cm^3\ g^{-}$	69 $\mu mol\ g^{-1}\ h^{-1}$	99 (CO)		3	> 420nm 300 W Xe lamp	30	[168]
27	-5.68/-3.88^	1.8	Aqueous phase, in MeCN and water (2:1), BNAH as sacrificial reagent, TEA as base.	*Pd (0.35)	492	30 $cm^3\ g^{-}$	2.15 mmolg-1h-1 2.8 $\mu mol\ h^{-1}$	97 (CH_4)	0.1% (600 nm, 6h)	0.13	> 420nm 300 W Xe lamp	65	[169]
30	-6.40,-3.48^	2.92	1.2 bar, gas phase, in CO_2 with injected water, batch reactor for 24 hours.	*Pd	-	-	10.07 $\mu mol\ g^{-1}\ h^{-1}$	99 (CO)	-	2	> 420nm 300 W Xe lamp	104	[170]
35	-3.65/-5.87^	2.22	1.2 bar, gas phase, in CO_2 with injected water, batch reactor for 18 hours.	*Pd	-	-	12 $\mu mol\ g^{-1}\ h^{-1}$	-	0.00062		> 420nm 300 W Xe lamp	330	[171]
38	-3.67/-5.49^	1.82	1.2 bar, gas phase, in CO_2 with injected water, batch reactor for 24 hours.	*Pd	-	-	5 $\mu mol\ g^{-1}\ h^{-1}$	99 (CO)	-	-	> 420nm 300 W Xe lamp	-	[172]
43	-	2.66	Aqueous suspension, bipy, $CoCl_2$, MeCN :TEOA :H_2O (3 :1 :1)	CoCl2 Pd	-	-	1523.7 $\mu molg^{-1}h^{-1}$	38 (CO)	0.45 (420)	5	Orile Solar simulator 1.5 AM	25	[173]
pTA-Ph	-5.7'/-3.0	2.7	1.15 bar, recycling gas phase, hydrogen and CO_2	*Pd (15 ppm)	487	-	0.019	98 (CO)	0.088 (450 nm)	2	> 360 nm 300 W Xe lamp	<120	CH4

pTA-Ph	-5.7'/-3.0	2.7	1.15 bar, recycling gas phase, hydrogen and CO_2	*Pd (15 ppm) Cu (5)	487	-	0.05	94 (CO)		2	> 360 nm 300 W Xe lamp		CH4

In the HOMO and LUMO column, * denotes XPS, ^ CV, ‡ DFT, “ PESA In the co-catalyst column, the * denotes possible traces of metals present from polymerisation reaction which could influence performance. Energy levels from NHE converted from $E_{(abs)}=E_{(NHE)}+4.44$ V

1.4. Techniques and Concepts

Specific techniques and concepts used in this thesis are outlined below.

1.4.1. Optoelectronic Properties

1.4.1.1. Photoelectron spectroscopy in air (PESA)

Photoelectron spectroscopy in air (PESA) can be used to measure the ionisation potential or the work function of a material. This value is the energy required to remove an electron from a semiconductor and it corresponds to the HOMO energy level in polymers. The technique consists of shining a beam of monochromatic light onto a sample, and gradually increasing the photon energy. Once the incident photon energy is larger than the work function or ionisation energy of the semiconductor, the material will emit an electron. This electron will meet an oxygen atom and form a superoxide anion, which will be detected by the positively charged detector. [174,175]

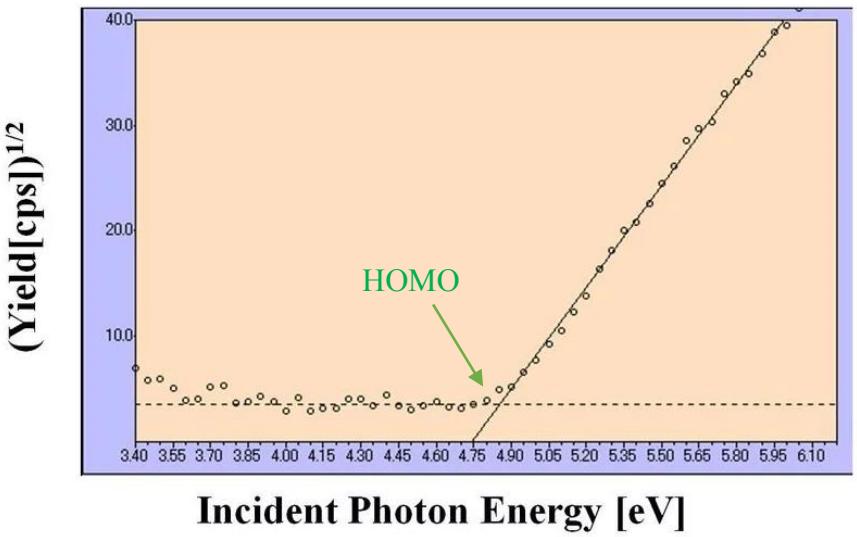


Figure 1.15: example of PESA spectra taken from ref.[176]

Plotting the photoelectron output vs UV energy gives a plot which begins to slope at the work function, which can then be estimated from the graph, as shown in **Figure 1.15**.

1.4.1.2. UV-Vis

UV-Vis is a common technique used when working with light absorbing materials. The spectrometer measures the intensity of light absorption at specific wavelengths of a material compared to a blank or reference sample. Plotting the absorbance obtained against the wavelength of light can then be used to obtain a spectrum from which the absorption maxima

and the absorption edge can be calculated. The absorption onset was measured from the intersection of a tangent to the steepest slope of the onset with a tangent to the baseline as shown in **Figure 1.16**, and corresponds to the lowest energy required for an electron in a HOMO to jump into a LUMO energy level, thus giving the HOMO-LUMO gap value. In most of the materials presented in this thesis, due to a lack of donor-acceptor hybridisation, the HOMO-LUMO gap and the bandgap of the material are likely very similar, and the value obtained from UV-Vis, as described below, was used in energy level diagrams.[177,178]

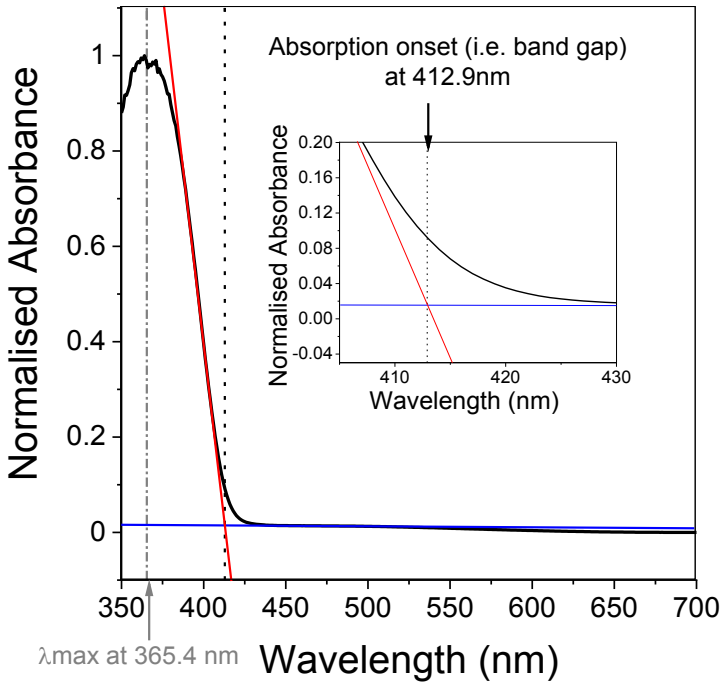


Figure 1.16: A method to obtain the bandgap of a polymer by construction from a UV-Vis spectrum, Figure adapted from Matt Rosenfeld Part II thesis.

Combining the bandgap measured using UV-Vis and the HOMO obtained from PESA, the LUMO can be calculated.

1.4.1.3. Time-correlated single photon counting (TCSPC)

Time-correlated single photon counting (TCSPC) is a fluorescence lifetimes measurement technique. The arrival of single photons to the detector from when the laser pulse is activated are compared to a reference signal. The reference signal is known as the instrument response function (IRF) which sets the minimum limit for detection. In measurements done in this study, the software of the system was used to deconvolute the decay data from the IRF and to perform

fittings, which can be multi-exponential, to obtain the decay numbers. Multiple components can make up the decay signal, these are partially related to decay processes. The decay law (equation 1.13) is based on first order kinetics, but often fluorescent decays can show multi-, mono- or non- exponential decays, this can be due to inhomogeneous excitation, quenching, aggregation and over environmental factors.[179–181]

$$I(t) = \sum_i \alpha_i \exp(-\frac{t}{\tau_i}) \qquad (1.13)$$

Equation 1.13 expresses the decay of the excited state of a molecule to the ground state, where I is the signal intensity, α is the contribution coefficient, τ is the lifetime of the component. This is defined as the time taken for the intensity of a signal to drop by 1/e (around 37%). TCSPC is a technique which bypasses the influence of variations in the excitation source, and since fluorescence lifetimes are an intrinsic property of a material, and are not dependent on concentration, the repeatability of measurements is safeguarded.

In TCSPC a sample is excited using a light source, the time taken for the photon to be detected is compared to the time when the excitation source was pulsed. This process is repeated tens of thousands of times to obtain a picture as each single photon is detected. TCSPC works best at times of ns, so can be used for organic materials easily, since normally these do not have as long-lived charges as inorganic materials. A monochromator is often used to obtain the desired fluorescence emissions. [182,183] Multiexponential fluorescence decays make use of intensity average lifetimes. These describe the average time a molecule can remain in the excited state. It can also define the average lifetime of different excited-state populations weighted by their contribution to the total fluorescence.[179,184] The average fluorescence lifetime (τ_{avg}) can be calculated using:

$$\tau_{avg} = \frac{\sum \alpha_i \tau_i^2}{\sum \alpha_i \tau_i} \qquad (1.14)$$

Fluorescence lifetimes were obtained by deconvolution of the IRF, therefore taking it into account, and by fitting the data to a multiexponential decay model using either in-house scripts or with the help of the DAS6, Horiba software. The IRF aids with taking into account instrumental factors, such as noise, or distortion from the instrument. This fluorescence signal can be interpreted by equation 1.15:

$$F(t) = \int_{-\infty}^{\infty} P(t - t')f(t')dt' \qquad (1.15)$$

P(t) is the prompt response of the instrument. The r.m.s. residue from the fit was used to ensure a good fit with the exponential chosen. Organic semiconductors show a mono-exponential decay when a single decaying state is present. Multi-exponential behaviour can be due to different factors, which increase the numbers of parameters influencing the decay kinetics, for example aggregation of the polymers, presence of singlet and triplet states, several bands contributing to the decay signal in a specific excitation range. [98,185,186]

1.4.1.4. Photoluminescence quantum yield (PLQY)

TCSPC can be used for the acquisition of time-resolved fluorescence data, it gives us information on the timescale of non-radiative decay. On the other hand, the photoluminescence quantum yield (PLQY) refers to the numbers of photons emitted per number of photons absorbed.[187,188] The measurements in this study were carried out using the integrating sphere method.

1.4.2. Material Properties

1.4.2.1. Brunauer–Emmett–Teller (BET)

BET analysis can measure the adsorption of gasses onto a surface. In a typical measurement, the sample is cooled to be able to detect adsorption and partial vacuum is used to alter the pressure of the system. Nitrogen is often used due to its wide availability, small size and strong interactions with solids when cooled. The adsorbent is physiosorbed, so the method is reversible, and the sample can be retrieved after usage. **Figure 1.17** shows the stages of adsorption of a typical gas in a solid. First molecules begin absorbing randomly onto sites, at low pressures. As the pressure is increased a monolayer begins to form, which can often fill up the smallest pores (micropores), increasing the pressure further results in multilayer formation, where a layer begins to cover the first monolayer, eventually causing a full build up and complete coverage by the gas of the structure. Micropores are defined as pores with a diameter of less than 2 nm, mesopores are between 2 and 50 nm, while macropores describe any pore with a dimeter larger than 50 nm. [189–191]

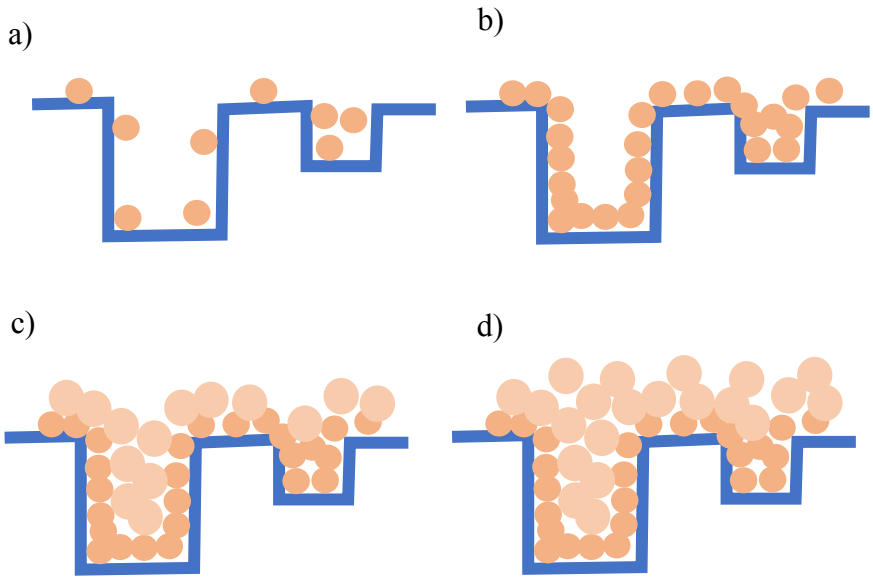


Figure 1.17: Gas adsorption stages diagram, a) shows the beginning of pore filling and micropore filling, b) monolayer formation c) formation of multilayer d) fully filled pore.

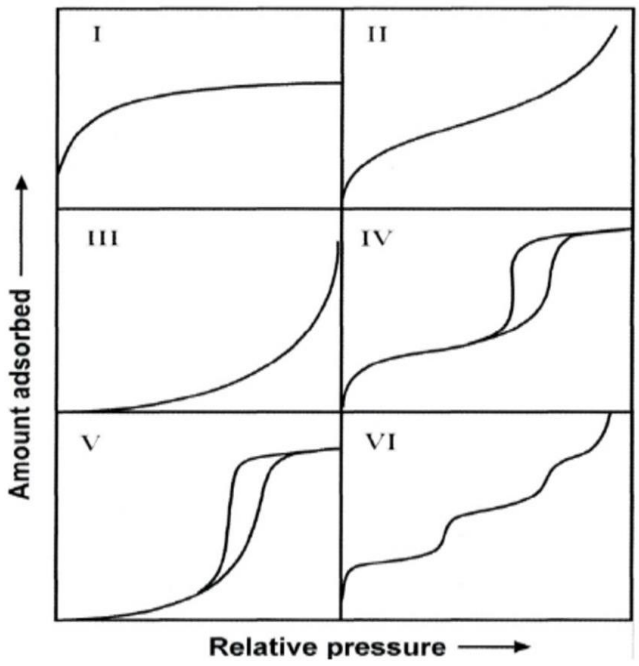


Figure 1.18: Isotherm types, image is from ref.[192] duplicated with permission.

Figure 1.18 highlights the types of curves that can be obtained from a BET, the shape of which can be important in discerning the nature of the porosity of the material. Type I isotherms normally correspond to microporous solids with small external surfaces, monolayer absorption is the defining feature of this shape. Type II tend to correspond to unrestricted mono and multilayer adsorption, which refer to macroporous or non-porous materials. Type III shows very little to no monolayer formation, and just unrestricted multilayer formation. Type IV starts similarly to Type II, indicating monolayer formation, but is then followed by multilayer.

Capillary formation can be observed in some cases when gasses can absorb into small capillary pores when p_0 is below the saturation pressure. This is always seen in Type V, which follows the same trend, but without the monolayer formation. Type VI represents step-wise multilayer absorption, each step height shows a monolayer capacity for each monolayer absorbed. Type IV is further shown in **Figure 1.19**, since most polymers observed exhibit microporous and Type IV character. [192,193]

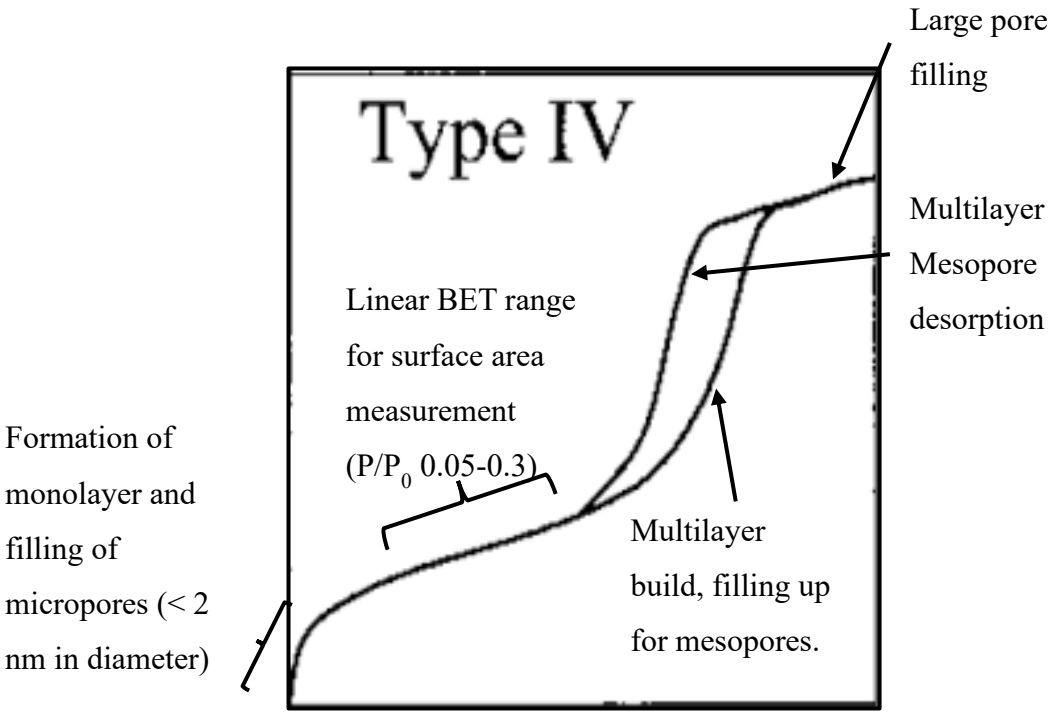


Figure 1.19: description of features of a typical Type IV isotherm, adapted from ref. [193] with permission.

In a Type IV isotherm, the first part of the curve, normally below $p/p_0 = 0.05$, has a sharp incline indicative of micropores and monolayer formation which ends at the knee of the curve. The next portion of the curve is the straight line in which BET behaviour is followed and is used to measure the surface area of the sample. Following this linear area, past around $p/p_0 = 0.3$, multilayer formation is observed with another sharp incline, which is indicative of larger pores.

The linear area of the BET curve is used to apply the BET equation to calculate the surface area of a sample. The typical linear BET equation is:

$$\frac{1}{W(p/p°-1)} = \frac{C-1}{W_m C}(p/p_o) + \frac{1}{W_m C} \qquad (1.16)$$

Where W is the quantity of adsorbed gas, p is the equilibrium pressure of the adsorbate, p_0 is the saturation pressure of the adsorbate, c is a BET constant, W_m is the hypothetical weight of a monolayer of adsorbate.

Plotting $\frac{1}{W(p/p°-1)}$ vs $p/p°$ has a slope $s = \frac{C-1}{W_m C}$ and intercept $i = \frac{1}{W_m C}$.

The monolayer weight can then be obtained from the reciprocal of the sum of the slope and the intercept:

$$W_m = \frac{1}{s+i} \tag{1.17}$$

From this value, the total surface area (S_t) can be derived, using:

$$S_t = \frac{W_m N_A A_{CS}}{M} \tag{1.18}$$

where N_A is Avogadro's number (6.023 x 10^{23}), A_{CS} is the cross-sectional area of one molecule of adsorbate (16.2 Å^2 for nitrogen), M is the molecular weight of the adsorbate (28 gmol^{-1} for nitrogen).

1.4.2.2. Inductively coupled plasma mass spectrometry (ICP-MS) and digestion

ICP-MS is an elemental analysis technique. The sample is ionised using plasma, the ions are measured by the mass-spec detector. It is an ideal technique for trace materials, with sensitivities of up to ppt. This system is particularly useful for calculating trace metal amounts in the polymers synthesised in this study.[194–196] For the digestion, polymer samples (between 3mg and 5 mg) were precisely weighed out and diluted with 2 mL nitric acid in clean Falcon Tubes and sealed. The digestion was carried out over a 2 hour period at a temperature of 200 °C. The cooled down resulting mixture was diluted in water to 100 mL, and the solutions were given for ICP-MS analysis.

1.4.3. Techniques

1.4.3.1. ALD

Atomic Layer Deposition (ALD) is chemical vapour deposition technique, which involves reactants in the vapour phase in an activated environment and the subsequent formation of stable, irreversible solid products. It is a chemisorption technique, which is self-limiting, and therefore vaunts atomic precision and layer-by-layer growth, idea for the controlled production of thin films.[197] Controlling the number of cycles controls the thickness of the film closely, and

the atomic precision of ALD allows for full pin-hole free coverage. Making it an excellent technique for ETL formation in photocathodes.[198,199]

The general mechanism of ALD is illustrated in **Figure 1.20**. Firstly, a substrate is placed into the chamber. Best results have been observed when the surface is activated, which allows chemisorption to occur. For organic materials, this can be done by pulsing the oxidant first, in this case water, then followed by the metal oxide precursor, a vapour reactant.[200,201] In this case Tetrakis(dimethylamido)titanium(IV) (TDMAT) was used. TDMAT is pulsed in the chamber, leading to the first gas-solid reaction, whereby the precursor is chemisorbed onto the activated substrate surface. This is a self-limiting step, because once the functional groups on the substrate have reacted with the precursor, they do not decompose or react with itself. The excess precursor and reaction products are then purged out, leaving behind a TDMAT functionalised surface. The second cycle pulses the oxygen source, in this case water, which causes the second gas-solid reaction, which formed an oxide layer, also self-limiting. Excess by-products, reactants and water are purged out, and the entire cycle is repeated, until the required thickness or cycle number is achieved.[197,202]

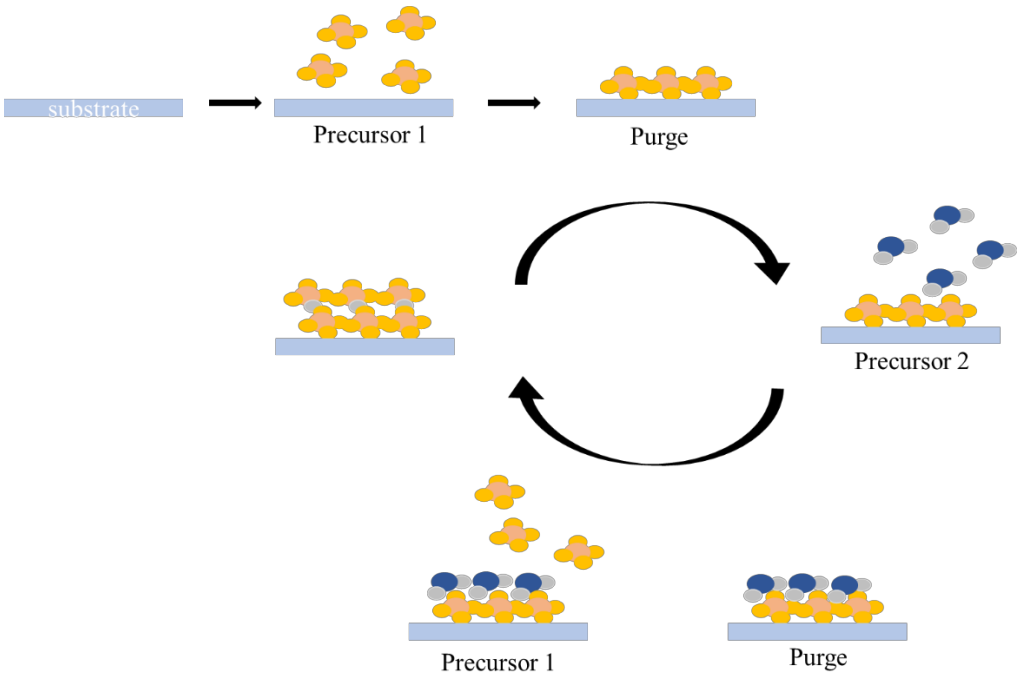


Figure 1.20: Schematic of ALD function

To form a chemical bond, functionalities must be present on the surface of the material. The activation energy is around 60-100 kJ/mol and the adsorption enthalpies over 40 kJ/mol. (0.4 eV), so it is a process that requires careful tuning. There are 3 main types of growth modes. (1) If the interface energy is less than the surface energy of the solids, so the interface created is

energetically favoured, a smooth thin film growth- layer by layer, would be obtained. This is ideal behaviour and called Frank-Van der Merwe Growth. (2) If the interface energy is higher and interface formation is not favoured, island growth (Volmer-Weber Growth) would be observed. This is due to a high contact angle, which would cause the precursors to not spread and form small particles instead. It is energetically less demanding to grow a film on top of th formed oxide than on its initial substrate (3) Stranski-Krastanov growth can be observed if in the beginning, the first few layers are favoured, but a mismatch is observed if the formation of the oxide on the oxide is not favoured, again nanoparticle formation would be seen instead after the formation of a thin initial film. Conversely, if the chemisorption on top of the substrate is unfavourable, substrate inhibited growth can be observed. This is likely due to defects in the substrate driving the deposition, leading to inhomogeneous growth, which requires a lot of cycled before a monolayer is formed.[200,203–205] These are shown in **Figure 1.21** below.

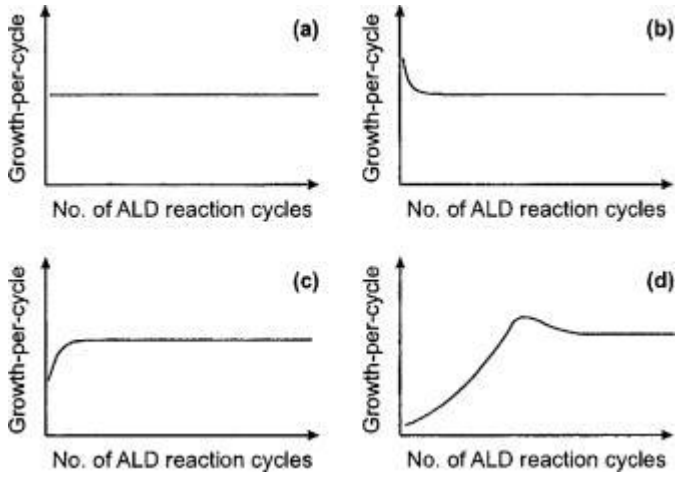


Figure 1.21: Figure showing the ALD growth times where (a) shows linear growth- Frank-Van der Merwe Growth, (b) shows Volmer-Weber Growth while (c) and (d) show two types of Stranski-Krastanov growth. This figure was reproduced from [206] with permission.

The Growth Per Cycle (GPC) rate can be obtained by inserting a silicon wafer in the chamber with the samples and measuring the thickness obtained.

1.4.3.2. Calculating parameters in photocathode chopped light curves.

Figure 1.22,**Error! Reference source not found.** highlights the parameters important in chopped light current density vs potential curves for evaluating photocathodes. [207,208]

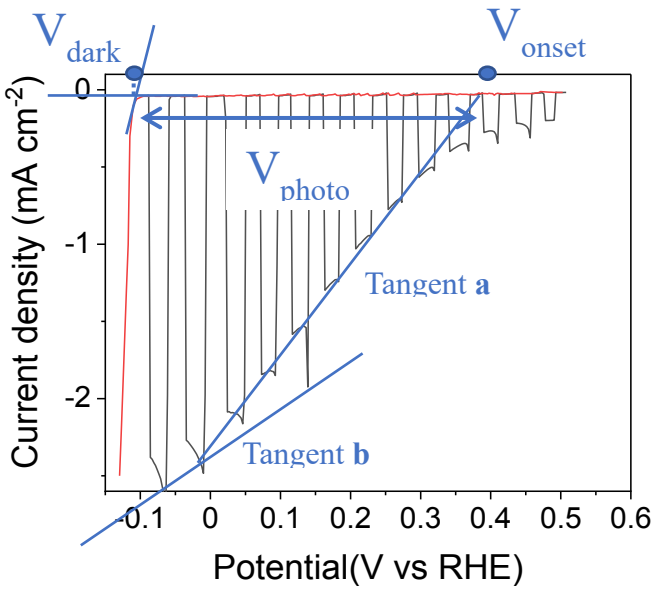


Figure 1.22: Explanation of parameters extracted from chopped light curves monitoring photocathode performance, where V_{onset} is extrapolated from tangent a, V_{dark} is the dark onset potential, obtained from the dark current, V_{photo} is calculated from the difference between the two. Crossover potential is where tangent a and b meet.

The photocathode applied potentials were converted from the Ag/AgCl (sat'd KCl) scale to the RHE scale using equations (1.19) and (1.20).

$$E_{RHE} = E_{Applied} + E^{\Theta}_{Ag/AgCl} + 0.059\,V * pH \quad (1.19)$$

$$\text{where } E^{\Theta}_{Ag/AgCl} = 0.1976 \text{ V} \quad (1.20)$$

1.4.3.3. Organic photovoltaics (OPV) basic theory

OPV was used in this study to assess the device feasibility prior to photocathode fabrication. JV curves are typically used to evaluate the performance of solar cells, as shown in the example in **Figure 1.23**.

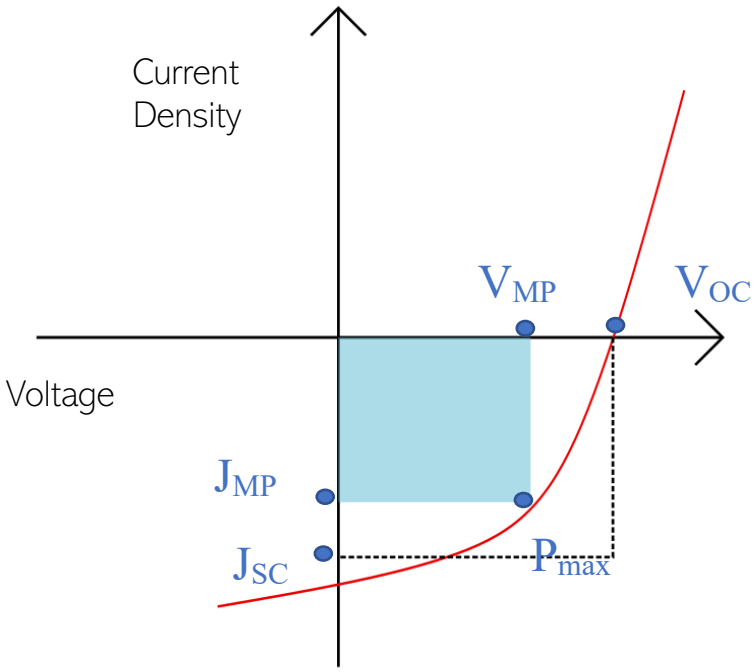


Figure 1.23: Typical current density vs voltage curve for a solar cell

Power conversion efficiency (PCE) is calculated according to Equation 1.21 where P_{in} is the total incident optical power, P_m the maximum electrical power generated, V_{OC} the open circuit voltage, J_{SC} the short circuit current density and FF refers to the fill factor.

$$PCE = \frac{P_m}{P_{in}} = \frac{V_{OC} \times J_{SC} \times FF}{P_{in}} \qquad (1.21)$$

Where the fill factor is defined as:

$$FF = \frac{J_{MP} \times V_{MP}}{J_{SC} \times V_{OC}} \qquad (1.22)$$

J_{MP} refers to the current density at maximum power and V_{MP} is the voltage at maximum power, as shown in **Figure 1.23**.[64]

The Shockley diode equation is used to model the ideal behaviour of a solar cell. It is important in the design to minimise series resistance (R_S) in a solar cell, which refers to the resistances at energetic barriers and within the layers. Good energy alignment can aid this. While shunt resistance (R_{SH}), which refers to resistance to other pathways in the device, should be maximised to prevent losses in current. [23,209]

1.5. Project Aims and Thesis Outline

The work presented in this thesis is motivated by the growing need for alternatives to fossil fuels, the potential of solar energy and addressing the issues of its intermittent supply, transport, and storage. It was hypothesised that organic semiconductors would offer valuable properties and would therefore be promising candidates in the formation of solar fuels. The aim of this study was to investigate the role of organic semiconductors in this application by supplying further research in the field. This was done both in terms of material design, as well as testing through the photocatalysis process, to aid the field by supplying a new class of materials as well as by supporting standardisation and investigating testing conditions. **Chapter 2** of this thesis is focused on photoelectrochemistry for hydrogen production, specifically on photocathodes tackling the reduction reaction. Organic semiconductors have shown promise in this field, but stability has been an ongoing issue, normally due to poor adhesion between layers. To address this issue, a functionalised overlayer containing glycol chains and a phosphonate anchor group was employed on top of the organic blend layer of the photocathodes. The chapter outlines the increase in nucleation of the TiO_2 layer deposited via ALD over the blend, and the subsequent increase in stability observed. The findings from the chapter outline the potential of functionalities and synthetic modifications that could be employed by organic photocathodes to reach higher stabilities and therefore take a step closer to commerciality of organic photocathodes. The focus of the thesis will then shift towards one step, unassisted carbon dioxide photoreduction for the production of solar fuels, directly tackling the aim of furthering research and understanding in organic materials and their testing for solar fuels production. **Chapter 3** is focused on the design, build and calibration of a testing set-up for carbon dioxide photoreduction. The set-up was focused on gas phase testing, but with the flexibility of adding solution phase testing too. The chapter outlines the chosen design and reasoning, the calibrations done with reference gasses and the tests carried out using commercially available standard benchmarking materials. The chapter further outlines benchmarking and standardisation considerations which are lacking in the field, and required for furthering work in this area. **Chapter 4** focuses on the synthesis, characterisation and testing of a triptycene based series of solution processable and porous polymers, tested in the **Chapter 3** reactor. The features of these polymers were related to performance as single component photocatalysts for carbon dioxide photoreduction, using hydrogen in the oxidation reaction. PL decay kinetics and increased pore sizes showed a correlation with increased product formation. The incorporation of copper as a co-catalyst showed an increase in rate, and

the polymers were mixed in an attempt to form heterojunctions, to improve charge separation. These findings were taken to design the series of spiro based porous polymers outlined in **Chapter 5**, which also showed promise in carbon dioxide photoreduction in the gas phase and begin paving the way for intelligent design of solution processable porous polymers in solar fuels. These two material-based chapters outline a class of solution processable, porous materials that offer great promise for use in photocatalysis. These materials take full advantage of the properties offered by organic materials over inorganic ones, especially that of solubility in common solvents while maintaining a high surface area. The findings from these help pave the way towards intelligent synthetic design of materials in this application. The findings from these studies are summarised in **Chapter 6** where future work is also outlined.

1.6. References

(1) Tripati, A. K.; Roberts, C. D.; Eagle, R. A. Coupling of CO2 and Ice Sheet Stability over Major Climate Transitions of the Last 20 Million Years. *Science (80-.).* **2009**, *326* (5958), 1394–1397. https://doi.org/10.1126/science.1178296.

(2) Gornitz, V.; Oppenheimer, M.; Kopp, R.; Orton, P.; Buchanan, M.; Lin, N.; Horton, R.; Bader, D. New York City Panel on Climate Change 2019 Report Chapter 3: Sea Level Rise. *Ann. N. Y. Acad. Sci.* **2019**, *1439* (1), 71–94. https://doi.org/10.1111/nyas.14006.

(3) Florides, G. A.; Christodoulides, P. Global Warming and Carbon Dioxide through Sciences. *Environment International*. Elsevier Ltd February 1, 2009, pp 390–401. https://doi.org/10.1016/j.envint.2008.07.007.

(4) Allen, M. R.; Pauline Dube, O.; Solecki, W.; Aragón-Durand, F.; Cramer France, W.; Humphreys, S.; Dasgupta, P.; Millar, R.; Dube, O.; Solecki, W.; Aragón-Durand, F.; Cramer, W.; Humphreys, S.; Kainuma, M.; Kala, J.; Mahowald, N.; Mulugetta, Y.; Perez, R.; Wairiu, M.; Zickfeld, K.; Zhai, P.; Pörtner, H.; Roberts, D.; Skea, J.; Shukla, P.; Pirani, A.; Moufouma-Okia, W.; Péan, C.; Pidcock, R.; Connors, S.; Matthews, J.; Chen, Y.; Zhou, X.; Gomis, M.; Lonnoy, E.; Maycock, T.; Tignor, M.; Waterfield, T. *Framing and Context. In: Global Warming of 1.5°C. An IPCC Special Report on the Impacts of Global Warming of 1.5°C above Pre-Industrial Levels and Related Global Greenhouse Gas Emission Pathways, in the Context of Strengthening the Global Response to the Threat of Climate Change, Sustainable Development, and Efforts to Eradicate Poverty*; Australia, 2018.

(5) Yoro, K. O.; Daramola, M. O. CO2 Emission Sources, Greenhouse Gases, and the Global Warming Effect. *Adv. Carbon Capture Methods, Technol. Appl.* **2020**, 3–28. https://doi.org/10.1016/B978-0-12-819657-1.00001-3.

(6) *NASA: Climate Change and Global Warming*. https://climate.nasa.gov/ (accessed 2020-04-24).

(7) Olah, G. A.; Prakash, G. K. S.; Goeppert, A. Anthropogenic Chemical Carbon Cycle for a Sustainable Future. *J. Am. Chem. Soc.* **2011**, *133* (33), 12881–12898. https://doi.org/10.1021/JA202642Y.

(8) Solomon, S.; Plattner, G. K.; Knutti, R.; Friedlingstein, P. Irreversible Climate Change Due to Carbon Dioxide Emissions. *Proc. Natl. Acad. Sci. U. S. A.* **2009**, *106* (6), 1704–1709. https://doi.org/10.1073/PNAS.0812721106/SUPPL_FILE/0812721106SI.PDF.

(9) Paris Agreement. *Int. Leg. Mater.* **2016**, *55*.

(10) Savaresi, A. The Paris Agreement: A New Beginning? *https://doi.org/10.1080/02646811.2016.1133983* **2016**, *34* (1), 16–26. https://doi.org/10.1080/02646811.2016.1133983.

(11) *Renewable Electricity – Analysis - IEA*; 2022.

(12) Heffron, R.; Halbrügge, S.; Körner, M. F.; Obeng-Darko, N. A.; Sumarno, T.; Wagner, J.; Weibelzahl, M. Justice in Solar Energy Development. *Sol. Energy* **2021**, *218*, 68–75. https://doi.org/10.1016/J.SOLENER.2021.01.072.

(13) Panwar, N. L.; Kaushik, S. C.; Kothari, S. Role of Renewable Energy Sources in Environmental Protection: A Review. *Renewable and Sustainable Energy Reviews*. 2011, pp 1513–1524. https://doi.org/10.1016/j.rser.2010.11.037.

(14) Thirugnanasambandam, M.; Iniyan, S.; Goic, R. A Review of Solar Thermal Technologies. *Renew. Sustain. Energy Rev.* **2010**, *14* (1), 312–322. https://doi.org/10.1016/J.RSER.2009.07.014.

(15) *Renewables 2019 Global Status Report*; Paris, 2019.

(16) Köhler, A.; Bässler, H. Electronic Processes in Organic Semiconductors: An Introduction. *Electron. Process. Org. Semicond. An Introd.* **2015**, 1–405. https://doi.org/10.1002/9783527685172.

(17) *Reference Air Mass 1.5 Spectra | Grid Modernization | NREL*. https://www.nrel.gov/grid/solar-resource/spectra-am1.5.html (accessed 2022-11-18).

(18) Cleveland, C. J.; Morris, C. *Handbook of Energy. Volume II_ Chronologies, Top Ten Lists, and Word Clouds*; Elsevier, 2014; Vol. II.

(19) Fraunhofer ISE. *Photovoltaics report 24/02/2022*. https://www.ise.fraunhofer.de/content/dam/ise/de/documents/publications/studies/Photovoltaics-Report.pdf (accessed 2023-02-14).

(20) Bódis, K.; Kougias, I.; Taylor, N.; Jäger-Waldau, A. Solar Photovoltaic Electricity Generation: A Lifeline for the European Coal Regions in Transition. *Sustain. 2019, Vol. 11, Page 3703* **2019**, *11* (13), 3703. https://doi.org/10.3390/SU11133703.

(21) Evans, S. Solar Is Now 'Cheapest Electricity in History', Confirms IEA. *Carbon Brief*. October 13, 2020.

(22) Nwaigwe, K. N.; Mutabilwa, P.; Dintwa, E. An Overview of Solar Power (PV Systems) Integration into Electricity Grids. *Mater. Sci. Energy Technol.* **2019**, *2* (3), 629–633. https://doi.org/10.1016/J.MSET.2019.07.002.

(23) Ramalingam, K.; Indulkar, C. Solar Energy and Photovoltaic Technology. *Distrib. Gener. Syst. Des. Oper. Grid Integr.* **2017**, 69–147. https://doi.org/10.1016/B978-0-12-804208-3.00003-0.

(24) Tuller, H. L. Solar to Fuels Conversion Technologies: A Perspective. *Mater. Renew. Sustain. Energy* **2017**, *6* (1), 1–16. https://doi.org/10.1007/S40243-017-0088-2/FIGURES/6.

(25) Rodriguez, C. A.; Modestino, M. A.; Psaltis, D.; Moser, C. Design and Cost Considerations for Practical Solar-Hydrogen Generators. *Energy Environ. Sci.* **2014**, *7* (12), 3828–3835. https://doi.org/10.1039/C4EE01453G.

(26) Herron, J. A.; Kim, J.; Upadhye, A. A.; Huber, G. W.; Maravelias, C. T. A General Framework for the Assessment of Solar Fuel Technologies. *Energy Environ. Sci.* **2014**, *8* (1), 126–157. https://doi.org/10.1039/C4EE01958J.

(27) Melchionna, M.; Fornasiero, P. Updates on the Roadmap for Photocatalysis. *ACS Catal.* **2020**, *10* (10), 5493–5501. https://doi.org/10.1021/ACSCATAL.0C01204/ASSET/IMAGES/LARGE/CS0C01204_0005.JPEG.

(28) Hoffert, M. I.; Caldeira, K.; Benford, G.; Criswell, D. R.; Green, C.; Herzog, H.; Jain, A. K.; Kheshgi, H. S.; Lackner, K. S.; Lewis, J. S.; Lightfoot, H. D.; Manheimer, W.; Mankins, J. C.; Mauel, M. E.; Perkins, L. J.; Schlesinger, M. E.; Volk, T.; Wigley, T. M. L. Advanced Technology Paths to Global Climate Stability: Energy for a Greenhouse Planet. *Science* **2002**, *298* (5595), 981–987. https://doi.org/10.1126/science.1072357.

(29) Zhu, S.; Wang, D. Photocatalysis: Basic Principles, Diverse Forms of Implementations and Emerging Scientific Opportunities. *Advanced Energy Materials*. Wiley-VCH Verlag December 6, 2017. https://doi.org/10.1002/aenm.201700841.

(30) Bockris, J. O. M. The Origin of Ideas on a Hydrogen Economy and Its Solution to the Decay of the Environment. *Int. J. Hydrogen Energy* **2002**, *27* (7–8), 731–740. https://doi.org/10.1016/S0360-

3199(01)00154-9.

(31) Bockris, J. O. M. The Hydrogen Economy: Its History. *Int. J. Hydrogen Energy* **2013**, *38* (6), 2579–2588. https://doi.org/10.1016/J.IJHYDENE.2012.12.026.

(32) Bockris, J. O.; Khan, S. U. M. The Electrochemistry of Cleaner Environments. *Surf. Electrochem.* **1993**, 927–976. https://doi.org/10.1007/978-1-4615-3040-4_10.

(33) Vezirolu, T. N.; Barbir, F. Hydrogen: The Wonder Fuel. *Int. J. Hydrogen Energy* **1992**, *17* (6), 391–404. https://doi.org/10.1016/0360-3199(92)90183-W.

(34) Hydrogen: The Fuel of the Future? | The Economist. *The Economist*. 2021.

(35) Santos, E.; Quaino, P.; Schmickler, W. Theory of Electrocatalysis: Hydrogen Evolution and More. *Phys. Chem. Chem. Phys.* **2012**, *14* (32), 11224–11233. https://doi.org/10.1039/C2CP40717E.

(36) Rothschild, A.; Dotan, H. Beating the Efficiency of Photovoltaics-Powered Electrolysis with Tandem Cell Photoelectrolysis. *ACS Energy Lett.* **2017**, *2* (1), 45–51. https://doi.org/10.1021/ACSENERGYLETT.6B00610/ASSET/IMAGES/LARGE/NZ-2016-006107_0005.JPEG.

(37) Rosen, M. A.; Koohi-Fayegh, S. The Prospects for Hydrogen as an Energy Carrier: An Overview of Hydrogen Energy and Hydrogen Energy Systems. *Energy, Ecol. Environ.* **2016**, *1* (1), 10–29. https://doi.org/10.1007/S40974-016-0005-Z/TABLES/7.

(38) Kalamaras, C. M.; Efstathiou, A. M.; Al-Assaf, Y.; Poullikkas, A. Conference Paper Hydrogen Production Technologies: Current State and Future Developments. *Conf. Pap. Energy* **2013**, *2013*. https://doi.org/10.1155/2013/690627.

(39) Shiva Kumar, S.; Himabindu, V. Hydrogen Production by PEM Water Electrolysis – A Review. *Mater. Sci. Energy Technol.* **2019**, *2* (3), 442–454. https://doi.org/10.1016/J.MSET.2019.03.002.

(40) Kumaravel, V.; Kang, M. Photocatalytic Hydrogen Evolution. *Catal. 2020, Vol. 10, Page 492* **2020**, *10* (5), 492. https://doi.org/10.3390/CATAL10050492.

(41) Bangjun, W.; Feng, Z.; Feng, J.; Yu, P.; Cui, L. Decision Making on Investments in Photovoltaic Power Generation Projects Based on Renewable Portfolio Standard: Perspective of Real Option. *Renew. Energy* **2022**, *189*, 1033–1045. https://doi.org/10.1016/J.RENENE.2022.02.112.

(42) He, J.; Janáky, C. Recent Advances in Solar-Driven Carbon Dioxide Conversion: Expectations versus Reality. *ACS Energy Lett.* **2020**, *5* (6), 1996–2014. https://doi.org/10.1021/ACSENERGYLETT.0C00645/ASSET/IMAGES/LARGE/NZ0C00645_0002.JPEG.

(43) González-Castaño, M.; Dorneanu, B.; Arellano-García, H. The Reverse Water Gas Shift Reaction: A Process Systems Engineering Perspective. *React. Chem. Eng.* **2021**, *6* (6), 954–976. https://doi.org/10.1039/D0RE00478B.

(44) Bozzano, G.; Manenti, F. Efficient Methanol Synthesis: Perspectives, Technologies and Optimization Strategies. *Prog. Energy Combust. Sci.* **2016**, *56*, 71–105. https://doi.org/10.1016/J.PECS.2016.06.001.

(45) Olah, G. A. Beyond Oil and Gas: The Methanol Economy. *Angew. Chemie - Int. Ed.* **2005**, *44* (18), 2636–2639. https://doi.org/10.1002/ANIE.200462121.

(46) Elfasakhany, A. Investigations on the Effects of Ethanol–Methanol–Gasoline Blends in a Spark-Ignition Engine: Performance and Emissions Analysis. *Eng. Sci. Technol. an Int. J.* **2015**, *18* (4), 713–719. https://doi.org/10.1016/J.JESTCH.2015.05.003.

(47) Deka, T. J.; Osman, A. I.; Baruah, D. C.; Rooney, D. W. Methanol Fuel Production, Utilization, and Techno-Economy: A Review. *Environ. Chem. Lett. 2022 206* **2022**, *20* (6), 3525–3554. https://doi.org/10.1007/S10311-022-01485-Y.

(48) Pandey, S. A Critical Review: Application of Methanol as a Fuel for Internal Combustion Engines and Effects of Blending Methanol with Diesel/Biodiesel/Ethanol on Performance, Emission, and Combustion Characteristics of Engines. *Heat Transf.* **2022**, *51* (4), 3334–3352. https://doi.org/10.1002/HTJ.22453.

(49) Zheng, Y.; Wang, J.; Yu, B.; Zhang, W.; Chen, J.; Qiao, J.; Zhang, J. A Review of High Temperature Co-Electrolysis of H2O and CO2 to Produce Sustainable Fuels Using Solid Oxide Electrolysis Cells (SOECs): Advanced Materials and Technology. *Chem. Soc. Rev.* **2017**, *46* (5), 1427–1463. https://doi.org/10.1039/C6CS00403B.

(50) Cheng, K.; Kang, J.; King, D. L.; Subramanian, V.; Zhou, C.; Zhang, Q.; Wang, Y. Advances in Catalysis for Syngas Conversion to Hydrocarbons. *Adv. Catal.* **2017**, *60*, 125–208. https://doi.org/10.1016/BS.ACAT.2017.09.003.

(51) Mignard, D.; Pritchard, C. Processes for the Synthesis of Liquid Fuels from CO2 and Marine Energy. *Chem. Eng. Res. Des.* **2006**, *84* (9 A), 828–836. https://doi.org/10.1205/cherd.05204.

(52) Davis, B. H. Fischer-Tropsch Synthesis: Current Mechanism and Futuristic Needs. *Fuel Process. Technol.* **2001**, *71* (1–3), 157–166. https://doi.org/10.1016/S0378-3820(01)00144-8.

(53) Dry, M. E. The Fischer–Tropsch Process: 1950–2000. *Catal. Today* **2002**, *71* (3–4), 227–241. https://doi.org/10.1016/S0920-5861(01)00453-9.

(54) Mampilli, J. S.; Syam, C. S. S.; Jith, K. P. A.; Rajan, A.; Rathish, T. R.; James, A. Design of Methane/Oxygen Fuelled Bipropellant Rocket Engine. *AIP Conf. Proc.* **2021**, *2358* (1), 050021. https://doi.org/10.1063/5.0058359.

(55) Arutyunov, V.; Savchenko, V.; Sedov, I.; Arutyunov, A.; Nikitin, A. The Fuel of Our Future: Hydrogen or Methane? *Methane 2022, Vol. 1, Pages 96-106* **2022**, *1* (2), 96–106. https://doi.org/10.3390/METHANE1020009.

(56) Vogt, C.; Monai, M.; Jan Kramer, G.; Weckhuysen, B. M. The Renaissance of the Sabatier Reaction and Its Applications on Earth and in Space. *Nat. Catal.* **1929**. https://doi.org/10.1038/s41929-019-0244-4.

(57) Falcinelli, S. Fuel Production from Waste CO2 Using Renewable Energies. *Catal. Today* **2020**, *348*, 95–101. https://doi.org/10.1016/J.CATTOD.2019.08.041.

(58) Moioli, E.; Mutschler, R.; Züttel, A. Renewable Energy Storage via CO2 and H2 Conversion to Methane and Methanol: Assessment for Small Scale Applications. *Renew. Sustain. Energy Rev.* **2019**, *107*, 497–506. https://doi.org/10.1016/J.RSER.2019.03.022.

(59) Osterloh, F. E. Photocatalysis versus Photosynthesis: A Sensitivity Analysis of Devices for Solar Energy Conversion and Chemical Transformations. *ACS Energy Lett.* **2017**, *2* (2), 445–453. https://doi.org/10.1021/ACSENERGYLETT.6B00665/ASSET/IMAGES/LARGE/NZ-2016-006655_0003.JPEG.

(60) Stirbet, A.; Lazár, D.; Guo, Y.; Govindjee, G. Photosynthesis: Basics, History and Modelling. *Ann. Bot.* **2020**, *126* (4), 511–537. https://doi.org/10.1093/AOB/MCZ171.

(61) Larkum, A. W. D. Limitations and Prospects of Natural Photosynthesis for Bioenergy Production. *Curr. Opin. Biotechnol.* **2010**, *21* (3), 271–276. https://doi.org/10.1016/J.COPBIO.2010.03.004.

(62) Ng, B.-J.; Kurnianditia Putri, L.; Ying Kong, X.; Wen Teh, Y.; Pasbakhsh, P.; Chai, S.-P.; Ng, B.; Putri, L. K.; Kong, X. Y.; Teh, Y. W.; Chai, S.; Pasbakhsh, P. Z-Scheme Photocatalytic Systems for Solar Water Splitting. *Adv. Sci.* **2020**, *7* (7), 1903171. https://doi.org/10.1002/ADVS.201903171.

(63) Phillips, L. Solar Energy. *Manag. Glob. Warm. An Interface Technol. Hum. Issues* **2019**, 317–332. https://doi.org/10.1016/B978-0-12-814104-5.00009-0.

(64) Brabec, C. J.; Sariciftci, N. S.; Hummelen, J. C. Plastic Solar Cells**. *Adv. Funct. Mater.* **2001**, *11* (1), 15–26. https://doi.org/10.1002/1616-3028.

(65) Lee, Y. J.; Adkison, B. L.; Xu, L.; Kramer, A. A.; Hsu, J. W. P. Comparison of Conventional and Inverted Organic Photovoltaic Devices with Controlled Illumination Area and Extraction Layers. *Sol. Energy Mater. Sol. Cells* **2016**, *144*, 592–599. https://doi.org/10.1016/J.SOLMAT.2015.09.059.

(66) Jia, J.; Seitz, L. C.; Benck, J. D.; Huo, Y.; Chen, Y.; Ng, J. W. D.; Bilir, T.; Harris, J. S.; Jaramillo, T. F. Solar Water Splitting by Photovoltaic-Electrolysis with a Solar-to-Hydrogen Efficiency over 30%. *Nat. Commun.* **2016**, *7*, 13237. https://doi.org/10.1038/ncomms13237.

(67) Reece, S. Y.; Hamel, J. A.; Sung, K.; Jarvi, T. D.; Esswein, A. J.; Pijpers, J. J. H.; Nocera, D. G. Wireless

Solar Water Splitting Using Silicon-Based Semiconductors and Earth-Abundant Catalysts. *Science (80-.).* **2011**, *334* (6056), 645–648. https://doi.org/10.1126/science.1209816.

(68) Andrei, V.; Ucoski, G. M.; Pornrungroj, C.; Uswachoke, C.; Wang, Q.; Achilleos, D. S.; Kasap, H.; Sokol, K. P.; Jagt, R. A.; Lu, H.; Lawson, T.; Wagner, A.; Pike, S. D.; Wright, D. S.; Hoye, R. L. Z.; MacManus-Driscoll, J. L.; Joyce, H. J.; Friend, R. H.; Reisner, E. Floating Perovskite-BiVO4 Devices for Scalable Solar Fuel Production. *Nat. 2022 6087923* **2022**, *608* (7923), 518–522. https://doi.org/10.1038/s41586-022-04978-6.

(69) Ye, S.; Zhang, F. Floating Artificial Leaves Buoy the Promise of Solar Fuels. *Joule* **2022**, *6* (10), 2246–2247. https://doi.org/10.1016/J.JOULE.2022.09.015.

(70) Arunachalam, P.; Al Mayouf, A. M. Photoelectrochemical Water Splitting. *Noble Met. Oxide Hybrid Nanoparticles Fundam. Appl.* **2019**, 585–606. https://doi.org/10.1016/B978-0-12-814134-2.00028-0.

(71) Kalamaras, E.; Maroto-Valer, M. M.; Shao, M.; Xuan, J.; Wang, H. Solar Carbon Fuel via Photoelectrochemistry. *Catal. Today* **2018**, *317*, 56–75. https://doi.org/10.1016/J.CATTOD.2018.02.045.

(72) Peter, L. M. Photoelectrochemistry: From Basic Principles to Photocatalysis. In *RSC Energy and Environment Series*; Royal Society of Chemistry, 2016; Vol. 2016-January, pp 3–28. https://doi.org/10.1039/9781782622338-00001.

(73) Ahmed, M.; Dincer, I. A Review on Photoelectrochemical Hydrogen Production Systems: Challenges and Future Directions. *Int. J. Hydrogen Energy* **2019**, *44* (5), 2474–2507. https://doi.org/10.1016/j.ijhydene.2018.12.037.

(74) Walter, M. G.; Warren, E. L.; McKone, J. R.; Boettcher, S. W.; Mi, Q.; Santori, E. A.; Lewis, N. S. Solar Water Splitting Cells. *Chem. Rev.* **2010**, *110* (11), 6446–6473. https://doi.org/10.1021/cr1002326.

(75) Bellani, S.; Antognazza, M. R.; Bonaccorso, F. Carbon-Based Photocathode Materials for Solar Hydrogen Production. *Adv. Mater.* **2019**, *31* (9), 1801446. https://doi.org/10.1002/adma.201801446.

(76) Chen, X.; Shen, S.; Guo, L.; Mao, S. S. Semiconductor-Based Photocatalytic Hydrogen Generation. *Chem. Rev.* **2010**, *110* (11), 6503–6570. https://doi.org/10.1021/cr1001645.

(77) Stolarczyk, J. K.; Bhattacharyya, S.; Polavarapu, L.; Feldmann, J. Challenges and Prospects in Solar Water Splitting and CO $_2$ Reduction with Inorganic and Hybrid Nanostructures. *ACS Catal.* **2018**, *8* (4), 3602–3635. https://doi.org/10.1021/acscatal.8b00791.

(78) D., W. A Short History of Electrochemistry-Part 2. *Galvanotechnik* **2005**, *96* (8), 1820–1828.

(79) Li, X.; Yu, J.; Jaroniec, M. Hierarchical Photocatalysts. *Chem. Soc. Rev.* **2016**, *45* (9), 2603–2636. https://doi.org/10.1039/c5cs00838g.

(80) Sordello, F.; Calza, P.; Minero, C.; Malato, S.; Minella, M. More than One Century of History for Photocatalysis, from Past, Present and Future Perspectives. *Catal. 2022, Vol. 12, Page 1572* **2022**, *12* (12), 1572. https://doi.org/10.3390/CATAL12121572.

(81) Markham, M. C. Photocatalytic Properties of Oxides. *J. Chem. Educ.* **1955**, *32* (10), 540–543. https://doi.org/10.1021/ED032P540.

(82) Painter, D. S. Oil and Geopolitics: The Oil Crises of the 1970s and the Cold War. *Hist. Soc. Res.* **2014**, *39* (4), 186–208. https://doi.org/10.12759/hsr.39.2014.4.

(83) Fujishima, A.; Honda, K. Electrochemical Photolysis of Water at a Semiconductor Electrode. *Nature* **1972**, *238* (5358), 37–38. https://doi.org/10.1038/238037a0.

(84) O'Regan, B.; Grätzel, M. A Low-Cost, High-Efficiency Solar Cell Based on Dye-Sensitized Colloidal TiO2 Films. *Nature* **1991**, *353* (6346), 737–740. https://doi.org/10.1038/353737a0.

(85) Zhu, S.; Wang, D. Photocatalysis: Basic Principles, Diverse Forms of Implementations and Emerging Scientific Opportunities. *Adv. Energy Mater.* **2017**, *7* (23), 1700841. https://doi.org/10.1002/AENM.201700841.

(86) Calza, P.; Minella, M.; Demarchis, L.; Sordello, F.; Minero, C. Photocatalytic Rate Dependence on Light Absorption Properties of Different TiO2 Specimens. *Catal. Today* **2020**, *340*, 12–18.

https://doi.org/10.1016/J.CATTOD.2018.10.013.

(87) Scuseria, G. E. Advancing Solid-State Band Gap Predictions. *Proc. Natl. Acad. Sci.* **2021**, *118* (35), e2113648118. https://doi.org/10.1073/PNAS.2113648118.

(88) Anastassakis, E. M.; Joannopoulos, J. D. The Physics of Semiconductors; Springer Science and Business Media LLC: Heidelberg, 1990; pp 1–842. https://doi.org/10.1142/9789814540216.

(89) Yanagi, R.; Zhao, T.; Solanki, D.; Pan, Z.; Hu, S. Charge Separation in Photocatalysts: Mechanisms, Physical Parameters, and Design Principles. *ACS Energy Lett.* **2022**, *7* (1), 432–452. https://doi.org/10.1021/ACSENERGYLETT.1C02516/ASSET/IMAGES/MEDIUM/NZ1C02516_0010.GIF.

(90) Frenkel, J. On the Transformation of Light into Heat in Solids. I. *Phys. Rev.* **1931**, *37* (1), 17. https://doi.org/10.1103/PhysRev.37.17.

(91) Wannier, G. H. The Structure of Electronic Excitation Levels in Insulating Crystals. *Phys. Rev.* **1937**, *52* (3), 191. https://doi.org/10.1103/PhysRev.52.191.

(92) Peng, W. T.; Brey, D.; Giannini, S.; Dell'Angelo, D.; Burghardt, I.; Blumberger, J. Exciton Dissociation in a Model Organic Interface: Excitonic State-Based Surface Hopping versus Multiconfigurational Time-Dependent Hartree. *J. Phys. Chem. Lett.* **2022**, *13* (31), 7105–7112. https://doi.org/10.1021/ACS.JPCLETT.2C01928/ASSET/IMAGES/LARGE/JZ2C01928_0004.JPEG.

(93) Fukuhara, T.; Tamai, Y.; Ohkita, H. Nongeminate Charge Recombination in Organic Photovoltaics. *Sustain. Energy Fuels* **2020**, *4* (9), 4321–4351. https://doi.org/10.1039/D0SE00310G.

(94) Lakowicz, J. R. Principles of Fluorescence Spectroscopy. *Princ. Fluoresc. Spectrosc.* **2006**, 1–954. https://doi.org/10.1007/978-0-387-46312-4.

(95) Friend, R. H.; Phillips, M.; Rao, A.; Wilson, M. W. B.; Li, Z.; McNeill, C. R. Excitons and Charges at Organic Semiconductor Heterojunctions. *Faraday Discuss.* **2012**, *155* (0), 339–348. https://doi.org/10.1039/c1fd00104c.

(96) Low, J.; Yu, J.; Jaroniec, M.; Wageh, S.; Al-Ghamdi J X Low, A. A.; Yu, J. G.; Wageh, S.; Al-Ghamdi, A. A.; Jaroniec, M. Heterojunction Photocatalysts. *Adv. Mater.* **2017**, *29* (20), 1601694. https://doi.org/10.1002/ADMA.201601694.

(97) Wang, Q.; Zhang, L.; Liu, X.; Li, S. Two-Dimensional Semiconductor Heterojunctions for Optoelectronics and Electronics. *Front. Energy Res.* **2021**, *9*, 833. https://doi.org/10.3389/FENRG.2021.802055/BIBTEX.

(98) Dimitrov, S. D.; Schroeder, B. C.; Nielsen, C. B.; Bronstein, H.; Fei, Z.; McCulloch, I.; Heeney, M.; Durrant, J. R. Singlet Exciton Lifetimes in Conjugated Polymer Films for Organic Solar Cells. *Polym. 2016, Vol. 8, Page 14* **2016**, *8* (1), 14. https://doi.org/10.3390/POLYM8010014.

(99) Zhang, L.; Mohamed, H. H.; Dillert, R.; Bahnemann, D. Kinetics and Mechanisms of Charge Transfer Processes in Photocatalytic Systems: A Review. *J. Photochem. Photobiol. C Photochem. Rev.* **2012**, *13* (4), 263–276. https://doi.org/10.1016/J.JPHOTOCHEMREV.2012.07.002.

(100) Coropceanu, V.; Chen, X. K.; Wang, T.; Zheng, Z.; Brédas, J. L. Charge-Transfer Electronic States in Organic Solar Cells. *Nat. Rev. Mater. 2019 411* **2019**, *4* (11), 689–707. https://doi.org/10.1038/s41578-019-0137-9.

(101) Alcácer, L. Electronic Structure of Organic Semiconductors: Polymers and Small Molecules. *Electron. Struct. Org. Semicond. Polym. small Mol.* **2018**. https://doi.org/10.1088/2053-2571/AADDD8.

(102) Kosco, J.; Moruzzi, F.; Willner, B.; McCulloch, I. Photocatalysts Based on Organic Semiconductors with Tunable Energy Levels for Solar Fuel Applications. *Adv. Energy Mater.* **2020**, *10* (39), 2001935. https://doi.org/10.1002/aenm.202001935.

(103) Yang, J.; Wang, D.; Han, H.; Li, C. Roles of Cocatalysts in Photocatalysis and Photoelectrocatalysis. *Acc. Chem. Res.* **2013**, *46* (8), 1900–1909. https://doi.org/10.1021/AR300227E/ASSET/IMAGES/MEDIUM/AR-2012-00227E_0010.GIF.

(104) Adamu, A.; Russo-Abegão, F.; Boodhoo, K. Process Intensification Technologies for CO2 Capture and

Conversion – a Review. *BMC Chem. Eng.* **2020**, *2* (1), 1–18. https://doi.org/10.1186/s42480-019-0026-4.

(105) Ooka, H.; Figueiredo, M. C.; Koper, M. T. M. Competition between Hydrogen Evolution and Carbon Dioxide Reduction on Copper Electrodes in Mildly Acidic Media. *Langmuir* **2017**, *33* (37), 9307–9313. https://doi.org/10.1021/acs.langmuir.7b00696.

(106) Carroll, J. J.; Slupsky, J. D.; Mather, A. E. The Solubility of Carbon Dioxide in Water at Low Pressure. *J. Phys. Chem. Ref. Data* **2009**, *20* (6), 1201. https://doi.org/10.1063/1.555900.

(107) Li, X.; Yu, J.; Jaroniec, M.; Chen, X. Cocatalysts for Selective Photoreduction of CO 2 into Solar Fuels. *Chemical Reviews*. American Chemical Society March 27, 2019, pp 3962–4179. https://doi.org/10.1021/acs.chemrev.8b00400.

(108) Chang, X.; Wang, T.; Gong, J. CO $_2$ Photo-Reduction: Insights into CO $_2$ Activation and Reaction on Surfaces of Photocatalysts. *Energy Environ. Sci.* **2016**, *9* (7), 2177–2196. https://doi.org/10.1039/C6EE00383D.

(109) Fu, Z.; Yang, Q.; Liu, Z.; Chen, F.; Yao, F.; Xie, T.; Zhong, Y.; Wang, D.; Li, J.; Li, X.; Zeng, G. Photocatalytic Conversion of Carbon Dioxide: From Products to Design the Catalysts. *J. CO2 Util.* **2019**, *34*, 63–73. https://doi.org/10.1016/j.jcou.2019.05.032.

(110) Xu, Y.; Mao, N.; Zhang, C.; Wang, X.; Zeng, J.; Chen, Y.; Wang, F.; Jiang, J. X. Rational Design of Donor-Π-Acceptor Conjugated Microporous Polymers for Photocatalytic Hydrogen Production. *Appl. Catal. B Environ.* **2018**, *228*, 1–9. https://doi.org/10.1016/j.apcatb.2018.01.073.

(111) Sun, Z.; Talreja, N.; Tao, H.; Texter, J.; Muhler, M.; Strunk, J.; Chen, J. Catalysis of Carbon Dioxide Photoreduction on Nanosheets: Fundamentals and Challenges. *Angew. Chemie Int. Ed.* **2018**, *57* (26), 7610–7627. https://doi.org/10.1002/anie.201710509.

(112) Aeshala, L. M.; Uppaluri, R.; Verma, A. Electrochemical Conversion of CO2 to Fuels: Tuning of the Reaction Zone Using Suitable Functional Groups in a Solid Polymer Electrolyte. *Phys. Chem. Chem. Phys.* **2014**, *16* (33), 17588–17594. https://doi.org/10.1039/C4CP02389G.

(113) Chang, G.; Shang, Z.; Yu, T.; Yang, L. Rational Design of a Novel Indole-Based Microporous Organic Polymer: Enhanced Carbon Dioxide Uptake via Local Dipole–π Interactions. *J. Mater. Chem. A* **2016**, *4* (7), 2517–2523. https://doi.org/10.1039/C5TA08705H.

(114) Chang, X.; Wang, T.; Gong, J. CO2 Photo-Reduction: Insights into CO2 Activation and Reaction on Surfaces of Photocatalysts. *Energy and Environmental Science*. Royal Society of Chemistry July 1, 2016, pp 2177–2196. https://doi.org/10.1039/c6ee00383d.

(115) Nautiyal, R.; Tavar, D.; Suryavanshi, U.; Singh, G.; Singh, A.; Vinu, A.; Mane, G. P. Advanced Nanomaterials for Highly Efficient CO2 Photoreduction and Photocatalytic Hydrogen Evolution. *http://www.tandfonline.com/action/journalInformation?show=aimsScope&journalCode=tsta20#.VmBmuzZFCUk* **2022**, *23* (1), 866–894. https://doi.org/10.1080/14686996.2022.2149036.

(116) Bandyopadhyay, S.; Anil, A. G.; James, A.; Patra, A. Multifunctional Porous Organic Polymers: Tuning of Porosity, CO $_2$, and H $_2$ Storage and Visible-Light-Driven Photocatalysis. *ACS Appl. Mater. Interfaces* **2016**, *8* (41), 27669–27678. https://doi.org/10.1021/acsami.6b08331.

(117) Tu, W.; Zhou, Y.; Zou, Z. Photocatalytic Conversion of CO2 into Renewable Hydrocarbon Fuels: State-of-the-Art Accomplishment, Challenges, and Prospects. *Advanced Materials*. Wiley-VCH Verlag July 16, 2014, pp 4607–4626. https://doi.org/10.1002/adma.201400087.

(118) Fu, J.; Jiang, K.; Qiu, X.; Yu, J.; Liu, M. Product Selectivity of Photocatalytic CO2 Reduction Reactions. *Materials Today*. Elsevier B.V. January 1, 2020, pp 222–243. https://doi.org/10.1016/j.mattod.2019.06.009.

(119) Ozin, G. A. Throwing New Light on the Reduction of CO2. *Adv. Mater.* **2015**, *27* (11), 1957–1963. https://doi.org/10.1002/ADMA.201500116.

(120) Tountas, A. A.; Peng, X.; Tavasoli, A. V.; Duchesne, P. N.; Dingle, T. L.; Dong, Y.; Hurtado, L.; Mohan, A.; Sun, W.; Ulmer, U.; Wang, L.; Wood, T. E.; Maravelias, C. T.; Sain, M. M.; Ozin, G. A. Towards Solar Methanol: Past, Present, and Future. *Adv. Sci.* **2019**, *6* (8), 1801903. https://doi.org/10.1002/advs.201801903.

(121) Jovan, D. J.; Dolanc, G. Can Green Hydrogen Production Be Economically Viable under Current Market Conditions. *Energies* **2020**, *13* (24). https://doi.org/10.3390/EN13246599.

(122) Porosoff, M. D.; Yan, B.; Chen, J. G. Catalytic Reduction of CO2 by H2 for Synthesis of CO, Methanol and Hydrocarbons: Challenges and Opportunities. *Energy Environ. Sci.* **2016**, *9* (1), 62–73. https://doi.org/10.1039/C5EE02657A.

(123) Wang, Y.; Xia, Q. Fischer-Tropsch Synthesis Steps into the Solar Era: Lower Olefins from Syngas. *Chem* **2018**, *4* (12), 2741–2743. https://doi.org/10.1016/J.CHEMPR.2018.11.020.

(124) Herron, J. A.; Kim, J.; Upadhye, A. A.; Huber, G. W.; Maravelias, C. T. A General Framework for the Assessment of Solar Fuel Technologies. *Energy Environ. Sci.* **2014**, *8* (1), 126–157. https://doi.org/10.1039/C4EE01958J.

(125) Von Der Assen, N.; Voll, P.; Peters, M.; Bardow, A. Life Cycle Assessment of CO2 Capture and Utilization: A Tutorial Review. *Chem. Soc. Rev.* **2014**, *43* (23), 7982–7994. https://doi.org/10.1039/C3CS60373C.

(126) Zhang, T.; Li, Z.; Shi, R.; Ma, Y.; Zhao, J. Photodriven CO2 Hydrogenation into Diverse Products: Recent Progress and Perspective. *J. Phys. Chem. Lett.* **2022**, *13* (23), 5291–5303. https://doi.org/10.1021/ACS.JPCLETT.2C01159/ASSET/IMAGES/LARGE/JZ2C01159_0013.JPEG.

(127) Kondratenko, E. V.; Mul, G.; Baltrusaitis, J.; Larrazábal, G. O.; Pérez-Ramírez, J. Status and Perspectives of CO 2 Conversion into Fuels and Chemicals by Catalytic, Photocatalytic and Electrocatalytic Processes. *Energy Environ. Sci.* **2013**, *6* (11), 3112–3135. https://doi.org/10.1039/C3EE41272E.

(128) Li, Y. F.; Soheilnia, N.; Greiner, M.; Ulmer, U.; Wood, T.; Jelle, A. A.; Dong, Y.; Yin Wong, A. P.; Jia, J.; Ozin, G. A. Pd@H y WO 3- x Nanowires Efficiently Catalyze the CO 2 Heterogeneous Reduction Reaction with a Pronounced Light Effect. *ACS Appl. Mater. Interfaces* **2019**, *11* (6), 5610–5615. https://doi.org/10.1021/ACSAMI.8B04982/ASSET/IMAGES/LARGE/AM-2018-04982H_0005.JPEG.

(129) Li, Y. F.; Lu, W.; Chen, K.; Duchesne, P.; Jelle, A.; Xia, M.; Wood, T. E.; Ulmer, U.; Ozin, G. A. Cu Atoms on Nanowire Pd/HyWO3- x Bronzes Enhance the Solar Reverse Water Gas Shift Reaction. *J. Am. Chem. Soc.* **2019**, *141* (38), 14991–14996. https://doi.org/10.1021/JACS.9B08030/SUPPL_FILE/JA9B08030_SI_001.PDF.

(130) Protti, S.; Albini, A.; Serpone, N. Photocatalytic Generation of Solar Fuels from the Reduction of H2O and CO2: A Look at the Patent Literature. *Phys. Chem. Chem. Phys.* **2014**, *16* (37), 19790–19827. https://doi.org/10.1039/C4CP02828G.

(131) Li, N.; Liu, M.; Yang, B.; Shu, W.; Shen, Q.; Liu, M.; Zhou, J. Enhanced Photocatalytic Performance toward CO2 Hydrogenation over Nanosized TiO2-Loaded Pd under UV Irradiation. *J. Phys. Chem. C* **2017**, *121* (5), 2923–2932. https://doi.org/10.1021/ACS.JPCC.6B12683.

(132) Das, S.; Wan Daud, W. M. A. A Review on Advances in Photocatalysts towards CO2conversion. *RSC Advances*. Royal Society of Chemistry 2014, pp 20856–20893. https://doi.org/10.1039/c4ra01769b.

(133) Liu, L.; Li, Y. Understanding the Reaction Mechanism of Photocatalytic Reduction of CO2 with H2O on TiO2-Based Photocatalysts: A Review. *Aerosol Air Qual. Res.* **2014**, *14* (2), 453–469. https://doi.org/10.4209/AAQR.2013.06.0186.

(134) Teramura, K.; Okuoka, S. ichi; Tsuneoka, H.; Shishido, T.; Tanaka, T. Photocatalytic Reduction of CO2 Using H2 as Reductant over ATaO3 Photocatalysts (A = Li, Na, K). *Appl. Catal. B Environ.* **2010**, *96* (3–4), 565–568. https://doi.org/10.1016/j.apcatb.2010.03.021.

(135) Mateo, D.; Albero, J.; García, H. Graphene Supported NiO/Ni Nanoparticles as Efficient Photocatalyst for Gas Phase CO2 Reduction with Hydrogen. *Appl. Catal. B Environ.* **2018**, *224*, 563–571. https://doi.org/10.1016/J.APCATB.2017.10.071.

(136) Xiong, H.; Dong, Y.; Liu, D.; Long, R.; Kong, T.; Xiong, Y. Recent Advances in Porous Materials for Photocatalytic CO 2 Reduction. *J. Phys. Chem. Lett* **2022**, *2022*, 1272–1282. https://doi.org/10.1021/acs.jpclett.1c03204.

(137) Zhang, L.; Wang, W.; Wang, H.; Ma, X.; Bian, Z. Design of Inorganic–Organic Hybrid Photocatalytic Systems for Enhanced CO2 Reduction under Visible Light. *Chem. Eng. Sci.* **2019**, *207*, 1246–1255.

https://doi.org/10.1016/j.ces.2019.07.049.

(138) Maeda, K. Metal-Complex/Semiconductor Hybrid Photocatalysts and Photoelectrodes for CO_2 Reduction Driven by Visible Light. *Adv. Mater.* **2019**, *31* (25), 1808205. https://doi.org/10.1002/adma.201808205.

(139) Won, D. Il; Lee, J. S.; Cheong, H. Y.; Cho, M.; Jung, W. J.; Son, H. J.; Pac, C.; Kang, S. O. Organic-Inorganic Hybrid Photocatalyst for Carbon Dioxide Reduction. *Faraday Discuss.* **2017**, *198* (0), 337–351. https://doi.org/10.1039/c6fd00222f.

(140) Won, D. Il; Lee, J. S.; Ji, J. M.; Jung, W. J.; Son, H. J.; Pac, C.; Kang, S. O. Highly Robust Hybrid Photocatalyst for Carbon Dioxide Reduction: Tuning and Optimization of Catalytic Activities of Dye/TiO2/Re(I) Organic-Inorganic Ternary Systems. *J. Am. Chem. Soc.* **2015**, *137* (42), 13679–13690. https://doi.org/10.1021/jacs.5b08890.

(141) Maeda, K.; An, D.; Kumara Ranasinghe, C. S.; Uchiyama, T.; Kuriki, R.; Kanazawa, T.; Lu, D.; Nozawa, S.; Yamakata, A.; Uchimoto, Y.; Ishitani, O. Visible-Light CO2 Reduction over a Ruthenium(Ii)-Complex/C3N4 Hybrid Photocatalyst: The Promotional Effect of Silver Species. *J. Mater. Chem. A* **2018**, *6* (20), 9708–9715. https://doi.org/10.1039/c8ta03245a.

(142) Yu, B.; Li, L.; Liu, S.; Wang, H.; Liu, H.; Lin, C.; Liu, C.; Wu, H.; Zhou, W.; Li, X.; Wang, T.; Chen, B.; Jiang, J. Robust Biological Hydrogen-Bonded Organic Framework with Post-Functionalized Rhenium(I) Sites for Efficient Heterogeneous Visible-Light-Driven CO2 Reduction. *Angew. Chemie* **2021**, *133* (16), 9065–9071. https://doi.org/10.1002/ANGE.202016710.

(143) Zhang, S.; Wang, S.; Guo, L.; Chen, H.; Tan, B.; Jin, S. An Artificial Photosynthesis System Comprising a Covalent Triazine Framework as an Electron Relay Facilitator for Photochemical Carbon Dioxide Reduction. *J. Mater. Chem. C* **2019**, *8* (1), 192–200. https://doi.org/10.1039/c9tc05297f.

(144) Fu, Y.; Zhu, X.; Huang, L.; Zhang, X.; Zhang, F.; Zhu, W. Azine-Based Covalent Organic Frameworks as Metal-Free Visible Light Photocatalysts for CO2 Reduction with H2O. *Appl. Catal. B Environ.* **2018**, *239*, 46–51. https://doi.org/10.1016/J.APCATB.2018.08.004.

(145) Hu, X.-L.; Li, H.-G.; Tan, B.-E. COFs-Based Porous Materials for Photocatalytic Applications. *Chinese J. Polym. Sci. 2020 387* **2020**, *38* (7), 673–684. https://doi.org/10.1007/S10118-020-2394-X.

(146) Li, J.; Zhao, D.; Liu, J.; Liu, A.; Ma, D. Covalent Organic Frameworks: A Promising Materials Platform for Photocatalytic CO2 Reductions. *Molecules* **2020**, *25* (10). https://doi.org/10.3390/MOLECULES25102425.

(147) Yang, S.; Hu, W.; Zhang, X.; He, P.; Pattengale, B.; Liu, C.; Cendejas, M.; Hermans, I.; Zhang, X.; Zhang, J.; Huang, J. 2D Covalent Organic Frameworks as Intrinsic Photocatalysts for Visible Light-Driven CO2 Reduction. *J. Am. Chem. Soc.* **2018**, *140* (44), 14614–14618. https://doi.org/10.1021/JACS.8B09705/SUPPL_FILE/JA8B09705_SI_001.PDF.

(148) Zhong, H.; Hong, Z.; Yang, C.; Li, L.; Xu, Y.; Wang, X.; Wang, R. A Covalent Triazine-Based Framework Consisting of Donor–Acceptor Dyads for Visible-Light-Driven Photocatalytic CO2 Reduction. *ChemSusChem* **2019**, *12* (19), 4493–4499. https://doi.org/10.1002/CSSC.201901997.

(149) Akhundi, A.; Habibi-Yangjeh, A.; Abitorabi, M.; Rahim Pouran, S. Review on Photocatalytic Conversion of Carbon Dioxide to Value-Added Compounds and Renewable Fuels by Graphitic Carbon Nitride-Based Photocatalysts. *Catalysis Reviews - Science and Engineering*. Taylor and Francis Inc. October 2, 2019, pp 595–628. https://doi.org/10.1080/01614940.2019.1654224.

(150) Fang, Y.; Wang, X. Photocatalytic CO2 Conversion by Polymeric Carbon Nitrides. *Chem. Commun.* **2018**, *54* (45), 5674–5687. https://doi.org/10.1039/c8cc02046a.

(151) Shen, M.; Zhang, L.; Wang, M.; Tian, J.; Jin, X.; Guo, L.; Wang, L.; Shi, J. Carbon-Vacancy Modified Graphitic Carbon Nitride: Enhanced CO 2 Photocatalytic Reduction Performance and Mechanism Probing. *J. Mater. Chem. A* **2019**, *7* (4), 1556–1563. https://doi.org/10.1039/c8ta09302d.

(152) Schukraft, G. E. M.; Woodward, D. R. T.; Kumar, D. S.; Sachs, D. M.; Eslava, D. S.; Petit, D. C. Hypercrosslinked Polymers as a Photocatalytic Platform for Visible-Light-Driven CO2 Photoreduction Using H2O. *ChemSusChem* **2021**, *14* (7), 1720. https://doi.org/10.1002/CSSC.202002824.

(153) Zhang, K.; Goswami, S.; Noh, H.; Lu, Z.; Sheridan, T.; Duan, J.; Dong, W.; Hupp, J. T. An Iron-Porphyrin

Grafted Metal–Organic Framework as a Heterogeneous Catalyst for the Photochemical Reduction of CO2. *J. Photochem. Photobiol.* **2022**, *10*, 100111. https://doi.org/10.1016/J.JPAP.2022.100111.

(154) Akaike, K.; Aoyama, K.; Dekubo, S.; Onishi, A.; Kanai, K. Characterizing Electronic Structure near the Energy Gap of Graphitic Carbon Nitride Based on Rational Interpretation of Chemical Analysis. *Chem. Mater.* **2018**, *30* (7), 2341–2352. https://doi.org/10.1021/ACS.CHEMMATER.7B05316/ASSET/IMAGES/MEDIUM/CM-2017-053164_M001.GIF.

(155) Talapaneni, S. N.; Singh, G.; Kim, I. Y.; AlBahily, K.; Al-Muhtaseb, A. H.; Karakoti, A. S.; Tavakkoli, E.; Vinu, A. Nanostructured Carbon Nitrides for CO $_2$ Capture and Conversion. *Adv. Mater.* **2019**, 1904635. https://doi.org/10.1002/adma.201904635.

(156) Xia, P.; Antonietti, M.; Zhu, B.; Heil, T.; Yu, J.; Cao, S. Designing Defective Crystalline Carbon Nitride to Enable Selective CO $_2$ Photoreduction in the Gas Phase. *Adv. Funct. Mater.* **2019**, *29* (15), 1900093. https://doi.org/10.1002/adfm.201900093.

(157) Qiu, C.; Wang, S.; Zuo, J.; Zhang, B. Photocatalytic CO2 Reduction Coupled with Alcohol Oxidation over Porous Carbon Nitride. *Catalysts* **2022**, *12* (6), 672. https://doi.org/10.3390/CATAL12060672/S1.

(158) Wang, K.; Li, Q.; Liu, B.; Cheng, B.; Ho, W.; Yu, J. Sulfur-Doped g-C3N4 with Enhanced Photocatalytic CO2-Reduction Performance. *Appl. Catal. B Environ.* **2015**, *176–177*, 44–52. https://doi.org/10.1016/j.apcatb.2015.03.045.

(159) Crake, A.; Christoforidis, K. C.; Godin, R.; Moss, B.; Kafizas, A.; Zafeiratos, S.; Durrant, J. R.; Petit, C. Titanium Dioxide/Carbon Nitride Nanosheet Nanocomposites for Gas Phase CO2 Photoreduction under UV-Visible Irradiation. *Appl. Catal. B Environ.* **2019**, *242*, 369–378. https://doi.org/10.1016/J.APCATB.2018.10.023.

(160) Yang, C.; Huang, W.; da Silva, L. C.; Zhang, K. A. I.; Wang, X. Functional Conjugated Polymers for CO $_2$ Reduction Using Visible Light. *Chem. - A Eur. J.* **2018**, *24* (66), 17454–17458. https://doi.org/10.1002/chem.201804496.

(161) Li, L.; Zhao, N.; Wei, W.; Sun, Y. A Review of Research Progress on CO2 Capture, Storage, and Utilization in Chinese Academy of Sciences. *Fuel* **2013**, *108*, 112–130. https://doi.org/10.1016/j.fuel.2011.08.022.

(162) Yang, C.; Huang, W.; da Silva, L. C.; Zhang, K. A. I.; Wang, X. Functional Conjugated Polymers for CO2 Reduction Using Visible Light. *Chem. - A Eur. J.* **2018**, *24* (66), 17454–17458. https://doi.org/10.1002/chem.201804496.

(163) Chen, Y.; Ji, G.; Guo, S.; Yu, B.; Zhao, Y.; Wu, Y.; Zhang, H.; Liu, Z.; Han, B.; Liu, Z. Visible-Light-Driven Conversion of CO2 from Air to CO Using an Ionic Liquid and a Conjugated Polymer. *Green Chem.* **2017**, *19* (24), 5777–5781. https://doi.org/10.1039/c7gc02346d.

(164) Dai, C.; Zhong, L.; Gong, X.; Zeng, L.; Xue, C.; Li, S.; Liu, B. Triphenylamine Based Conjugated Microporous Polymers for Selective Photoreduction of CO2 to CO under Visible Light. *Green Chem.* **2019**, *21* (24), 6606–6610. https://doi.org/10.1039/c9gc03131f.

(165) Yu, X.; Yang, Z.; Qiu, B.; Guo, S.; Yang, P.; Yu, B.; Zhang, H.; Zhao, Y.; Yang, X.; Han, B.; Liu, Z. Eosin Y-Functionalized Conjugated Organic Polymers for Visible-Light-Driven CO $_2$ Reduction with H $_2$ O to CO with High Efficiency. *Angew. Chemie Int. Ed.* **2019**, *58* (2), 632–636. https://doi.org/10.1002/anie.201812790.

(166) Lei, K.; Wang, D.; Ye, L.; Kou, M.; Deng, Y.; Ma, Z.; Wang, L.; Kong, Y. A Metal-Free Donor–Acceptor Covalent Organic Framework Photocatalyst for Visible-Light-Driven Reduction of CO2 with H2O. *ChemSusChem* **2020**, *13* (7), 1725–1729. https://doi.org/10.1002/CSSC.201903545.

(167) Wu, W.; Dai, C.; Wu, M.; Chen, Y.; Zeng, C.; Li, F. Red-Light-Driven CO2 Photoreduction into CH4 and CO Enabled by Narrow-Gap Conjugated Microporous Polymers. *Sol. RRL* **2023**, *7* (2), 2200907. https://doi.org/10.1002/SOLR.202200907.

(168) Wang, Y.; Ji, G.; Ye, W.; Zhang, F.; Wang, Y.; Zhao, Y.; Liu, Z. DFT-Assisted Design of D-A Conjugated Polymers for Photocatalytic Reduction of Carbon Dioxide. *ACS Sustain. Chem. Eng.* **2022**, *10* (29), 9460–9468.

https://doi.org/10.1021/ACSSUSCHEMENG.2C01875/ASSET/IMAGES/LARGE/SC2C01875_0005.JPEG.

(169) Barman, S.; Singh, A.; Rahimi, F. A.; Maji, T. K. Metal-Free Catalysis: A Redox-Active Donor-Acceptor Conjugated Microporous Polymer for Selective Visible-Light-Driven CO2Reduction to CH4. *J. Am. Chem. Soc.* **2021**, *143* (39), 16284–16292. https://doi.org/10.1021/JACS.1C07916/ASSET/IMAGES/LARGE/JA1C07916_0004.JPEG.

(170) Lai, W. C.; Wang, S. H.; Sun, H. S.; Liao, C. W.; Liu, T. Y.; Lee, H. T.; Yang, H. R.; Wang, L.; Lai, Y. Y. Stable and Exclusive Formation of CO from CO2 Photoreduction with H2O Facilitated by Linear Fluorene and Naphthalene Diimide-Based Conjugated Polymers. *ACS Appl. Polym. Mater.* **2022**, *4* (1), 521–526. https://doi.org/10.1021/ACSAPM.1C01419/SUPPL_FILE/AP1C01419_SI_001.PDF.

(171) Wang, S. H.; Khurshid, F.; Chen, P. Z.; Lai, Y. R.; Cai, C. W.; Chung, P. W.; Hayashi, M.; Jeng, R. J.; Rwei, S. P.; Wang, L. Solution-Processable Naphthalene Diimide-Based Conjugated Polymers as Organocatalysts for Photocatalytic CO2 Reaction with Extremely Stable Catalytic Activity for Over 330 Hours. *Chem. Mater.* **2022**, *34* (11), 4955–4963. https://doi.org/10.1021/ACS.CHEMMATER.2C00168/SUPPL_FILE/CM2C00168_SI_001.PDF.

(172) Wang, S. H.; Chen, P. Z.; Chen, Y. Y.; Khurshid, F.; Cai, C. W.; Lai, Y. Y.; Chung, P. W.; Jeng, R. J.; Rwei, S. P.; Wang, L. Naphthalene Diimide-Based Donor-Acceptor-Donor Small Molecules as Metal-Free Organocatalysts for Photocatalytic CO2Reaction. *ACS Appl. Mater. Interfaces* **2022**, *14* (38), 43109–43115. https://doi.org/10.1021/ACSAMI.2C08531/ASSET/IMAGES/LARGE/AM2C08531_0006.JPEG.

(173) Fu, Z.; Vogel, A.; Zwijnenburg, M. A.; Cooper, A. I.; Sprick, R. S. Photocatalytic Syngas Production Using Conjugated Organic Polymers. *J. Mater. Chem. A* **2021**, *9* (7), 4291–4296. https://doi.org/10.1039/D0TA09613J.

(174) ControlEquipment. *Model AC-3*. https://controlequipment.com.au/wp-content/uploads/2022/11/AC-3.pdf (accessed 2023-03-06).

(175) Yamashita, D.; Nakajima, Y.; Ishizaki, A.; Uda, M. Photoelectron Spectrometer Equipped with Open Counter for Electronic Structures of Organic Materials. *J. Surf. Anal.* **2008**, *14* (4), 433–436.

(176) *PESA: Riken AC-2 Photoelectron Spectrometer | Stanford Nano Shared Facilities*. https://snsf.stanford.edu/facilities/xsa/pesa (accessed 2023-03-06).

(177) Picollo, M.; Aceto, M.; Vitorino, T. UV-Vis Spectroscopy. *Phys. Sci. Rev.* **2019**, *4* (4). https://doi.org/10.1515/PSR-2018-0008.

(178) Diffey, B. L. Sources and Measurement of Ultraviolet Radiation. *Methods* **2002**, *28* (1), 4–13. https://doi.org/10.1016/S1046-2023(02)00204-9.

(179) Sillen, A.; Engelborghs, Y. The Correct Use of "Average" Fluorescence Parameters. *Photochem. Photobiol.* **1998**, *67* (5), 475–486. https://doi.org/10.1111/J.1751-1097.1998.TB09082.X.

(180) Instrumentation for Fluorescence Spectroscopy. *Princ. Fluoresc. Spectrosc.* **2006**, 27–61. https://doi.org/10.1007/978-0-387-46312-4_2.

(181) Chirvony, V. S.; Sekerbayev, K. S.; Pashaei Adl, H.; Suárez, I.; Taurbayev, Y. T.; Gualdrón-Reyes, A. F.; Mora-Seró, I.; Martínez-Pastor, J. P. Interpretation of the Photoluminescence Decay Kinetics in Metal Halide Perovskite Nanocrystals and Thin Polycrystalline Films. *J. Lumin.* **2020**, *221*, 117092. https://doi.org/10.1016/J.JLUMIN.2020.117092.

(182) Becker, W. The Bh TCSPC Handbook Ninth Edition Time-Correlated Single Photon Counting Modules SPC-130EMN, SPC-130EMNX SPC-130IN, SPC-130INX SPC-150N, SPC-150NX, SPC-150NXX SPC-160 SPC-160PCIE SPC-180N, SPC-180NX, SPC-180NXX Detectors, Lasers and Peripheral Devices Simple-Tau Systems Technical Principles TCSPC Applications FLIM Systems Applications in Life Sciences Clinical FLIM Applications SPCM Software SPCImage NG Data Analysis Software.

(183) Duncan, R. R.; Bergmann, A.; Cousin, M. A.; Apps, D. K.; Shipston, M. J. Multi-Dimensional Time-Correlated Single Photon Counting (TCSPC) Fluorescence Lifetime Imaging Microscopy (FLIM) to Detect FRET in Cells. *J. Microsc.* **2004**, *215* (Pt 1), 1. https://doi.org/10.1111/J.0022-2720.2004.01343.X.

(184) Zatryb, G.; Klak, M. M. On the Choice of Proper Average Lifetime Formula for an Ensemble of Emitters Showing Non-Single Exponential Photoluminescence Decay. *J. Phys. Condens. Matter* **2020**, *32* (41), 415902. https://doi.org/10.1088/1361-648X/AB9BCC.

(185) Mikhnenko, O. V.; Blom, P. W. M.; Nguyen, T. Q. Exciton Diffusion in Organic Semiconductors. *Energy Environ. Sci.* **2015**, *8* (7), 1867–1888. https://doi.org/10.1039/C5EE00925A.

(186) Sajjad, M. T.; Ruseckas, A.; Samuel, I. D. W. Enhancing Exciton Diffusion Length Provides New Opportunities for Organic Photovoltaics. *Matter* **2020**, *3* (2), 341–354. https://doi.org/10.1016/J.MATT.2020.06.028.

(187) Fries, F.; Reineke, S. Statistical Treatment of Photoluminescence Quantum Yield Measurements. *Sci. Reports 2019 91* **2019**, *9* (1), 1–6. https://doi.org/10.1038/s41598-019-51718-4.

(188) Jones, M.; Scholes, G. D. On the Use of Time-Resolved Photoluminescence as a Probe of Nanocrystal Photoexcitation Dynamics. *J. Mater. Chem.* **2010**, *20* (18), 3533–3538. https://doi.org/10.1039/C000165A.

(189) *2.3: BET Surface Area Analysis of Nanoparticles - Chemistry LibreTexts*. https://chem.libretexts.org/Bookshelves/Analytical_Chemistry/Physical_Methods_in_Chemistry_and_Nano_Science_(Barron)/02%3A_Physical_and_Thermal_Analysis/2.03%3A_BET_Surface_Area_Analysis_of_Nanoparticles (accessed 2023-03-07).

(190) Naderi, M. Surface Area: Brunauer–Emmett–Teller (BET). *Prog. Filtr. Sep.* **2015**, 585–608. https://doi.org/10.1016/B978-0-12-384746-1.00014-8.

(191) Bai, Y.; Wilbraham, L.; Gao, H.; Clowes, R.; Yang, H.; Zwijnenburg, M. A.; Cooper, A. I.; Sprick, R. S. Photocatalytic Polymers of Intrinsic Microporosity for Hydrogen Production from Water. *J. Mater. Chem. A* **2021**, *9* (35), 19958–19964. https://doi.org/10.1039/D1TA03098A.

(192) Alothman, Z. A. A Review: Fundamental Aspects of Silicate Mesoporous Materials. *Materials (Basel).* **2012**, *5* (12), 2874–2902. https://doi.org/10.3390/MA5122874.

(193) Lundstedt, C. *BET Theory and how its used to calculate surface area HORIBA Scientific Particle Analysis*. https://static.horiba.com/fileadmin/Horiba/Products/Scientific/Particle_Characterization/Webinars/Slides/BET_Theory_Explained.pdf (accessed 2023-03-07).

(194) Greenfield, S. Inductively Coupled Plasmas in Atomic Fluorescence Spectrometry. A Review. *J. Anal. At. Spectrom.* **1994**, *9* (5), 565–592. https://doi.org/10.1039/JA9940900565.

(195) Goenaga-Infante, H.; Bartczak, D. Single Particle Inductively Coupled Plasma Mass Spectrometry (SpICP-MS). *Charact. Nanoparticles Meas. Process. Nanoparticles* **2020**, 65–77. https://doi.org/10.1016/B978-0-12-814182-3.00003-1.

(196) Palchoudhury, S.; Baalousha, M.; Lead, J. R. Methods for Measuring Concentration (Mass, Surface Area and Number) of Nanomaterials. *Front. Nanosci.* **2015**, *8*, 153–181. https://doi.org/10.1016/B978-0-08-099948-7.00005-1.

(197) George, S. M. Atomic Layer Deposition: An Overview. *Chem. Rev.* **2010**, *110* (1), 111–131. https://doi.org/10.1021/cr900056b.

(198) Mackus, A. J. M.; Weber, M. J.; Thissen, N. F. W.; Garcia-Alonso, D.; Vervuurt, R. H. J.; Assali, S.; Bol, A. A.; Verheijen, M. A.; Kessels, W. M. M. Atomic Layer Deposition of Pd and Pt Nanoparticles for Catalysis: On the Mechanisms of Nanoparticle Formation. *Nanotechnology* **2015**, *27* (3), 034001. https://doi.org/10.1088/0957-4484/27/3/034001.

(199) Elam, J. W.; Nelson, C. E.; Grubbs, R. K.; George, S. M. Nucleation and Growth during Tungsten Atomic Layer Deposition on SiO2 Surfaces. *Thin Solid Films* **2001**, *386* (1), 41–52. https://doi.org/10.1016/S0040-6090(01)00762-3.

(200) Steier, L.; Bellani, S.; Rojas, H. C.; Pan, L.; Laitinen, M.; Sajavaara, T.; Di Fonzo, F.; Grätzel, M.; Antognazza, M. R.; Mayer, M. T. Stabilizing Organic Photocathodes by Low-Temperature Atomic Layer Deposition of TiO2. *Sustain. Energy Fuels* **2017**, *1* (9), 1915–1920. https://doi.org/10.1039/c7se00421d.

(201) Francàs, L.; Burns, E.; Steier, L.; Cha, H.; Solà-Hernández, L.; Li, X.; Shakya Tuladhar, P.; Bofill, R.; García-Antón, J.; Sala, X.; Durrant, J. R. Rational Design of a Neutral PH Functional and Stable Organic Photocathode. *Chem. Commun.* **2018**, *54* (45), 5732–5735. https://doi.org/10.1039/c8cc01736k.

(202) Leskelä, M.; Niinistö, J.; Ritala, M. Atomic Layer Deposition. *Compr. Mater. Process.* **2014**, *4*, 101–123. https://doi.org/10.1016/B978-0-08-096532-1.00401-5.

(203) Johnson, R. W.; Hultqvist, A.; Bent, S. F. A Brief Review of Atomic Layer Deposition: From Fundamentals to Applications. *Mater. Today* **2014**, *17* (5), 236–246. https://doi.org/10.1016/j.mattod.2014.04.026.

(204) Niemelä, J. P.; Marin, G.; Karppinen, M. Titanium Dioxide Thin Films by Atomic Layer Deposition: A Review. *Semicond. Sci. Technol.* **2017**, *32* (9), 093005. https://doi.org/10.1088/1361-6641/aa78ce.

(205) Chen, Y. W.; Prange, J. D.; Dühnen, S.; Park, Y.; Gunji, M.; Chidsey, C. E. D.; McIntyre, P. C. Atomic Layer-Deposited Tunnel Oxide Stabilizes Silicon Photoanodes for Water Oxidation. *Nat. Mater.* **2011**, *10* (7), 539–544. https://doi.org/10.1038/nmat3047.

(206) Puurunen, R. L.; Vandervorst, W. Island Growth as a Growth Mode in Atomic Layer Deposition: A Phenomenological Model. *J. Appl. Phys.* **2004**, *96* (12), 7686. https://doi.org/10.1063/1.1810193.

(207) Schürch, D.; Currao, A.; Sarkar, S.; Hodes, G.; Calzaferri, G. The Silver Chloride Photoanode in Photoelectrochemical Water Splitting. *J. Phys. Chem. B* **2002**, *106* (49), 12764–12775. https://doi.org/10.1021/JP0265081/ASSET/IMAGES/LARGE/JP0265081F00014.JPEG.

(208) Steier, L.; Holliday, S. A Bright Outlook on Organic Photoelectrochemical Cells for Water Splitting. *J. Mater. Chem. A* **2018**, *6* (44), 21809–21826. https://doi.org/10.1039/C8TA07036A.

(209) Salameh, Z. Photovoltaic. *Renew. Energy Syst. Des.* **2014**, 33–113. https://doi.org/10.1016/B978-0-12-374991-8.00002-7.

2. Organic Photocathodes with anchor groups for improved Electron Transporting Layer formation via Atomic Layer Deposition for Hydrogen Production

Contents

2. ORGANIC PHOTOCATHODES WITH ANCHOR GROUPS FOR IMPROVED ELECTRON TRANSPORTING LAYER FORMATION VIA ATOMIC LAYER DEPOSITION FOR HYDROGEN PRODUCTION 57

2.1. General Information and Attributions 62

2.2. Introduction 62

2.2.1. General Principles 62

2.2.2. State of the Art and Considerations 63

2.2.3. Project Aims 68

2.3. All Polymer Photocathodes 68

2.4. NDI Polymer synthesis and characterisation 70

2.5. Results and Discussion 71

2.5.1. TEM and Contact Angle Measurements 71

2.5.2. Organic Photovoltaic Devices 73

2.5.3. Glycol Overlayer on Top of BHJ- OPV 75

2.6. Photocathodes 78

2.6.1. Photocathode architecture 78

2.6.2. Linear Sweep Curves 81

2.6.3. Stability Studies 82

2.7. Conclusion and Future Outlook 83

2.8. Experimental 84

2.8.1. General Methods 84

2.8.2. Polymer Synthesis and Characterisation 88

2.9. References 90

2.10. Appendix 95

List of Figures

Figure 2.1: Schematic illustrating general organic photocathode architecture. 64

Figure 2.2: Investigation of a correlation between blend hydrophilicity and the nucleation behaviour of ALD TiO_2 Contact angles (a-c) as summarised in Table 2.2 of a droplet of water on a device containing a) **N2200**, b) **p(NDI-90-Phos)**, c) **p(g-NDI-90-Phos)**. Corresponding SEM images of devices each containing PCE12 blended with d) **N2200**, e) **p(NDI-90-Phos)** and f) **p(g-NDI-90-Phos)** coated with 50 cycles of TiO_2 by ALD. 50 TDMAT/water cycles at 75 °C correspond to 2.2 nm on Si wafers (GPC = 0.044 nm/cycle). 72

Figure 2.3: a) OPV performance of devices in the architecture: ITO/**HTL**/**PCE12**:**N2200**/**ETL**/Ag b) OPV performance of devices in the architecture: ITO/MoO_3/**PCE12**:**acceptor**/ZnO/Ag 74

Figure 2.4: OPV performance of devices in the architecture: ITO/MoO_3/**PCE12**:acceptor/acceptor overlayer/ZnO/Ag 76

Figure 2.5: UV-Vis spectra of the blend with and without overlayer of a) a **PCE12:N2200** device and b) a **PCE12**: **p(NDI-90-Phos)** device 77

Figure 2.6: Contact angles of the blend with and without the glycolated overlayer 77

Figure 2.7: Schematic representation of the photocathodes fabricated in this study, including the energy levels of each layer. HTL: hole transporting layer, ETL: electron transporting layer: BHJ: bulk heterojunction, IL: interlayer, cat: co-catalyst. 79

Figure 2.8: Pictures showing examples of photocathodes. a) showing photocathodes prior to soldering thin contact wire and epoxy covering, showing the clean back ITO contact, obtained by wiping with solvent and use of thermal tape. b) example of degradation of photocathode at the interface between ITO and MoO_3, due to testing at higher pH than 1.3. c) examples of fabricated photocathodes. 80

Figure 2.9: Potential-pH diagram of Mo-H_2O system. Published from ref[70], reprinted with permission. 81

Figure 2.10: Chopped current-density potential curves for the organic photocathodes. Carried out under 1 sun illumination in a three electrode cell at pH 1 (0.3 M H_2SO_4 + 0.5 M Na_2SO_4). A) with the architecture of ITO/MoO_3/BHJ/TiO_2/RuO-NPs. B) with the architecture of ITO/MoO_3/BHJ/overlayer/TiO_2/RuO-NPs. 82

Figure 2.11:Chronoamperometry for the two devices, a) architecture of ITO/MoO_3/**N2200**:**PCE12**/TiO_2 b) architecture of ITO/MoO_3/**N2200**:**PCE12**/ **p(g-NDI-90-**

Phos)/TiO_2. Inserts show a zoomed section of the graph to show the shutter in operation, turning the light on and off to compare between photocurrent and darkcurrent. 83
Figure 2.12: Cyclic Voltammetry data of a) **p(NDI-90-Phos)** and b) **p(g-NDI-90-Phos),** carried out and plotted by Dr Matthew Bidwell.[62].....95
Figure 2.13: UV-Vis data in solution (a) and thin film (b) for both **p(NDI-90-Phos)** and **p(g-NDI-90-Phos)** carried out and plotted by Dr Matthew Bidwell.[62] 96
Figure 2.14: PESA of **p(g-NDI-90-Phos)** 96
Figure 2.15: Reprised Figure **2.10a**, to show tangents used to obtain values for **Table 2.7** ..97
Figure 2.16: Reprised **Figure 2.10b** to show tangents used to obtain values for **Table 2.7** ..97
Figure 2.17: reprisal of **Figure 2.2 f,** showing the zoomed out SEM of **p(g-NDI-90-Phos),** spots were identified using ImageJ, and the areas calculated. 98
Figure 2.18: zoomed in SEM images of samples containing a) **N2200**, b) **p(NDI-90-Phos) c) p(g-NDI-90-Phos)** respectively, with 50 cycles of TiO_2. The images are zoomed in to be the same size, from Figure 2.2. 98

List of Tables

Table 2.1: Table showing an overview on organic photocathodes from literature. 67

Table 2.2: Table summarising contact angles of the polymer blends and TEM of ALD growth 72

Table 2.3: Summarising preliminary OPV results varying HTL and ETL 73

Table 2.4: Summarising preliminary OPV results using the different acceptors. 75

Table 2.5: Summary of OPV performance upon addition of the **p(g-NDI-90-Phos)** overlayer. 76

Table 2.6: Summary of contact angle measurement comparing blends with overlayer on top, and without. 78

Table 2.7: Table summarising the data obtained from JV curves and chronoamperometry for the devices with and without the glycol based overlayer 82

2.1. General Information and Attributions

*The synthesis of **p(g-NDI-90-Br)** was developed by Dr. Matthew Bidwell (Imperial College London), who also ran cyclic voltammetry on **p(g-NDI-90-Phos).** OPV devices and testing, after initial trial done by the author, were carried out by Dr Tack Ho Lee (Durrant group, Imperial College London). ALD thickness measurements to determine the growth rate were carried out by Dikshita Bhattacharyya (Steier Group, Imperial College London). SEM was carried out with Ben Bowers (Steier Group, Imperial College London) and Dr Ludmilla Steier.*

This project focuses on photo-electrochemistry for hydrogen evolution, using organic semiconductors. In this study, the organic blend of the photocathode active layer was modified by addition of an overlayer containing an anchoring group and glycolated chain, which was thought to increase the nucleation by atomic layer deposition (ALD) and yielded a higher stability than the organic blend unmodified. This is a great proof of concept in the use of interlayers and functional groups which exhibit small modifications to the side chains of the polymers and can effectively improve interfaces in organic photocathode devices.

This chapter will first expand on photocathode theory and principles and will then include an introduction into the field of photocathodes, before explaining the project aims, results and finally conclusions.

2.2. Introduction

2.2.1. General Principles

As outlined in **Chapter 1,** photoelectrochemistry proceeds via: 1) excitation of the semiconductor to generate an exciton 2) migration of these charges to the semiconductor surface to interfaces where transporting layers and co-catalysts are used. 3) once at the surface the charges transferred to reactive sites at the interface with the electrolyte, they can take part in chemical reactions, or be mopped up at the electrode. Electrons in the reductive half reaction able to make H_2 or solar fuels and holes in the oxidative half reactions producing oxygen or an oxidised material. In practice, many processes can occur within the system that might decrease the total amount of hydrogen produced. Competing with charge migration is charge recombination, whereby the holes and electrons recombine, thus stopping them from travelling to the electrolyte to produce the wanted products, the pathway is known as a "deactivation pathway" for this reason. Efficient separation of charges is very important in efficient photoelectrochemical cell design. Photogenerated Hydrogen and oxygen may also recombine to form water, reversing water splitting.[1,2]

Photocathodes in conjunction with photoanodes have the potential of achieving bias-less water splitting.[3] Focusing on the reduction and oxidation reactions separately enables optimisation for each half reaction.[4] This study will focus on photocathodes.

2.2.2. State of the Art and Considerations

Since the development of TiO_2 as a photocatalyst, in the last few decades, various materials have been developed and tested in photo electrochemistry for fuel production. Including metal oxides, chalcogens, III-V inorganic semiconductors and silicon based materials.[5–9] Inorganic materials are at the forefront of performance, achieving photocurrent densities of almost 30 $mAcm^{-2}$.[10] In recent years organic semiconducting materials for hydrogen production have gained interest. Their appeal centres on their unique ability to allow for precise molecular tuning, which allows for easier energy level control and attainable narrower bandgaps, their potential for high mobility as well as their solubility and use of generally inexpensive materials which both allow for ease of processibility and scalability. These materials have the potential to offer solutions which satisfy the efficiency, stability, and economic viability required for this application.[1,11,12] Techniques used for OPV devices, both in material design and device engineering have shown the great potential of these materials in PEC research.[13]

In order for organic materials to be optimised for photoelectrochemistry, photocurrent, photovoltage and stability should be optimised.[14] Photocurrent density is primarily controlled by incident light absorbed, i.e. the energy absorbed by the semiconductor due to its bandgap. As previously mentioned, electrical losses due to charges not contributing to photoelectrochemistry should be carefully mitigated via optimisation, to reduce recombination. This can be done by controlling layer thickness, matching energy levels to improve charge separation by introducing energy gradients and by reducing reflection through incorporating transparency of other layers within the device, and optimising interfaces. Photovoltage can be increased by good matching of the donor and acceptor or passivating the surface to decrease losses. The use of a catalyst on top of the interface layers can lower the overpotential required for HER.[15] An optimised system includes a donor with a wide bandgap (1.65-1.8 eV) coupled with an acceptor with a narrow bandgap (0.95-1.2 eV).[16]

Stability has been a challenging aspect in photocathode research, and still one of the largest barriers in the viability of PEC water splitting in industry. Commonly, instability arises from photo-corrosion of materials upon contact with the electrolyte and from trapped charges within interface layers and in the bulk. Strategies to increase stability include protective layers,

improved interfaces between layers, use of less harsh pH conditions in the electrolyte and stability of the semiconducting blends. [17–19]

Sakai *et al* first reported on the use of conjugated organic polymers, with a metal oxide in 2006.[20] In this study TiO_2 nanoparticles and **PEDOT**:**PSS** bilayers were deposited on a quartz substrate, with interdigitated Pt electrodes. A reversible change in conductivity and photocurrent was observed in the presence of UV and visible light. With UV light causing photogenerated TiO_2 electrons, thus reducing conductivity, while visible light promoted the oxidation of **PEDOT**. Conductivity was recovered in dark conditions. This work focused on photoinduced tuning of conductivity but was one of the first examples of mechanistic insight in using organic and inorganic hybrid systems for photo-electrochemistry. In organic photovoltaics it is widely reported that the inclusion of interface layers, optimised for hole and electron transport respectively vastly increase performance.[21] The same has been shown with organic photocathodes, with electron transporting layers optimising charge transport and potential alignment gradient.[22] Most published work on organic photocathodes involves an organic blend bulk heterojunction, with organic or inorganic hole transporting layers, leading to a contact electrode, and metal oxides as the electron transporting layers, with a co-catalyst deposited on top.

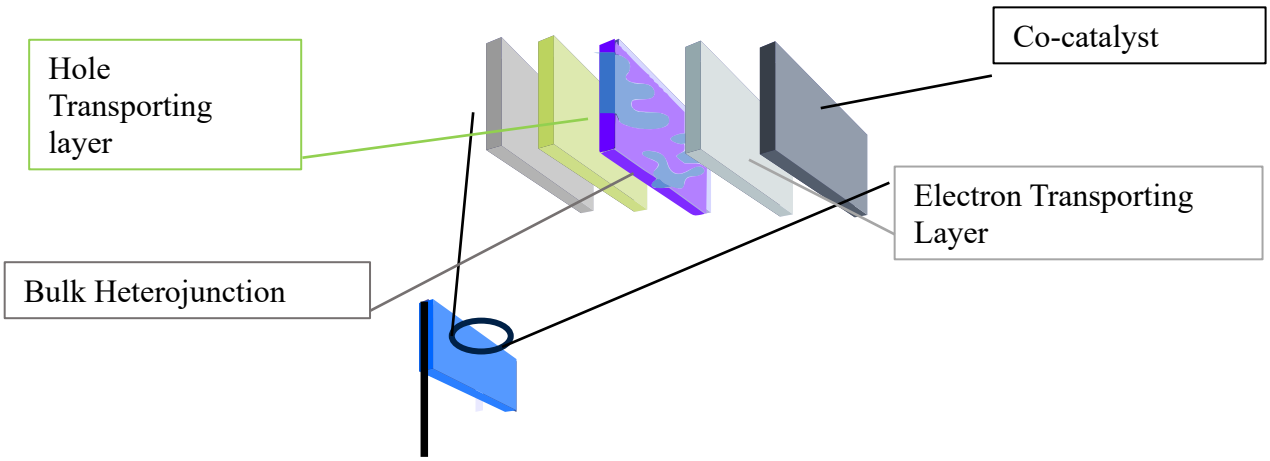


Figure 2.1: Schematic illustrating general organic photocathode architecture.

This architecture, illustrated in **Figure 2.1**, has been the most successful so far in the field of organic photocathodes.

A typical system, consisting of a bulk-heterojunction of poly(3-hexylthiophene) and phenyl-(C_{61} or C_{71} fullerene)-butyric acid methyl ester (**P3HT**:**PCBM**) has been conventionally used in photocathode literature.[23,24] Haro *et al* reported a hydrogen evolution rate of 1.5 $\mu molh^{-1}cm^{-}$

^{2} with stability of over 3 hours using the **P3HT**:**PCBM** blend. The group used crosslinked insoluble **PEDOT**:**PSS** as the hole transporting layer and a low temperature deposition method for titanium oxide. The work elucidated a link between the thickness of the TiOx/Pt layer affording a trade-off between high current achieved and high stability.[25] Due to the instability of **PEDOT** in water, there has been an interest in optimising a hole diffusion layer without its inclusion. The success of a metal oxide HTL relies on matching its work function to the ionization potential of the donor material.[26] Rojas *et al* achieved very high photocurrents with the architecture FTO/CuI/**P3HT**:**PCBM**/TiO2/Pt under acidic conditions, with a notable current of -8 $mAcm^{-2}$ and 100% Faradaic efficiency. The works focused on using solution processed CuI as the hole transporting layer, with an increased stability compared to **PEDOT**:**PSS**, as well as the use of Polyethylenimine (PEI) as a protective coating. This and consequent works from the group also showed the importance of favourable energetic alignment in photocathode design, in order to facilitate exciton separation and to avoid hole and electron recombination.[27] Najafi *et al* reported on the use of spin-coated WS_2 flakes films as an HTL for **P3HT**:**PCBM** based devices. It was found that gold doping effectively increased activity and the work function of the pristine WS_2 films by enabling better collection of holes.[28] Similarly, Bellani *et al* reported on devices incorporating MoS_2 flakes as hole transporting layers, the study employed layered crystals to increase efficiency in photocathodes, increasing photocurrents via tuning of morphology and fermi level of the layer. P-type chemical doping was shown to increase photocurrent 6-fold compared to pristine undoped MoS_2. Mezzetti *et al*'s study using WO_3 as the HTL focused on compatibility of the blends with the metal oxides and the optimisation of this interface in order to increase photocathode stability.[29] Bourgeteau *et al* reported on the use of MoS_3 as a co-catalyst with an increased photocurrent, studying in detail the effect of MoS_3 thickness and the incorporation of TiO_2 to optimise electron transport between charge generation and catalyst.[30] In their 2017 paper on solution processed organic photocathodes, the group compared graphene oxide, nickel oxide or molybdenum oxide.[31,32] The study showed a correlation between increasing performance and increasing work function of the HTL. Larger potential differences between the HTL Fermi level and that of the electrolyte forms the beneficial potential gradient to suppress recombination and facilitate charge transfer to the electrolyte.[33]

Yao *et al* focused on how charge accumulation affects stability in organic photocathodes.[34] The optimised blend was a polymer-polymer non-fullerene heterojunction of **PTB7-Th:PDI-V.** The group used sacrificial Eu^{3+} in different concentrations and measurement conditions to

control the charge transfer rate at the aqueous interface of the photocathodes. It should be noted that the group did not use an ETL in their architecture, to specifically investigate the robustness of the organic blend. Out of the catalysts attempted, it was found that for this polymer-polymer blend, RuO_3 NPs gave the highest operational stability. The choice of a thin layer (10 nm) of MoO_3 as the hole transporting layer vastly increased performance, the group showed negligible photoactivity of this oxide by itself, confirming its role to be that of a charge transfer layer. The group found that an accumulation of charge on the order of μCcm^{-2} caused irreversible degradation of the organic blend. On the order of $nCcm^{-2}$, stability was achievable. The group elucidated the importance of full coverage of the layers on either side of the BHJ for effective charge transport and increased operational stability. Francás *et al* reported an increased offset potential when using replacing **P3HT** with PCDTBT. NiO was used as the HTL to replace the water reactive **PEDOT**. Although NiO caused a decrease in overall current, the stability was greatly increased, this was hypothesised to be due to increased adhesion. Similarly, the use of a TiO_2 ALD ETL layer as a protective coating and effective transporting layer vastly increased stability, with the group reporting an operational stability of 5 hours.[35] This example of rational design and layer optimisation has been further developed within this study.

More recently, higher stability photocathodes have been achieved. Seo *et al*, increased the stability of their **PEDOT**:**PSS**/**PTB7-Th:EH-IDTBR**/Pt NPs device by metal encapsulation and achieving maintained photocurrent over 30 hours, with only 95% degradation. The metal encapsulation was shown to impede electrolyte penetration into the organic semiconductor and provide passivation, as shown by the high stability of the device despite the low stability of the blend in water.[36]

To satisfy the energetic demands of efficient bulk heterojunction formation, much of the research in this field has focused on inherently electrochemically unstable materials. These therefore rely on protective layers, in order to separate the unstable heterojunction from the electrolyte.[37] This method has indeed given good results in the field, but falls short if the passivating layer is not pin-hole free and itself stable. TiO_2 has shown great promise for this application due to its stability in pH 0-14 electrolytes and over large overpotentials. Using ALD has been an excellent technique for forming pin-hole free layers, especially for inorganic materials. Steier *et al* reported on a new low temperature method for atom layer deposition of titanium oxide on organic photocathodes. The interfacial layer was important for efficient charge transport between the BHJ and the catalyst layers. The use of ALD enabled a pinhole

free barrier in order to decrease water penetration into the photoactive layer, thus increasing overall stability and performance.[38] TiO_2 has a conduction minimum well matched to that of **PCBM**, in tandem with its stability in water, it made it an ideal material as a full coverage ETL. Although ALD had been previously used for applications using inorganic blends, this study paved the way for using this technique on organic semiconductors.[39] The method was optimised to be at 80 degrees, using TDMAT (Tetrakis(dimethylamido)titanium(IV)) as the TiO_2 precursor and water as the source of oxygen. It was found that a thinner layer of TiO_2 did not provide sufficient corrosion protection on organic materials, this was attributed to irregular ALD growth on polymer films, which might proceed by island growth, thus required increased thickness to form the full pin-hole free layer.

The literature outlined above is presented in **Table 2.1** below summarises, for ease of comparison between some of the key developments in the field or organic photocathodes in recent years.

Table 2.1: Table showing an overview on organic photocathodes from literature.

Cathode	**V_0 [V *vs.* R HE]**	**$J_{0\ VRHE}$ [mA cm^{-2}]**	**Stability/ h**	**Electrolyte**	**Ref.**
PEDOT:PSS/P3HT:PCBM /LiF/Al/Ti/MoS_x	0.39	−7.90	0.75	H_2SO_4 0.5 M (pH 0.6)	[40]
CuI/P3HT:PCBM/TiO_2/ RuO_2	0.48	−3.61	3.5	0.1 M Na_2SO_4 (pH 1.36)	[38]
WO_3/P3HT:PCBM/TiO_2/P t	0.41	−2.48	10	0.1 M H_2SO_4 (pH 1.37)	[29]
PEDOT:PSS/PCDTBT:PC BM/TiO_2/RuO_2	0.58	−2.85	-		[41]
NiO/PCDTBT:PCBM/TiO $_2$/RuO_2	0.41	−1.45	5	0.1 M phosphate buffer (pH 7)	[41]
PEDOT:PSS/TiO_2	0.001	-0.0005	-	-	[20]
FTO/CuI/P3HT:PCBM/Ti O_2/Pt	0.602	-3.02	0.6	0.1 M H2SO4 (pH 1.37)	[42]
ITO/x-PEDOT:PSS/PH3T:PCBM /TIO_2/Pt	-	-1	3	0.1 M Na_2SO_4 (pH 1.36)	[25]
MoS_2/P3HT:PCBM/TiO_2/ MoS_3	0.55	-1.21	0.5	H_2SO_4 0.5 M (pH 1)	[43]
MoO_3/PTB7-Th/PDI-V/RuO_2	0.67	-8	12	0.3 M H_2SO_4+ 0.5 M Na_2SO_4	[34]

				(pH 1)	
MoO_3/P3HT:PCBM/TiO_2	0.67	-3	2	0.1 M Na_2SO_4 (pH 1.37)	[31]
MoO_3/P3HT:PCBM/TiO_2	0.41	-2.2	-	0.5 M H_2SO_4 (pH 1)	[44]
NiOx/P3HT:PCBM/TiO_2	0.34	-1.3	-	0.5 M H_2SO_4 (pH 1)	[44]
WS_2/P3HT:PCBM/TiO_2/MoS_3	0.66	-4.14	1	0.5 M H_2SO_4	[28]
PEDOT:PSS/PTB7-Th:EH-IDTBR/Pt NPs	1	-12.3	30	0.5 M H_2SO_4	[36]

2.2.3. Project Aims

The aim of this work is to increase operation stability of organic photocathodes. The use of TiO_2 as the ETL of the device, deposited via ALD is a great barrier, as long as a pin-hole free layer is achieved. However, when using organic heterojunctions, pin-hole free ALD is difficult to achieve due to a lack of active groups which can irreversibly bind to the precursor in the chemisorption cycle. Therefore, for better coverage, a very thick layer of TiO_2 ALD is required, which can contribute to losses in PCE. To encourage adhesion between the blend and the TiO_2 this study will introduce anchor groups and glycol functionalities, to activate the polymer surface and act as nucleation sites. Organophosphates have been reported as effective anchoring groups on metal oxides.[45] In this study phosphonate anchoring groups were used to increase interactions between metal oxides and organic polymers to improve interactions at the layer interfaces within the device.[46] It is believed that the ester to acid oxidation will occur during the ALD oxidation cycle. It is thought that this post fabrication modification will remove any extra processing required, since the acid bearing polymer would lose solubility and processability. **PCE12** (2.41 eV) was chosen as the wide bandgap polymer donor and was coupled with the narrow bandgap polymer acceptor **N2200** (1.45 eV) with matched energy levels. This blend has been shown to be reasonably tolerant to blend ratios and changes, and has shown promising stability under CV, as well as good OPV performance, which all bode well for ALD stability, operational stability and reasonable PCE. [47,48]

2.3. All Polymer Photocathodes

The advantages of organic photocathodes include the low cost of materials, and the potential for high stability. This project focuses on techniques that could improve stability, by improve

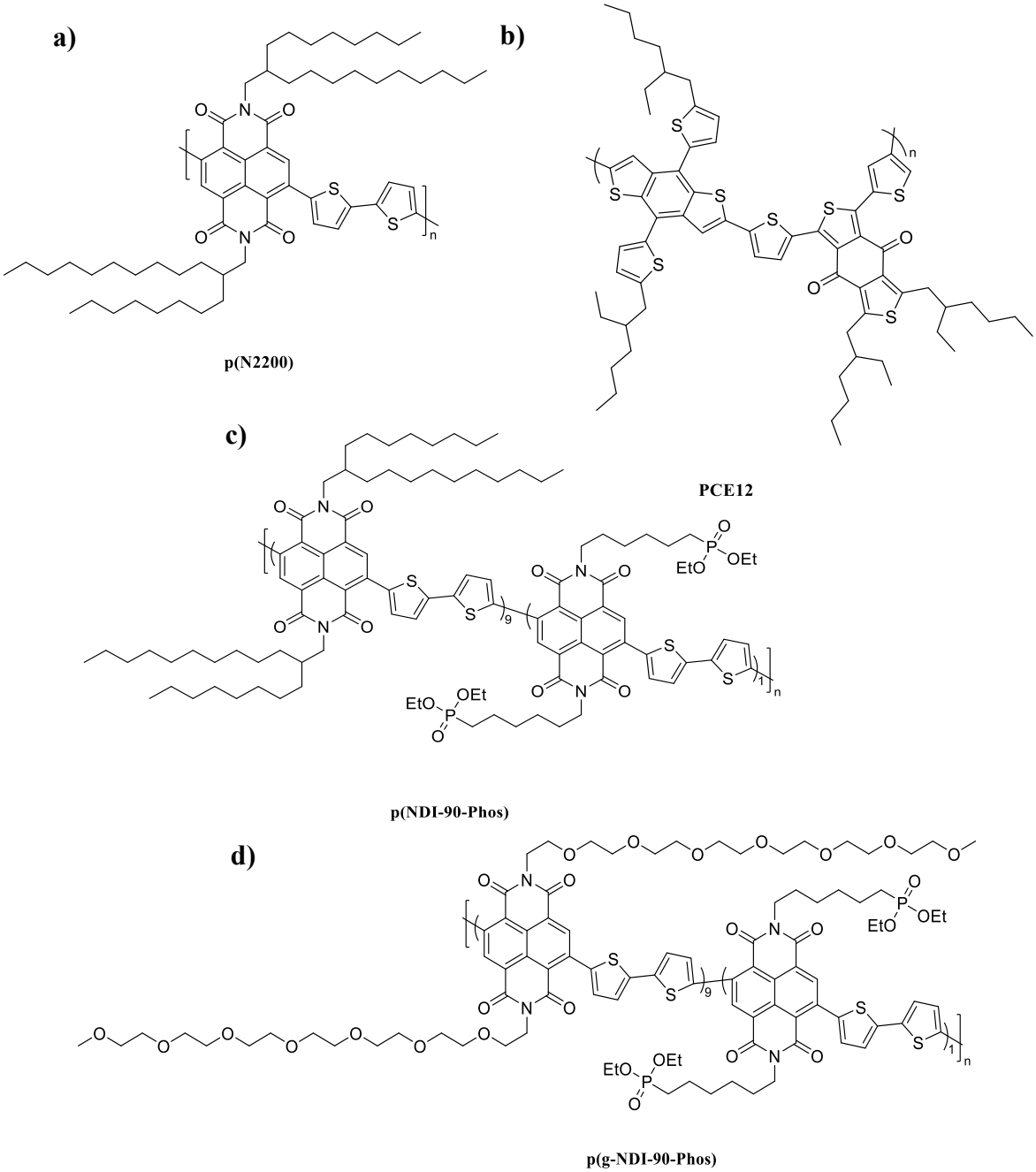
adhesions between layers. **PCE12** and **N2200** (i.e. polymer : polymer) solar cells have shown to be tolerant to composition changes compared to its polymer: small molecule analogues. The blend was very stable as an OPV, reaching efficiencies of 11% and was found to be stable in electrolyte under cyclic voltammetry, making it a promising candidate for a stable photocathode.[49 50]

The blend is, however, quite hydrophobic, which decreases the likelihood of good adhesion with the metal oxide charge transporting layers within the photocathode, which would cause delamination due to charge build up and therefore poor stability and performance. Furthermore, this would not allow for ALD growth at all since chemical bond formation is required. In order to improve this property, anchor groups and glycolation were employed as techniques to increase the adhesion between layers. ALD was used to deposit the electron transporting layer of TiO_2, which also acted as a protective layer to increase the overall stability by encapsulating the device. It should be noted that employing this technique, which has been shown to be effective in increasing device stability, can also lead to an overall decrease in the series resistance of the device and lower the photovoltage. This is especially true for organic materials, since, in order to obtain a good, pinhole free layer, thick films are required.[51,52] As mentioned above, it has been shown that thin TiO_2 overlayers of less than 100 nm on organic photocathodes did not provide enough corrosion protection. The same was not observed for inorganic materials. This could be due to non-uniform growth of the TiO_2 layer by ALD, either by island growth or nucleation, which therefore require a film of over 100 nm for a continuous ETL.[53] It was hypothesised therefore, that the inclusion of functional groups which were more likely to interact with the ALD precursors, might increase the ALD growth at the beginning of the process, thus forming a continuous layer, without the need for such high thickness, in order to the keep the stability of the device, without lowering performance. The acceptor polymer was chosen for modification, since in organic photocathodes it is the ETL that is then in contact with the electrolyte and therefore is ideally deposited on by ALD. Furthermore, modifying the **N2200** structure ensured that, since the side chains were altered and not the backbone, energetic properties (FMOs) would be only minimally altered. Phosphonic esters and phosphonic acids have been shown to interact with titania before, so these were chosen as anchor groups.[45] Another advantage of this functionalisation is its ease of preparation, and oxidation of the functional group is likely to occur under ALD conditions.

2.4. NDI Polymer synthesis and characterisation

The polymers utilised in this study are shown in

Scheme 2.1, **a**) **N2200** and **b**) **PCE12** are commercially available and widely studied acceptor and donor polymers respectively. **c)** and **d)** are modified analogues of N2200 synthesised for this work.[54]



Scheme 2.1: Chemical structures of the polymers explored in this chapter.

Dr Matthew Bidwell developed the synthesis of an alkyl halide side chain-functionalised NDI unit using of a one-pot in-situ deprotection and imidisation reaction, which formed **p(NDI-90-**

Br) (**SI Scheme 2.2**) Post-polymerisation functionalisation of **p(NDI-90-Br)** was carried out. This was chosen for ease of synthesis. **p(NDI-90-Br)** was reacted with triethyl phosphite to achieve S_N2 attack of the nucleophilic phosphite, at the electrophilic halide-bonded carbon in a Michaelis–Arbuzov reaction, to achieve a phosphite ester, post polymerisation, forming **p(NDI-90-Phos)**.[55,56] It was found that **p(NDI-90-Br)** solubilised with vigorous stirring in triethyl phosphite, and over 24 hours at 135 ^oC. It was found that precipitating the polymers in MeOH caused the polymers to become insoluble in chloroform, it was hypothesised this was due to some hydration of the phosphate species into phosphoric acid. Precipitation into ethyl acetate (EA) and hexane (1:1) was therefore done. This was taken into consideration as an interesting pathway, since ALD uses a pulse of water prior to the TDMAT precursor pulse, which could partially hydrolyse the ester of the polymer, in-situ, thus causing a stronger interaction with the ALD layer, without compromising on solubility. It should also be noted that only 10 % of the polymer was substituted with Br and then Phos, since higher percentages of substitution led to insolubility in common chlorinated solvents. The same reaction was carried out on the glycolated polymer, yielding similar results to form **p(g-NDI-90-Phos).**

2.5. Results and Discussion

2.5.1. TEM and Contact Angle Measurements

To probe the hydrophilicity of the active layers, comparing between the **N2200** derivatives, contact angles measurements were taken. The active layers were spin-coated from 10 $mgml^{-1}$ solutions, in chlorobenzene for **N2200** and **p(NDI-90-Phos)** and chloroform for **p(g-NDI-90-Phos)**. 1 mL of water was dropped onto the devices and the contact angle measured immediately. The contact angle between water and the **N2200** surface was the highest obtained, at 93.3^o. This was expected since **N2200** contained the least number of heteroatoms per repeat unit, making it the most hydrophobic of the polymers. The presence of 10% substituted phosphate ester groups decreased the contact angle to 90.1^o. The small change between the two materials is attributed to the low percentage of phosphonate substituted monomer units, meaning the overall structure remains highly hydrophobic. It is likely that in the presence of water pulses in the ALD, the phosphonic ester functional groups are hydrolysed to phosphonic acid, which would further decrease the contact angle *in-situ*.[57] Phosphonic acids have been shown to have even more favourable interactions with TiO_2 than their ester equivalents, making the oxidised in situ product more likely to aid ALD deposition.[58] The presence of highly hydrophilic glycol chains in **p(g-NDI-90-Phos)** lowered the contact angle more considerably to 61.6^o. The results are summarised in **Figure 2.2** and **Table 2.2.**

Table 2.2: Table summarising contact angles of the polymer blends and TEM of ALD growth

Sample	Contact Angle (°)	Area of a typical nucleated particle after 50 cycles of TiO2 ALD (nm^2)*	Relative Coverage of nucleated particles after 50 cycles of TiO2 ALD (a.u)*
N2200	93.3	73 ± 19	98
p(NDI-90-Phos)	90.1	132 ± 24	165
p(g-NDI-90-Phos)	61.6	227 ± 31	280

*Contact angle taken obtained when placing a 1 mL droplet of distilled water on top of an ITO slide with the active layer spin-coated on top, including **PCE12** being constant throughout and the different **N2200** derivatives mixed in. SEM was carried out on a device containing the same active layers, on which a thin ALD film of TiO_2 was deposited of 50 cycles. On a silicon wafer that would correspond to a growth rate of 0.044 nm per cycle at 75°C. *done by SEM*

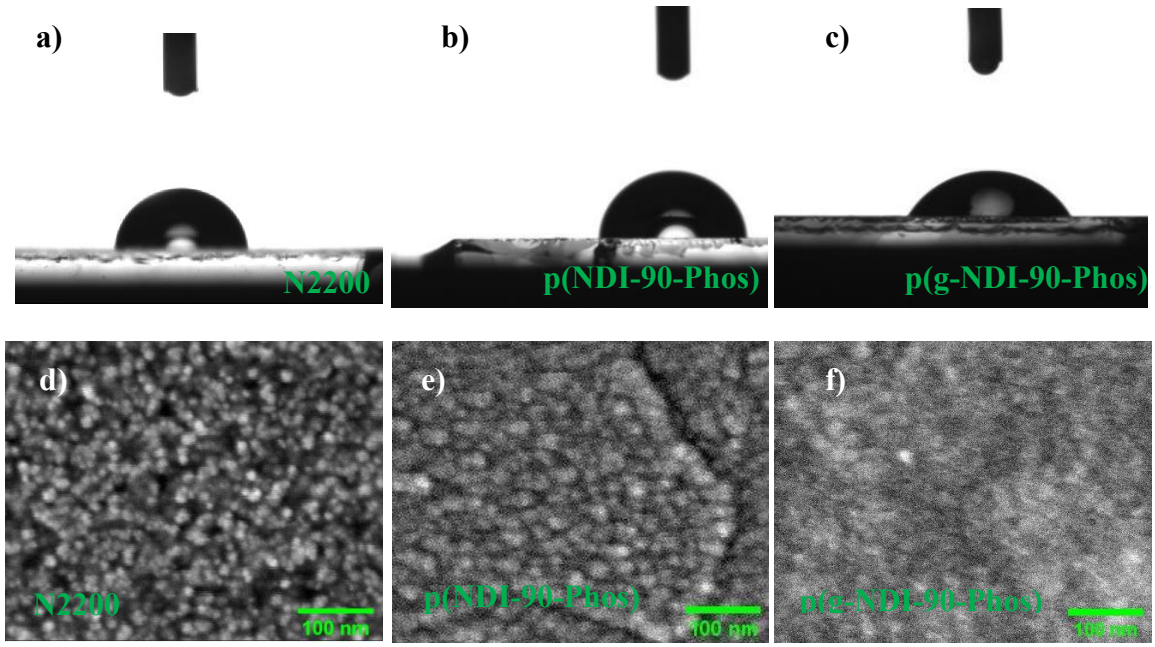


Figure 2.2: Investigation of a correlation between blend hydrophilicity and the nucleation behaviour of ALD TiO_2 Contact angles (a-c) as summarised in Table 2.2 of a droplet of water on a device containing a) **N2200**, b) **p(NDI-90-Phos)**, c) **p(g-NDI-90-Phos)**. Corresponding SEM images of devices each containing PCE12 blended with d) **N2200**, e) **p(NDI-90-Phos)** and f) **p(g-NDI-90-Phos)** coated with 50 cycles of TiO_2 by ALD. 50 TDMAT/water cycles at 75 °C correspond to 2.2 nm on Si wafers (GPC = 0.044 nm/cycle).

In order to probe the nucleation phase of TiO_2 ALD growth on the polymers, ITO devices were made with MoO_3, and a BHJ made up of the **PCE12** donor and each of the **N2200, p(NDI-90-Phos)** and **p(g-NDI-90-Phos)** acceptor polymers, in a ratio of 1:1 donor to acceptor. By running 50 cycles of ALD, it was possible to see the beginning of the formation of the TiO_2 layer by nucleation growth. Image J was used to calculate the area of the nucleation spots seen

on SEM, as well as the relative overall coverage of TiO_2 on the samples.[59] For the spots, 5 were chosen within the SEM image and an average of the area was taken. The area covered was calculated using the contrast between spots and background from ImageJ. Appendix figures, **Figure 2.17** and **Figure 2.18** show how the spot areas and coverage were calculated using Image J. It should be noted that the SEM of **p(g-NDI-90-Phos)** was blurrier than the others, which could contribute to a larger error margin. It was found that as hydrophilicity increased, so did the spot area and relative coverage, supporting the idea that these anchoring groups and heteroatoms aid in the formation of a more compact TiO_2 layer. It can be inferred that **p(g-NDI-90-Phos)** was at a more advanced growth stage since there was an increased coverage, compared to the **p(NDI-90-Phos)**, which in turn showed better nucleation than **N2200** alone. These results for **p(g-NDI-90-Phos)** were promising and indicate the strategy of using anchor groups and heteroatoms with favourable interactions to the ALD precursor and oxidiser may aid in the desired pinhole free, linear growth required. This material was therefore chosen for further study, by moving onto OPV data.

2.5.2. Organic Photovoltaic Devices

Since the characterisation and nucleation of TiO_2 was promising for these materials, OPV devices were made. It is common for OPV devices to be made prior to testing as photocathodes in order to see the voltage and currents achieved, since the same photovoltage of an OPV can in theory be achieved in a buried junction photocathode.[32] If efficiencies are very low on the OPV stage, photocathodes are unlikely to function well when stability and electrolyte interactions can confuse the picture of general ETL/BH/HTL efficiency. OPV fabrication is also much faster, and therefore ideal for screening blends prior to photocathode fabrication.

Table 2.3: Summarising preliminary OPV results varying HTL and ETL

HTL	ETL	J_{SC} (mAcm^{-2})	V_{OC} (V)	FF	PCE (%)
MoO_3*	PDINO*	11.2	0.809	0.618	5.60
MoO_3	ZnO$	11.4	0.863	0.658	6.50
NiO^	PDINO	9.13	0.835	0.176	1.35
NiO	ZnO	10.9	0.862	0.173	1.63

** **PDINO** (N,N'-Bis(N,N-dimethylpropan-1-amine oxide)perylene-3,4,9,10-tetracarboxylic diimide) deposited by thermal evaporation in a vacuum chamber*

$ spin-coated onto the ITO substrates in ambient conditions, from zinc acetate dihydrate in 2-methoxyethanol in a concentration of 100 mg mL^{-1} and 60 µL of ethanolamine at 1000 rpm for 40 seconds

^ from nickel(II) acetate tetrahydrate (52 mg in 1 mL methoxyethanol and 12 µl ethanolamine), also spincoated at 1000 rpm for 40 seconds

***PCE12** was used as received. The 1:1 **PCE12**:acceptor solutions were made in CB 20 mg ml^{-1} with 1 vol% DIO, glycolated acceptors used the same conditions but were spin-coated in chloroform.*

Firstly, different HTLs and ETLs were compared, as shown in **Figure 2.3** and summarised in **Table 2.3**, to optimise the performance of **PCE12:N2200** in devices, prior to including the synthetic modifications to **N2200**. NiO has been successfully employed as an effective HTL in photocathodes, and was therefore also attempted in this application.[41] It has been previously shown that a small decrease in performance is to be expected, however, as seen in **Figure 2.3a)**, the decrease in fill factor and efficiency were quite extreme compared to MoO_3. Two potential reasons suggest this. Firstly, an increased series resistance which would hinder the performance of our photocathodes more drastically than expected. It is believed that this is likely due to NiO altering the surface upon which the blend is spincoated. Secondly, **Figure 2.3a)** strikingly shows a much later onset in the J-V curve, delayed by around 300 mV. This matches a potential misalignment with the blend and the NiO. Possibly a favourable interface energy between the NiO and the acceptor could cause less of the donor to come into contact with the metal oxide. Furthermore, the method of NiO formation was found to be much less reliable than MoO_3, which was deposited on the devices via thermal evaporation. Because of these, MoO_3 was employed as the HTL of choice in this study, motivated by the high stability achieved with this material in literature.[60]

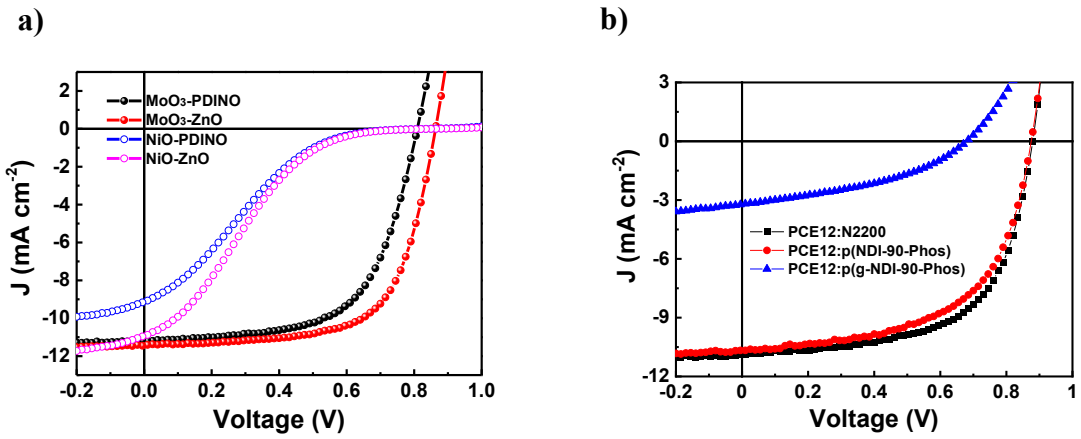


Figure 2.3: a) OPV performance of devices in the architecture: ITO/**HTL**/**PCE12**:**N2200**/**ETL**/Ag b) OPV performance of devices in the architecture: ITO/MoO_3/**PCE12**:**acceptor**/ZnO/Ag

As seen in **Figure 2.3b** and **Table 2.4** the incorporation of **p(NDI-90-Phos)** did not drastically alter device performance, while the incorporation of glycol groups in **p(g-NDI-90-Phos)** yielded a much lower J_{SC} and fill factor, with a performance decrease from 5.85% on the **N2200** device to 0.87% with **p(g-NDI-90-Phos).** It seems that that the inclusion of 10 % anchor group did not drastically alter polymer properties, but the incorporation of a glycol chain has a more

significant effect on the blend. Glycol chains can disrupt polymer packing significantly, leading to a decrease in miscibility with the donor polymer and decrease in effective formation of the heterojunction, which is the likely cause for the decrease in J_{SC} and FF.[61]

Table 2.4: Summarising preliminary OPV results using the different acceptors.

HTL	Acceptor	J_{SC} ($mAcm^{-2}$)	V_{OC} (V)	FF	PCE (%)
MoO_3	**N2200**	10.9	0.88	0.613	5.85
MoO_3	**p(NDI-90-Phos)**	10.7	0.875	0.577	5.39
MoO_3	**p(g-NDI-90-Phos)**	3.21	0.68	0.399	0.87

***PCE12**:acceptor=1:1 in CB 10mg ml-1 with 1 vol% DIO*
***PCE12**:* **p(g-NDI-90-Phos)** *=1:1 in CF 10mg ml-1 with 1 vol% DIO*

It was noted that **PCE12:N2200** and **PCE12:p(NDI-90-Phos)** had better solubility in chlorobenzene (CB), while **p(g-NDI-90-Phos)** was more soluble in chloroform (CF), with limited solubility in CB. These solubility properties were taken advantage of in the fabrication of the devices including the overlayer, explained in **Section 2.5.3** below, to ensure minimal damage to the active layer blend upon spin coating of the overlayer on top.

2.5.3. Glycol Overlayer on Top of BHJ- OPV

Since the glycolated polymer had a negative effect on performance but seemed to have a positive effect on ALD growth, it was thought that instead of replacing **N2200**, it could be used as a thin overlayer, on top of the BHJ for the photocathodes. The hypothesis was that this would allow the benefits of light absorption, charge transport and morphology of the **N2200**, but with the hydrophilicity and improved TiO_2 coverage of the **p(g-NDI-90-Phos).**

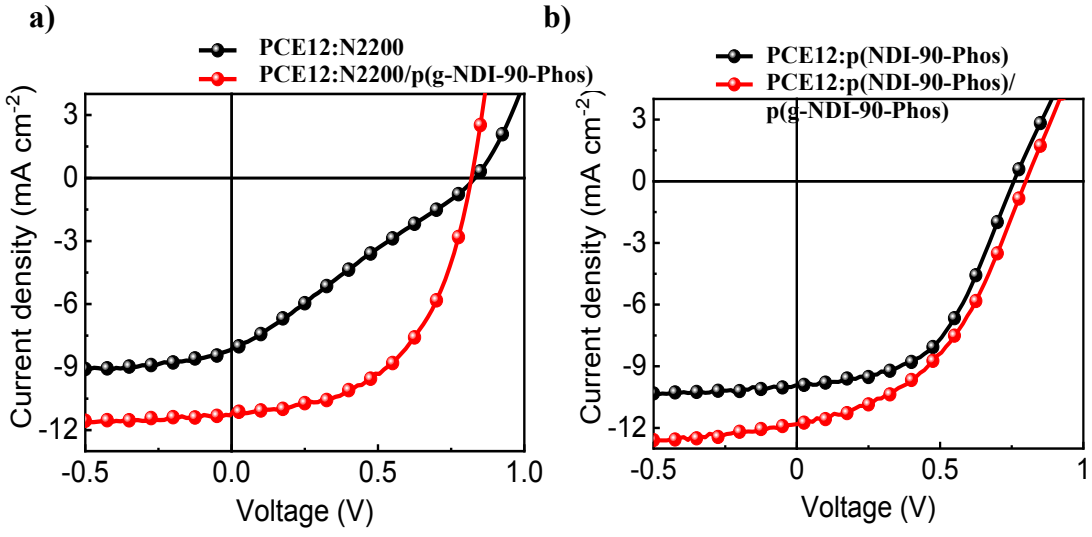


Figure 2.4: OPV performance of devices in the architecture: ITO/MoO_3/**PCE12**:acceptor/acceptor overlayer/ZnO/Ag

performance. It should be noted that the performances are lower than previous studies. This is due to a new batch of purchased **N2200**, and a new synthesised batch of **p(NDI-90-Phos).** The results should therefore be compared to each other in trend rather than to previous results. It should also serve as a reminder of the importance of batch repeatability in organic polymers.

Table 2.5: Summary of OPV performance upon addition of the **p(g-NDI-90-Phos)** overlayer.

Acceptor	Overlayer	J_{SC} ($mAcm^{-2}$)	V_{OC} (V)	FF	PCE (%)
N2200	-	8.14	0.831	0.258	1.75
	p(g-NDI-90-Phos)	11.2	0.820	0.528	4.85
p(NDI-90-Phos)	-	1.74	0.618	0.460	0.50
	p(g-NDI-90-Phos)	7.83	0.656	0.468	2.41

The incorporation of this thin glycolated layer was very promising. Not only did it maintain performance, (unlike fully replacing **N2200** with **p(g-NDI-90-Phos)**, but the overlayer was actually found to increase performance, tripling when using **N2200** and quadrupling with **p(NDI-90-Phos).** This could partly be due to an increase in light absorption, or due to the incorporation of a third component in the heterojunction cascade. It could also be due to increased adhesion to the metal oxide used as the OPV ETL, this would also explain the high FF increase using the **N2200** polymer. In order to find out more about the overlayer, UV-Vis spectra were compared, as were contact angle measurements.

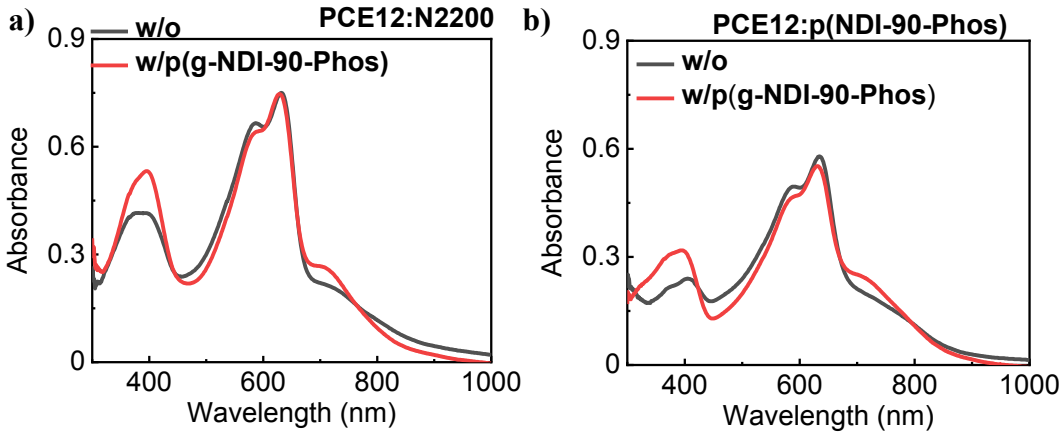


Figure 2.5: UV-Vis spectra of the blend with and without overlayer of a) a **PCE12:N2200** device and b) a **PCE12**:**p(NDI-90-Phos)** device.

UV-Vis spectra of the thin film of the blend on ITO is presented in **Figure 2.5**. A slight increase in absorbance at 400 and 700 nm was observed upon addition of the thin overlayer. This supports that the overlayer is indeed present, but unlikely to be solely responsible for the increase in performance just by light absorption.

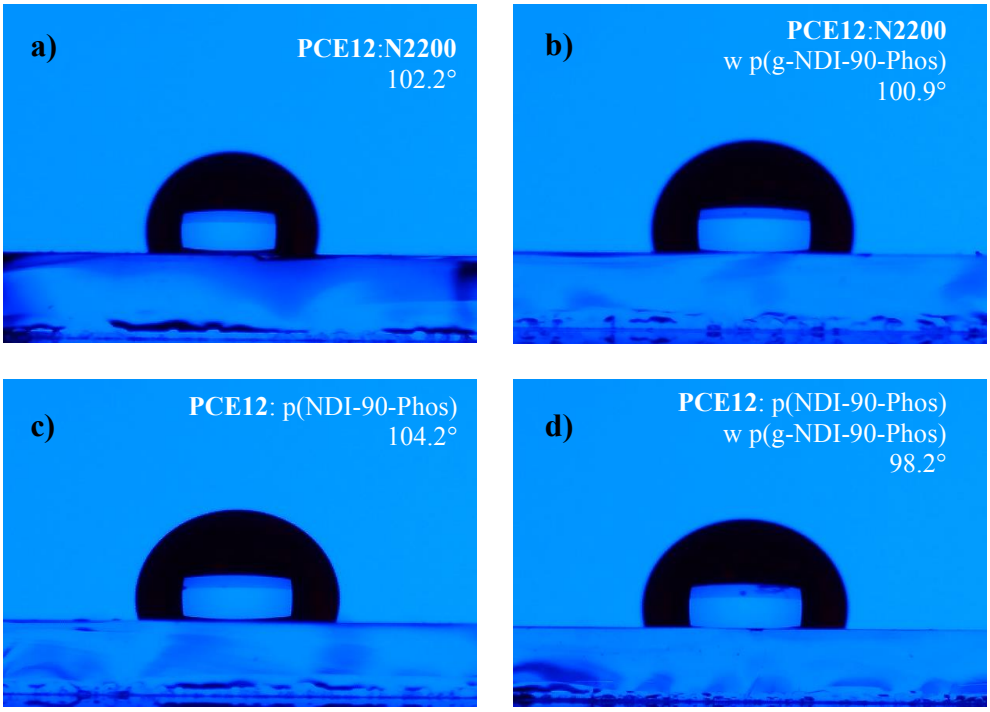


Figure 2.6: Contact angles of the blend with and without the glycolated overlayer

Contact angle measurements were repeated on the blend, including the glycolated overlayer to monitor any changes in hydrophilicity, and can be seen in **Figure 2.6** and summarised in **Table 2.6**.

Table 2.6: Summary of contact angle measurement comparing blends with overlayer on top, and without.

Acceptor	Overlayer	Contact angle (°)
N2200	-	102.2
	yes	100.9
p(NDI-90-Phos)	-	104.2
	yes	98.2

As can be seen from **Figure 2.6**, there was a small decrease observed upon addition of the **p(g-NDI-90-Phos)** in both the **N2200** and the **p(g-NDI-90-Phos)** films, which does further support the presence of the overlayer. However, the difference is quite small, this is likely due to the glycolated layer of the film being very thin, and therefore the dominant hydrophilicity comes from the blend underneath.

2.6. Photocathodes

Following from the OPV screening described above, the mesoporous ITO was discounted, NiO was swapped for MoO_3, and instead of using glycolation in the polymer blend, the presence of an overlayer of **p(g-NDI-90-Phos)** was investigated.

2.6.1. Photocathode architecture

The architecture of the **N2200**:**PCE12** polymers is shown below. The values for the active layer polymers were obtained from cyclic voltammetry and UV-Vis, whereby the polymers were dropcast onto the working electrode with 0.1 M tetrabutylammonium hexafluorophosphate as the supporting electrolyte in degassed acetonitrile. (Appendix **Figure 2.12** and **Figure 2.13**).[62] TiO_2 was taken from literature.[35] **p(g-NDI-90-Phos)** was taken from PESA. (Appendix **Figure 2.14**), which obtained the IP value, EA was calculated from subtracting the optical band gap from the IP value obtained in PESA. The calculation did not take into account binding energy.[63,64] The shift in energy levels of the interlayer could be partially due to surface photovoltage (which is the potential difference between contact under illumination versus in the dark), which can affect the PESA reading.[65,66] The glycolated polymer may also exhibit a red-shifted adsorption and narrower bandgap than the alkylated

polymer, possibly due to smaller π–π stacking distance of the backbone of the glycolated polymer which does not have branched side chains, like the alkylated one which can disrupt packing. [67]

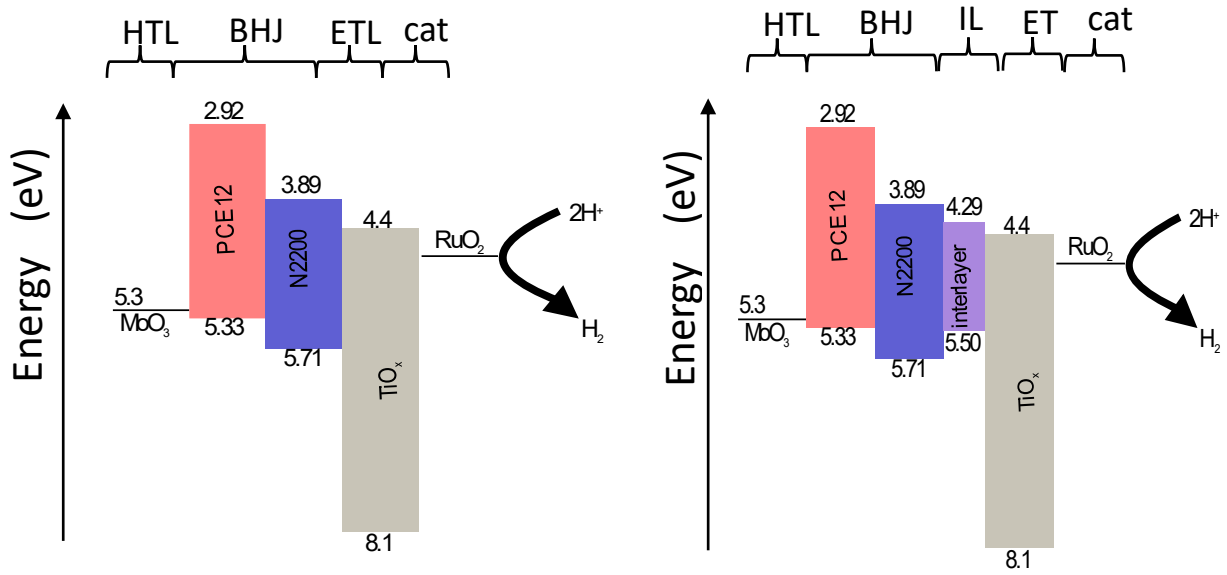


Figure 2.7: Schematic representation of the photocathodes fabricated in this study, including the energy levels of each layer. HTL: hole transporting layer, ETL: electron transporting layer: BHJ: bulk heterojunction, IL: interlayer, cat: co-catalyst.

Figure 2.7 shows the configurations of photocathodes with and without the **p(g-NDI-90-Phos)** interlayer, that were used in this study. The hole transporting layer eventually used was molybdenum oxide, this layer is used to transport holes from the active layer to the electrode (ITO= indium tin oxide). The BHJ is the organic layer comprised of a donor and acceptor, its function is to absorb light, and, since it is a type II heterojunction, it also drives the separation between polarons formed, since the electrons preferentially travel to the electron acceptor (**N2200**), while the holes preferentially travel to the more electron donating polymer (**PCE12**). The electron transporting layer in this case was TiO_2, and it transports electrons from the active layer to the co-catalyst site. RuO_2 nanoparticles, deposited via spincoating, act as co-catalysts, providing an active site for proton reduction. These have shown promise in this application due to their appropriate energy levels, good stability and easy to form.[41]

In order to obtain the growth rate of the ALD process, a silicon wafer was placed in the ALD chamber with the polymers, and a reflectometer was used to measure the thickness of the TiO_2 layer formed on the silicon wafer. Dividing the thickness by the number of cycles gave the growth rate of the layer per cycle, which was in this case 0.044 nm per cycle. It should be noted that the growth rate of the silicon wafer is likely not exactly the same as the growth rate on a

polymer surface. Metal oxides on polymers normally proceed with Volmer-Weber Growth rather than linear growth, which is more common on silicon wafers. Cross-sectional SEM could be used in order to calculate the final thickness of the TiO_2 layer on the polymer. [68]

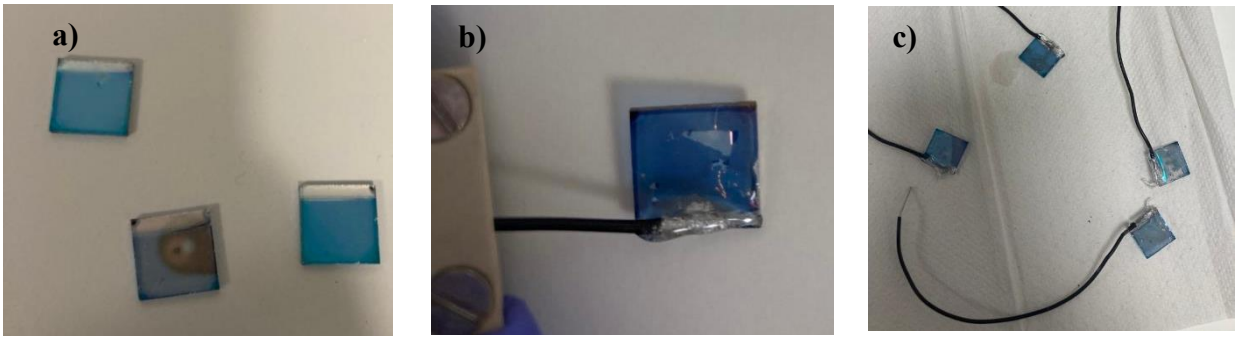


Figure 2.8: Pictures showing examples of photocathodes. a) showing photocathodes prior to soldering thin contact wire and epoxy covering, showing the clean back ITO contact, obtained by wiping with solvent and use of thermal tape. b) example of degradation of photocathode at the interface between ITO and MoO_3, due to testing at higher pH than 1.3. c) examples of fabricated photocathodes.

Pictures showing examples of photocathodes can be seen in **Figure 2.8.** Preparation of the photocathodes is described in detail in the experimental, but as seen in **Figure 2.8a)** the devices show a transparent part to the device, which is the back ITO contact upon which the wire is attached to the device. **Figure 2.8b)** shows degradation of the device, obtained when testing at pH7 in phosphate buffer. The degradation has a straight line at the point of contact of MoO_3, indicating that the HTL degraded at neutral pH.[69] and **Figure 2.8c)** shows typical photocathode devices after fabrication, including the soldering of conducting wire and the use of a thin layer of epoxy to ensure the wire is not in contact with any electrolyte.

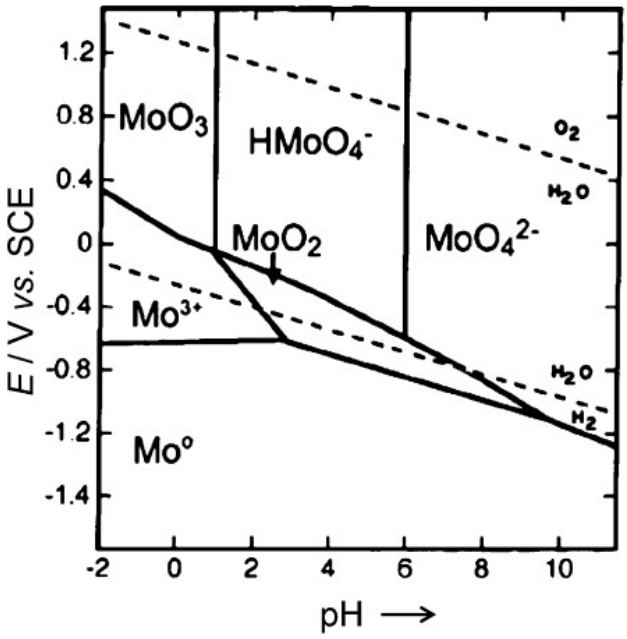


Figure 2.9: Potential-pH diagram of Mo-H_2O system. Published from ref[70], reprinted with permission.

The Pourbaix diagram reproduced in **Figure 2.9** shows that MoO_3 is thermodynamically stable at pH 0-1 for the potentials used in this study.[70] Although the organic material is less stable in these conditions, good encapsulation should ensure a decrease in degradation. Devices with MoO_3 have been shown to yield photocathodes with good stability in an organic photocathode, and was therefore deemed feasible, despite the change in pH required in testing.[71]

2.6.2. Linear Sweep Curves

Current-density potential curves of the organic photocathodes are presented in **Figure 2.10,** photocathode performance was evaluated in pH 1, the electrolyte was made up of 0.3 M H_2SO_4 + 0.5 M Na_2SO_4.

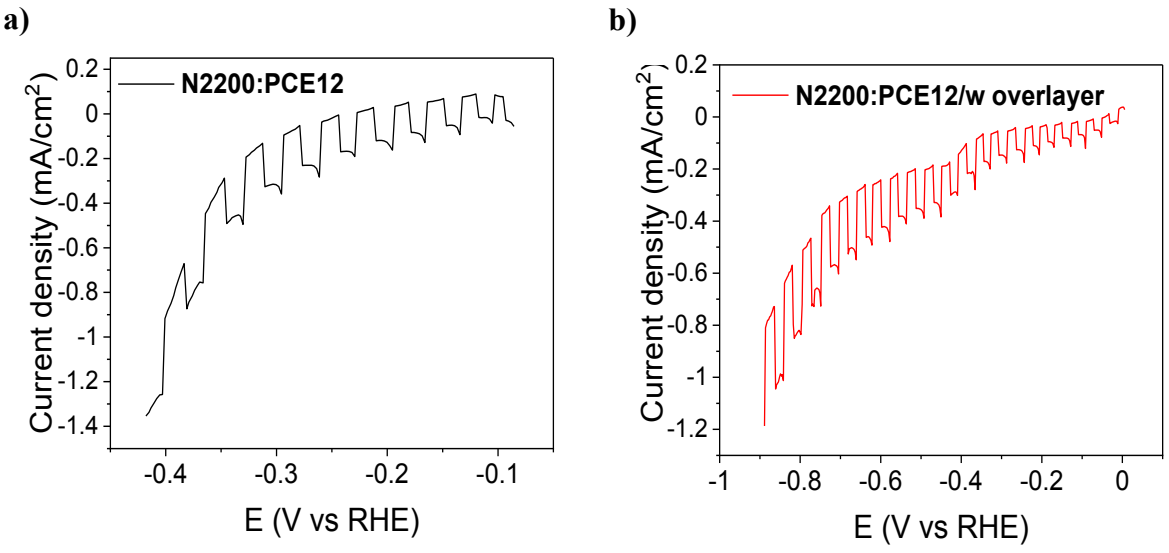


Figure 2.10: Chopped current-density potential curves for the organic photocathodes. Carried out under 1 sun illumination in a three electrode cell at pH 1 (0.3 M H_2SO_4 + 0.5 M Na_2SO_4). A) with the architecture of ITO/MoO_3/BHJ/TiO_2/RuO-NPs. B) with the architecture of ITO/MoO_3/BHJ/overlayer/TiO_2/RuO-NPs.

As seen in **Table 2.7**, the device contained the glycolated interlayer achieved a photovoltage of 0.7 V, which is almost as high as the Voc obtained in the OPV device. Also, a higher photocurrent is observed, than in the **N2200** device. However, when compared to literature (**Table 2.1**), the devices are not as high performing, they yield current density an order of magnitude lower than that obtained by the published reference device, shown for comparison in **Table 2.7**. The tangents used to calculate the values presented in **Table 2.7** are shown in the Appendix, **Figure 2.15** and **Figure 2.16**.

Table 2.7: Table summarising the data obtained from JV curves and chronoamperometry for the devices with and without the glycol based overlayer

Device	**Current (mA/cm^2) at crossover potential**	**Photovoltage (V)**	**Stability (h)**
N2200:PCE12	-0.3	0.35	1
N2200:PCE12- p(g-NDI-90-Phos)	-0.6	0.72	6
PEDOT/PCDTBT: PCBM/TiO2-ALD/RuO2-NP- reference[41]	-3.4	0.7	5

It is possible that performance could be optimised by utilising a thinner TiO_2 layer, or by modifying the HTL, so that the material could be tested in pH7.

2.6.3. Stability Studies

Although the current density obtained was not as high as published values, stability was tested to investigate if the presence of **p(g-NDI-90-Phos)** and increased nucleation growth of the ETL influenced stability. Chronoamperometry was employed to probe the stability of the two devices as shown in **Figure 2.11**

Interestingly, when just **N2200** was used, the stability was relatively low, since after 1 hour the activity decreased to 0 (**Figure 2.11a**). However, the device containing the glycolated

interlayer retained activity until the 6-hour mark, after which no photocurrent was detected, as no change could be observed with the light on or off. (**Figure 2.11b**).

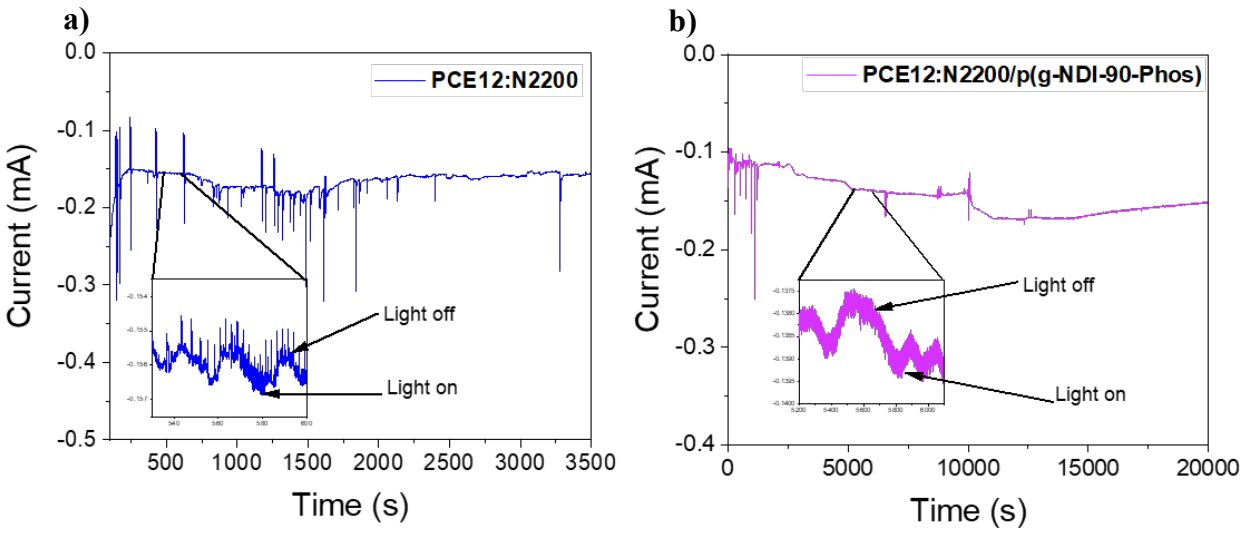


Figure 2.11:Chronoamperometry for the two devices, a) architecture of ITO/MoO_3/**N2200**:**PCE12**/TiO_2 b) architecture of ITO/MoO_3/**N2200**:**PCE12**/ **p(g-NDI-90-Phos)**/TiO_2. Inserts show a zoomed section of the graph to show the shutter in operation, turning the light on and off to compare between photocurrent and darkcurrent.

The large spikes were observed in when the light was turned off and then back on. The stability was monitored until no photocurrent could be seen. The smaller stepwise spikes correspond to turning off the light shutter and then back on, to check if the dark current value had changed.

This supported the hypothesis that by increasing the adhesion between layers and likely creating a better TiO_2 layer, the stability of the device increases from about 1 hour to about 6 hours. Cross-sectional SEM would be ideal to truly figure out any thickness difference in the samples and SEM should be carried out to confirm the coverage of the photocathode after the full ALD cycles.

Although these numbers are not state of the art, as of time of writing, the project was successful as a proof of concept for the use of glycol chains in thin interlayers and anchor groups for increase ALD nucleation for better organic photocathodes. This exciting result can open a myriad of possibilities to address adhesion issues in organic photocathodes.

2.7. Conclusion and Future Outlook

A photocathode based on the water stable blend **PCE12**:**N2200** was investigated in this study. **N2200** was modified by the insertion of phosphonate-based anchor groups and by using glycolated side chains instead of alkyl side chains. It was found that a thin glycolated interlayer, spin coated on top of the **PCE12**:**N2200** blend with 10% substituted phosphonate anchor

groups, was a successful strategy to increase the stability of a photocathode, likely due to the increased functionalities that allow the surface of the BHJ layer to be activated, for more effective TiO_2 growth by ALD. The results indicate that the increase in functional groups on the polymer surface slightly improves the hydrophilicity and thereby increases the number of nucleation sides during the initial few ALD cycles of TiO_2 which would favour the growth of a thin film with fewer pin-holes or grain boundaries. Indeed, SEM images point towards a more homogenous TiO_2 film on the polymer blend with glycolated side chains. Employing this strategy only as an overlayer treatment on top of the standard PCE12:N2200 blend shows to increase the stability of the polymer photocathode in electrolyte solution under operating conditions. Although this study was an interesting proof of concept, further work is required to make use of anchor groups and adjusted functionalities to effectively improve adhesion between layers in photocathodes. Firstly, working with this blend, it would be beneficial to swap the HTL for one that better suits the stability of the blend, so that functions at more neutral pH. Some studies have shown MoO_3 to be a poor HTL on average for photocathodes.[29] This would allow this same architecture to produce better performing and more stable photocathodes. Secondly, it would also be beneficial to isolate the effects of anchor groups from glycolation, by further investigating performance with and without each of these factors. Further SEM studies with various cycle numbers of ALD would also aid in better discerning nucleation and layer growth for different samples. This study focused on phosphonate as an anchor group for TiO_2, however, **p(g-NDI-90-Br*)*** could be modified to obtain a variety of functionalities on the Br, such as azides or hydroxamate groups, which have the potential to bind even more favourably to TiO_2.[72] Building a library of potential anchor groups, tailored to specific metal oxides could potentially give the sought-after stability of several tens of hours to make these more commercially viable resources. In conjunction to testing anchor groups, it would be ideal to run a study on the thickness required of ALD deposited ETL layers. Here the aim would be to minimise ETL thickness, to aid overall performance, while still retaining a pin hole free nature.

2.8. Experimental

2.8.1. General Methods

Nuclear Magnetic Resonance Spectroscopy

Solution state ^{1}H, $^{13}C\{^{1}H\}$ and ^{31}P Nuclear magnetic resonance spectra were recorded at 400 and 75 MHz respectively using a Bruker 400 NMR spectrometer, at ambient temperature.

Chemical shifts were reported in units of parts per million (ppm, δ) in solutions of $CDCl_3$, and referenced using the residual $CDCl_3$ (7.26 ppm) as an internal standard. Where interpretable, coupling constants (*J*) are reported in Hz and splitting patterns reported as s (singlet), d (doublet), t (triplet) and m (multiplet). All NMR data were analysed using MestReNova software.

Molecular Weight Analysis

Molecular Weight data was recorder and analysed on an Agilent $CHCl_3$ GPC (1200 series). Polymers were dissolved in the concentration 1 $mgml^{-1}$ and filtered prior to injection.

Mass Spectrometry

Mass spectrometry was carried out on a Micromass LCT Premier spectrometer.

Contact Angle

Contact angle measurements were carried out using DROPimage, a 1mL droplet of water was measured using a Teflon syringe and imaged, DROPimage software was used for calculating the contact angle.

Scanning Electron Microscopy (SEM)

SEM images were taken on a Zeiss Auriga Cross Beam SEM. Samples were spin-coated on ITO and contacted to SEM plates with copper tape. Image J was used for analysis.

Photo-Electron Spectroscopy in Air (PESA)

PESA was recorded on a KP Technology APS02 system over wavelengths of ca. 180 – 280 nm. Samples were prepared by spin-coating from a concentrated solution (ca. 10 mg mL^{-1}) of polymer in chloroform onto ITO-coated glass slides.

UV-Visible Absorption Spectroscopy

UV-Vis absorption spectra were recorded on a Cary 60 Agilent Technologies UV-Vis Spectrometer.

Electrochemical Measurements

Electrochemical Measurements were performed using an Autolab PGSTAT101 potentiostat. Photocurrent measurements were performed in pH 1, 0.3 M H_2SO_4 + 0.5 M Na_2SO_4 solution. 1 M NaOH aqueous solution (pH 13.6) using a three-electrode configuration, with a Pt wire

counter electrode and an Ag/AgCl, KCl (sat'd) reference electrode. 1.5 AM sunlight (100 $mWcm^{-2}$ was simulated using a 450 W xenon lamp (Osram) equipped with a filter. (3 mm Schott) and masking the area to 0.79 cm^2.

Organic Photovoltaic Devices (OPV) Fabrication

OPV experiments used Oriel Instruments Xenon lamp calibrated to a Si reference cell (AM1.5G, 100 mW cm^{-2}) irradiation and a Keithley 2400 source meter. External quantum efficiency (EQE) measurements were performed using a Bentham PVE300 with monochromatic light from a dual xenon/quartz halogen light source.

ITO cleaning

ITO substrates were sonicated in detergent water, distilled water, acetone and isopropanol for 5 minutes each, and the devices were subsequently treated using O_2 plasma treatment (12 min at 3 mbar O_2 at 155 W), prior to HTL deposition.

MoO_3 layer

MoO_3 10 nm was deposited by thermal evaporation in a vacuum chamber at $\approx 10^{-7}$ mbar.

ZnO layer

zinc acetate dihydrate in 2-methoxyethanol in a concentration of 100 mg mL^{-1} and 60 µL of ethanolamine were used to form the precursor solution, which was then spin-coated onto the ITO substrates in ambient conditions.

NiO layer

Nickel oxide (NiO) was prepared from nickel(II) acetate tetrahydrate (52 mg in 1 mL methoxyethanol and 12 µl ethanolamine) The NiO solution was filtered through a 0.45 micron PTFE filter and spincoated directly onto clean ITO at 4000 rpm for 45 s. The annealed at 250 °C for 20 min and post-treated with O_2 plasma prior to BHJ film deposition.

MoO_3/Ag layer (OPV studies)

MoO_3/Ag (10/100 nm) was deposited by thermal evaporation in a vacuum chamber at $\approx 10^{-7}$ mbar.

BHJ layer and overlayer

PCE12 was used as received. The 1:1 **PCE12**:acceptor solutions were made in CB 20 mg ml^{-1} with 1 vol% DIO, glycolated acceptors used the same conditions but were spin-coated in chloroform. The active layer was spin-coated at 1000 rpm for 40 seconds. The overlayer was made in the concentration of 5 mg ml^{-1} and spin-coated at 4000 rpm from chloroform. A thin strip was wiped clean with chloroform to reveal the ITO back contact.

Photocathode Fabrication

Atomic layer deposition of TiO_2

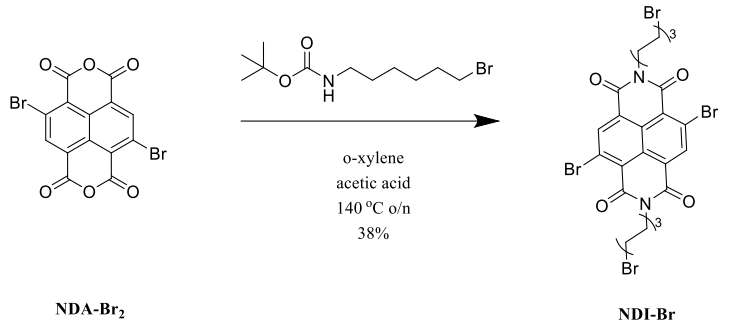
Atomic layer deposition (ALD) was used to deposit the TiO_2 ETL. The precursor, tetrakis(dimethylamido) titanium, (TDMAT) was heated to 75 °C, while water was held at room temperature. The pulse, hold and purge times were 0.1 s/10 s/60 s for TDMAT and 0.015 s/10 s/60 s for H_2O, with 10 sccm N_2 flow. The samples were loaded into the ALD chamber at 30 °C to prevent degradation of the polymer blend, deposition occurred at 75 °C.[68] The substrates were heated only after evacuating the chamber to ~0.3 mbar under N_2 (Carbagas, 99.999% pure) flow. The strip that was previously cleaned with chloroform, was covered in thermal capton tape, to keep the ITO contact clean and TiO_2 free. The growth rate was measured to be 0.44 Å per cycle, obtained from a Si wafer and measured by a reflectometer (F20, Filmetrics). The deposition was run until 100 nm were deposited, for the photocathodes, and the equivalent of 15 nm for the devices used for the SEM images.

RuO_2 deposition

RuO_2 nanoparticles were prepared through a hydrothermal method previously published.[35] 10 $mgml^{-1}$ of RuO_2 NPs in methanol were sonicated for 2 hours and stirred at room temperature for 48 hours. 30 µl of the suspension was spin-coated onto the ETL layer at 4000 rpm for 40 s. A wire was soldered to the ITO back contact on the strip that had been left. Epoxy resin was secured around the edges of the wire to avoid direct contact between electrolyte and wire.

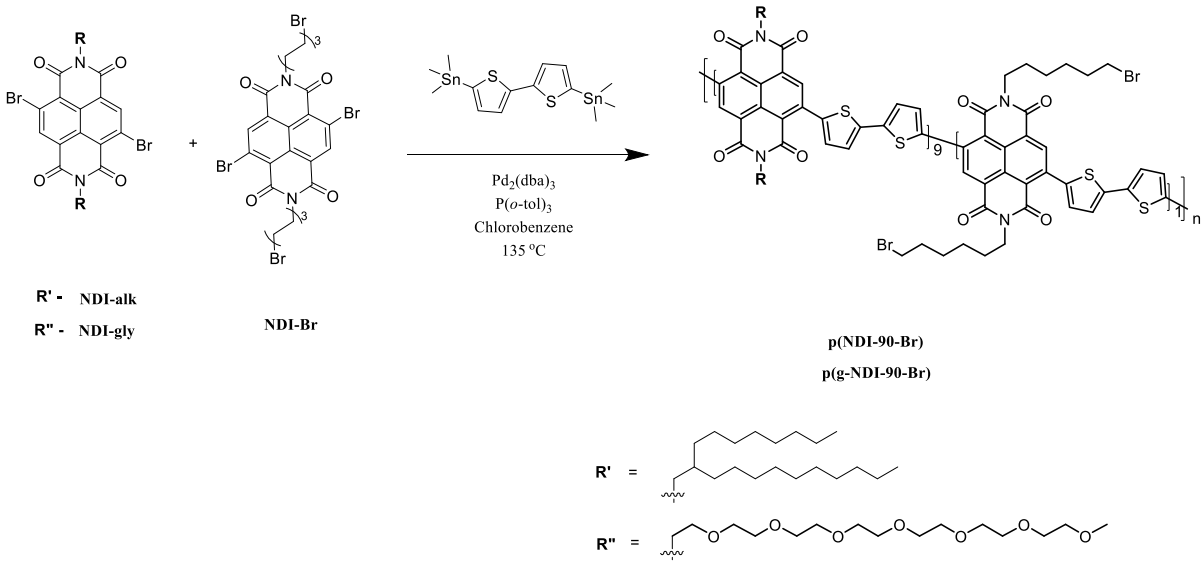
2.8.2. Polymer Synthesis and Characterisation

NDI-Br₂ *was synthesised by Dr Weimin Zhang (McCulloch Group, KAUSR University) and used with no further purification. N2200 was purchased from Ossila (34 kDa)*



Scheme 2.2: route to **NDI-Br**

The synthesis of **NDI-Br** was produced by Dr Matthew Bidwell (Imperial College London). [62]



Scheme 2.3: production of **p(NDI-90-Br**) and **p(g-NDI-90-Br),** repeated from Dr Matthew Bidwell

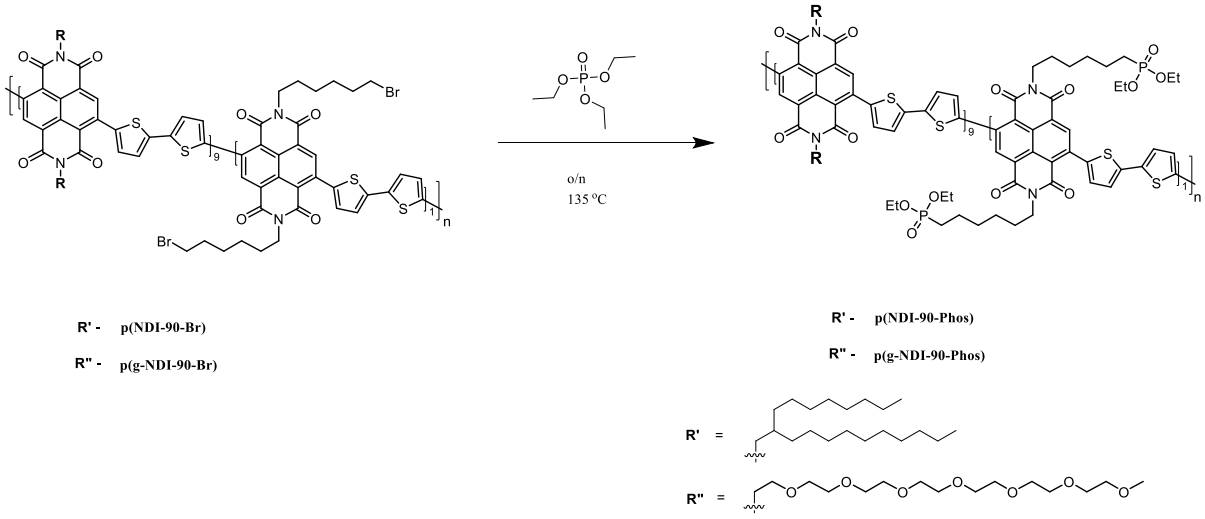
NDI-alk (0.9 equiv, 116.2 mg, 117.8 μmol), **NDI-Br** (0.1 equiv, 9.8 mg, 13.3 μmol) and 5,5'-bis(trimethylstannyl)-2,2'- bithiophene (1.0 equiv, 64.4 mg, 131.2 μmol), were loaded into a microwave vial, along with $Pd_2(dba)_3$ (0.02 equiv, 2.4 mg, 2.6 μmol) and P(*o*-tol)$_3$ (0.08 equiv, 3.2 mg, 10.5 μmol). The solids were degassed under nitrogen for 15 min. then degassed, anhydrous

chlorobenzene (2.5 mL) was added. The mixture was inserted into a 110 °C oil bath and stirred for 16 hours. The polymers were then end capped using the procedure detailed below. The mixture was then allowed to cool to room temperature, precipitated into EA:hexane 1:2, and purified via Soxhlet extraction into hexane, EA, MeOH, THF and finally collected in chloroform and chlorobenzene. The resulting solution was reduced *in vacuo* and the dark blue polymer was precipitated into EA:hexane 1:2, and thoroughly dried, giving **p(NDI-90-Br)** (78 mg, 60%, ^{1}H NMR (400 MHz, chloroform-*d*) δ 8.87 (s), 7.37 (br s), 1.55 – 0.89 (m). GPC (chloroform): M_n = 95.7.0 kDa, M_w = 159.3 kDa.

The same procedure was employed to form **p(g-NDI-90-Br),** using **NDI-gly** (0.9 equiv, 102.4 mg, 95.8 μmol), **NDI-Br** (0.1 equiv, 8.0 mg, 10.7 μmol), 5,5'-bis(trimethylstannyl)-2,2'-bithiophene (1.0 equiv, 32.2 mg, 106.2 μmol), $Pd_2(dba)_3$ (0.02 equiv, 2.0 mg, 1.1 μmol) and P(*o*-tol)$_3$ (0.08 equiv, 2.6 mg, 8.5 μmol), in degassed CB. The polymer was purified in the same manner, yielding a dark blue polymer (74.8 mg, 67%) as a dark blue solid. ^{1}H NMR (400 MHz, chloroform-d) δ 8.85 (s), 7.34 (d), 4.44 (br s), 3.88 – 3.24 (m), 1.49 (br s). GPC (chloroform): Mn = 46.3 kDa, Mw = 69.2 kDa.

Polymer end-capping procedure:

2-(tributylstannyl)thiophene (0.1 mL) was diluted with 0.5 mL of degassed chlorobenzene, and $Pd_2(dba)_3$ (1 mg). 0.1 mL of this solution was added to the polymer mixture under nitrogen and allowed to react for 1 hour. Similarly a solution of 2-bromothiophene (0.1 mL) in 0.5 mL degassed chlorobenzene was made, with $Pd_2(dba)_3$ (1 mg). 0.1 mL of this solution was subsequently added and also allowed to stir for 1 hour. The polymers were then allowed to cool to room temperature, precipitated and purified as described.



Scheme 2.4: production of **p(NDI-90-Br**) and **p(g-NDI-90-Br),** supervised by Dr Matthew Bidwell

In order to obtain the phosphonic esters, the following procedure was used: the obtained **p(NDI-90-Br)** or **p(g-NDI-90-Br)** was placed in a dry microwave vial, with degassed triethyl phosphite (4 mL) under nitrogen and heated for 16 hours at 135 °C, with vigorous stirring. The reaction was allowed to cool to room temperature and precipitated in EA:hexane 2:1, filtered and washed with EA until triethyl phosphite was completely removed. In the case of **p(NDI-90-Br)** this yielded **p(NDI-90-Phos)** (quantitative yield) as a dark blue polymer, ^{1}H NMR (400 MHz, chloroform-*d*) δ 1.24 – 1.51 (m), 0.86 (s). ^{31}P {^{1}H} NMR (202 MHz, chloroform-*d*) δ 32.2 (s). In the case of **p(g-NDI-90-Br)** this yielded **p(g-NDI-90-Phos)** (quantitative yield) also as a dark blue polymer, ^{1}H NMR (400 MHz, chloroform-*d*) 8.84 (s), 7.36 (m), 4.44 (br s), 4.08 (m) 3.84 – 3.36 (m), 1.32 (m). ^{31}P {^{1}H} NMR (202 MHz, 313 K, chloroform-*d*) δ 32.1 (s).[73]

2.9. References

(1) Otep, S.; Michinobu, T.; Zhang, Q. Pure Organic Semiconductor-Based Photoelectrodes for Water Splitting. *Sol. RRL* **2020**, *4* (8). https://doi.org/10.1002/solr.201900395.

(2) Kim, J. H.; Kaneko, H.; Minegishi, T.; Kubota, J.; Domen, K.; Lee, J. S. Overall Photoelectrochemical Water Splitting Using Tandem Cell under Simulated Sunlight. *ChemSusChem* **2016**, *9* (1), 61–66. https://doi.org/10.1002/CSSC.201501401.

(3) Abe, T.; Chiba, J.; Ishidoya, M.; Nagai, K. Organophotocatalysis System of p/n Bilayers for Wide Visible-Light-Induced Molecular Hydrogen Evolution. *RSC Adv.* **2012**, *2* (21), 7992–7996. https://doi.org/10.1039/c2ra21281a.

(4) Walter, M. G.; Warren, E. L.; McKone, J. R.; Boettcher, S. W.; Mi, Q.; Santori, E. A.; Lewis, N. S. Solar Water Splitting Cells. *Chem. Rev.* **2010**, *110* (11), 6446–6473. https://doi.org/10.1021/cr1002326.

(5) Fujishima, A.; Honda, K. Electrochemical Photolysis of Water at a Semiconductor Electrode. *Nature*

1972, *238* (5358), 37–38. https://doi.org/10.1038/238037a0.

(6) Ros, C.; Andreu, T.; Morante, J. R. Photoelectrochemical Water Splitting: A Road from Stable Metal Oxides to Protected Thin Film Solar Cells. *J. Mater. Chem. A* **2020**, *8* (21), 10625–10669. https://doi.org/10.1039/d0ta02755c.

(7) Chandrasekaran, S.; Yao, L.; Deng, L.; Bowen, C.; Zhang, Y.; Chen, S.; Lin, Z.; Peng, F.; Zhang, P. Recent Advances in Metal Sulfides: From Controlled Fabrication to Electrocatalytic, Photocatalytic and Photoelectrochemical Water Splitting and Beyond. *Chem. Soc. Rev.* **2019**, *48* (15), 4178–4280. https://doi.org/10.1039/c8cs00664d.

(8) Zheng, J.; Zhou, H.; Zou, Y.; Wang, R.; Lyu, Y.; Jiang, S. P.; Wang, S. Efficiency and Stability of Narrow-Gap Semiconductor-Based Photoelectrodes. *Energy Environ. Sci.* **2019**, *12* (8), 2345–2374. https://doi.org/10.1039/c9ee00524b.

(9) Jian, J.; Sun, J. A Review of Recent Progress on Silicon Carbide for Photoelectrochemical Water Splitting. *Sol. RRL* **2020**, *4* (7), 2000111. https://doi.org/10.1002/solr.202000111.

(10) Yang, W.; Kim, J. H.; Hutter, O. S.; Phillips, L. J.; Tan, J.; Park, J.; Lee, H.; Major, J. D.; Lee, J. S.; Moon, J. Benchmark Performance of Low-Cost Sb2Se3 Photocathodes for Unassisted Solar Overall Water Splitting. *Nat. Commun.* **2020**, *11* (1), 1–10. https://doi.org/10.1038/s41467-020-14704-3.

(11) Kosco, J.; Moruzzi, F.; Willner, B.; McCulloch, I. Photocatalysts Based on Organic Semiconductors with Tunable Energy Levels for Solar Fuel Applications. *Adv. Energy Mater.* **2020**, *10* (39), 2001935. https://doi.org/10.1002/aenm.202001935.

(12) Kang, I.; Yun, H. J.; Chung, D. S.; Kwon, S. K.; Kim, Y. H. Record High Hole Mobility in Polymer Semiconductors via Side-Chain Engineering. *J. Am. Chem. Soc.* **2013**, *135* (40), 14896–14899. https://doi.org/10.1021/ja405112s.

(13) Steier, L.; Holliday, S. A Bright Outlook on Organic Photoelectrochemical Cells for Water Splitting. *J. Mater. Chem. A* **2018**, *6* (44), 21809–21826. https://doi.org/10.1039/C8TA07036A.

(14) Yang, W.; Prabhakar, R. R.; Tan, J.; Tilley, S. D.; Moon, J. Strategies for Enhancing the Photocurrent, Photovoltage, and Stability of Photoelectrodes for Photoelectrochemical Water Splitting. *Chem. Soc. Rev.* **2019**, *48* (19), 4979–5015. https://doi.org/10.1039/c8cs00997j.

(15) Arunachalam, P.; Nagai, K.; Amer, M. S.; Ghanem, M. A.; Ramalingam, R. J.; Al-Mayouf, A. M. Recent Developments in the Use of Heterogeneous Semiconductor Photocatalyst Based Materials for a Visible-Light-Inducedwater-Splitting System-a Brief Review. *Catalysts* **2021**, *11* (2), 1–27. https://doi.org/10.3390/catal11020160.

(16) Hu, S.; Xiang, C.; Haussener, S.; Berger, A. D.; Lewis, N. S. An Analysis of the Optimal Band Gaps of Light Absorbers in Integrated Tandem Photoelectrochemical Water-Splitting Systems. *Energy Environ. Sci.* **2013**, *6* (10), 2984–2993. https://doi.org/10.1039/c3ee40453f.

(17) Bae, D.; Seger, B.; Vesborg, P. C. K.; Hansen, O.; Chorkendorff, I. Strategies for Stable Water Splitting: Via Protected Photoelectrodes. *Chem. Soc. Rev.* **2017**, *46* (7), 1933–1954. https://doi.org/10.1039/c6cs00918b.

(18) Rojas, H. C.; Bellani, S.; Sarduy, E. A.; Fumagalli, F.; Mayer, M. T.; Schreier, M.; Grätzel, M.; Di Fonzo, F.; Antognazza, M. R. All Solution-Processed, Hybrid Organic-Inorganic Photocathode for Hydrogen Evolution. *ACS Omega* **2017**, *2* (7), 3424–3431. https://doi.org/10.1021/acsomega.7b00558.

(19) Francàs, L.; Burns, E.; Steier, L.; Cha, H.; Solà-Hernández, L.; Li, X.; Shakya Tuladhar, P.; Bofill, R.; García-Antón, J.; Sala, X.; Durrant, J. R. Rational Design of a Neutral PH Functional and Stable Organic Photocathode. *Chem. Commun.* **2018**, *54* (45), 5732–5735. https://doi.org/10.1039/c8cc01736k.

(20) Sakai, N.; Prasad, G. K.; Ebina, Y.; Takada, K.; Sasaki, T. Layer-by-Layer Assembled TiO2 Nanoparticle/PEDOT-PSS Composite Films for Switching of Electric Conductivity in Response to Ultraviolet and Visible Light. *Chem. Mater.* **2006**, *18* (16), 3596–3598. https://doi.org/10.1021/cm060696g.

(21) Chen, L. M.; Xu, Z.; Hong, Z.; Yang, Y. Interface Investigation and Engineering - Achieving High Performance Polymer Photovoltaic Devices. *J. Mater. Chem.* **2010**, *20* (13), 2575–2598.

https://doi.org/10.1039/b925382c.

(22) Guerrero, A.; Haro, M.; Bellani, S.; Antognazza, M. R.; Meda, L.; Gimenez, S.; Bisquert, J. Organic Photoelectrochemical Cells with Quantitative Photocarrier Conversion. *Energy Environ. Sci.* **2014**, *7* (11), 3666–3673. https://doi.org/10.1039/c4ee01775g.

(23) Lanzarini, E.; Antognazza, M. R.; Biso, M.; Ansaldo, A.; Laudato, L.; Bruno, P.; Metrangolo, P.; Resnati, G.; Ricci, D.; Lanzani, G. Polymer-Based Photocatalytic Hydrogen Generation. *J. Phys. Chem. C* **2012**, *116* (20), 10944–10949. https://doi.org/10.1021/jp212107f.

(24) Huang, Q.; Ye, Z.; Xiao, X. Recent Progress in Photocathodes for Hydrogen Evolution. *J. Mater. Chem. A* **2015**, *3* (31), 15824–15837. https://doi.org/10.1039/c5ta03594e.

(25) Haro, M.; Solis, C.; Molina, G.; Otero, L.; Bisquert, J.; Gimenez, S.; Guerrero, A. Toward Stable Solar Hydrogen Generation Using Organic Photoelectrochemical Cells. *J. Phys. Chem. C* **2015**, *119* (12), 6488–6494. https://doi.org/10.1021/acs.jpcc.5b01420.

(26) Mauger, S. A.; Li, J.; Özmen, Ö. T.; Yang, A. Y.; Friedrich, S.; Rail, M. D.; Berben, L. A.; Moulé, A. J. High Work-Function Hole Transport Layers by Self-Assembly Using a Fluorinated Additive. *J. Mater. Chem. C* **2014**, *2* (1), 115–123. https://doi.org/10.1039/c3tc30973h.

(27) Rojas, H. C.; Bellani, S.; Fumagalli, F.; Tullii, G.; Leonardi, S.; Mayer, M. T.; Schreier, M.; Grätzel, M.; Lanzani, G.; Di Fonzo, F.; Antognazza, M. R. Polymer-Based Photocathodes with a Solution-Processable Cuprous Iodide Anode Layer and a Polyethyleneimine Protective Coating. *Energy Environ. Sci.* **2016**, *9* (12), 3710–3723. https://doi.org/10.1039/c6ee01655c.

(28) Najafi, L.; Romano, V.; Oropesa-Nuñez, R.; Prato, M.; Lauciello, S.; D'Angelo, G.; Bellani, S.; Bonaccorso, F. Hybrid Organic/Inorganic Photocathodes Based on WS 2 Flakes as Hole Transporting Layer Material . *Small Struct.* **2021**, *2* (3), 2000098. https://doi.org/10.1002/sstr.202000098.

(29) Mezzetti, A.; Fumagalli, F.; Alfano, A.; Iadicicco, D.; Antognazza, M. R.; Di Fonzo, F. Stable Hybrid Organic/Inorganic Photocathodes for Hydrogen Evolution with Amorphous WO3 Hole Selective Contacts. *Faraday Discuss.* **2017**, *198* (0), 433–448. https://doi.org/10.1039/c6fd00216a.

(30) Bourgeteau, T.; Tondelier, D.; Geffroy, B.; Brisse, R.; Laberty-Robert, C.; Campidelli, S.; De Bettignies, R.; Artero, V.; Palacin, S.; Jousselme, B. A H2-Evolving Photocathode Based on Direct Sensitization of MoS3 with an Organic Photovoltaic Cell. *Energy Environ. Sci.* **2013**, *6* (9), 2706–2713. https://doi.org/10.1039/c3ee41321g.

(31) Fumagalli, F.; Bellani, S.; Schreier, M.; Leonardi, S.; Rojas, H. C.; Ghadirzadeh, A.; Tullii, G.; Savoini, A.; Marra, G.; Meda, L.; Grätzel, M.; Lanzani, G.; Mayer, M. T.; Antognazza, M. R.; Di Fonzo, F. Hybrid Organic-Inorganic H2-Evolving Photocathodes: Understanding the Route towards High Performance Organic Photoelectrochemical Water Splitting. *J. Mater. Chem. A* **2016**, *4* (6), 2178–2187. https://doi.org/10.1039/c5ta09330a.

(32) Bourgeteau, T.; Tondelier, D.; Geffroy, B.; Brisse, R.; Campidelli, S.; Cornut, R.; Jousselme, B. All Solution-Processed Organic Photocathodes with Increased Efficiency and Stability via the Tuning of the Hole-Extracting Layer. *J. Mater. Chem. A* **2016**, *4* (13), 4831–4839. https://doi.org/10.1039/c6ta01320a.

(33) Fumagalli, F.; Bellani, S.; Schreier, M.; Leonardi, S.; Rojas, H. C.; Ghadirzadeh, A.; Tullii, G.; Savoini, A.; Marra, G.; Meda, L.; Grätzel, M.; Lanzani, G.; Mayer, M. T.; Antognazza, M. R.; Di Fonzo, F. Hybrid Organic-Inorganic H2-Evolving Photocathodes: Understanding the Route towards High Performance Organic Photoelectrochemical Water Splitting. *J. Mater. Chem. A* **2016**, *4* (6), 2178–2187. https://doi.org/10.1039/c5ta09330a.

(34) Yao, L.; Guijarro, N.; Boudoire, F.; Liu, Y.; Rahmanudin, A.; Wells, R. A.; Sekar, A.; Cho, H. H.; Yum, J. H.; Le Formal, F.; Sivula, K. Establishing Stability in Organic Semiconductor Photocathodes for Solar Hydrogen Production. *J. Am. Chem. Soc.* **2020**, *142* (17), 7795–7802. https://doi.org/10.1021/jacs.0c00126.

(35) Francàs, L.; Burns, E.; Steier, L.; Cha, H.; Solà-Hernández, L.; Li, X.; Shakya Tuladhar, P.; Bofill, R.; García-Antón, J.; Sala, X.; Durrant, J. R. Rational Design of a Neutral PH Functional and Stable Organic Photocathode. *Chem. Commun.* **2018**, *54* (45), 5732–5735. https://doi.org/10.1039/C8CC01736K.

(36) Seo, S.; Lee, J. H.; Kim, Y.; Kim, S.; Yoon, C. J.; Choi, H.; Lee, S.; Lee, K.; Kim, H.; Lee, S. A Long-

Term Stable Organic Semiconductor Photocathode-Based Photoelectrochemical Module System for Hydrogen Production. *J. Mater. Chem. A* **2022**, *10* (25), 13247–13253. https://doi.org/10.1039/D2TA02322A.

(37) Hu, S.; Lewis, N. S.; Ager, J. W.; Yang, J.; McKone, J. R.; Strandwitz, N. C. Thin-Film Materials for the Protection of Semiconducting Photoelectrodes in Solar-Fuel Generators. *J. Phys. Chem. C* **2015**, *119* (43), 24201–24228. https://doi.org/10.1021/acs.jpcc.5b05976.

(38) Steier, L.; Bellani, S.; Rojas, H. C.; Pan, L.; Laitinen, M.; Sajavaara, T.; Di Fonzo, F.; Grätzel, M.; Antognazza, M. R.; Mayer, M. T. Stabilizing Organic Photocathodes by Low-Temperature Atomic Layer Deposition of TiO2. *Sustain. Energy Fuels* **2017**, *1* (9), 1915–1920. https://doi.org/10.1039/c7se00421d.

(39) Seger, B.; Tilley, D. S.; Pedersen, T.; Vesborg, P. C. K.; Hansen, O.; Grätzel, M.; Chorkendorff, I. Silicon Protected with Atomic Layer Deposited TiO2: Durability Studies of Photocathodic H2 Evolution. *RSC Adv.* **2013**, *3* (48), 25902–25907. https://doi.org/10.1039/c3ra45966g.

(40) Bourgeteau, T.; Tondelier, D.; Geffroy, B.; Brisse, R.; Cornut, R.; Artero, V.; Jousselme, B. Enhancing the Performances of P3HT:PCBM-MoS3-Based H2-Evolving Photocathodes with Interfacial Layers. *ACS Appl. Mater. Interfaces* **2015**, *7* (30), 16395–16403. https://doi.org/10.1021/acsami.5b03532.

(41) Francàs, L.; Burns, E.; Steier, L.; Cha, H.; Solà-Hernández, L.; Li, X.; Shakya Tuladhar, P.; Bofill, R.; García-Antón, J.; Sala, X.; Durrant, J. R. Rational Design of a Neutral PH Functional and Stable Organic Photocathode. *Chem. Commun.* **2018**, *54* (45), 5732–5735. https://doi.org/10.1039/c8cc01736k.

(42) Rojas, H. C.; Bellani, S.; Sarduy, E. A.; Fumagalli, F.; Mayer, M. T.; Schreier, M.; Grätzel, M.; Di Fonzo, F.; Antognazza, M. R. All Solution-Processed, Hybrid Organic-Inorganic Photocathode for Hydrogen Evolution. *ACS Omega* **2017**, *2* (7), 3424–3431. https://doi.org/10.1021/acsomega.7b00558.

(43) Bellani, S.; Najafi, L.; Capasso, A.; Del Rio Castillo, A. E.; Antognazza, M. R.; Bonaccorso, F. Few-Layer MoS2flakes as a Hole-Selective Layer for Solution-Processed Hybrid Organic Hydrogen-Evolving Photocathodes. *J. Mater. Chem. A* **2017**, *5* (9), 4384–4396. https://doi.org/10.1039/c6ta10572f.

(44) Bourgeteau, T.; Tondelier, D.; Geffroy, B.; Brisse, R.; Campidelli, S.; Cornut, R.; Jousselme, B. All Solution-Processed Organic Photocathodes with Increased Efficiency and Stability via the Tuning of the Hole-Extracting Layer. *J. Mater. Chem. A* **2016**, *4* (13), 4831–4839. https://doi.org/10.1039/c6ta01320a.

(45) Boissezon, R.; Muller, J.; Beaugeard, V.; Monge, S.; Robin, J.-J. Organophosphonates as Anchoring Agents onto Metal Oxide-Based Materials: Synthesis and Applications. **2014**. https://doi.org/10.1039/c4ra05414h.

(46) Raza, M.; Bachinger, A.; Zahn, N.; Kickelbick, G. Interaction and UV-Stability of Various Organic Capping Agents on the Surface of Anatase Nanoparticles. *Materials (Basel).* **2014**, *7* (4), 2890–2912. https://doi.org/10.3390/ma7042890.

(47) Zhao, W.; Qian, D.; Zhang, S.; Li, S.; Inganäs, O.; Gao, F.; Hou, J. Fullerene-Free Polymer Solar Cells with over 11% Efficiency and Excellent Thermal Stability. *Adv. Mater.* **2016**, *28* (23), 4734–4739. https://doi.org/10.1002/adma.201600281.

(48) Yan, H.; Chen, Z.; Zheng, Y.; Newman, C.; Quinn, J. R.; Dötz, F.; Kastler, M.; Facchetti, A. A High-Mobility Electron-Transporting Polymer for Printed Transistors. *Nature* **2009**, *457* (7230), 679–686. https://doi.org/10.1038/nature07727.

(49) Zhang, Y.; Xu, Y.; Ford, M. J.; Li, F.; Sun, J.; Ling, X.; Wang, Y.; Gu, J.; Yuan, J.; Ma, W.; Zhang, Y.; Xu, Y.; Li, F.; Sun, J.; Ling, X.; Wang, Y.; Gu, J.; Yuan, J.; Ma, W.; Ford, M. J. Thermally Stable All-Polymer Solar Cells with High Tolerance on Blend Ratios. *Adv. Energy Mater.* **2018**, *8* (18), 1800029. https://doi.org/10.1002/AENM.201800029.

(50) Facchetti, A. Polymer Donor–Polymer Acceptor (All-Polymer) Solar Cells. *Mater. Today* **2013**, *16* (4), 123–132. https://doi.org/10.1016/J.MATTOD.2013.04.005.

(51) Bae, D.; Pedersen, T.; Seger, B.; Iandolo, B.; Hansen, O.; Vesborg, P. C. K.; Chorkendorff, I. Carrier-Selective p- and n-Contacts for Efficient and Stable Photocatalytic Water Reduction. *Catal. Today* **2017**, *290*, 59–64. https://doi.org/10.1016/J.CATTOD.2016.11.028.

(52) He, Y.; Hamann, T.; Wang, D. Thin Film Photoelectrodes for Solar Water Splitting. *Chem. Soc. Rev.*

2019, *48* (7), 2182–2215. https://doi.org/10.1039/C8CS00868J.

(53) Steier, L.; Bellani, S.; Rojas, H. C.; Pan, L.; Laitinen, M.; Sajavaara, T.; Di Fonzo, F.; Grätzel, M.; Antognazza, M. R.; Mayer, M. T. Stabilizing Organic Photocathodes by Low-Temperature Atomic Layer Deposition of TiO2. *Sustain. Energy Fuels* **2017**, *1* (9), 1915–1920. https://doi.org/10.1039/c7se00421d.

(54) Robitaille, A.; Jenekhe, S. A.; Leclerc, M. Poly(Naphthalene Diimide- Alt-Bithiophene) Prepared by Direct (Hetero)Arylation Polymerization for Efficient All-Polymer Solar Cells. *Chem. Mater.* **2018**, *30* (15), 5353–5361. https://doi.org/10.1021/ACS.CHEMMATER.8B02160/SUPPL_FILE/CM8B02160_SI_001.PDF.

(55) Michaelis, A.; Kaehne, R. Ueber Das Verhalten Der Jodalkyle Gegen Die Sogen. Phosphorigsäureester Oder O-Phosphine. *Berichte der Dtsch. Chem. Gesellschaft* **1898**, *31* (1), 1048–1055. https://doi.org/10.1002/CBER.189803101190.

(56) Arbuzov, A. E. On the Structure of Phosphonic Acid and Its Derivates:... - Google Scholar. *J. Russ. Phys. Chem. Soc.* **1906**, 687.

(57) Harsági, N.; Keglevich, G. The Hydrolysis of Phosphinates and Phosphonates: A Review. *Molecules* **2021**, *26* (10). https://doi.org/10.3390/MOLECULES26102840.

(58) Wagstaffe, M.; Thomas, A. G.; Jackman, M. J.; Torres-Molina, M.; Syres, K. L.; Handrup, K. An Experimental Investigation of the Adsorption of a Phosphonic Acid on the Anatase TiO2(101) Surface. *J. Phys. Chem. C* **2016**, *120* (3), 1693–1700. https://doi.org/10.1021/ACS.JPCC.5B11258/ASSET/IMAGES/LARGE/JP-2015-112583_0009.JPEG.

(59) Guerra-Nuñez, C.; Putz, B.; Savu, R.; Li, M.; Zhang, Y.; Erni, R.; Mochkalev, S.; Michler, J.; Park, H. G.; Utke, I. The Nucleation, Radial Growth, and Bonding of TiO2 Deposited via Atomic Layer Deposition on Single-Walled Carbon Nanotubes. *Appl. Surf. Sci.* **2021**, *555*, 149662. https://doi.org/10.1016/J.APSUSC.2021.149662.

(60) Shi, W.; Li, D.; Fan, W.; Ma, J.; Li, C.; Yu, W.; Shi, J.; Li, C. Nonfullerene Bulk Heterojunction-Based Photocathodes for Highly Efficient Solar Hydrogen Production in Acidic and Neutral Solutions. *Adv. Funct. Mater.* **2020**, *30* (46). https://doi.org/10.1002/adfm.202003399.

(61) Moro, S.; Siemons, N.; Drury, O.; Warr, D. A.; Moriarty, T. A.; Perdigão, L. M. A.; Pearce, D.; Moser, M.; Hallani, R. K.; Parker, J.; McCulloch, I.; Frost, J. M.; Nelson, J.; Costantini, G. The Effect of Glycol Side Chains on the Assembly and Microstructure of Conjugated Polymers. *ACS Nano* **2022**. https://doi.org/10.1021/ACSNANO.2C09464/ASSET/IMAGES/LARGE/NN2C09464_0007.JPEG.

(62) Bidwell, M. W. Developing Organic Semiconducting Materials for Organic Photovoltaics and Photocatalytic Water Splitting Applications, Imperial College London, 2021.

(63) Giovannitti, A.; Maria, I. P.; Hanifi, D.; Donahue, M. J.; Bryant, D.; Barth, K. J.; Makdah, B. E.; Savva, A.; Moia, D.; Zetek, M.; Barnes, P. R. F.; Reid, O. G.; Inal, S.; Rumbles, G.; Malliaras, G. G.; Nelson, J.; Rivnay, J.; McCulloch, I. The Role of the Side Chain on the Performance of N-Type Conjugated Polymers in Aqueous Electrolytes. *Chem. Mater.* **2018**, *30* (9), 2945–2953. https://doi.org/10.1021/ACS.CHEMMATER.8B00321/ASSET/IMAGES/LARGE/CM-2018-003219_0004.JPEG.

(64) He, Y.; Kukhta, N. A.; Marks, A.; Luscombe, C. K. The Effect of Side Chain Engineering on Conjugated Polymers in Organic Electrochemical Transistors for Bioelectronic Applications. *J. Mater. Chem. C* **2022**, *10* (7), 2314. https://doi.org/10.1039/D1TC05229B.

(65) Bertrandie, J.; Han, J.; De Castro, C. S. P.; Yengel, E.; Gorenflot, J.; Anthopoulos, T.; Laquai, F.; Sharma, A.; Baran, D.; Bertrandie, J.; Han, J.; De Castro, C. S. P.; Yengel, E.; Gorenflot, J.; Anthopoulos, T.; Laquai, F.; Sharma, A.; Baran, D. The Energy Level Conundrum of Organic Semiconductors in Solar Cells. *Adv. Mater.* **2022**, *34* (35), 2202575. https://doi.org/10.1002/ADMA.202202575.

(66) Murthy, L. N. S.; Barrera, D.; Xu, L.; Gadh, A.; Cao, F. Y.; Tseng, C. C.; Cheng, Y. J.; Hsu, J. W. P. Probing Defect States in Organic Polymers and Bulk Heterojunctions Using Surface Photovoltage Spectroscopy. *J. Phys. Chem. C* **2019**, *123* (17), 10795–10801. https://doi.org/10.1021/ACS.JPCC.9B01667/ASSET/IMAGES/MEDIUM/JP-2019-01667Y_M002.GIF.

(67) Meng, B.; Song, H.; Chen, X.; Xie, Z.; Liu, J.; Wang, L. Replacing Alkyl with Oligo(Ethylene Glycol) as

Side Chains of Conjugated Polymers for Close π-π Stacking. *Macromolecules* **2015**, *48* (13), 4357–4363. https://doi.org/10.1021/ACS.MACROMOL.5B00702/SUPPL_FILE/MA5B00702_SI_001.PDF.

(68) Steier, L.; Bellani, S.; Rojas, H. C.; Pan, L.; Laitinen, M.; Sajavaara, T.; Di Fonzo, F.; Grätzel, M.; Antognazza, M. R.; Mayer, M. T. Stabilizing Organic Photocathodes by Low-Temperature Atomic Layer Deposition of TiO2. *Sustain. Energy Fuels* **2017**, *1* (9), 1915–1920. https://doi.org/10.1039/c7se00421d.

(69) Perry, S. C.; Gateman, S. M.; Stephens, L. I.; Lacasse, R.; Schulz, R.; Mauzeroll, J. Pourbaix Diagrams as a Simple Route to First Principles Corrosion Simulation. *J. Electrochem. Soc.* **2019**, *166* (11), C3186–C3192. https://doi.org/10.1149/2.0111911JES/XML.

(70) Saji, V. S.; Lee, C. W. Molybdenum, Molybdenum Oxides, and Their Electrochemistry. *ChemSusChem* **2012**, *5* (7), 1146–1161. https://doi.org/10.1002/CSSC.201100660.

(71) Yao, L.; Guijarro, N.; Boudoire, F.; Liu, Y.; Rahmanudin, A.; Wells, R. A.; Sekar, A.; Cho, H. H.; Yum, J. H.; Le Formal, F.; Sivula, K. Establishing Stability in Organic Semiconductor Photocathodes for Solar Hydrogen Production. *J. Am. Chem. Soc.* **2020**, *142* (17), 7795–7802. https://doi.org/10.1021/jacs.0c00126.

(72) Zhang, L.; Cole, J. M. Anchoring Groups for Dye-Sensitized Solar Cells. *ACS Appl. Mater. Interfaces* **2015**, *7* (6), 3427–3455. https://doi.org/10.1021/AM507334M/ASSET/IMAGES/LARGE/AM-2014-07334M_0006.JPEG.

(73) Hepworth, J. D.; Gabbut, C. D.; Mark Heron, B. Pyrans and Their Benzo Derivatives: Synthesis. *Compr. Heterocycl. Chem. II A Rev. Lit. 1982-1995* **1996**, *5*, 351–468. https://doi.org/10.1016/B978-008096518-5.00111-8.

2.10. Appendix

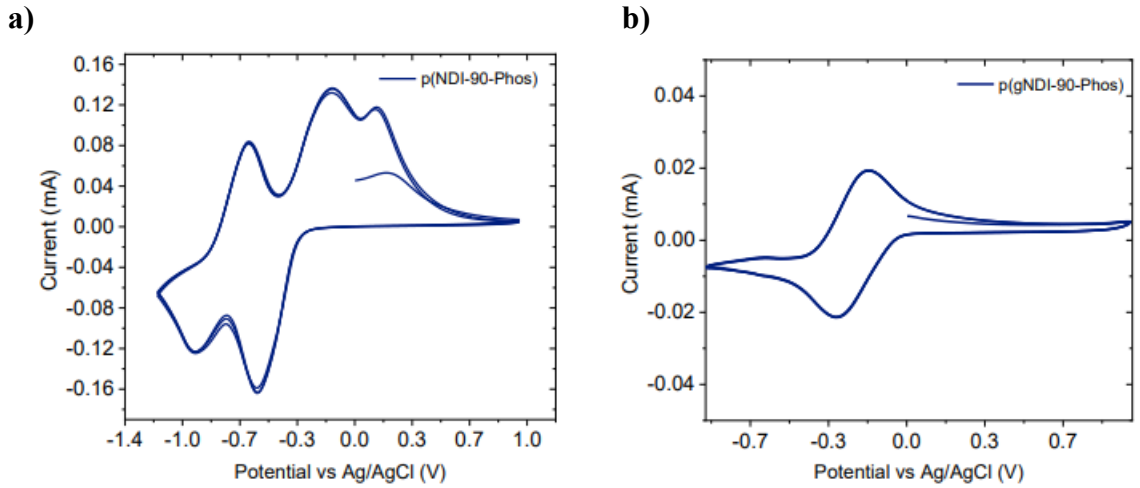


Figure 2.12: Cyclic Voltammetry data of a) **p(NDI-90-Phos)** and b) **p(g-NDI-90-Phos),** carried out and plotted by Dr Matthew Bidwell.[62]

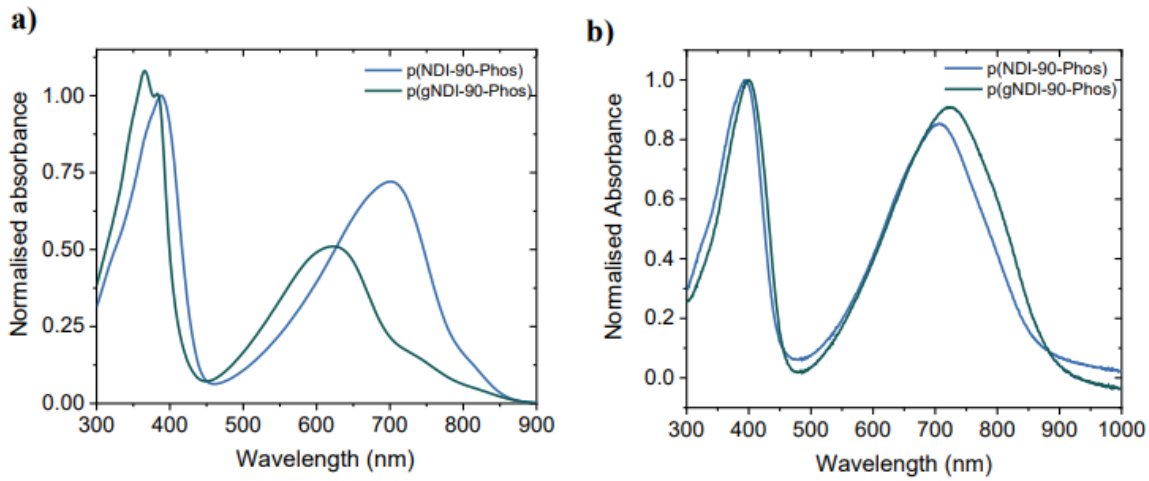


Figure 2.13: UV-Vis data in solution (a) and thin film (b) for both **p(NDI-90-Phos)** and **p(g-NDI-90-Phos)** carried out and plotted by Dr Matthew Bidwell.[62]

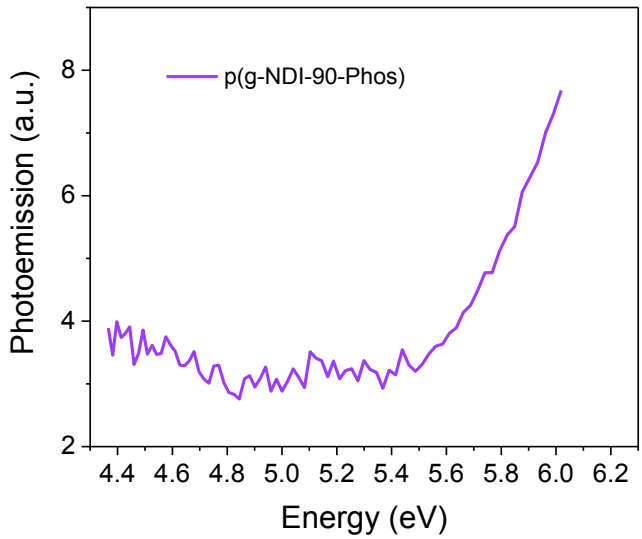


Figure 2.14: PESA of **p(g-NDI-90-Phos)**

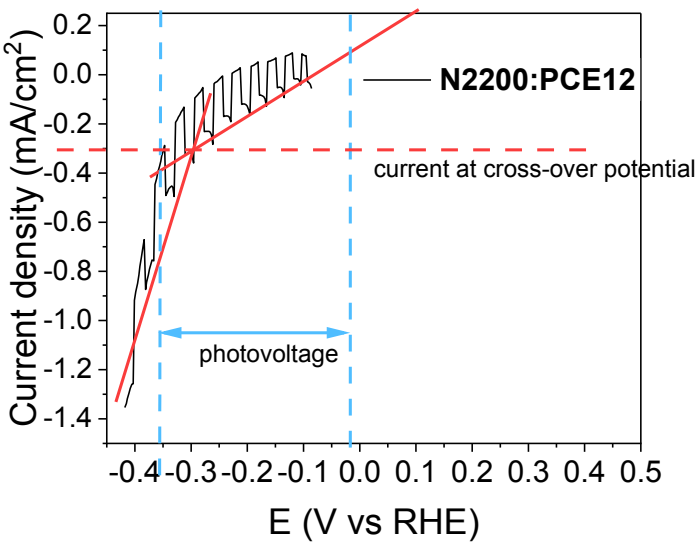


Figure 2.15: Reprised Figure **2.10a**, to show tangents used to obtain values for **Table 2.7**

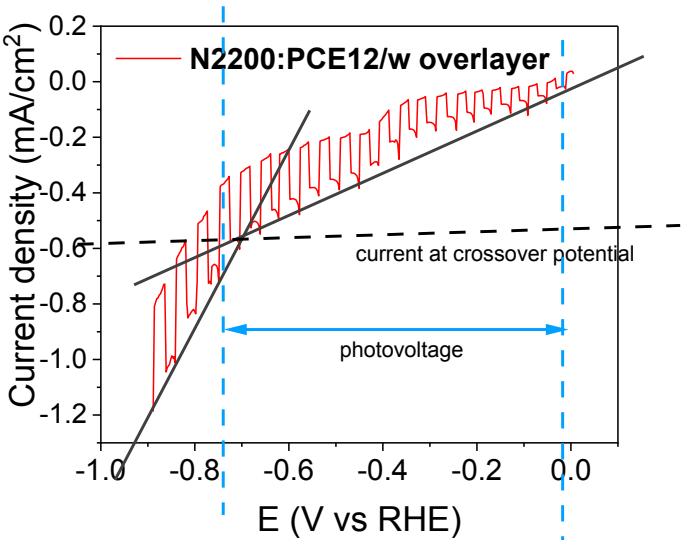


Figure 2.16: Reprised **Figure 2.10b** to show tangents used to obtain values for **Table 2.7**

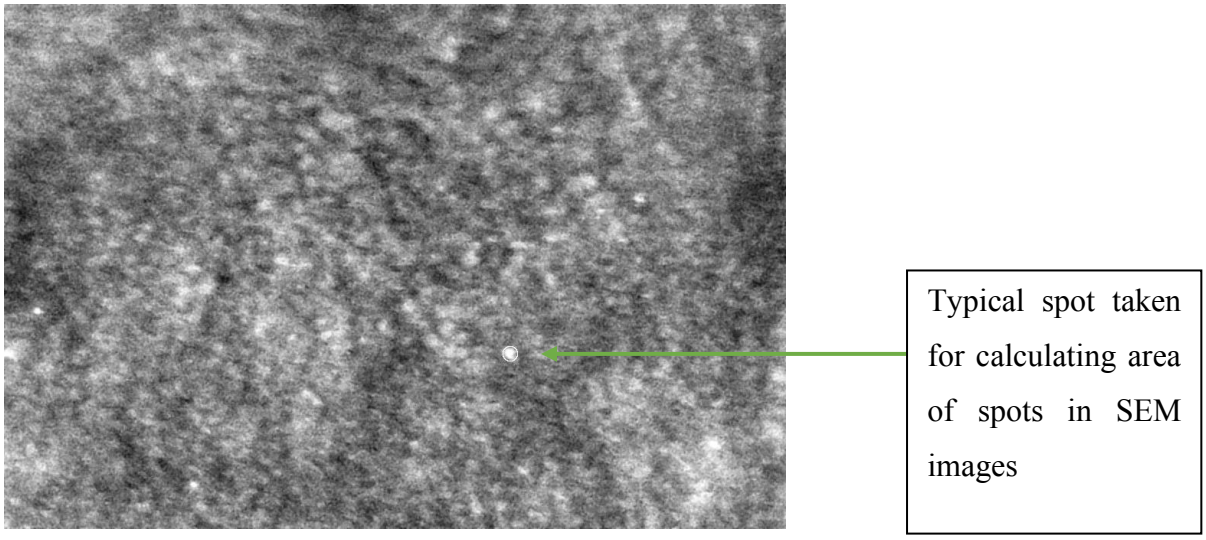


Figure 2.17: reprisal of **Figure 2.2 f,** showing the zoomed out SEM of **p(g-NDI-90-Phos),** spots were identified using ImageJ, and the areas calculated.

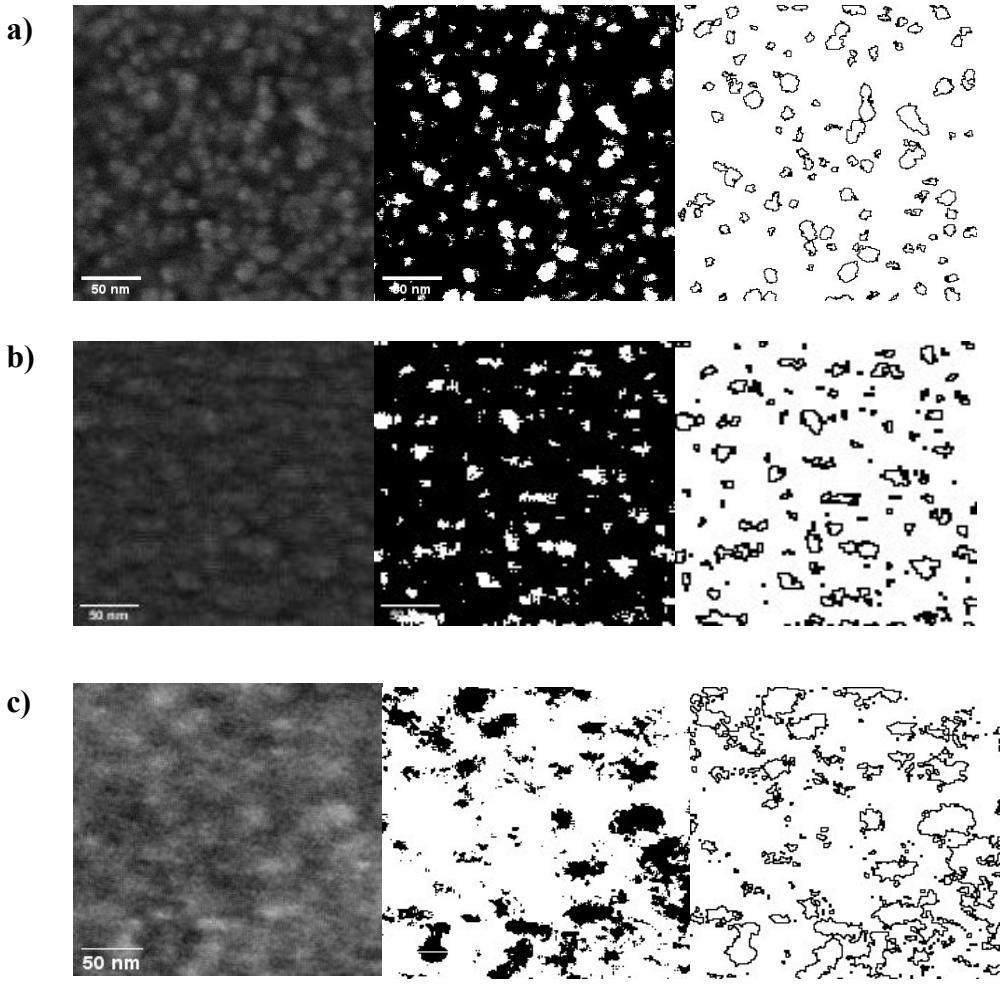


Figure 2.18: zoomed in SEM images of samples containing a) **N2200**, b) **p(NDI-90-Phos) c) p(g-NDI-90-Phos)** respectively, with 50 cycles of TiO_2. The images are zoomed in to be the same size, from Figure 2.2.

3. Gas Phase Carbon Dioxide Photoreduction Testing Design

Contents

3. GAS PHASE CARBON DIOXIDE PHOTOREDUCTION TESTING DESIGN....99

3.1. General Information and Attributions 103

3.2. Introduction 103

3.2.1. Benchmarking in Photocatalysis 103

3.2.1.1. Medium 104

3.2.1.2. Light Sources 105

3.2.1.3. Reactors 105

3.2.1.4. Temperature 106

3.3. Set-up Building and Optimisation for CO_2 Photocatalysis 106

3.3.1. Set-up design and operation 106

3.3.1.1. Parts 106

3.3.1.2. Set-up diagram 107

3.3.1.3. Light source 109

3.3.1.4. Temperature, Pressure and Gas Flow 111

3.3.1.5. Reactor design 112

3.3.1.6. Calibration and GC detection 114

3.3.1.7. Batch vs loop testing 115

3.3.1.8. Titanium Dioxide 116

3.3.2. Solution Testing 116

3.3.3. Calculations 118

3.3.3.1. Calculations for reactor volume 118

3.3.3.2. Calculations for number of moles 119

3.3.3.3. Calculations for AQY 120

3.3.3.4. Calculations for Selectivity 120

3.4. Reporting Results- Evaluating Performance 121

3.4.1. Units, mass, and surface area corrections 121

3.4.2. Controls 123

3.5. Future Work and Set-up Flexibility 124

3.6. Experimental and Parts 125

3.7. References 127

List of Figures

Figure 3.1: Schematic of the CO_2 photocatalysis set-up 108
Figure 3.2: Picture of the built set-up, under 1 sun illumination 109
Figure 3.3: Asahi 303-Max Xenon Lamp, image taken from[38] 109
Figure 3.4: a) Spectrum with various filter for Asahi 303-Max Xenon Lamp, image taken from [39]. b) mirror module obtained experimentally with Asahi Lamp using UV-Vis filter, compared to Reference Air Mass 1.5 Spectra obtained from[40] 110
Figure 3.5: Reactor under light with a) 500 nm filter b) 450 filter 111
Figure 3.6: scroll pump obtained from Makuhari Messe Co., Ltd.[44] 112
Figure 3.7: schematic of reactor design 113
Figure 3.8: Pictures taken of the reactor. 113
Figure 3.9: Calibration graphs for a) batch process, b) continuous process 115
Figure 3.10: Depicting additional piece of metal for gas bubbling inside the reactor for solution-based testing 117
Figure 3.11: a) Performance evaluation of **Bpy-sp^{2}c-COF** in the solution phase version of the reactor. b) Performance evaluation of **TiO_2** in the solution phase version of the reactor 117
Figure 3.12: Figure reproduced from ref [59] with permission, showing a typical rate of reaction dependency on photocatalyst concentration. 118
Figure 3.13: Chromatogram of the reference gas mixture, top from FID, bottom from TCD 119
Figure 3.14: Graphs obtained of the formation of CO from TiO_2. a) shows the performance as µmol over time, b) is corrected for mass in g, c) is corrected for surface area in m^2. 121
Figure 3.15: Graphs obtained of the formation of CO from **pTA-Ph**. a) shows the performance as µmol over time, b) is corrected for mass in g, c) is corrected for surface area in m^2. 122
Figure 3.16: examples of polymers on glass substrates a) polymer that could be peeled off its glass support, b) image J grab showing process for area calculation, c) image J grab of calculated area 123

List of Tables

Table 3.1: Calibration Gas composition and GC detection limits 114

Table 3.2: Summary of rates of **TiO_2** samples and **pTA-Ph** with different mass and surface area loadings 122

3.1. General Information and Attributions

The CO_2 photocatalysis set-up was designed, built, tested, and optimised by the author. Polymers pTA-Ph and pTA are described in detail in ***Chapter 4.***

3.2. Introduction

A crucial part of verifying the use of organic semiconductors in carbon dioxide photoreduction is the ability to test the materials made. Furthermore, testing conditions are known to vastly alter photocatalytic results. As such, as part of this thesis, a testing set-up needed to be designed and built to effectively test materials in. This chapter will firstly outline general considerations to be taken when designing a set-up and standardising results in section 3.2.1, and then will go into detail on the final design choices and build, including parts and materials, in section 3.3. The chapter will finish with controls, calibrations and calculations done throughout in section 3.4. In the wider context of this thesis, the materials outlined in **Chapter 4** and **Chapter 5** were tested using this set-up. Over the course of building and designing it also became apparent how important and how much of a difference testing can make on the product rates, and how important it would be to be able to further standardise testing in this field, to be able to compare materials across research groups and advance this area of photocatalysis.

3.2.1. Benchmarking in Photocatalysis

Benchmarking is a practice normally pre agreed upon by a scientific community, that aims to standardise measurements to maximize reproducibility, relevance and accuracy.[1] It is important for advancing a scientific field because it allows more direct and fair comparison of data obtained from multiple sources, which would be otherwise difficult to compare.[2] Establishing a rigorous benchmarking procedure is especially important in photocatalysis due to the difficulty in standardising experiments, and the large numbers of parameters affecting photocatalysis. Multiple parameters can be used to report the efficacy of a photocatalysis or photocatalytic process to evaluate performance, these include: rate of product evolution, per gram or surface area, quantum yields, turn over numbers and frequencies. However it is difficult to pick a single parameter that can be directly compared over various set-ups and experiments.[3] In carbon dioxide photocatalysis factors such as: reactor size, temperature, pressure, medium, and surface area can drastically alter the rates and products formed. Current metrics, although useful for comparison, cannot consider each of these factors altogether. Therefore, when reporting results, in order to aid standardisation and benchmarking it is critical to include detailed information on the set-ups used for measuring and on the testing conditions.

It is also ideal to utilise a standard, commercially available compound, and compare any obtained results to that of the standard in the same conditions and set-up. This would enable better comparison between materials in literature.

3.2.1.1. Medium

In CO_2 photocatalysis the medium and conditions used can alter the efficiency and products formed dramatically. In aqueous phase a key disadvantage is the low solubility and transport of the CO_2 molecule in water. Since less CO_2 is present in the solution, especially near atmospheric pressures, less of it can reach the active sites. Often, this aids the competing reaction of hydrogen evolution, since not only is more water present, but also the reaction is relatively simpler to do. This is because thermodynamically, CO_2 tends to require a more negative reduction potential than hydrogen evolution, furthermore, carbon dioxide photocatalysis is a multielectron process, and requires more electrons to react than hydrogen evolution.[4] In order to address this, one approach has been investigating various solvent compositions. For example, Yang *et al,* achieved increased CO formation with a 1:4 ratio of acetonitrile to water.[5] This is likely due to the increased solubility of CO_2 in acetonitrile (0.27 M) or DMF (0.18 M) compared to water (0.04 M).[6] Another approach has been employing the use of ionic liquids, acting either as catalysts in themselves, or to increase CO_2 solubility in the medium.[7–10] Changing the pH can also be a good technique, the use of alkaline conditions has also been attempted in order to solvate carbon dioxide as carbonate ions, however care should be taken as this increases the reduction potentials required, and can also affect the hole scavenger that can be used, for the same reason.[11] The use of hole scavengers can also significantly alter the potential required. Their role is to reduce the holes in photocatalysis by donating electrons into them, which can happen prior to photoreduction, or after, mopping up any residual holes. Scavengers can bring about charge separation either by reductively quenching excitons, or by combining with the hole, or quenching any residual polarons.[12–14] In photocatalysis, the use of TEOA is quite common. Hole scavengers can decrease the overall usefulness of the process if the scavenger is used up not catalytically or if the products obtained are of lower commercial value.[15,16] An advantage of liquid phase carbon dioxide photocatalysis is the drive towards oxidised or liquid products such as methanol and formic acid.[17] Gas phase photocatalysis, however, allows the utilisation of carbon dioxide as is, it allows saturation with carbon dioxide and can use either hydrogen or water-vapour in the oxidation reaction, which enables the removal of a further scavenger. By bypassing the solubility issues, gas-phase photocatalysis has the potential to meet the requirements of commercialisation, arguably

bringing us closer to a set-up that can be utilised in industry.[18–20] The use of hydrogen as a scavenger removes the competing hydrogen evolution reaction completely. It also has the added advantage of tailoring ratios of gasses going into the system, which in turn can be more selective towards desirable products.[21] This study focuses on gas phase photocatalysis, to also fully take advantage of the porous nature of the materials chosen.

3.2.1.2. Light Sources

Various options for light sources exist. LED lights are low cost and have a relatively long life span, but light distribution needs to be carefully monitored.[22] Xenon arc lamps can provide the closest reproduction of solar light in the visible region, they also allow for strong lamps with a small surface area and do not break down if switched on and off rapidly. They, however do have a high cost and relatively low lifetime.[23] Mercury lamps are also a popular choice; they are known to warm up more slowly and with slightly lower efficiency that xenon lamps, but with a longer lifetime.[24] Halogen lamps do not weaken over time and require less power to operate, but emit more heat.[25] The best options appear to be xenon lamps due to their best spectral matching or LED lamps for good spectral matching but decreased cost. Testing should be corrected for 1 sun illumination for best standardisation. Light intensity and type can have a large impact on carbon dioxide photocatalysis as it directly impacts the photon flux in the reaction. It is especially important when calculating the apparent quantum yields (AQY) of the reactions, since both the power of the lamp and the wavelength must be carefully controlled in order to obtain a true photon energy value shone on the material.[26] Döscher *et al* highlight in their work the importance of area definition, illumination source configuration information to be present, and IPCE confirmation of the solar-generated potential.[27]

3.2.1.3. Reactors

Not only are volume, material, and design important, but also the kind of reactor chosen to match an experiment. Slurry reactors are defined by a gas-liquid system, whereby the solid catalyst is in suspension and stirred vigorously with the reactants. The air is replaced by carbon dioxide (in a carbon dioxide reaction) or with inert atmosphere in hydrogen evolution. In order to recover the catalyst, either filtration or centrifugation are required. [28] Fixed bed reactors are normally used in the gas phase, and required a powder to be attached to some form of support, such as a glass substrate, and gas is pumped through the reactor.[29] Monoliths reactors which contain materials supported by an inert channels structure have been shown to increase reaction rate over a single support fixed cell, but are not as easy to clean and make, and light perforation

is also limited.[30,31]The reactor type should be reported, as it can also have a large effect on measurements. The way the reactor is incorporated, with testing in batch or in flow or in a recycling environment should also be pointed out. When noting results, a blank with only the support should be run for calibration to ensure no impurities are present in the reactor.[32,33]

3.2.1.4. Temperature

Chen *et al*, observed the temperature dependence of TiO_2 in photocatalysis. It was found that under 50 ^oC the rate of reaction was directly proportional to the reaction temperature, likely due to faster movement of free charge carriers, higher mobility, and possibly better adsorption of reactants. However, at higher temperatures other factors such as catalyst degradation and increased recombination can have a negative effect on product formation.[34] Wang *et al* found that in methanol production using TiO_2, the rate also increased with increased temperature, due to faster desorption of the product from the catalyst active sites.[35] In general, shining solar light on a reactor over long periods of time is likely to increase the temperature, depending on the intensity of light and light source. For this reason, temperature should be monitored in a reaction, and techniques such as using a cooling jacket, or a condenser equipped reactor, and using materials which will maintain the temperature better should be techniques employed in photocatalysis.[36]

3.3. Set-up Building and Optimisation for CO_2 Photocatalysis

Considering the testing set-ups and conditions employed in literature and factors explained in section 3.2.1, a testing set-up design was proposed and built.[33,37] This section will focus on explaining the set-up.

3.3.1. Set-up design and operation

3.3.1.1. Parts

Tubing: specially cleaned stainless steel was used, to reduce any impurity possible: stainless steel is very stable, which decreases contamination from the metal itself; the special cleaning removed any lubricant impurities from factory production. These are often carbon based and could be a potential source of contamination.

Valves and parts: specially cleaned and in stainless steel. Check valves were employed after each mass flow controllers (MFC) to ensure no back-flow of gasses and doubled up as relief valves in case of pressure build up.

Sizing: from the gas lines and regulators to MFCs, 1/8-inch outer diameter (OD) was used, due to its flexible but sturdy nature. From the MFC to *V6*, ¼-inch OD sizing was utilized to give structure to the set-up and stop it from moving. 1/8-inch OD was employed again after V6, to minimize the volume of the tubing compared to the reactor, while also keeping a somewhat firm structure.

Connections: almost all connections were standard Swagelok, to ensure gas tightness. Ultra torr connections were used on either side of the reactor, so that it could easily be removed or replaced, while still maintaining a gas tight seal due to the o-ring present in ultra torr connections. Similarly, ultra torr was used on the metal to glass connection of the scroll pump, as is standard for a gas tight connection from metal to glass, again due to the thick o-ring. NPT connection with a special O_2 safe tape was used for the pressure gauge. Thread connectors with an o-ring were used on the MFC, which also doubled up as size adaptors to change from 1/8" to 1/4".

Mass Flow Controllers (MFCs): MFCs were obtained from Cole Parmer, with ±0.0005 ml/min precision, to obtain as accurate ratios as possible. They were employed to firstly control the flow rates going into the set-up, to keep with safety regulations and prevent overpressure or pressure build up. Secondly, they allowed for flow rate monitoring and setting to change gas ratios.

3.3.1.2. Set-up diagram

A schematic of the built set-up is shown in **Figure 3.1**. The "*V*" labels refer to valves in the system. A photograph of it is shown in **Figure 3.2**.

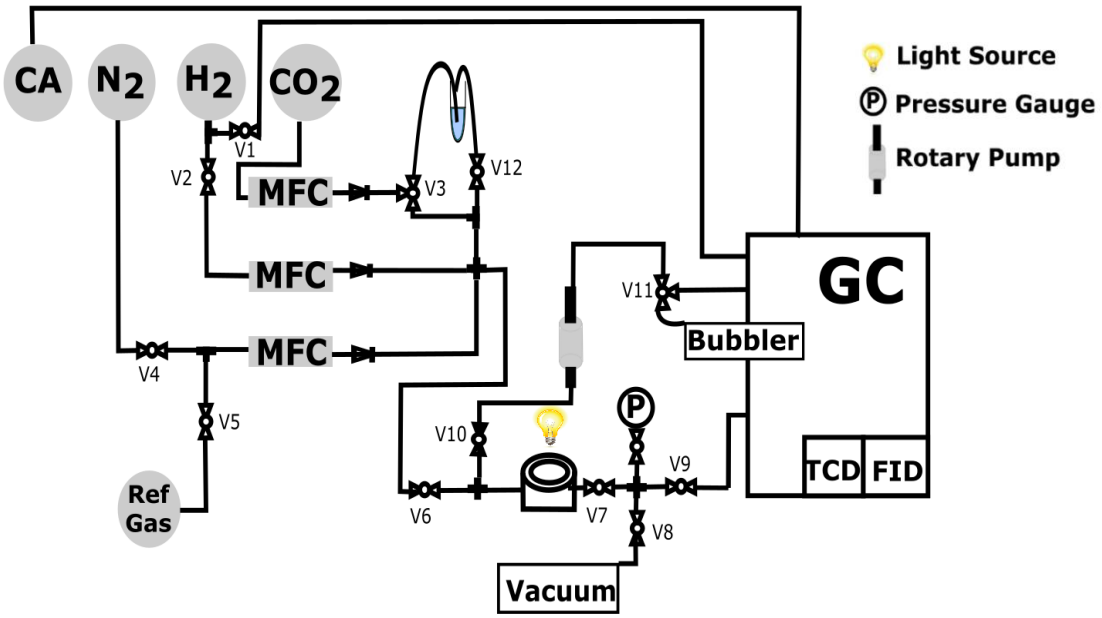


Figure 3.1: Schematic of the CO_2 photocatalysis set-up

To load an experiment, Schlenk techniques were utilized. A sample would be loaded into the reactor, *V6* would remain closed, *V11* would point into the scroll pump, not the bubbler, and *V8* would be opened to apply vacuum. To fill up the reactor, the wanted ratio would be set on the H_2 and CO_2 MFCs, *V3* would point towards the set-up rather than the bubbler. *V8* would then be closed and *V6* opened until atmospheric pressure would be reached. This process would be repeated 6-7 times.

By turning *V11* towards the bubbler and closing off *V10*, the pump would be bypassed. This would allow for either a flow through system, a continuous recycling system or a batch system. A flow through system would involve keeping *V9* open to allow bubbling out of the gasses. This, however, is not recommended for organic materials, due to the low activity so far compared to the sensitivity of the GC. Batch process would involve keeping *V10* closed, closing *V9* until the desired pressure was reached, then *V6* would be closed. Then *V7* would be closed, and the light turned on. Once the required time had passed, *V8* would be opened to evacuate the volume between *V7* and *V9*. It would then be filled by opening *V7* until equilibration, followed by injection into the GC. The batch process was useful for initial rate and to see initial activity of a sample and quick control experiments, but continuous operation was preferred for porous materials and for better kinetic runs and decreased human error, since manual valve opening was not required.

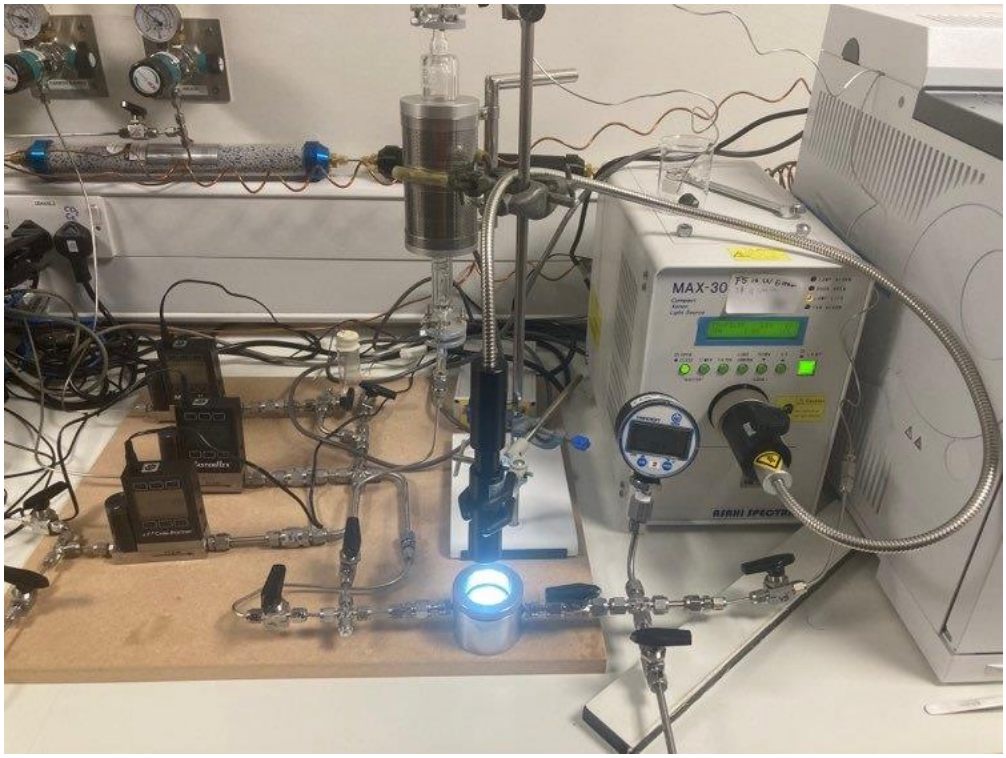


Figure 3.2: Picture of the built set-up, under 1 sun illumination

3.3.1.3. Light source

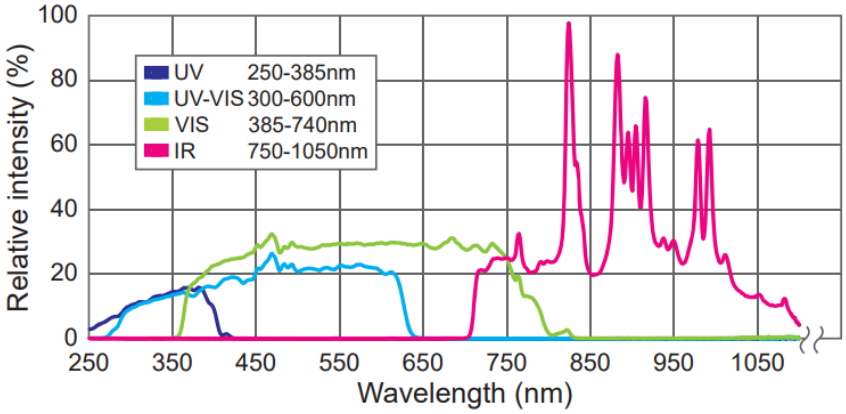
In order to calibrate light intensity to 1 sun, a UV-Vis filter with 300 nm cut-off was utilised. Although this was suitable for the polymers in these projects, the filters should be matched to the absorbance of the material needed, if not within the main UV-Vis region. **Figure 3.3** shows a picture of the lamp chosen for this set-up.



Figure 3.3: Asahi 303-Max Xenon Lamp, image taken from[38]

The incident light intensity was calibrated to 1 sun using a silicon photodiode.

a)



b)

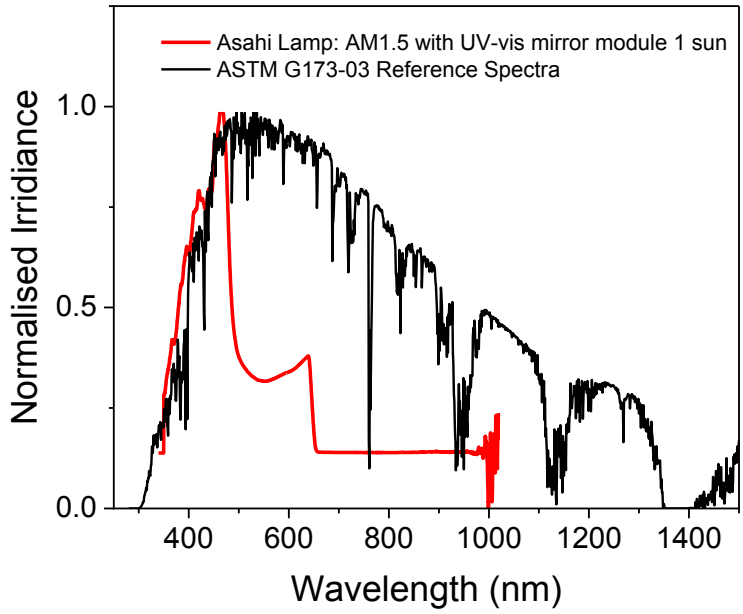


Figure 3.4: a) Spectrum with various filter for Asahi 303-Max Xenon Lamp, image taken from [39]. b) mirror module obtained experimentally with Asahi Lamp using UV-Vis filter, compared to Reference Air Mass 1.5 Spectra obtained from[40]

The light spectra obtained from using various cut-off filters available is shown in **Figure 3.4a).** The lamp also allowed for the insertion of monochromatic filters, which were particularly useful for AQY measurements. in **Figure 3.4b)** shows the comparison of the mirror module obtained experimentally with the available reference spectra of AM 1.5, obtained from ASTM G-173-03 from NREL.[41]. The spectra match in the areas of polymer absorbance, and the light source mirror module should be reported for each light source used to ensure repeatability in measurements. This filter was suitable for the polymers used, since it matches AM 1.5 in the areas at which polymers absorb, but could be changed if materials with different absorption maxima are tested.

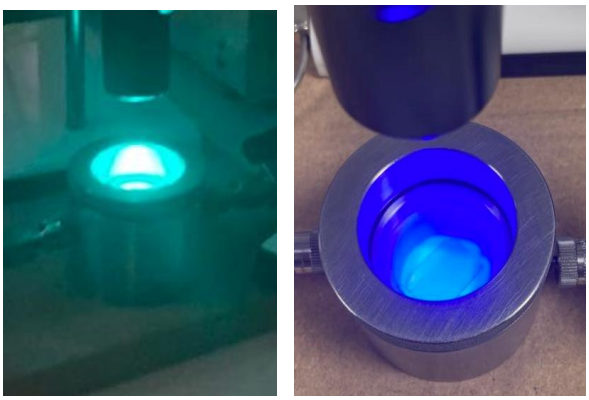


Figure 3.5: Reactor under light with a) 500 nm filter b) 450 filter

Figure 3.5 shows the reactor under two different light illuminations using 500 and 450 nm filter, for AQY measurements. For AQY measurements, light irradiance was measured using a calibrated spectrometer (Ocean Optics USB2000 calibrated with an Ocean Optics DH3-plus light source) fitted with a fibre optic cable and a 0.4778 cm^2 cosine corrector.

3.3.1.4. Temperature, Pressure and Gas Flow

The temperature was measured using a thermocouple attached to the set-up, in standard reactions under 12 hours of light illumination. It was found that the temperature rise was negligible, likely due to the gas-phase nature of the testing. When water, which has a greater heat capacity than hydrogen, was used to test for slurry reactor potential, the temperature rose and condensation was observed, therefore a cooling jacket needed to be fitted. Since the thermocouple was not fully gas tight, after ensuring no temperature change in the standards, the thermocouple was not used in final measurements. The reactions were kept at room temperature (21 ^oC) The pressure chosen in gas phase testing for the continuous reactor was 1.15 bar. This was a trade-off between a slight overpressure to increase the penetration of carbon dioxide into active sites, and wanting to keep a low overall pressure to drive down costs in scalability, and because the scroll pump used worked best at lower pressures.[42] Knowing the exact gas flow would be critical in a flow through system, since the volume of gas per minute would be used to calculate the moles of gas going into the reactor, and therefore would be used to figure out the rate of reaction.[43] However, since the products in this study were obtained in too low amounts to detect in a flow through system, and since it was beneficial to close the system and recycle the gas through, the absolute value of gas flow was not required. What was more important in the MFCs was the ratio of flow rates, in order to control the ratios of

hydrogen and carbon dioxide in the reactor. Heuristically a 1:3 ratio of CO_2:H_2 was chosen, since these are the ideal conditions for CO production.



Figure 3.6: scroll pump obtained from Makuhari Messe Co., Ltd.[44]

Figure 3.6 showed the scroll pump chosen for the experiments, it was secured with small clamps at the o-ring ball joint and Swagelok pipe reducer, the wire was attached to a controller which enabled control of the electromagnet speed, which moved the piston in the pump.

3.3.1.5. Reactor design

One of the main aims for reactor design was to obtain a flexible reactor that could be used in the gas and liquid phase and could withstand high pressures if required.

Important parameters that were considered when designing the reactor were:

- catalyst surface area
- volume
- ease of use (opening and closing, removing, and loading samples)
- gas tight

The reactor was designed by the author and build by KAUST mechanical workshop. **Figure 3.7** shows the drawing of the reactor design used to build it, and **Figure 3.8** shows the picture of the finished reactor. A fixed bed style of reactor was chosen due to the ease of loading and unloading materials.

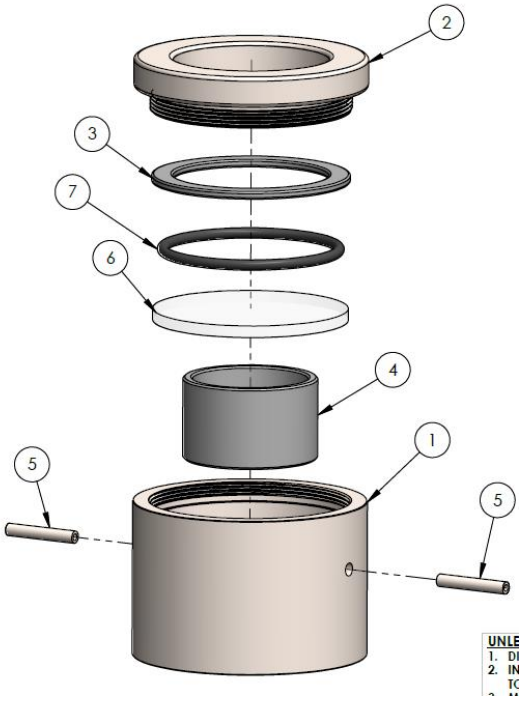


Figure 3.7: schematic of reactor design

Where:

1) reactor tube in stainless steel (SS 316)- (KAUST Workshop custom made)
2) cap in stainless steel- (KAUST Workshop custom made)
3) locking ring - PTFE (KAUST Workshop custom made)
4) Liner – PTFE (KAUST Workshop custom made)
5) Tube in 1/8" inch SS 316 (Swagelok)- to be connected with gas tight, removable Swagelok connections.
6) Quartz Window (UQG Optics- fused quartz window 5 cm diameter, 3 mm thickness)
7) Viton Rubber Ring (Viton 75)



Figure 3.8: Pictures taken of the reactor.

The volume of the reactor was calculated by placing an ultra-torr connection to the cross between *V6*, *V10* and *V7*, and attaching a glass tube with a valve of known volume. The change in pressure was monitored and the unknown volume was calculated via simultaneous equations. This was done at various starting pressures to decrease error. This method was used both for the looped set-up volume and the batch reactor volume (153 cm^3 and 18.5 cm^2 respectively).

3.3.1.6. Calibration and GC detection

The gasses present in the calibration gas, and information on how these were detected is summarised in **Table 3.1**

Table 3.1: Calibration Gas composition and GC detection limits

Compounds	**Concentration (ppm)**	**Detection Limit (ppm)**	**Detector**
H_2	1000	50	TCD
O_2	1000	50	TCD
CO_2	1000	n/a	n/a
CO	1000	5	FID
CH_4	1000	5	FID
N_2	Balance	n/a	n/a

The flame ionisation detector (FID) requires a flow of hydrogen and air (which supplies oxygen) that are ignited to supply a flame. The sample taken from the GC is broken down by the flame into ions. These in turn are collected on an electrode and produce and electrical signal. The advantages are its very high sensitivity and range of hydrocarbons it can detect. However, it does destroy the sample, and it cannot detect a carbon that does not contain hydrogen. Therefore, to detect carbon monoxide, the FID was equipped with a Jetanizer. A Jetanizer is a type of methanizer, which catalytically converts CO and CO_2 to methane, so that it can be detected on the FID. Since it does this directly at the FID, the column separation is observed as expected. The Jetanizer was chosen because it required no added parts or space, it contained no toxic metals (no nickel like a standard methanizer) and the installation was very quick and easy into the Agilent GC.[45] A thermal conductivity detector (TCD) compares the thermal conductivity of the sample to the carrier gas, and when a change is detected, a signal is produced. Using this detector in nitrogen is still useful, but the sensitivity is reduced compared

to a carrier gas such as helium or hydrogen. The FID was therefore relied on more heavily for the products obtained. [46] The GC was equipped with two columns, a Porapak and a MoleSieve. The first was used to start the gas separation of CO_2, CO and CH_4. Since the MoleSieve columns can be blocked by CO_2, a vent was put in place at the retention time of CO_2 so that it would not pass onto the MoleSieve. This second column was used to separate hydrogen and oxygen.[47] By altering the post run time, it was possible to set the GC to inject into the column loop from the reactor loop once per hour, making the photocatalysis process automated after sample loading.

3.3.1.7. Batch vs loop testing

The main method that was adopted to obtain results was the continuous flow recycling method explained above, which enabled the recycling of gasses and required the use of a scroll pump. However, the set-up was initially used in batch process. This is because it was much faster to check the set-up was functioning correctly and a good way to begin preliminary testing. The recycling method and batch processes yielded different results in magnitude. This is partly due to the larger volume, the circulating of gasses, and longer reaction times. The absolute number of moles of products was calculated by calibrating against the reference gas.

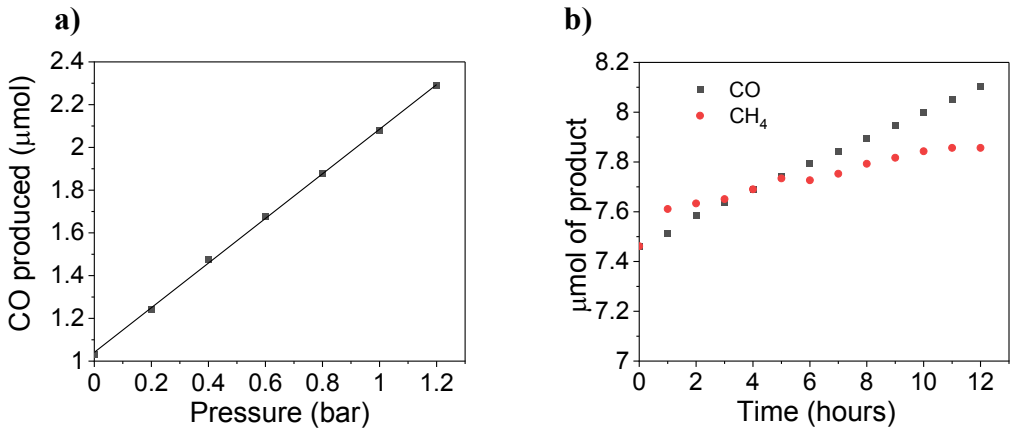


Figure 3.9: Calibration graphs for a) batch process, b) continuous process

Figure 3.9 shows the batch vs recycling calibrations. Since the batch process required different pressures, the reference gas was detected at different pressures and a gradient was calculated, the value of which was used to calibrate the results from the batch process. The recycling process was kept at the same pressure, but a slight increase could be seen due to a small amount of nitrogen entering the loop at each injection. This number was negligible, but the values obtained are shown in **Figure 3.9b).**

For the batch process, *V10* was closed off and *V11* was set to bubbler. *V9* and *V8* would be closed, but *V7* open. Gas would be flowed through by opening *V6* and, then using Schlenk techniques again by evacuating using *V8.* After several cycles, the pressure would be allowed to climb to 2 bar (higher pressure than the recycling process in order to be able to inject into the GC). *V7* and *V6* would then be shut and illumination would begin, making a closed system. After a reaction time of at least 3 hours, the volume betweeen *V7* and *V9* would be evacuated. Then *V7* could be opened until the pressure was equalised, and then closed. Then *V9* could be openeied while pressing the inject button manually on the GC. The gas would flow through the bubbler, until no bubbling was observed prior to injection so the pressure would be equalised each time.

3.3.1.8. Titanium Dioxide

TiO_2 was the breakthrough catalyst first reported in the 1970s by Honda and Fujishima for photocatalytic water splitting.[48] Since then, it has been used as a benchmark material in photocatalysis. It's abundant, low toxicity, electronic properties and high stability have made it the most studied photocatalyst so far, by itself, in different forms or doped, as a support and using other catalysts with it.[49,50] Importantly for this study it has also been used in direct hydrogenation of CO_2, which is of particular interest since the set-up was optimised for these same conditions.[51] Lo *et al* obtained a yield of around 1.1 $\mu molg^{-1}h^{-1}$ of CO in a hydrogen and carbon dioxide atmosphere similar to that presented in this study.[52] Much higher numbers have been reported, in the magnitude of mmol, when thermo-assisted conditions were used.[53,54] In this study, commercially available P25 TiO_2 was used to ensure the set-up was working correctly and as a comparison to other set-ups and testing conditions. It should be noted that TiO_2 is primarily a UV light absorber, since part of the UV spectrum is cut off in the set-up presented, a slightly lower rate than reports that employ UV light can be expected.

3.3.2. Solution Testing

The studies presented in this thesis focused on gas-phase testing, and the set-up was designed with this in mind. However, the set-up was also designed to be flexible, and solution testing was attempted, as a comparison to gas phase and other reactors.

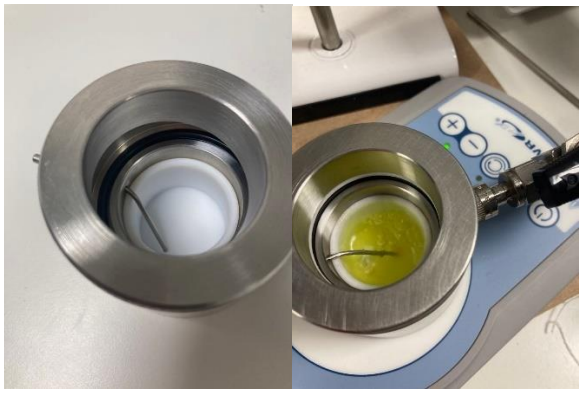


Figure 3.10: Depicting additional piece of metal for gas bubbling inside the reactor for solution-based testing.

In order to do this, a thin piece of 1/16-inch OD stainless steel was placed inside the reactor so that carbon dioxide could be bubbled through the solution, as shown in **Figure 3.10**. In order to evaluate the perfomance of the reactor, a covalent organic framework (COF) from literature was synthesied by Dr Catherine Aitchison, and used in the study, **Bpy-sp^{2}c-COF.** [55]

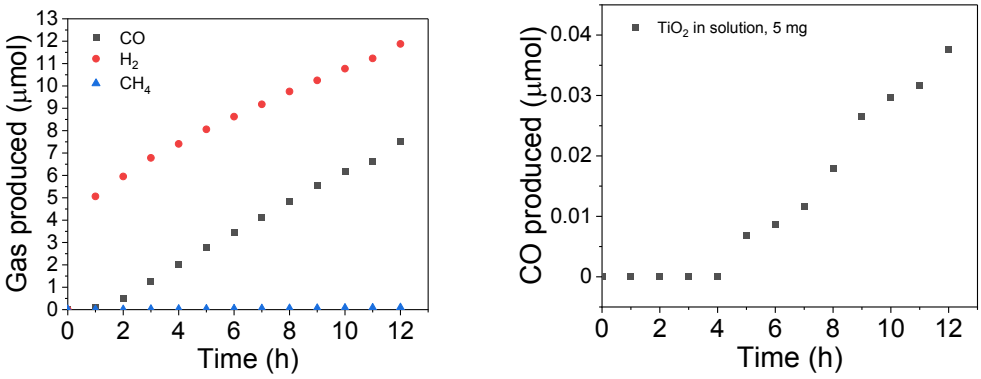


Figure 3.11: a) Performance evaluation of **Bpy-sp^{2}c-COF** in the solution phase version of the reactor. b) Performance evaluation of **TiO_2** in the solution phase version of the reactor

The performance of **Bpy-sp^{2}c-COF** was evaluated in the reactor and is presented in **Figure 3.11a)**. The conditions for solution based experiments, including the cobalt based co-catalyst, and solvent system have been previously optimised in literature, and have shown success with other organic materials, and were therefore utilised in this study as a means to evaluate performance.[56] Cobalt based co-catalysts have shown promise not just in the studies mentioned, but also in electrocatalysis for the reduction of CO_2.[57]

The conditions were the COF (5 mg), $CoCl_2$ (1 μmol), 2,2′-biyridine (2 mg) solvent (4 mL, MeCN/H_2O = 3 : 1), TEOA (1 mL), in a CO_2 atmosphere we stirred vigorously, using the recycling system equipped with the scroll pump. By calculating the slopes of the reactions, the average rates were calculated: CO was 137 $\mu molg^{-1}h^{-1}$, H_2 was 119 $\mu molg^{-1}h^{-1}$ and CH_4 was 1.6 $\mu molg^{-1}h^{-1}$. Taking the initial rate of hydrogen production, would give a rate of 480 $\mu molg^{-1}h^{-1}$. In literature the rate was around 500 $\mu molg^{-1}h^{-1}$. Considering the difference in conditions and lack of further optimisation this shows a good comparison to literature for materials tested in this reactor for solution phase photocatalysis. TiO_2 was evaluated in the same manner, the rate of CO is shown in **Figure 3.11b)**. The rate obtained was 0.9 $\mu molg^{-1}h^{-1}$, which is also comparable to other reactors and conditions, especially when optimisation was not done.[5811] For example, in water, Kočí *et al* report a yield of around 0.1 $\mu molg^{-1}h^{-1}$ CO production for a particle size of around 29 nm of TiO_2. [59]

For aqueous systems, **Figure 3.12** shows a typical graph obtained when comparing the rate of a reaction to the concentration of a reaction. By looking at curve, C, a plateau is reached around point B. After this, the rate remains the same, no matter the photocatalyst concentration. If the rate after the plateau was corrected for the amount of photocatalyst, there would be a decrease in rate per gram as photocatalyst concentration increases, which is misleading and highlights the importance of taking care when correcting by mass, even in solution testing.

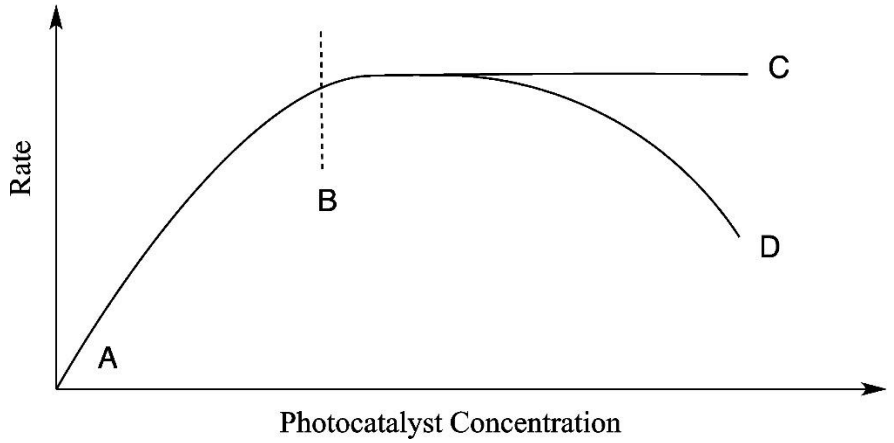


Figure 3.12: Figure reproduced from ref [60] with permission, showing a typical rate of reaction dependency on photocatalyst concentration.

3.3.3. Calculations

3.3.3.1. Calculations for reactor volume

The reactor volume was calculated by attaching a Schlenk tube of known volume and with a known pressure to the system, opening the system to it, monitoring the change in pressure and

from that calculating the unknown volume of the system. For the batch process, which excludes the GC and scroll pump, the total volume was 22 cm^3. For the recycling process the total volume was calculated to be 153 cm^3.

3.3.3.2. Calculations for number of moles

To calculate the number of moles in the reactor, the area of each peak in the GC was used and compared to the same peak given by the reference gas, which was of a known concentration. **Figure 3.13** shows a typical chromatogram of the reference gas, showing the retention times. The top chromatogram is produced from the FID and the bottom from the TCD. The sharp peaks at 1.3 and 2 min are from the quick valve change produced when venting out most of the carbon dioxide.

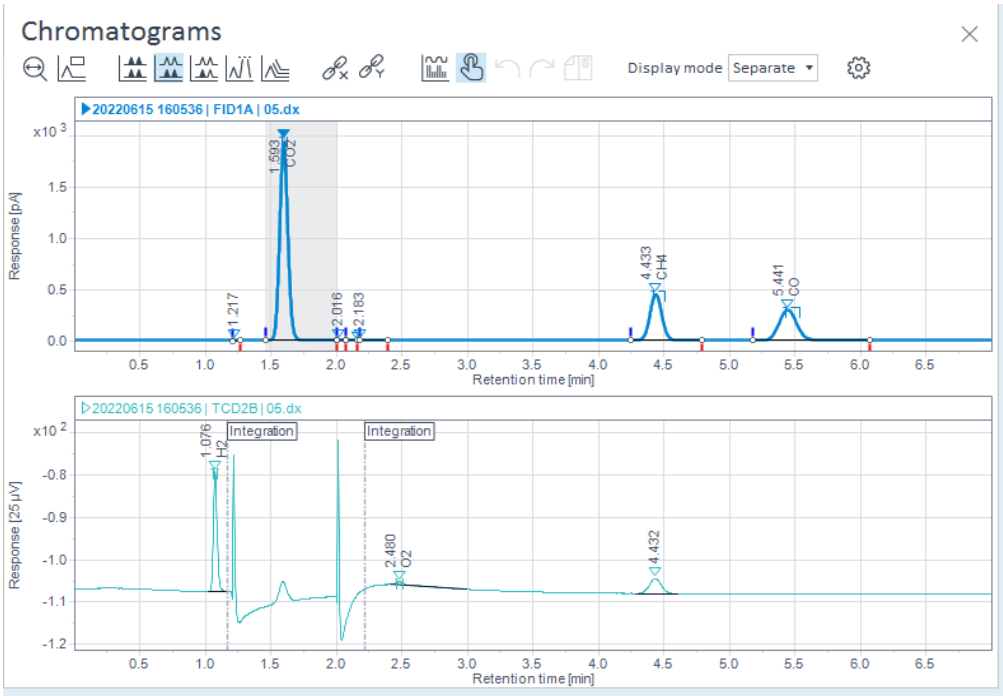


Figure 3.13: Chromatogram of the reference gas mixture, top from FID, bottom from TCD

The moles were calculated using the equations below:

$$moles\ in\ the\ reactor = \frac{pressure * volume\ of\ reactor}{RT} \tag{3.1}$$

Where R, the gas constant, was 8.314 JK^{-1} mol^{-1}. and T was temperature in Kelvin, pressure was measured in Pascals and the volume in m^3. The percentage of that volume taken up by a product gas, in this case CO is used as the example, was calculated as a ratio to the 1000 ppm reference peak of that same gas.

(3.2)

$$\%\ of\ CO = \frac{0.1}{area\ of\ CO\ in\ ref\ gas} * area\ of\ CO\ in\ sample$$

And finally, the moles of CO were calculated by:

$$moles\ of\ CO = \frac{moles\ in\ reactor}{100 * \%\ of\ CO} \quad (3.3)$$

The final number was converted to μmol as a more convenient unit.

3.3.3.3. Calculations for AQY

Ali *et al'*s overview on Benchmarking for Gas phase CO_2 photocatalysis offers great insight into the best ways of reporting readings, as well as detailing important factors affecting measurements.[33] Currently, different parameters are used for reporting photocatalysis results, both in carbon dioxide photoreduction and in hydrogen evolution. To truly be able to compare organic materials, it is imperative to standardize the reporting of results. To do this, Ali *et al* 's suggestion of using the value AQY seems to be a good way to incorporate the most important factors that affect photocatalysis, since this value comprises incident photons, reactor size, catalyst amount and electrons used up. AQY (%) is measure of how many incident photons excite electrons which then react to make products. It is calculated as a percentage of reacted electrons vs incident photons, as shown below[6162]

$$AQY\ (\%) = \frac{reacted\ electrons}{incident\ photons} X\ 100 \quad (3.4)$$

$$AQY\ (\%) = \frac{(m)\ x\ n\ xNa\ x\ h\ x\ c}{I\ x\ A\ x\ T\ x\ \lambda} X\ 100 \quad (3.5)$$

m = moles of products, n = no of electrons required to make a mole of product, N_A is Avogadro constant (6.022×10^{23}/mol), H is the Planck constant (6.626×10^{-34} J·s), c is the speed of light (3×108 m/s), A is the irradiation area (m^2), I is the intensity of irradiation light (Wm^{-2}), t is the photoreaction time (s), is the wavelength of the monochromatic light (nm).

3.3.3.4. Calculations for Selectivity

Specific product quantum yield (SPQY) should also be reported to show the selectivity of the reaction, using the equation below.

$$SPQY\ (\%) = \frac{\#electrons\ required\ per\ molecule * no\ of\ molecules\ of\ product}{number\ of\ incident\ photons} X\ 100 \quad (3.6)$$

For example, in the case of the specific product quantum yield of carbon monoxide, the calculation would be as below: (3.7)

$$SPQYco\ (\%) = \frac{2*no\ of\ molecules\ of\ product1}{number\ of\ incident\ photons} X\ 100$$

3.4. Reporting Results- Evaluating Performance

3.4.1. Units, mass, and surface area corrections

Active sites are critical in photocatalysis, the ability to identify the number of active sites can help quantify catalytic behaviour, especially in TON and TOF calculations. Although an increased surface area does tend to enhance photocatalytic rate due to an increased number of active sites, surface area measurements such as BET cannot be used, since they would assume the entire area is an active site.[63] However, even though the number of possible active sites might increase, the rate also heavily depends on diffusion of the reactants, mobility and longevity of charges, and illumination. Reporting as a function of illuminated area is therefore more reliable and beneficial. Ollis *et al*'s study looked at expressions relating reactor design to variables affecting photocatalytic reaction rate. With gas phase reactors, once optical density becomes substantial, accessibility of light is reached. Therefore the activities cannot be compared by illuminated mass, but by surface area.[64]

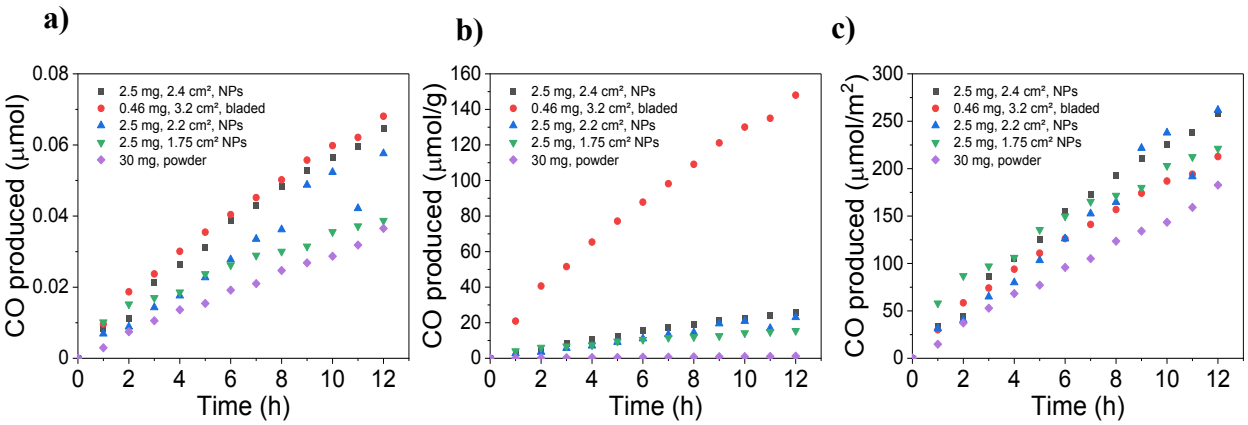


Figure 3.14: Graphs obtained of the formation of CO from TiO_2. a) shows the performance as µmol over time, b) is corrected for mass in g, c) is corrected for surface area in m^2.

This is reflected in **Figure 3.14**, whereby TiO_2 was tested at different masses and surface areas. **Figure 3.14b)** shows that correcting by mass skews the performance vastly, while correcting

by area (**Figure 3.14c**) is a better comparison. Since surface area and mass both can drastically change the performance rate numbers when reported, the most ideal approach for result reporting, when possible, would be to keep mass and surface area completely constant, and show a graph comparison of the µmol of product produced over time instead, similar to the graph shown in **Figure 3.14a)**. The slopes were used to calculate the rate of reactions of each of the data presented, these are summarised in **Table 3.2**.

Table 3.2: Summary of rates of **TiO_2** samples and **pTA-Ph** with different mass and surface area loadings

Material, mass, and surface area	CO produced ($\mu molh^{-1}$)	CO produced ($\mu molg^{-1}h^{-1}$)	CO produced ($\mu molm^{-2}h^{-1}$)
TiO_2, 2.5 mg, 2.4 cm^2, NPs	0.00536	2.14	21
TiO_2, 0.46 mg, 3.2 cm^2, bladed	0.00539	11.72	17
TiO_2, 2.5 mg, 2.2 cm^2, NPs	0.00466	1.86	21
TiO_2, 2.5 mg, 1.75 cm^2, NPs	0.00286	1.14	16
TiO_2, 30 mg, powder, no support	0.00288	0.10	14
pTA-Ph, 2 mg, 2.9 cm^2	0.019	9.5	66
pTA-Ph, 5 mg, 1.3 cm^2, $CHCl_3$ ppt	0.0077	1.5	60
pTA-Ph, 2 mg, 2.5 cm^2	0.018	8.8	71

A similar experiment was conducted on polymer **pTA-Ph**, to figure out if different methods of precipitation would give different illumination areas, and if these would give different results if corrected by area. This is summarised in **Figure 3.15**. The mass does appear to scale linearly with performance in these cases.

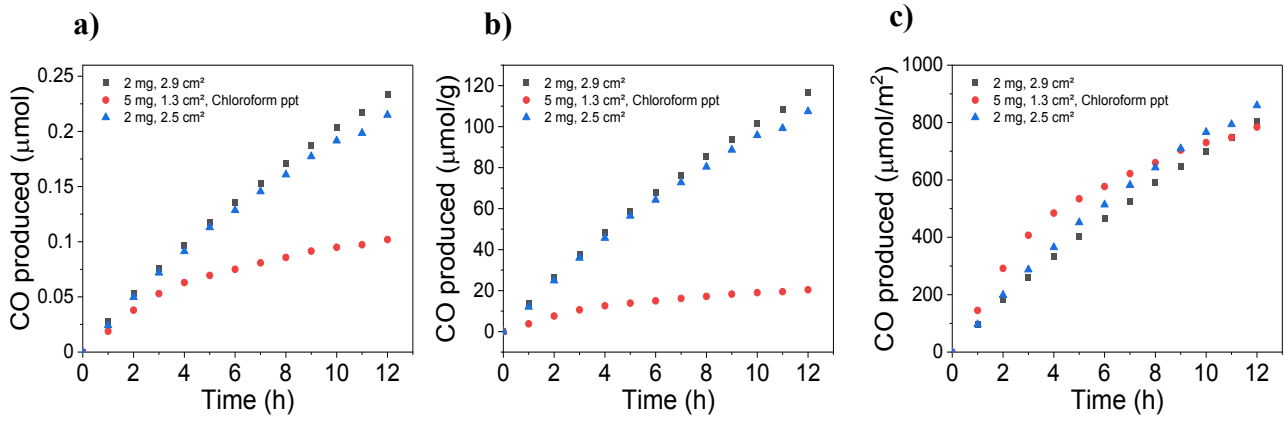


Figure 3.15: Graphs obtained of the formation of CO from **pTA-Ph**. a) shows the performance as µmol over time, b) is corrected for mass in g, c) is corrected for surface area in m^2.

Glass supports were cut to the same sizes in order to help maintain the sample area the same. The drop-cast samples were spread over the surface as much as possible. In order to obtain a good number estimate of the mass, image J was used. A picture of the samples with a ruler was taken to be able to scale the sample. Contrast between colour and white background, allowed for the particle counting and colour threshold to be applied from image J to obtain a better area estimate. This process is show in **Figure 3.16**, a) shows a polymer which was drop-cast but could be peeled off like a membrane, b) and c) show an example of image J grabs, of a sample that did not spread out evenly over the glass substrate.

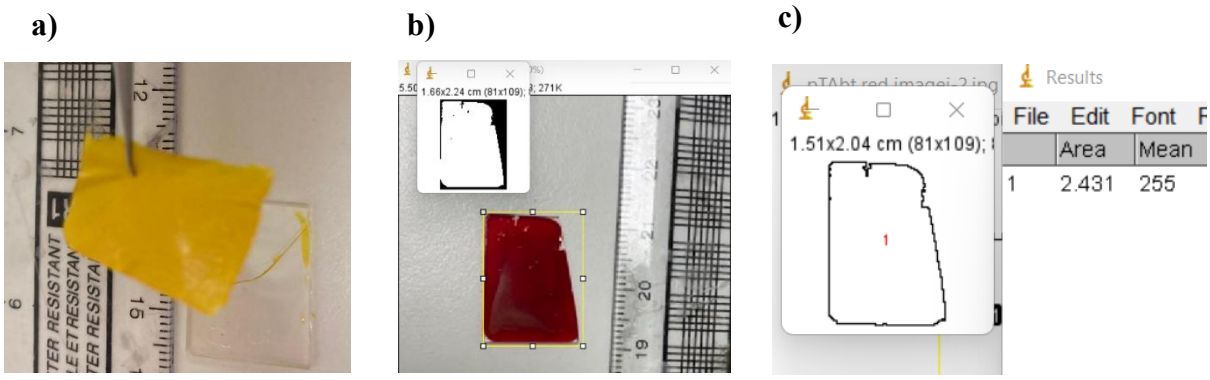


Figure 3.16: examples of polymers on glass substrates a) polymer that could be peeled off its glass support, b) image J grab showing process for area calculation, c) image J grab of calculated area

Recently, a possible new figure of merit was outlined by the Reisner group, the solar to value efficiency (STV) where the value of products and reactants is taken into consideration.[65,66] This could aid with describing solar fuels production as more hydrocarbon and potentially valuable products are produced.

3.4.2. Controls

Some organic materials are known to degrade under sun illumination.[67] Furthermore, it is widely accepted that in carbon dioxide photocatalysis, trapped carbon impurities from processing, or material synthesis can act as a carbon source in the system and can largely inflate the amount of products obtained, since the CO could come from the trapped carbon or carbon impurities, rather than from photocatalytic carbon dioxide reduction.[20,68,69] This issue is likely to decrease in importance as materials become higher performing, since the amounts of products will not be as low as they currently are in the field, (conventionally products are formed on the ppm scale still in this field). However, for now, it is imperative to run control

testing to ensure that the products are coming from photo-reduced carbon dioxide rather than from the degradation of the polymers.

One useful control is isotope labelling. By labelling with $^{13}CO_2$ and H_2 or $H_2{}^{18}O$ going into the reaction vessel and detecting if the products produced contain isotope labelled carbon or oxygen. In order to do this, either a mass spectrometer needs to be equipped to the GC, or enough products must be made that gas phase IR can be used.

Another way is to conduct control experiments which rule out degradation and trapped carbonaceous products. These include:

- Replacing the CO_2 with N_2 but retaining the illumination and H_2 content. No products should be detected.
- Replacing the H_2 with N_2 should also show no results, as hydrogen is necessary for the oxidation half reaction.
- Experiments under dark conditions to ensure the experiment does indeed require light to occur.
- Testing with no substrates to ensure no impurities are present in the set-up, gasses, or residues.

It should also be noted that, to minimise impurities, if the materials are organic, they should be thoroughly purified. If the materials are purely inorganic, carbon-based impurities can be removed by placing in a vacuum oven at high temperatures. This also highlights the importance of a very clean system; metal parts and pipes should be specially fabricated with no lubricants or organic materials, devices should be stored in glass containers, not in plastic. Solvents and gasses used should be of the highest purity. Device preparation is also of paramount importance, and each sample should be thoroughly dried prior to testing, to remove small volatile carbon products or any residual solvents.

3.5. Future Work and Set-up Flexibility

A set-up for carbon dioxide photoreduction in the gas phase was designed, built, and optimised. The set-up was calibrated with reference gas and using commercially available P25 TiO_2. Further chapters will utilise this set-up for material testing and screening. The set-up was built with flexibility in mind, the reactor could be removed at will to facilitate cleaning and to insert a different reactor if required. Solution testing was possible on the set-up as well despite the optimisation towards gas phase. A bubbler is also included in the design ready for future water

vapour experiments. This chapter also touched on results reporting and benchmarking in the field. For gas-phase photocatalysis, correcting for area of the substrate was a more accurate way of reporting rate than correcting by mass of catalyst. Benchmarking in CO_2 photocatalysis without a standardised set-up, illumination, and methodology is very challenging. But disclosing modifications, thoroughly describing experiments, and presenting raw data is certainly a step in the right direction. Comparing systems by testing known compounds is the best method we have for standardisation.

Future work on the set-up would include the incorporation of a trap equipped with a septum, especially if solution-based experiments are continued. This would be to fully protect the column from any water entering the GC and would allow for the removal of any liquid-based products if they are formed. Higher hydrocarbons should certainly be attempted. The incorporation of a mass Spectrometer to the GC for isotope labelling experiments would also be ideal.

3.6. Experimental and Parts

Mass Flow Controllers (MFCs)

Masterflex Proportional Flowmeter Controller, Mass; 50.0 mL/min Masterflex – Item # OU-32907-57 were purchased from Cole Parmer.

GC

The GC was an Agilent 8860 GC Custom System, equipped with FID and TCD detectors, with a series adaptor from the TCD to the FID. A 6-port gas sampling valve and column isolation and a heated automated valve box for 2 valves was chosen. The GC was equipped with two columns, a 6Ft 1/8 2mm Porapak Q 80/100 SST and a 6Ft 1/8 2mm MoleSieve 13X 60/80 SST. Nitrogen was the carrier gas.

Gas circulatory pump

Obtained from Makuhari Messe Co., Ltd, including a Power unit, 200-TN, a 2- Twin-drive magnet, DK-N, and a glass cylinder with Teflon coated plunger 2000N

Vacuum

High vacuum was an Edwards nXDS15i dry scroll pump.

Pressure Gauge

The pressure gauge used was an Ashcroft DG25 Digital Pressure Gauge with Backlight, 0 to 100 psi, fitted with at ¼" VCR fitting, with a threaded oxygen safe tape.

Jetanizer

ARC JT-INT-PK1 Intuvo/8890 was purchased from JSB UK and Ireland Ltd and fitted by the author.

Light Source

Xe lamp (Asahi Max 303) fitted with an ultraviolet–visible mirror module (350–800 nm)

Stirring Plate

The stirring plate used in solution-based experiments was an Edulab ultra-thin ISG magnetic stirrer and was placed underneath the reactor.

Substrate cleaning

the substrates were cut from glass microscope slides using a diamond pen, measuring 1.5 cm x 2cm. The glass slides were filed using sandpaper to achieve more uniform sizing. Image J was used to calculate the coverage.

3.7. References

(1) Bligaard, T.; Bullock, R. M.; Campbell, C. T.; Chen, J. G.; Gates, B. C.; Gorte, R. J.; Jones, C. W.; Jones, W. D.; Kitchin, J. R.; Scott, S. L. Toward Benchmarking in Catalysis Science: Best Practices, Challenges, and Opportunities. *ACS Catal.* **2016**, *6* (4), 2590–2602. https://doi.org/10.1021/ACSCATAL.6B00183/ASSET/IMAGES/LARGE/CS-2016-00183B_0008.JPEG.

(2) Indrakanti, V. P.; Kubicki, J. D.; Schobert, H. H. Photoinduced Activation of CO2 on Ti-Based Heterogeneous Catalysts: Current State, Chemical Physics-Based Insights and Outlook. *Energy Environ. Sci.* **2009**, *2* (7), 745–758. https://doi.org/10.1039/b822176f.

(3) Chen, D.; Zhang, X.; Lee, A. F. Synthetic Strategies to Nanostructured Photocatalysts for CO 2 Reduction to Solar Fuels and Chemicals. *J. Mater. Chem. A Mater. energy Sustain.* **2015**, *3*. https://doi.org/10.1039/c5ta01592h.

(4) Corma, A.; Garcia, H. Photocatalytic Reduction of CO2 for Fuel Production: Possibilities and Challenges. *J. Catal.* **2013**, *308*, 168–175. https://doi.org/10.1016/j.jcat.2013.06.008.

(5) Yang, C.; Huang, W.; da Silva, L. C.; Zhang, K. A. I.; Wang, X. Functional Conjugated Polymers for CO_2 Reduction Using Visible Light. *Chem. - A Eur. J.* **2018**, *24* (66), 17454–17458. https://doi.org/10.1002/chem.201804496.

(6) Piontek, S.; Junge Puring, K.; Siegmund, D.; Smialkowski, M.; Sinev, I.; Tetzlaff, D.; Roldan Cuenya, B.; Apfel, U. P. Bio-Inspired Design: Bulk Iron–Nickel Sulfide Allows for Efficient Solvent-Dependent CO2 Reduction. *Chem. Sci.* **2019**, *10* (4), 1075–1081. https://doi.org/10.1039/C8SC03555E.

(7) Peng, Y.; Szeto, K. C.; Santini, C. C.; Daniele, S. Ionic Liquids as Homogeneous Photocatalyst for CO2 Reduction in Protic Solvents. *Chem. Eng. J. Adv.* **2022**, *12*, 100379. https://doi.org/10.1016/J.CEJA.2022.100379.

(8) Ramdin, M.; De Loos, T. W.; Vlugt, T. J. H. State-of-the-Art of CO 2 Capture with Ionic Liquids. *Ind. Eng. Chem. Res.* **2012**, *51* (24), 8149–8177. https://doi.org/10.1021/ie3003705.

(9) Chen, Y.; Ji, G.; Guo, S.; Yu, B.; Zhao, Y.; Wu, Y.; Zhang, H.; Liu, Z.; Han, B.; Liu, Z. Visible-Light-Driven Conversion of CO2 from Air to CO Using an Ionic Liquid and a Conjugated Polymer. *Green Chem.* **2017**, *19* (24), 5777–5781. https://doi.org/10.1039/c7gc02346d.

(10) Lin, J.; Ding, Z.; Hou, Y.; Wang, X. Ionic Liquid Co-Catalyzed Artificial Photosynthesis of CO. *Sci. Reports 2013 31* **2013**, *3* (1), 1–5. https://doi.org/10.1038/srep01056.

(11) Dimitrijevic, N. M.; Vijayan, B. K.; Poluektov, O. G.; Rajh, T.; Gray, K. A.; He, H.; Zapol, P. Role of Water and Carbonates in Photocatalytic Transformation of CO 2 to CH4 on Titania. *J. Am. Chem. Soc.* **2011**, *133* (11), 3964–3971. https://doi.org/10.1021/JA108791U/SUPPL_FILE/JA108791U_SI_001.PDF.

(12) Yang, C.; Huang, W.; da Silva, L. C.; Zhang, K. A. I.; Wang, X. Functional Conjugated Polymers for CO2 Reduction Using Visible Light. *Chem. - A Eur. J.* **2018**, *24* (66), 17454–17458. https://doi.org/10.1002/chem.201804496.

(13) Nogueira, A. E.; Oliveira, J. A.; da Silva, G. T. S. T.; Ribeiro, C. Insights into the Role of CuO in the CO2 Photoreduction Process. *Sci. Rep.* **2019**, *9* (1), 1316. https://doi.org/10.1038/s41598-018-36683-8.

(14) Mureithi, A. W.; Sun, Y.; Mani, T.; Howell, A. R.; Zhao, J. Impact of Hole Scavengers on Photocatalytic Reduction of Nitrobenzene Using Cadmium Sulfide Quantum Dots. *Cell Reports Phys. Sci.* **2022**, *3*, 100889. https://doi.org/10.1016/j.xcrp.2022.100889.

(15) Das, R.; Chakraborty, S.; Peter, S. C. Systematic Assessment of Solvent Selection in Photocatalytic CO2Reduction. *ACS Energy Lett.* **2021**, *6* (9), 3270–3274. https://doi.org/10.1021/ACSENERGYLETT.1C01522/ASSET/IMAGES/LARGE/NZ1C01522_0003.JPEG.

(16) Lopis, A. D.; Choudhari, K. S.; Sai, R.; Kanakikodi, K. S.; Maradur, S. P.; Shivashankar, S. A.; Kulkarni, S. D. Laddered Type-1 Heterojunction: Harvesting Full-Solar-Spectrum in Scavenger Free Photocatalysis. *Sol. Energy* **2022**, *240*, 57–68. https://doi.org/10.1016/J.SOLENER.2022.05.022.

(17) Olivo, A.; Ghedini, E.; Signoretto, M.; Compagnoni, M.; Rossetti, I. Liquid vs. Gas Phase CO2 Photoreduction Process: Which Is the Effect of the Reaction Medium? *Energies* **2017**, *10* (9), 1394. https://doi.org/10.3390/en10091394.

(18) Detz, R. J.; Reek, J. N. H.; Van Der Zwaan, B. C. C. The Future of Solar Fuels: When Could They Become Competitive? *Energy Environ. Sci.* **2018**, *11* (7), 1653–1669. https://doi.org/10.1039/c8ee00111a.

(19) Van-Dal, É. S.; Bouallou, C. Design and Simulation of a Methanol Production Plant from CO2 Hydrogenation. *J. Clean. Prod.* **2013**, *57*, 38–45. https://doi.org/10.1016/j.jclepro.2013.06.008.

(20) Izumi, Y. Recent Advances in the Photocatalytic Conversion of Carbon Dioxide to Fuels with Water and/or Hydrogen Using Solar Energy and Beyond. *Coord. Chem. Rev.* **2013**, *257* (1), 171–186. https://doi.org/10.1016/j.ccr.2012.04.018.

(21) Lange, J. P. Methanol Synthesis: A Short Review of Technology Improvements. *Catal. Today* **2001**, *64* (1–2), 3–8. https://doi.org/10.1016/S0920-5861(00)00503-4.

(22) Jo, W. K.; Tayade, R. J. New Generation Energy-Efficient Light Source for Photocatalysis: LEDs for Environmental Applications. *Ind. Eng. Chem. Res.* **2014**, *53* (6), 2073–2084. https://doi.org/10.1021/IE404176G/SUPPL_FILE/IE404176G_SI_001.PDF.

(23) Finlayson-Pitts, B. J.; Pitts, J. N. Applications of Atmospheric Chemistry: Air Pollution Control Strategies and Risk Assessments for Tropospheric Ozone and Associated Photochemical Oxidants, Acids, Particles, and Hazardous Air Pollutants. *Chem. Up. Low. Atmos.* **2000**, 871–942. https://doi.org/10.1016/B978-012257060-5/50018-6.

(24) Martín-Sómer, M.; Pablos, C.; van Grieken, R.; Marugán, J. Influence of Light Distribution on the Performance of Photocatalytic Reactors: LED vs Mercury Lamps. *Appl. Catal. B Environ.* **2017**, *215*, 1–7. https://doi.org/10.1016/J.APCATB.2017.05.048.

(25) Oveisi, M.; Mahmoodi, N. M.; Asli, M. A. Halogen Lamp Activated Nanocomposites as Nanoporous Photocatalysts: Synthesis, Characterization, and Pollutant Degradation Mechanism. *J. Mol. Liq.* **2019**, *281*, 389–400. https://doi.org/10.1016/J.MOLLIQ.2019.02.069.

(26) Kisch, H. On the Problem of Comparing Rates or Apparent Quantum Yields in Heterogeneous Photocatalysis. *Angew. Chemie Int. Ed.* **2010**, *49* (50), 9588–9589. https://doi.org/10.1002/ANIE.201002653.

(27) Döscher, H.; Young, J. L.; Geisz, J. F.; Turner, J. A.; Deutsch, T. G. Solar-to-Hydrogen Efficiency: Shining Light on Photoelectrochemical Device Performance. *Energy Environ. Sci.* **2016**, *9* (1), 74–80. https://doi.org/10.1039/C5EE03206G.

(28) Castro, S.; Albo, J.; Irabien, A. Photoelectrochemical Reactors for CO 2 Utilization. *ACS Sustain. Chem. Eng.* **2018**, *6*, 15877−15894. https://doi.org/10.1021/acssuschemeng.8b03706.

(29) Reay, D.; Ramshaw, C.; Harvey, A. Reactors. *Process Intensif.* **2013**, 121–204. https://doi.org/10.1016/B978-0-08-098304-2.00005-5.

(30) Tahir, M.; Saidina Amin, N. Photocatalytic CO 2 Reduction with H 2 O Vapors Using Montmorillonite/ TiO 2 Supported Microchannel Monolith Photoreactor. **2013**. https://doi.org/10.1016/j.cej.2013.06.055.

(31) Rongé, J.; Bosserez, T.; Martel, D.; Nervi, C.; Boarino, L.; Taulelle, F.; Decher, G.; Bordiga, S.; Martens, J. A. Monolithic Cells for Solar Fuels. *Chem. Soc. Rev.* **2014**, *43* (23), 7963–7981. https://doi.org/10.1039/C3CS60424A.

(32) Colombo, E.; Ashokkumar, M. Comparison of the Photocatalytic Efficiencies of Continuous Stirred Tank Reactor (CSTR) and Batch Systems Using a Dispersed Micron Sized Photocatalyst. *RSC Adv.* **2017**, *7* (76), 48222–48229. https://doi.org/10.1039/c7ra09753k.

(33) Ali, S.; Flores, M. C.; Razzaq, A.; Sorcar, S.; Hiragond, C. B.; Kim, H. R.; Park, Y. H.; Hwang, Y.; Kim, H. S.; Kim, H.; Gong, E. H.; Lee, J.; Kim, D.; In, S.-I. Gas Phase Photocatalytic CO2 Reduction, "A Brief

Overview for Benchmarking." *Catalysts* **2019**, *9* (9), 727. https://doi.org/10.3390/catal9090727.

(34) Chen, Y. W.; Hsu, Y. H. Effects of Reaction Temperature on the Photocatalytic Activity of TiO2 with Pd and Cu Cocatalysts. *Catal. 2021, Vol. 11, Page 966* **2021**, *11* (8), 966. https://doi.org/10.3390/CATAL11080966.

(35) Wang, W.; Ku, Y. The Light Transmission and Distribution in an Optical Fiber Coated with TiO2 Particles. *Chemosphere* **2003**, *50* (8), 999–1006. https://doi.org/10.1016/S0045-6535(02)00641-0.

(36) Li, D.; Chen, Y.; Abanades, S.; Zhang, Z. Enhanced Activity of TiO2 by Concentrating Light for Photoreduction of CO2 with H2O to CH4. *Catal. Commun.* **2018**, *113*, 6–9. https://doi.org/10.1016/J.CATCOM.2018.05.005.

(37) Crake, A.; Christoforidis, K. C.; Godin, R.; Moss, B.; Kafizas, A.; Zafeiratos, S.; Durrant, J. R.; Petit, C. Titanium Dioxide/Carbon Nitride Nanosheet Nanocomposites for Gas Phase CO2 Photoreduction under UV-Visible Irradiation. *Appl. Catal. B Environ.* **2019**, *242*, 369–378. https://doi.org/10.1016/J.APCATB.2018.10.023.

(38) MAX-303 Xenon Light Source 300W Technical Information.

(39) *MAX-303 Xenon Light Source 300W | Asahi Spectra USA Inc.* https://www.asahi-spectra.com/opticalinstrument/max303.asp (accessed 2022-12-08).

(40) *Reference Air Mass 1.5 Spectra | Grid Modernization | NREL*. https://www.nrel.gov/grid/solar-resource/spectra-am1.5.html (accessed 2022-11-18).

(41) *Reference Air Mass 1.5 Spectra | Grid Modernization | NREL*. https://www.nrel.gov/grid/solar-resource/spectra-am1.5.html (accessed 2023-05-30).

(42) Schukraft, G. E. M.; Woodward, D. R. T.; Kumar, D. S.; Sachs, D. M.; Eslava, D. S.; Petit, D. C. Hypercrosslinked Polymers as a Photocatalytic Platform for Visible-Light-Driven CO2 Photoreduction Using H2O. *ChemSusChem* **2021**, *14* (7), 1720. https://doi.org/10.1002/CSSC.202002824.

(43) Oh, H.; Park, J.; Min, K.; Lee, E.; Jyoung, J. Y. Effects of Pore Size Gradient in the Substrate of a Gas Diffusion Layer on the Performance of a Proton Exchange Membrane Fuel Cell. *Appl. Energy* **2015**, *149*, 186–193. https://doi.org/10.1016/J.APENERGY.2015.03.072.

(44) *Company | Makuhari Messe*. https://www.m-messe.co.jp/en/organizers/company/ (accessed 2023-01-18).

(45) Luong, J.; Yang, X.; Hua, Y.; Yang, P.; Gras, R. Gas Chromatography with in Situ Catalytic Hydrogenolysis and Flame Ionization Detection for the Direct Measurement of Formaldehyde and Acetaldehyde in Challenging Matrices. *Anal. Chem.* **2018**, *90* (23), 13855–13859. https://doi.org/10.1021/ACS.ANALCHEM.8B04563/SUPPL_FILE/AC8B04563_SI_001.PDF.

(46) Budiman, H.; Nuryatini; Zuas, O. Comparison between GC-TCD and GC-FID for the Determination of Propane in Gas Mixture. *Procedia Chem.* **2015**, *16*, 465–472. https://doi.org/10.1016/J.PROCHE.2015.12.080.

(47) Bailey, L. D.; Beauchamp, E. G. GAS CHROMATOGRAPHY OF GASES EMANATING FROM A SATURATED SOIL SYSTEM. *Can. J. Soil Sci.* **1972**, *53*, 122–124.

(48) Fujishima, A.; Honda, K. Electrochemical Photolysis of Water at a Semiconductor Electrode. *Nature* **1972**, *238* (5358), 37–38. https://doi.org/10.1038/238037a0.

(49) Nakata, K.; Fujishima, A. TiO2 Photocatalysis: Design and Applications. *J. Photochem. Photobiol. C Photochem. Rev.* **2012**, *13* (3), 169–189. https://doi.org/10.1016/J.JPHOTOCHEMREV.2012.06.001.

(50) Coronado, J. M.; Hernández-Alonso, M. D. The Keys of Success: TiO2 as a Benchmark Photocatalyst. *Green Energy Technol.* **2013**, *71*, 85–101. https://doi.org/10.1007/978-1-4471-5061-9_5/COVER.

(51) Liu, J.; Li, C.; Wang, F.; He, S.; Chen, H.; Zhao, Y.; Wei, M.; Evans, D. G.; Duan, X. Enhanced Low-Temperature Activity of CO 2 Methanation over Highly-Dispersed Ni/TiO 2 Catalyst. *Catal. Sci. Technol.* **2013**, *3* (10), 2627–2633. https://doi.org/10.1039/C3CY00355H.

(52) Lo, C. C.; Hung, C. H.; Yuan, C. S.; Wu, J. F. Photoreduction of Carbon Dioxide with H2 and H2O over TiO2 and ZrO2 in a Circulated Photocatalytic Reactor. *Sol. Energy Mater. Sol. Cells* **2007**, *91* (19), 1765–

1774. https://doi.org/10.1016/J.SOLMAT.2007.06.003.

(53) Tang, Y.; Wu, S.; Wang, Y.; Song, L.; Yang, Z.; Guo, C.; Liu, J.; Wang, F. Photo-Assisted Catalytic CO2Hydrogenation to CO with Nearly 100% Selectivity over Rh/TiO2Catalysts. *Energy and Fuels* **2022**, *37*, 539–546. https://doi.org/10.1021/ACS.ENERGYFUELS.2C03604/ASSET/IMAGES/LARGE/EF2C03604_0006.JPEG.

(54) Wang, C.; Fang, S.; Xie, S.; Zheng, Y.; Hu, Y. H. Thermo-Photo Catalytic CO2 Hydrogenation over Ru/TiO2. *J. Mater. Chem. A* **2020**, *8* (15), 7390–7394. https://doi.org/10.1039/C9TA13275A.

(55) Fu, Z.; Wang, X.; Gardner, A. M.; Wang, X.; Chong, S. Y.; Neri, G.; Cowan, A. J.; Liu, L.; Li, X.; Vogel, A.; Clowes, R.; Bilton, M.; Chen, L.; Sprick, R. S.; Cooper, A. I. A Stable Covalent Organic Framework for Photocatalytic Carbon Dioxide Reduction. *Chem. Sci.* **2020**, *11* (2), 543–550. https://doi.org/10.1039/C9SC03800K.

(56) Fu, Z.; Vogel, A.; Zwijnenburg, M. A.; Cooper, A. I.; Sprick, R. S. Photocatalytic Syngas Production Using Conjugated Organic Polymers. *J. Mater. Chem. A* **2021**, *9* (7), 4291–4296. https://doi.org/10.1039/D0TA09613J.

(57) Du, P.; Eisenberg, R. Catalysts Made of Earth-Abundant Elements (Co, Ni, Fe) for Water Splitting: Recent Progress and Future Challenges. *Energy and Environmental Science*. March 2012, pp 6012–6021. https://doi.org/10.1039/c2ee03250c.

(58) Ola, O.; Maroto-Valer, M. M. Review of Material Design and Reactor Engineering on TiO2 Photocatalysis for CO2 Reduction. *J. Photochem. Photobiol. C Photochem. Rev.* **2015**, *24*, 16–42. https://doi.org/10.1016/j.jphotochemrev.2015.06.001.

(59) Kočí, K.; Obalová, L.; Matějová, L.; Plachá, D.; Lacný, Z.; Jirkovský, J.; Šolcová, O. Effect of TiO2 Particle Size on the Photocatalytic Reduction of CO2. *Appl. Catal. B Environ.* **2009**, *89* (3–4), 494–502. https://doi.org/10.1016/J.APCATB.2009.01.010.

(60) Kisch, H.; Bahnemann, D. Best Practice in Photocatalysis: Comparing Rates or Apparent Quantum Yields? *J. Phys. Chem. Lett.* **2015**, *6* (10), 1907–1910. https://doi.org/10.1021/ACS.JPCLETT.5B00521/ASSET/IMAGES/LARGE/JZ-2015-00521F_0004.JPEG.

(61) Zhang, G.; Ou, W.; Wang, J.; Xu, Y.; Xu, D.; Sun, T.; Xiao, S.; Wang, M.; Li, H.; Chen, W.; Su, C. Stable, Carrier Separation Tailorable Conjugated Microporous Polymers as a Platform for Highly Efficient Photocatalytic H2 Evolution. *Appl. Catal. B Environ.* **2019**, *245*, 114–121. https://doi.org/10.1016/j.apcatb.2018.12.007.

(62) Zhang, X. H.; Wang, X. P.; Xiao, J.; Wang, S. Y.; Huang, D. K.; Ding, X.; Xiang, Y. G.; Chen, H. Synthesis of 1,4-Diethynylbenzene-Based Conjugated Polymer Photocatalysts and Their Enhanced Visible/near-Infrared-Light-Driven Hydrogen Production Activity. *J. Catal.* **2017**, *350*, 64–71. https://doi.org/10.1016/j.jcat.2017.02.026.

(63) Augugliaro, V.; Litter, M.; Palmisano, L.; Soria, J. The Combination of Heterogeneous Photocatalysis with Chemical and Physical Operations: A Tool for Improving the Photoprocess Performance. *J. Photochem. Photobiol. C Photochem. Rev.* **2006**, *7* (4), 127–144. https://doi.org/10.1016/J.JPHOTOCHEMREV.2006.12.001.

(64) Ollis, D. F. Kinetic Disguises in Heterogeneous Photocatalysis. *Top. Catal. 2005 353* **2005**, *35* (3), 217–223. https://doi.org/10.1007/S11244-005-3827-Z.

(65) Reisner, E. EPFL Solar Fuels Standards and Benchmarking Workshop. EPFL December 6, 2021.

(66) Andrei, V.; Wang, Q.; Uekert, T.; Bhattacharjee, S.; Reisner, E. Solar Panel Technologies for Light-to-Chemical Conversion. *Acc. Chem. Res.* **2022**. https://doi.org/10.1021/ACS.ACCOUNTS.2C00477.

(67) Ohtani, B. Photocatalysis A to Z—What We Know and What We Do Not Know in a Scientific Sense. *J. Photochem. Photobiol. C Photochem. Rev.* **2010**, *11* (4), 157–178. https://doi.org/10.1016/J.JPHOTOCHEMREV.2011.02.001.

(68) Grigioni, I.; Dozzi, M. V.; Bernareggi, M.; Chiarello, G. L.; Selli, E. Photocatalytic CO2 Reduction vs.

H2 Production: The Effects of Surface Carbon-Containing Impurities on the Performance of TiO2-Based Photocatalysts. *Catal. Today* **2017**, *281*, 214–220. https://doi.org/10.1016/J.CATTOD.2016.05.040.

(69) Zhang, W.; Mohamed, A. R.; Ong, W.-J. Z-Scheme Photocatalytic Systems for Carbon Dioxide Reduction: Where Are We Now? *Angew. Chemie* **2020**, ange.201914925. https://doi.org/10.1002/ange.201914925.

4. Chapter 4: Iptycene based Solution-Processable Polymers of Intrinsic Microporosity for Carbon Dioxide Photoreduction.

Contents

4. CHAPTER 4: IPTYCENE BASED SOLUTION-PROCESSABLE POLYMERS OF INTRINSIC MICROPOROSITY FOR CARBON DIOXIDE PHOTOREDUCTION. 132

4.1. General Information and Attributions 137

4.2. Introduction 137

4.2.1. Project Aims 137

4.3. Results and Discussion 138

4.3.1. Polymer Synthesis and Characterisation 138

4.3.1.1. Polymer structures and synthesis 138

4.3.1.2. Optoelectronic Properties and DFT calculations 141

4.3.1.3. Residual Metal Content 148

4.3.1.4. Porosity 149

4.3.2. Polymers in Photocatalysis 151

4.3.2.1. Single Component Performance 152

4.3.2.2. Presence of added palladium 157

4.3.2.3. Probing synthetic design 158

4.3.2.4. Hydrogen evolution experiments 160

4.3.2.5. CO_2 photocatalysis in water 161

4.3.3. Copper co-catalyst 161

4.3.3.1. Polymer Blends 169

4.4. Conclusions and Future Work 173

4.5. Experimental 175

4.5.1. Methods and Materials 175

4.5.2. Synthesis 177

4.6. Chapter 4 Appendix 186

4.7. References 189

List of Figures

Figure 4.1: Iptycene-based structure of **pTA**.....138
Figure 4.2: Representation of the contour curves of the frontier molecular orbitals obtained by DFT, where a) HOMO of pTA-BT b) LUMO of pTA-BT c) HOMO of pTA-Ph d) LUMO of pTA-Ph e) HOMO of pTA-Th f) LUMO of pTA-Th g) HOMO of pTA h) LUMO of pTA. Energy minima was first found using MMFF94, and then geometrically optimised with B3LYP-D3/6-31G(d,p). Gaussview was used to visualise the orbitals, optimised structures and angled. The red and green lobes represent the phases of the molecular orbitals. 142
Figure 4.3: Diagram of predicted polymer energy levels by DFT.....143
Figure 4.4: a) Normalised UV-Visible thin-film spectra of the polymers b) PL spectra of polymers films upon 400 nm excitation, corrected by the number of absorbed photons, c) Energy level diagram, values derived from PESA and UV-Vis bandgap edge, * taken from literature [20]. d) Comparison of the PL decay kinetics of polymers films, excited at 404 nm, and recorded at different polymer emission wavelengths, e) PL emission decay kinetics of polymers solutions upon 404 nm excitation wavelength and probed at the emission maximum.....146
Figure 4.5: PL decay kinetics of polymer films measured at different emission wavelength upon 404 nm excitation wavelength 404 nm. 147
Figure 4.6: BET isotherms run in nitrogen. Dotted lines represent desorption, filled lines adsorption. Average pore diameters presented in embedded graphs. a) **pTA**, b) **pTA-Ph**, c) **pTA-Th**, d) **pTA-BT**.....150
Figure 4.7: CO production over time from the polymers with no added co-catalyst. CO_2 and H_2 were in a 1:3 ratio and at 1.15 bar. 152
Figure 4.8: a) Rate of formation of CO and CO and CH_4 by **pTA** b) Rates of CO production showing control conditions. Firstly, rate obtained in testing conditions, then replacing H_2 with N_2, then replacing CO_2 with N_2, then in inert atmosphere and finally with normal conditions but under no illumination.....154
Figure 4.9: $^{12}CO_2$ and isotopic $^{13}CO_2$ measurements. Mass spectrum chromatogram of pTA illustrating the ^{13}CO (m/z = 29) peak observed with a) $^{12}CO_2$ overnight, b) $^{13}CO_2$ at time zero and c) $^{13}CO_2$ overnight, showing the ^{13}CO (m/z = 29) peak observed. D) shows the mass spectrum of ^{12}CO e) shows the mass spectrum of ^{13}CO. 156
Figure 4.10: Graph showing the kinetic curves of added palladium. 157
Figure 4.11 Graphs illustrating trends comparing polymer reduction rate to specific factors. For each graph, the secondary y-axis highlights the rate of CO production, and the polymers

are ordered in order of highest rate. a) palladium content over rate trend shows surface area against rate trend b) BET surface areas over rate trend c) Shows the number of the largest peak in the pore distribution seen over rate trend d) LUMO level over rate trend. e) molecular weight over rate trend f) Photoluminescence lifetimes over rate trend 158
Figure 4.12: Rate of Hydrogen production over time, conditions: 2 mg of polymer, 0.2 mol l^{-1} ascorbic acid (20 ml), pH 2, 5% (10 µg) Pt, 300 W Xe lamp (350 to 800 nm), 160 cm^2 reactor. 160
Figure 4.13: CO production over 12 hours by **pTA** in aqueous conditions. Conditions: 5 mg of polymer, 10 mg 2,2′-bipyridine and 5 µmol cobalt(ii) chloride, a mixture of acetonitrile, water and triethanolamine (3 : 1 : 1 vol, 5 mL), were charged to a vial, the suspension was ultrasonicated for 20 minutes. The contents were transferred to the same reactor as that used for gas phase photocatalysis, the solution was purged with CO_2 for 2 hours. 161
Figure 4.14: CO production including CuI as a co-catalyst and comparing to no added metal catalyst. 162
Figure 4.15 a-d: PL e PL spectra of pristine polymers as well as polymers in the presence of CuI, the measurements were carried out in hydrogen to mimic photocatalysis conditions... 164
Figure 4.16: Comparison PL decay kinetics of polymer films with/without CuI measured a the maximum PL intensity. Excitation wavelength 404 nm 165
Figure 4.17: TEM images showing copper nanoparticles formed on a **pTA-Ph** polymer film after operation 166
Figure 4.18: XPS data showing CuI with and without exposure to photocatalytic conditions in the reactor and compared to reference materials. Both figures show Cu^0 and Cu^+ as references, p1 and p2 refer to different points on the surface on which the measurement was focused and "UV" highlights the samples which were exposed to light and H_2:CO_2. a) shows the Cu LMM Auger peak, b) shows the Cu $2p_{3/2}$ XPS peak. 167
Figure 4.19:a) carbon monoxide production comparison between **pTA-Th** and **pTA-BT** as single component and together as a blend b) rate of carbon monoxide dependent on the ratio of **pTA-Th** and **pTA-BT** polymer blends..... 169
Figure 4.20: Comparison of the a) UV-Vis and b-c) PL spectra of neat polymer films and heterojunction **pTA**:**Th**:**pTA-BT** 1:1. (prepared using 0.25 mg). Excitation wavelength of 400 nm (b) and 575 nm(c). 170
Figure 4.21: Rate of CO produced in blends a) comparing the blend pf pTA and pTA:BT to the single components b) comparing the blend of pTA-Ph and pTA-Th to its single components. 171

Figure 4.22: Comparison of the a) UV-Vis and b-c) PL spectra of neat polymer films and heterojunction **pTA**:**pTA-BT** 1:1. (prepared using 0.25 mg). Excitation wavelength of 400 nm (b) and 550 nm(c).....172
Figure 4.23: PESA of a) **pDHT**, b) **pTA**, c)**pTA-Ph**, d) **pTA-Th**, e) **pTA-BT**.....186
Figure 4.24: BET figure of **pDHT**.....186
Figure 4.25: Example of **pTA** sample pre-testing 188

List of Tables

Table 4.1: Summary of optoelectronic properties of the polymers and DFT bond angles. 144
Table 4.2: Summary of photoluminescence data and PLQY data 148
Table 4.3: Residual metal content in the polymers 149
Table 4.4: Summary of BET surface area and average pore size 151
Table 4.5: Summary of rates of CO production. Rates were calculated from the slope of the curves. *Selectivity calculated as a percentage of CO detected vs CH_4. 153
Table 4.6: Rate with added palladium to **pTA** 157
Table 4.7: Table summarising rates with copper iodide compared to without 163
Table 4.8: Calculations table for the photoluminescence lifetime of polymers films upon 404 nm excitation wavelength. 187
Table 4.9: Table summarising control experiments on the polymers 188

4.1. General Information and Attributions

Dr Weimin Zhang (McCulloch Group, KAUST) and Dr Balaji Purushothaman (McCulloch Group, KAUST), worked on the synthetic route to the polymers. PL measurements were done by Dr Soranyel Gonzalez-Carrero (Durrant Group, Imperial College London). DFT calculations were done by Junfu Tiang (McCulloch Group, Oxford University), ***pDHT*** *was synthesised by Maryam Alsufayani (McCulloch Group, Oxford University). TEM was done by Dr. Catherine Aitchison (McCulloch Group, Oxford University), XPS was done by Dr Joshua Gibbs (Henry Royce Institute, Oxford University).* ***P3HT*** *was purchased from Ossila (****P3HT****-Mw = 57). ICP-MS was carried out by Dr Trang Quynh To (Centre for the Environment, University of Oxford. Ed Rattner and Yasmine Baghdadi (Eslava Group, Department of Chemical Engineering, Imperial College London) carried out the isotope labelled experiments with the author on their batch-based set-up. Hydrogen evolution experiments were first carried out by Dr Jan Kosco (McCulloch Group, KAUST) and repeated by the author. A part of this chapter was adapted into a manuscript, submitted to Nature Communications as of March 2023.*

4.2. Introduction

Following from building the set-up in **Chapter 3** and taking inspiration from basic principles learnt from **Chapter 2**, the focus of the thesis was then shifted towards organic semiconductor materials for unassisted photocatalysis. This chapter investigates the use of solution processable, conjugated polymers of intrinsic microporosity, in carbon dioxide photoreduction in hydrogen. The polymers were designed with properties adept to gas phase photocatalysis in mind.

4.2.1. Project Aims

The properties focused on for polymer design were porosity, conjugation and processability. Porosity has been shown to be advantageous in gas phase photocatalysis. A high surface area increases the number of active sites in a reaction, and therefore increases the overall rate. Porosity in the structure can increase gas penetration, which has been shown to be beneficial in gas phase carbon dioxide reduction in the presence of hydrogen.[1] Conjugation is given by a delocalised system of π-electrons and was critical for the absorption of light to occur and the transport of charges to active sites.[2] Processibility was targeted to fully take advantage of the benefits granted by organic materials. A polymer that is soluble in common solvents, such as chloroform, can be more easily synthesised and characterised. Good solubility ensures the

polymer does not crash out in polymerisation and can therefore achieve higher molecular weight. It also enables better purification than an insoluble compound.[3] Furthermore, the solubility of a polymer in common solvents enables good processability. In fact, the polymers can be spin-coated, drop cast, mixed with other polymers to form heterojunctions, or nanoparticles. These increase the flexibility in terms of uses of organic polymers.[4]

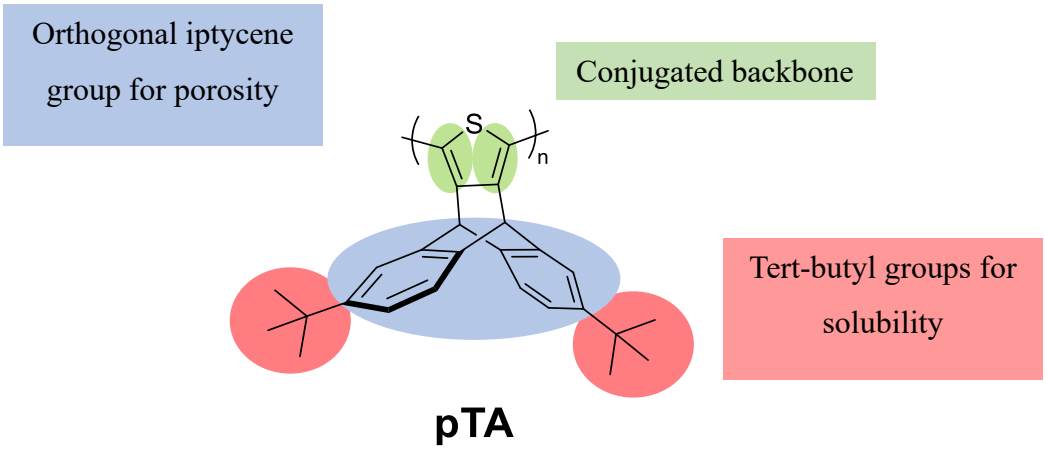


Figure 4.1: Iptycene-based structure of **pTA**

Figure 4.1 illustrates the rigid monomer upon which the study was developed. The conjugated backbone is based on **p3HT**, made up of a conjugated thiophene, giving the polymers its core optoelectronic properties. The orthogonal, rigid, iptycene unit gave the polymer its porous structure, making the obtained compounds polymers of intrinsic microporosity (PIMs). These microporous materials, are characterised by a network of small voids, (normally less than 2 nm in width) which are formed due to the polymer's inability to pack effectively, due to rigid or twisted repeating structures within the polymer chains.[5,6] The addition of *tert*-butyl groups further inhibited chain packing, thus improving upon the surface area, but their main function was the impart solubility to the polymers.

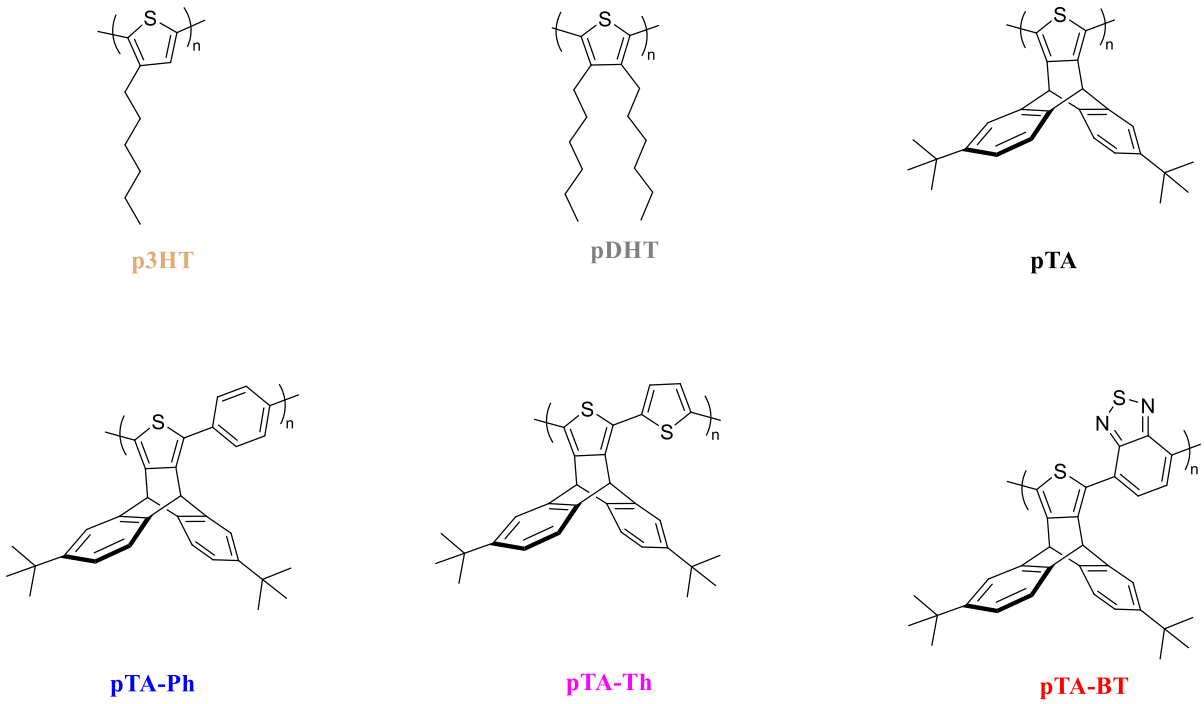
4.3. Results and Discussion

4.3.1. Polymer Synthesis and Characterisation

4.3.1.1. Polymer structures and synthesis

The polymers presented in this study are shown in **Scheme 4.1. p3HT** was commercially available and purchased as a standard measurement upon which to improve. It was initially chosen as a donating material, since its energy levels straddle the potentials for carbon dioxide reduction and hydrogen oxidation, and this study aimed to improve upon its structure by incorporation of features that would aid carbon dioxide photocatalysis.[7] **pDHT**, synthesised by

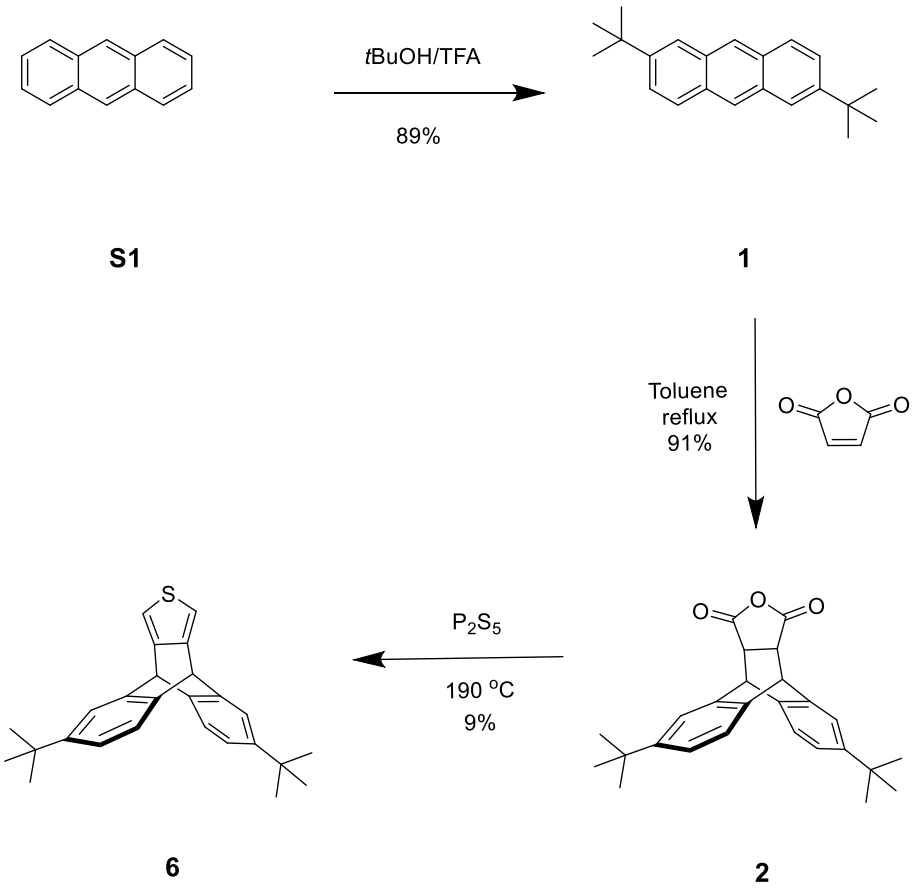
Maryam Alsufayani, is similar in structure to **p3HT** with an added alkyl chain. The purpose was to use it as a control polymer, to see if the porosity of the polymers came from the rigid iptycene structure or if the addition of a further amorphous alkyl chain had a sufficient impact on morphology and packing. The series then proceeds to the **pTA**, which has the same thiophene back-bone as **p3HT** and **pDHT**, but with the added iptycene rigid unit. The homopolymer, **pTA**, was formed from the rigid monomer**,** using iron coupling chemistry. To further investigate functionalities, energy levels and morphological properties, three further polymers were synthesised, derived from the **pTA** monomer, and 3 co-monomers: a benzothiadiazole moiety (BT), a thiophene (Th) and phenyl (Ph).



Scheme 4.1: Illustration of the polymers presented in this study.

Initially a version of **pTA** without *tert*-butyl groups was utilised. However, the resulting polymer exhibited very limited solubility in hot chloroform at molecular weights of less than 5 kDa, which would have made it essentially an oligomer. Furthermore, solubility largely facilitates polymerisations, therefore with an insoluble polymer, not only are high molecular weights harder to reach, but the polymerisation yields are more likely to stay low, as the polymer can quickly precipitate out of solution and stop growing.[3] The *tert*-butyl group was therefore incorporated within the first reaction step, to ensure the property of solubility was

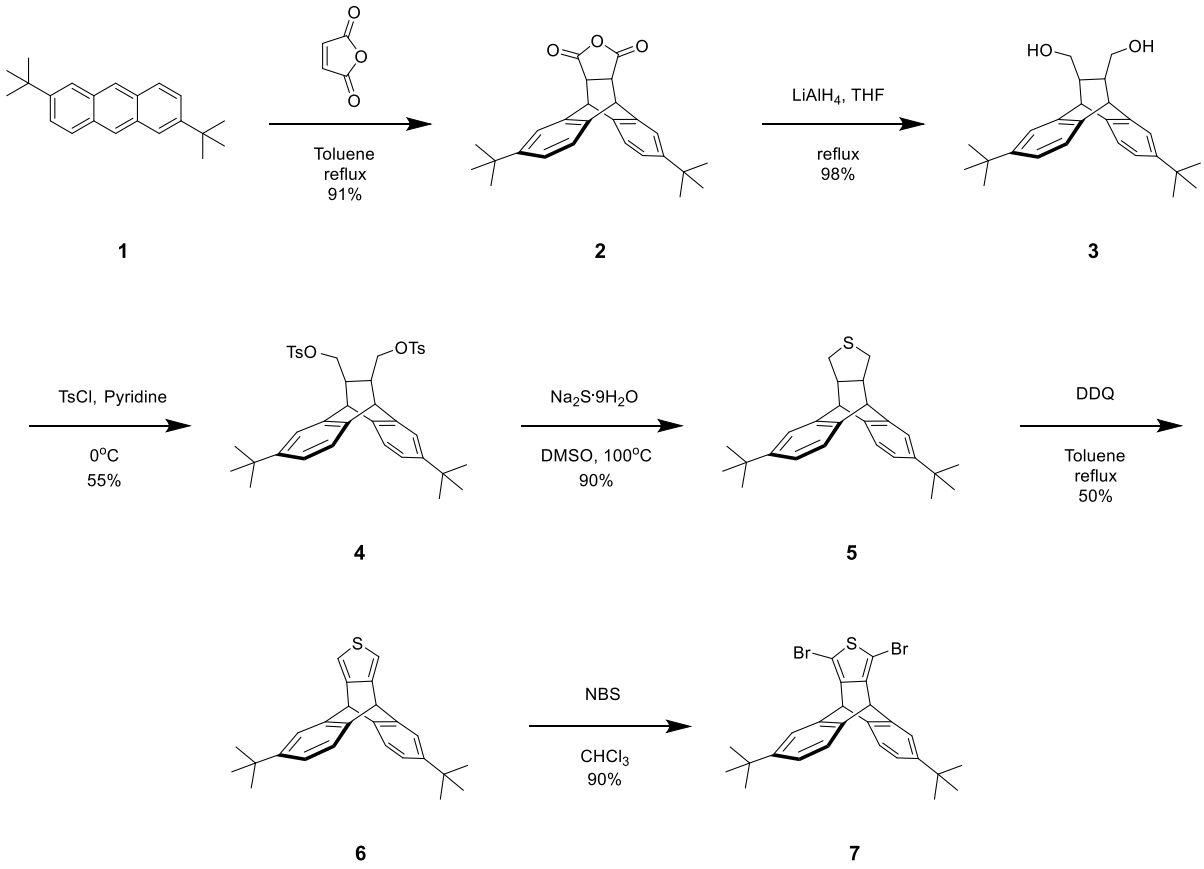
maintained. Formation of the **pTA** monomer (compound **6**) is shown in **Scheme 4.2** and **Scheme 4.3**.[8]



Scheme 4.2: First synthetic route for monomer **6** via Route 1.

Route 1 was attempted in collaboration with Dr Weimin Zhang *(McCulloch Group, KAUST),* with high yields until compound **2.** For the last step, utilising P_2S_5 was very low yielding, toxic and tedious to work with, and so alternatives were sought.

Route 2, shown in **Scheme 4.3**, was created by Dr Weimin Zhang *(McCulloch Group, KAUST)* and Dr Balaji Purushothaman *(McCulloch Group, KAUST),* who initially sent the author the compounds. The author also used this synthetic route in polymer scale up.



Scheme 4.3: Synthetic route for the formation of monomers **6** and **7** via Route 2.

Route 2 retains the initial Diels-Alder step from route 1.[9] Compound **3** was formed by reducing the anhydride using lithium aluminium hydride, which was then converted to a tosylate using tosyl chloride. Compound **5** was formed by reacting the ditosylate with sodium sulfide.[10] Addition of the oxidant DDQ to dehydrogenate compound **5** formed the thiophene-based compound **6**. Compound **6** was used for polymerisations using $FeCl_3$ for **pTA**. NBS was then utilised to brominate compound **6** to compound **7**, which was used in the Stille polymerisation of **pTA-Th** and the Suzuki polymerisations of **pTA-Ph**, and **pTA-BT**. [11]

4.3.1.2. Optoelectronic Properties and DFT calculations

BT was chosen due to its electron withdrawing nature, which was assumed would decrease the HOMO and LUMO. Th was thought to decrease the band gap, raising the HOMO and lowering the LUMO due to a more planarising monomer than a repeated rigid iptycene unit. Ph was thought would deepen the HOMO due to a lower contribution to electron density and a larger dihedral twisting compared to **pTA** or **pTA-Th** due to the four alpha hydrogens on the phenyl ring.

To examine impact of chemical structure on the electronic delocalization and conformation of the backbone, the polymers were truncated as a trimer and simulated by density functional theory (DFT) simulations.

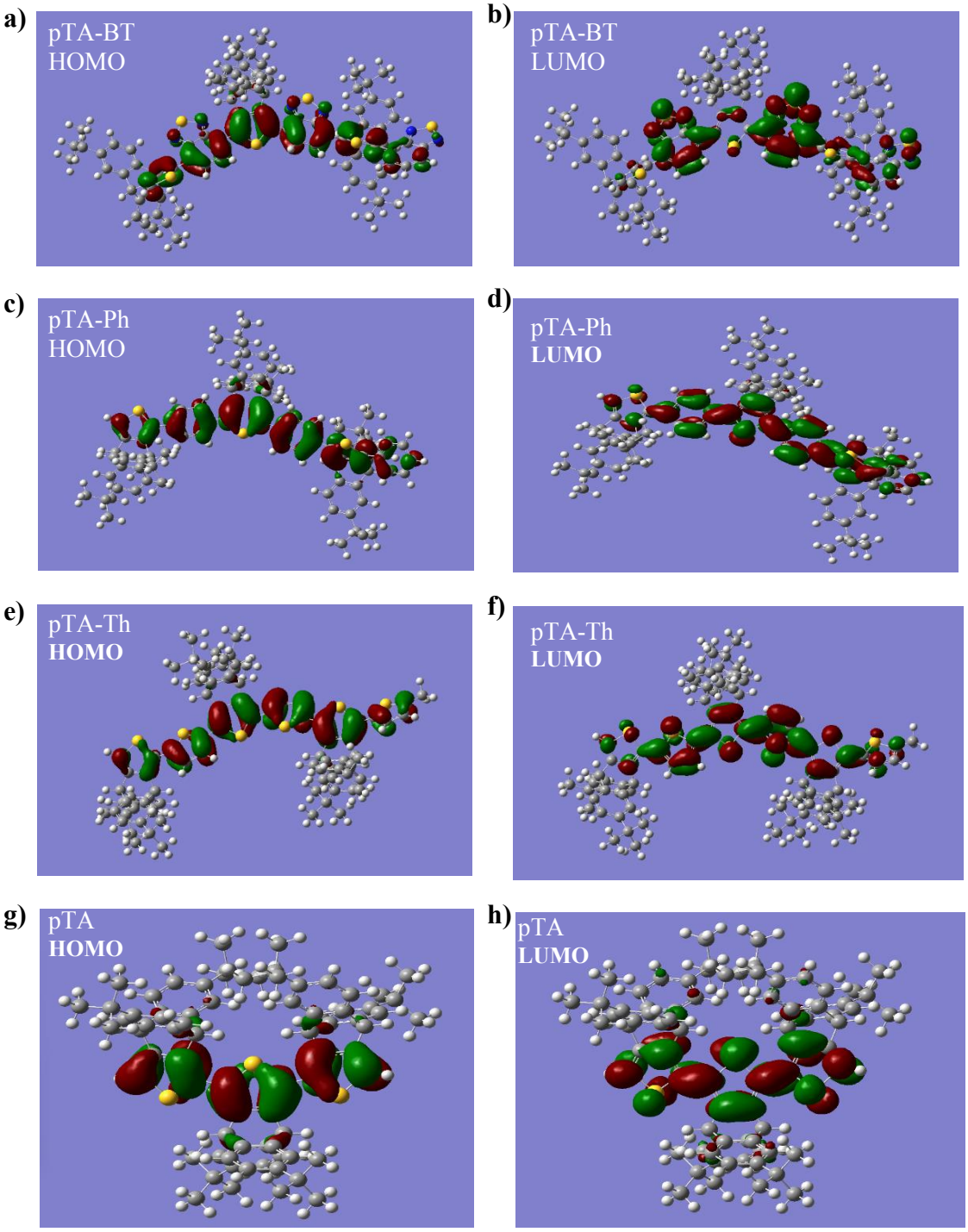


Figure 4.2: Representation of the contour curves of the frontier molecular orbitals obtained by DFT, where a) HOMO of pTA-BT b) LUMO of pTA-BT c) HOMO of pTA-Ph d) LUMO of pTA-Ph e) HOMO of pTA-Th f) LUMO of pTA-Th g) HOMO of pTA h) LUMO of pTA. Energy minima was first found using MMFF94, and then geometrically optimised with B3LYP-D3/6-31G(d,p). Gaussview was used to visualise the orbitals, optimised structures and angled. The red and green lobes represent the phases of the molecular orbitals.

The oligomers were first energy minimized with MMFF94 and further geometrically optimized with B3LYP-D3/6-31G(d,p) using Gaussian09. 6-31g(d,p) is a split valence double zeta basis set, commonly used for polymers and often limited by the cluster computing power. B3LYP was the hybrid functional used, and D3 was implemented as a correction to account for dispersive interactions. In polymers pi-pi stacking is significant, and dispersive corrections should be taken into consideration.[12] **Figure 4.2** shows the distribution of HOMO and LUMO character through the structure and the polymer backbone conformation estimations. Donor-acceptor character was probed, to predict charge transfer throughout the polymers. It was found that the HOMO density was spread quite evenly through each polymer. LUMO density was also spread-out quite evenly for each polymer, except for **pTA-BT**, in which the LUMO density was found to reside on the BT unit, which was the more electron accepting group.[13–15] **pTA** has a dihedral angle of 24.4°, **pTA-Th** has a more variable bond angle, with an average of 37.9°, **pTA-Ph** and **pTA-BT** had a dihedral angle of 48.5° and 44.3° respectively. These steric properties were reflected in the materials' FMO energies.

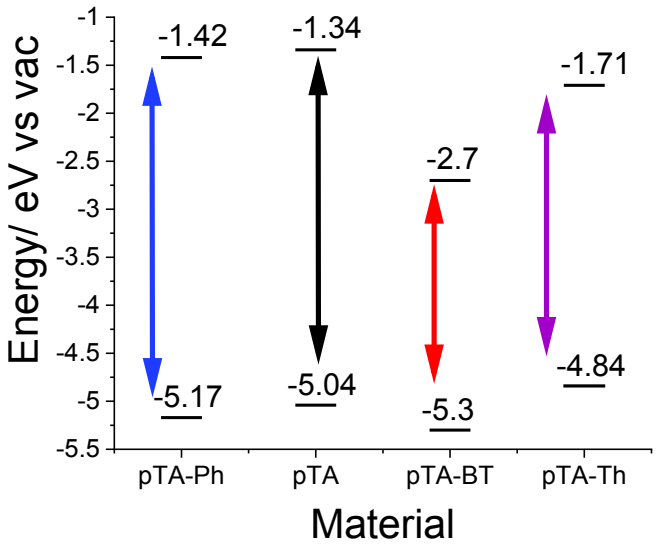


Figure 4.3: Diagram of predicted polymer energy levels by DFT

Figure 4.3 showed the energy level predictions estimated using DFT, which mirror the expected trend, with a deepening of the HOMO and LUMO in **pTA-BT** compared to **pTA**, and a deepening of the LUMO and raising of the HOMO for **pTA-Th** as predicted above. These confirmations increased the overall confidence in synthesising the polymers for this application.

PESA (appendix 1) was used to measure the HOMO energies of the polymers experimentally. The values are summarised in **Table 4.1**. The HOMOs obtained are slightly lower than those predicted from DFT, but the trend largely mirrored that obtained computationally. **pTA**, showed a HOMO of 5.6 eV, which is considerably deeper than **p3HT** (5.2 eV).[16] This was likely due to a dihedral twist between the thiophene monomers forced by the steric repulsion of neighbouring rigid iptycene units. Addition of Th did indeed show a shallower HOMO than **pTA**, likely due to the alternating rigid repeat iptycene units and the planarising unsubstituted thiophene which caused an increased overall planarity.[17] **pTA-BT** exhibited a deeper HOMO than **pTA**, as expected due to the BT unit having an electron withdrawing effect, and as seen by DFT, a more pronounced difference in localisation of the LUMO and HOMO. **pTA-Ph** also exhibited a deeper HOMO than **pTA**, this is possibly due the a degree of dihedral twisting due to the four alpha hydrogens on the phenyl ring, mentioned above.[18] The control polymer, **pDHT** also had a deeper HOMO than either **pTA** or **p3HT**, attributed to dihedral twisting due to the repulsion of the two alkyl chains on the disubstituted thiophenes.

Table 4.1: Summary of optoelectronic properties of the polymers and DFT bond angles.

Polymer	IP (eV)*	E_g (eV)#	EA (eV)*	PL max (nm)	PL lifetime (t_{avg} [a]) (ns)	DFT dihedral bond angle (°)
pTA	5.6	2.3	3.3	550	0.75	24.4
pTA -Ph	5.7	2.7	3.0	467	2.34	48.5
pTA -Th	5.4	2.1	3.3	563	0.56	37.9
pTA -BT	5.9	2.1	3.8	647	0.41	44.3
pDHT	5.7	2.9	2.8	423	-	-

IP : ionisation potential from PESA, EA: electron affinity, E_g: optical bandgap. PL: photoluminescence Measurements carried out in:
**Estimated from the EA and E_g.*
#Thin film on ITO spin-coated from 10 mgml^{-1} $CHCl_3$ solution.

Figure 4.4a) shows the UV-Vis spectra of the polymers on thin film, with data also summarised above (**Table 4.1**.). This data was used to obtain the bandgap of the polymers experimentally. Electron Affinity (EA) data was calculated from the addition of the optical bandgap to the HOMO values obtained from PESA (appendix 1). **Figure 4.4b)** shows the photoluminescence of the polymers on thin film. All polymer films showed broad PL emission bands, with maximum at 467, 475, 550, 563 and 647 nm for **pTA-Ph**, **pDHT**, **pTA**, **pTA-Th** and **pTA-**

BT, respectively. The comparison of the PL intensity on film, showed the polymer **pTA-Ph** emission is four times higher than **pTA** and even higher to the other polymers.

The energy level diagram obtained from PESA and UV-Vis, highlighting the HOMO and LUMO values of the polymers is shown in **Figure 4.4c).** The values for CO_2 reduction to CO and for hydrogen oxidation are shown as dotted lines. The potential for water oxidation is also included for reference. As seen from the diagram, the energy level trend agreed with that obtained from DFT, with just **pTA-Ph** exhibiting a higher LUMO than **pTA**. As can be seen from the diagram, the experimentally obtained values show these polymers to straddle the potentials of CO_2 reduction and hydrogen oxidation, so all the polymers could favourably drive both carbon dioxide reduction to carbon monoxide, and hydrogen oxidation to H^+, they were therefore deemed suitable for CO_2 photocatalysis testing.[19]

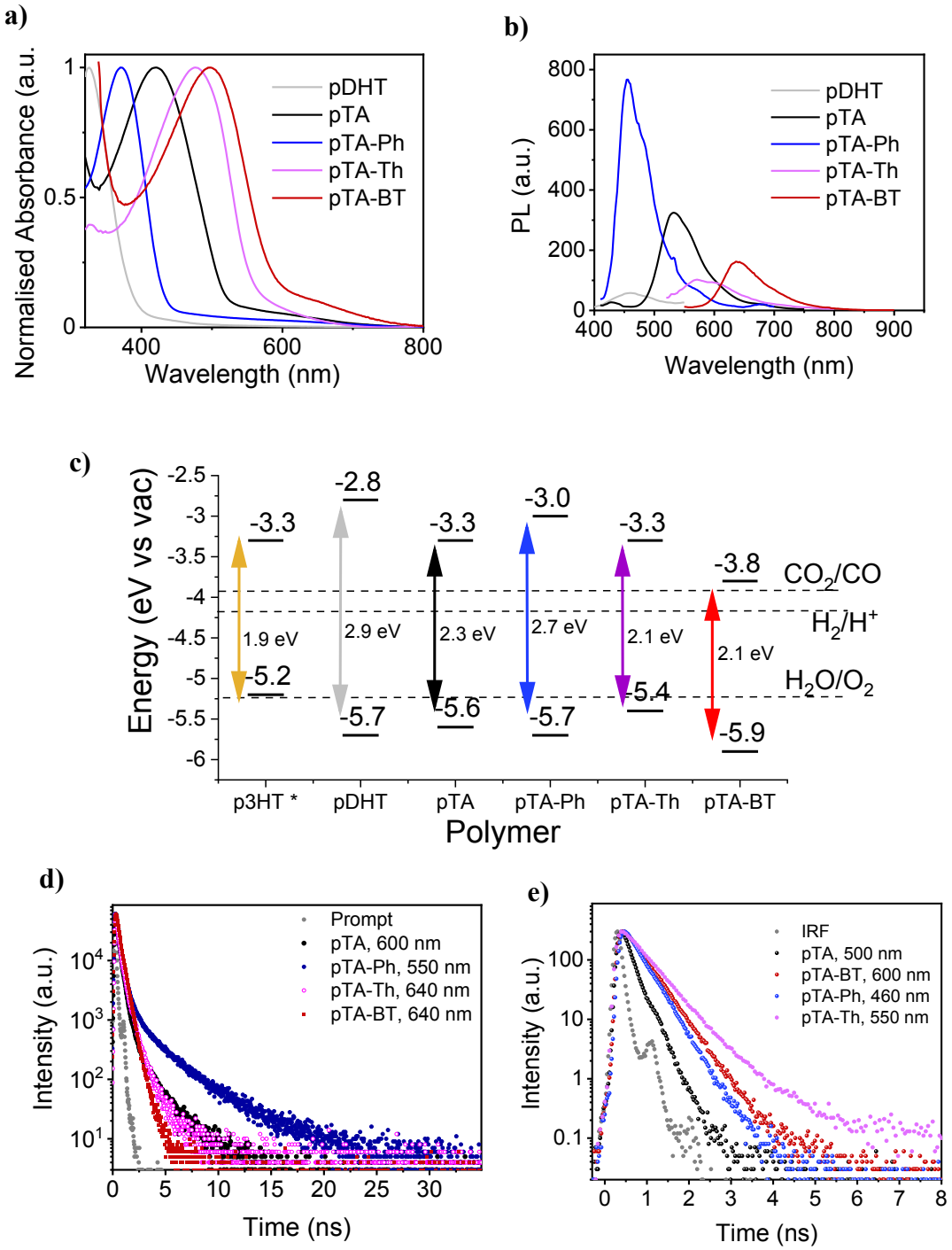


Figure 4.4: a) Normalised UV-Visible thin-film spectra of the polymers b) PL spectra of polymers films upon 400 nm excitation, corrected by the number of absorbed photons, c) Energy level diagram, values derived from PESA and UV-Vis bandgap edge, * taken from literature [20]. d) Comparison of the PL decay kinetics of polymers films, excited at 404 nm, and recorded at different polymer emission wavelengths, e) PL emission decay kinetics of polymers solutions upon 404 nm excitation wavelength and probed at the emission maximum.

To further investigate the excited states of the polymers, time-correlated single photon counting (TCSPC) was used. This enabled the obtaining of fluorescence lifetimes.

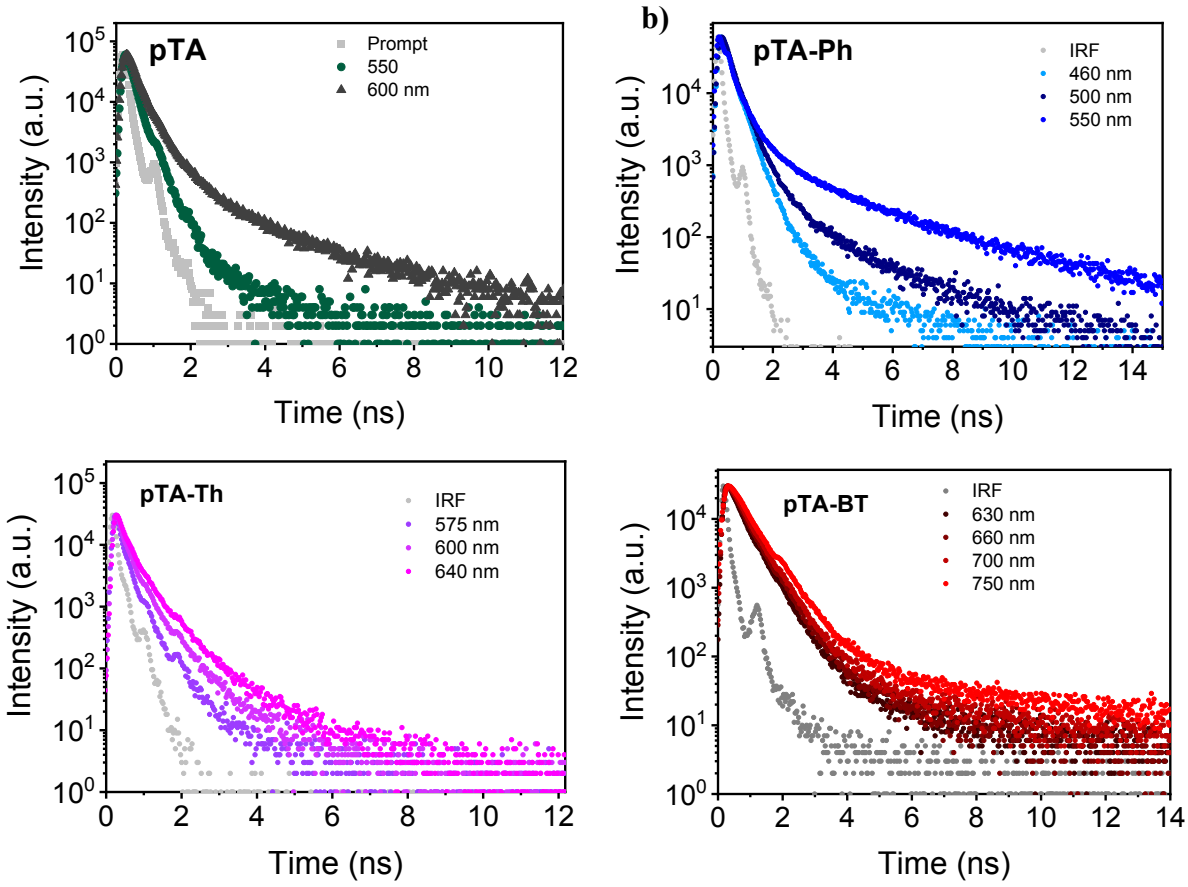


Figure 4.5: PL decay kinetics of polymer films measured at different emission wavelength upon 404 nm excitation wavelength 404 nm.

Analysis of the PL decays in the polymer films showed a multiexponential decay, dependent on the emission wavelengths, as shown in **Figure 4.4d)** and **Figure 4.5.**

The IRF, was the signal of the reference of this system, measured at the excitation wavelength 404 nm, the artefact in the IRF is part of the sample used as reference and taken into account in the calculations. This bump observed in the IRF could be due to "afterpulsing" whereby photoelectrons, unrelated to a just detected photon, are scattered and then re-enter the system with a delay, and are recorded forming an artefact as shown in the IRF.[21] The PL decays values were obtained after deconvoluting using the IRF signal, using the Software. The average lifetimes of the polymers were measured at the PL peak maximum. And the numbers were calculated to be 0.75, 2.34, 0.56 and 0.41 ns for **pTA**, **pTA-Ph**, **pTA-Th** and **pTA-BT** respectively. PL decay for **pDHT** was non-detectable. In contrast, in solution, the films showed a mono-exponential PL decay, (**Figure 4.4e),** which was also not dependant on emission

wavelength, this indicates the decay of a single emissive specie in solution, it is interpreted to correspond to the decay of a singlet exciton to the ground state. This is similar to other polythiophenes such as **p3HT** and **p7BT**, which also exhibit mono-exponential decay in solution, but a broader formation of electronic states due to polymer aggregation in films and intermolecular interactions so multiexponential decay was observed. [22–25] As seen above, time-correlated single photon counting (TCSPC) can be used for the acquisition of time-resolved fluorescence data. It provides information on the timescale of non-radiative decay.[26,27] The decay lifetimes can be used as a numerical description of the PL decay kinetics. Lower radiative decay, suggests less charges are recombining, and therefore it is more likely that charges can take part in chemical reactions. It is an important metric in photocatalysis, since longer lived charges, are more likely to migrate to an active site and take part in chemistry.[28]Another important measurement that can be obtained from photoluminescence is the photoluminescence quantum yield (PLQY), which refers to the numbers of photons emitted per number of photons absorbed.[29]

Table 4.2: Summary of photoluminescence data and PLQY data

Sample	PL max	PLQY (%)	PLQY max
pTA	550	23 ± 2	24.5
pTA-Ph	467	15 *± 6	20.7 *
pTA-Th	563	16 ± 2	18.3
pTA-BT	647	13 ± 1	13.8

Plqy excitation 404 nm
**detector limit*

The PLQY obtained for the porous polymers is summarised in **Table 4.2**. The PL maximum is the wavelength at which maximum intensity in photoluminescence was obtained. The PLQY is given as a percentage, and it is an average of several measurements of the same films over different areas of the film. The PLQY max column refers to the maximum value obtained from the repeat measurements, and PLQY (%) refers to the average. The PLQY of the **pTA-Ph** sample could not be easily calculated since the maximum was too close to the detector limit.

4.3.1.3. Residual Metal Content

Reporting the residual metal content in the polymers is very important in photocatalysis since it can affect the formation of products, and mechanism. In this case, residual palladium, and iron from carbon coupling chemistry, especially in the final polymerisation reactions, can form metal catalyst particles within the bulk of the conjugated polymers.[30] ICP-MS was used to

calculate the amount of residual metals within the polymers after washing with sodium diethyldithiocarbamate, which is especially good at scavenging palladium.[31]

Table 4.3: Residual metal content in the polymers

Polymer	Pd (ppm)	Fe (ppm)	Sn (ppm)
pTA	-	26	-
pTA -Ph	15	-	-
pTA -Th	23	-	4
pTA -BT	31	-	-
pDHT	19	47	-

Table 4.3 shows the residual amounts of palladium and iron found in the polymers after scavenging. The amounts are between 15 and 50 ppm of residual metal. Each polymer was washed 6 times. **pDHT** was washed 3 additional times, but it was challenging to reduce the amount of metal catalyst, likely due to the very sticky nature of the polymer. Metal impurities can influence photocatalytic activity in a variety of ways. Palladium, for example has the potential to enhance photocatalytic rates by acting as a co-catalyst and aiding the suppression of charge recombination.[32–34] The presence of palladium has been shown to increase the rate of product formation in carbon dioxide photocatalysis both in carbon nitrides and on titanium dioxide. [35,36] However, impurities can also have a detrimental effect on rates of photocatalysis.[37] The opposite effect to charge recombination suppression can be observed if the metal impurity acts as a recombination centre. Impurities could also decrease rate of photocatalysis due to active site poisoning, or by facilitating competing side reactions.[38–40] In high loadings metal impurities could absorb light parasitically and decrease the overall photocatalysis rate. [41]

4.3.1.4. Porosity

In order to calculate the surface areas of the polymers, and probe gas adsorption, BET analysis was carried out on the polymer powders. The BET isotherms obtained are show in **Figure 4.6**, with surface areas and average pore sizes summarised in **Table 4.4**. The typical BET surface area for solution processable conjugated polymers is between 5-20 m^2g^{-1}.[42] The BET surface area of **pDHT** was found to be 29 m^2g^{-1} (isotherm in appendix **Figure 4.24**)

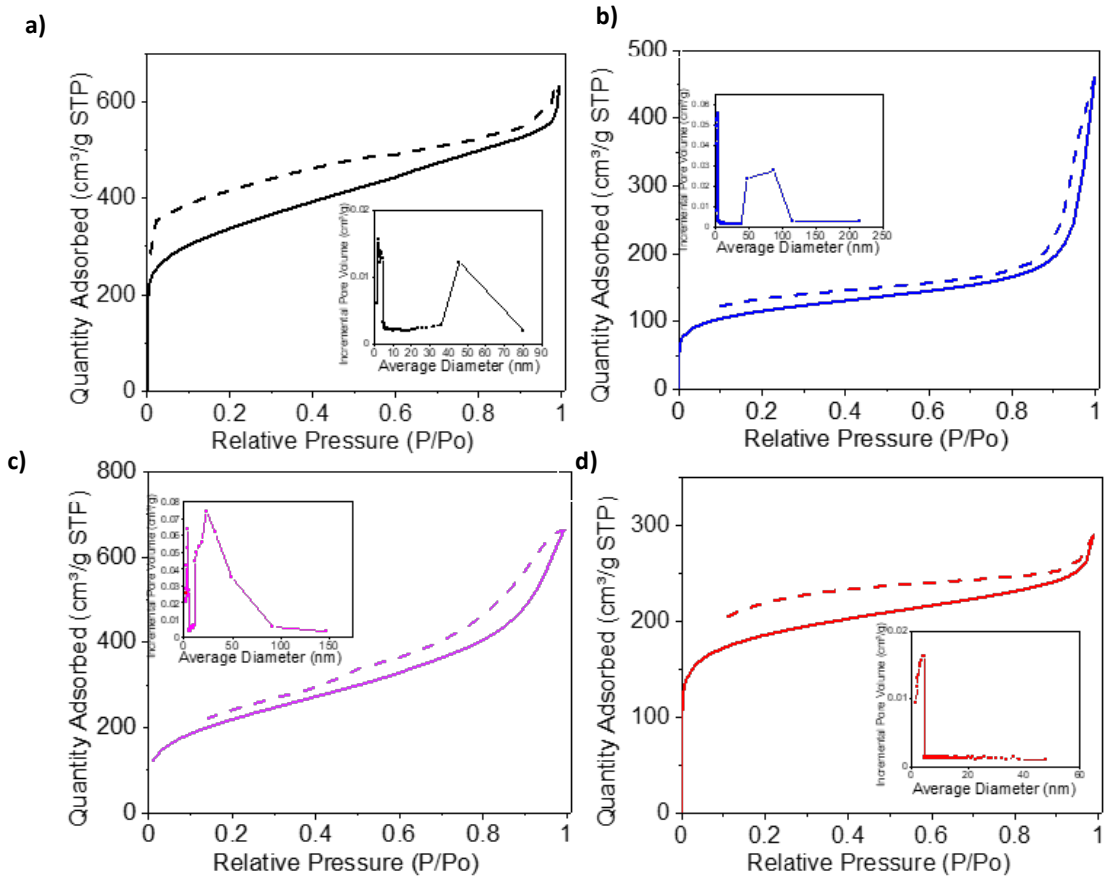


Figure 4.6: BET isotherms run in nitrogen. Dotted lines represent desorption, filled lines adsorption. Average pore diameters presented in embedded graphs. a) **pTA**, b) **pTA-Ph**, c) **pTA-Th**, d) **pTA-BT**.

The shapes of the isotherms are indicative of microporous structures. Between 0 and about 0.05 P/P_0 the sharp incline is indicative of Langmuir behaviour, whereby a monolayer absorption and micropore filling is occurring. Since the absorption of most of the polymers shows a sharp incline until around 100 cm^3g^{-1}, the polymers can be thought of as microporous. Around 0.05 P/P_0, the linear range for BET isotherm surface area calculations begins, a knee is formed in the shape, at this stage the monolayer is completed, and a multilayer can begin to fill up, as well as any mesopores. Towards the end of the graph, a sharp incline nearing 1 P/P_0 is indicate of macropores in the structure.[43]

Table 4.4: Summary of BET surface area and average pore size

Polymer	Bet surface area (m^2g^{-1})	Average pore size (nm)	Largest pore size distribution (nm)
pTA	862	3.5	45
pTA -Ph	487	4.5	70
pTA -Th	761	5.3	30
pTA -BT	596	3.6	5

The largest surface area was measured for **pTA**, at 862 m^2g^{-1}, which is among the highest ever reported for a solution processable conjugated polymer. Each thiophene on the backbone of **pTA** was functionalised with the rigid unit, thus creating the highest surface area out of the series. It was followed by **pTA-Th** with 761 m^2g^{-1}. **pTA-Ph** and **pTA-BT** exhibited surface areas of 487 and 596 m^2g^{-1} respectively. These numbers are at least an order of magnitude higher than most linear polymers, including the control, **pDHT**. This shows the necessity of a rigid unit for achieving intrinsic porosity. The amorphous alkyl chains on **pDHT** may slightly increase surface areas due to decreased packing, but the rigid unit is crucial for microporosity and higher surface areas. The average pore sizes of the polymers were between 3.5 and 5.3 nm. However, the embedded graphs in **Figure 4.6** show that there is a distribution of pore sizes present. **pTA-BT** showed mainly just micropores, with a peak at around 4 nm, **pTA-Th**, however, showed a distribution of mesopores, around 30 nm. Similarly, **pTA** showed a distribution of pores around 45 nm. **pTA-Ph** exhibited some macroporosity, show by a distribution of pores between 50 and 100 nm, supported by the sharp incline nearing 1 P/P_0 in its isotherm.

4.3.2. Polymers in Photocatalysis

Photocatalysis measurements were carried out in the custom-built set-up outlined in **Chapter 3**. Due to the nature of hydrogen assisted reduction of carbon dioxide, the polymers were first tested by themselves as single component "catalysts", focusing on gas phase testing primarily. It was then sought to investigate the addition of a co-catalyst and the creation of two-component blends, with the aim to improve product evolution.

4.3.2.1. Single Component Performance

The polymers were tested in gas phase photocatalysis, using a CO_2:H_2 atmosphere in the ratio 1:3. The ratio 1:3 was chosen due to its theoretically ideal ratio for the production of methanol via the hydrogenation of carbon dioxide, coveted due to the high value of the product.[44] Varying the ratios to 1:4, 1:9 and 1:1 did not have a significant effect on the rate of reactions, likely due to the small amounts of products obtained compared to the amount of gasses in the systems (on the level of hundreds of ppm maximum). The main product detected, by GC, was carbon monoxide. This is promising as an initial step and proof of concept, since carbon monoxide formation is mechanistically often the first step towards methanol synthesis. However, no methanol was seen with the use of these polymers only, and further optimisations to the system (likely an increase in temperature) and to the materials (including strategies to improve the rate of reaction) would be required in order to increase the likelihood of obtaining products other than CO. The performances of the polymers were evaluated as production of carbon monoxide, over time. The polymers were compared to commercially available standards, namely carbon nitride, titanium dioxide, and **p3HT**. To minimise the factors affecting photocatalysis, the amount of polymer used and illumination surface areas were kept as equal as possible, at 2 mg (±0.2 mg) and a surface area of 3 cm^2 (±0.4 cm^2).

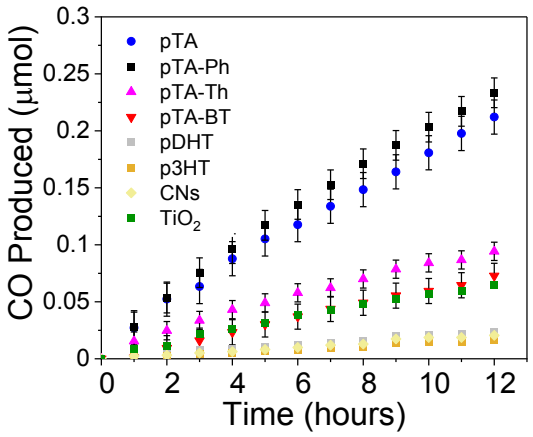


Figure 4.7: CO production over time from the polymers with no added co-catalyst. CO_2 and H_2 were in a 1:3 ratio and at 1.15 bar.

The kinetic curves of the polymers can be seen in **Figure 4.7** and are summarised in **Table 4.5**.

Table 4.5: Summary of rates of CO production. Rates were calculated from the slope of the curves. *Selectivity calculated as a percentage of CO detected vs CH_4.

Polymer	Rate (μmol h^{-1})	Selectivity to CO production (%)*	Rate (μmol $h^{-1}g^{-1}$)	Rate (μmol $h^{-1}m^{-2}$)
pTA	0.017 ±0.001	87	8.5 ± 0.5	53 ± 3
pTA -Ph	0.019 ±0.001	98	9.5 ± 0.5	66 ± 4
pTA -Th	0.007 ±0.001	98	3.7 ± 0.5	25 ± 3
pTA -BT	0.006 ±0.001	99	3.1 ± 0.5	21 ± 4
pDHT	0.002 ±0.0006	-	0.9 ± 0.3	10 ± 3
p3HT	0.0014 ±0.0005		0.7 ± 0.3	5 ± 2
CNs	0.002 ±0.0004	-	0.9 ± 0.2	6 ± 2
TiO_2	0.005 ±0.001	96	2.1 ± 0.5	21 ± 5

The trend of polymer performance was **pTA-Ph**, **pTA**, **pTA-Th** and **pTA-BT**, exhibiting rates of 65.7 μmol $h^{-1}m^{-2}$, 53.1 μmol $h^{-1}m^{-2}$, 25.0 μmol $h^{-1}m^{-2}$ and 20.9 μmol $h^{-1}m^{-2}$ respectively. The AQY of **pTA-Ph**, the highest performing single component polymer at 450 nm was 0.88%. All polymers outperformed the control polymer **pDHT** (10.2 μmol $h^{-1}m^{-2}$), as well as commercially available **p3HT** (5.2 μmol $h^{-1}m^{-2}$).

These rates are lower overall compared to other published work, but reaction conditions are largely different.[45] In order to obtain a stronger comparison, as highlighted in **Chapter 3**, the polymer rates were calibrated against commercially available standards, carbon nitride and titanium dioxide (P25).[46] (TiO_2), drop-cast from sonicated TiO_2 P25, produced CO at a rate of 21.4 μmol $h^{-1}m^{-2}$, which is comparable to published rates in similar circular photocatalytic reactors in literature, oxidising hydrogen rather than water or another sacrificial reagent.[47,48] The rate of **pTA-BT** was similar to that of TiO_2, but the other porous polymers outperformed it, with **pTA-Ph** accumulating more than 3 times as much CO product. Carbon nitride was also chosen as a good literature material comparison, since its 2.7 eV bandgap is energetically similar to the polymers presented in this study, and it is widely known as a carbon-based photocatalytic material.[49–51] The rate obtained by carbon nitride was 5.9 μmol $h^{-1}m^{-2}$, more than 10 times lower than **pTA-Ph**.

Figure 4.7 highlights the importance of porosity in gas phase carbon dioxide photocatalysis, since the porous polymers vastly outperformed the non-porous **pDHT** and **p3HT**.

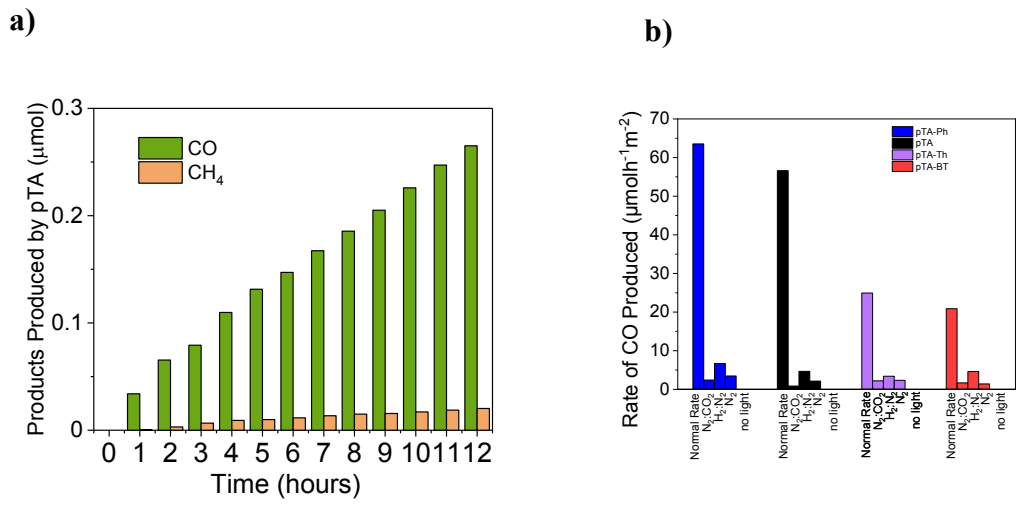


Figure 4.8: a) Rate of formation of CO and CO and CH_4 by **pTA** b) Rates of CO production showing control conditions. Firstly, rate obtained in testing conditions, then replacing H_2 with N_2, then replacing CO_2 with N_2, then in inert atmosphere and finally with normal conditions but under no illumination.

The polymers obtained predominantly carbon monoxide as their main product with a selectivity of 98% or above, expect for **pTA**. **Figure 4.8b)** shows the products detected for this polymer were 13% CH_4 and 87% CO. Methane is arguably a more exciting product than carbon monoxide as it could potentially be utilised as a solar fuel without further reaction. It should be noted that this same selectivity was not seen in the batch reactor system, which showed **pTA** as forming over 99% CO. This was quite an interesting result, and this should be looked at in more detail in future studies focusing on product selectivity. A possible explanation could be that the specific active sites or pore sizes of **pTA** were inducive to producing more methane than other polymers from carbon monoxide, in the gas recycling nature of the testing.

Early work in carbon dioxide photo hydrogenation, showed the potential for carbon based impurities and residue trapped in the materials tested for photocatalysis to be the source for CO formation, rather than carbon dioxide itself.[52] Because of this, it is necessary, with any photocatalyst used to employ control testing, to prove that the products are coming from the carbon dioxide and hydrogen gas provided**. Figure 4.8b)** highlights the control experiments done on the polymers, to provide evidence that the polymers are acting photocatalytically. The polymers were dried very thoroughly prior to placement in the reactor, and then left under high vacuum in the reactor for a minimum of 3 hours to ensure the removal of any residual oxygen, water or even small organic impurities. Schlenk techniques were also utilised, and the reactor was evacuated and refilled 7 times prior to the measurements starting. When the measurements were done in darkness, no products were detected at all. Some CO was detected under light

illumination, especially when the polymers were tested in a pure hydrogen atmosphere under illumination, with no carbon dioxide present. This was, however, around 5% of the overall rate, which supports the idea that most carbon is coming from carbon dioxide, rather than from any polymer impurity, but it does suggest that over time, in such reducing conditions the polymer does begin to degrade.

On top of the controls, to further verify that the polymers were producing CO, isotope labelling studies with $^{13}CO_2$ were carried out. **Figure 4.9** shows the spectra obtained via isotope labelling experiments. ^{13}CO was observed after light irradiation overnight but was not observed in a $^{12}CO_2$ run nor in a dark run, further highlighting the catalytic nature of the polymers. To note, isotope labelled studies were done in a batch system, rather than in the recycling system.

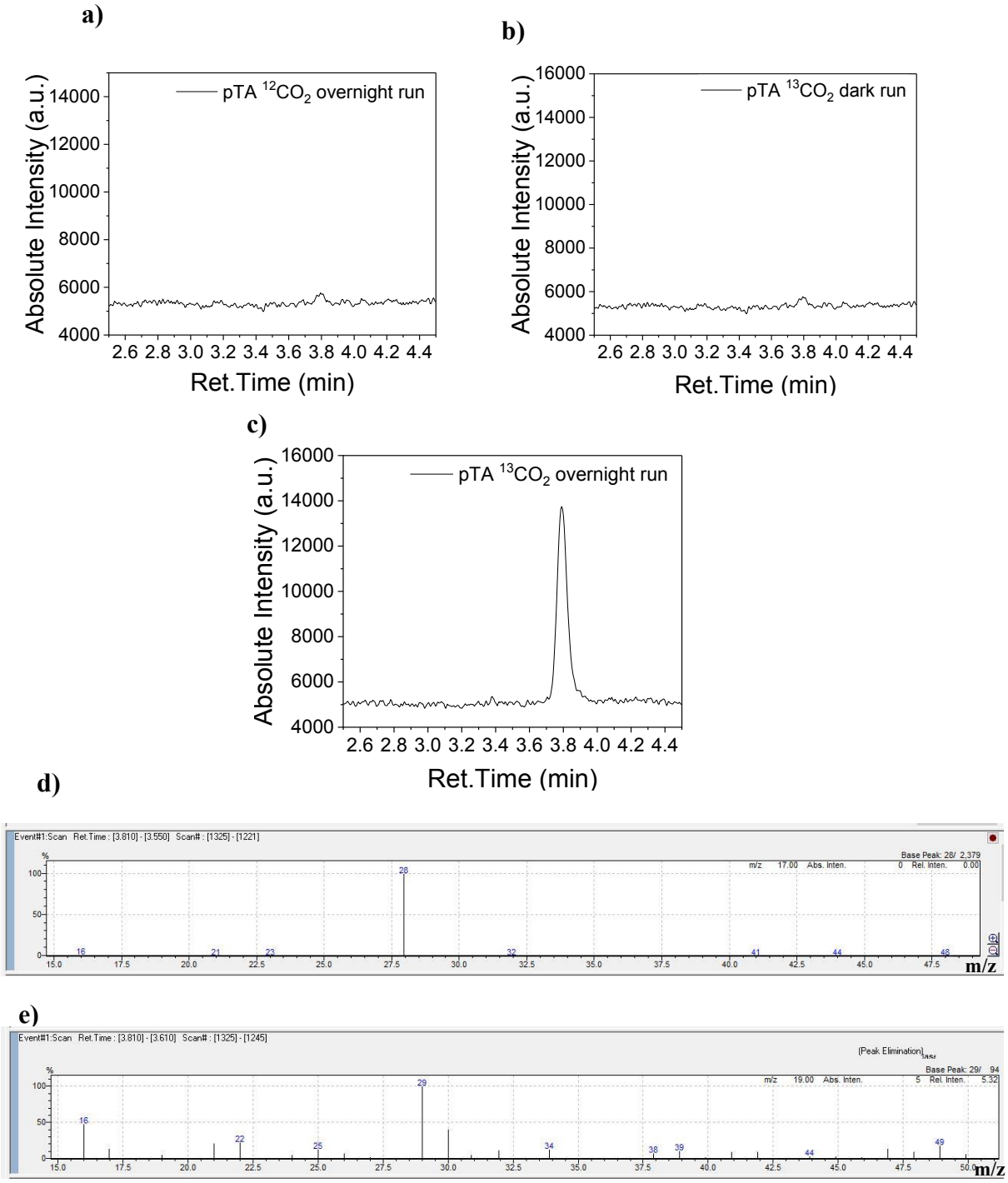


Figure 4.9: $^{12}CO_2$ and isotopic $^{13}CO_2$ measurements. Mass spectrum chromatogram of pTA illustrating the ^{13}CO (m/z = 29) peak observed with a) $^{12}CO_2$ overnight, b) $^{13}CO_2$ at time zero and c) $^{13}CO_2$ overnight, showing the ^{13}CO (m/z = 29) peak observed. D) shows the mass spectrum of ^{12}CO e) shows the mass spectrum of ^{13}CO.

4.3.2.2. Presence of added palladium.

As mentioned in section 4.3.1.3, palladium can influence the rate of photocatalysis.

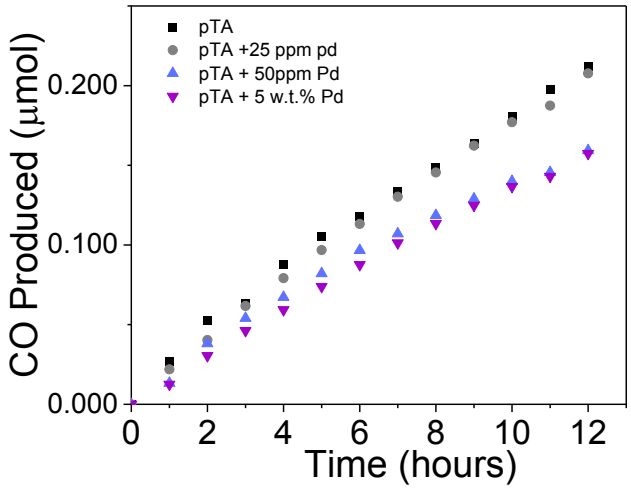


Figure 4.10: Graph showing the kinetic curves of added palladium.

Since **pTA** was formed using an iron-based catalyst, any palladium residual in the polymer from previous synthesis steps was too minute to be detectable by ICP-MS. Therefore, palladium was added to **pTA** and tested in the reactor to investigate its effect on the rate of carbon monoxide formation. **Figure 4.10** and **Table 4.6** show the results obtained.

Table 4.6: Rate with added palladium to **pTA**

Polymer	**Rate (μmol $h^{-1}g^{-1}$)**
pTA	8.49
pTA + 25 ppm Pd	8.48
pTA + 50 ppm Pd	6.57
pTA + 5 w.t.% Pd	6.52

The addition of 25 ppm of palladium decreased the rate of carbon monoxide production within the error of **pTA** with no added palladium. However, the addition of 50 ppm of palladium decreased the rate by about 20%. The addition of a much larger amount of palladium (5 w.t.%) has a very similar effect to 50 ppm. Interestingly the selectivity upon addition of 50 ppm of palladium and 5 w.t.% palladium to the polymer led to a selectivity of over 97% of CO. It was concluded that the presence of added palladium has somewhat of an effect in decreasing the

rate of reaction but was not truly proportional to the amount of palladium. It is thought that other factors would have a larger effect and contribute more to the overall error of the rates. However, this should still be noted as a possible effect, and polymers should be washed as best as possible prior to photocatalytic testing, with the aim of keeping numbers as similar as possible in direct comparisons.

4.3.2.3. Probing synthetic design

The rates of reaction obtained did show an advantage in having a structure of intrinsic porosity over carbon monoxide production. However, there was still a range of rates achieved by the four porous polymers. It was hoped that exploring these in more detail would allow some further insight into intelligent polymer design, and the factors that most affect CO production.

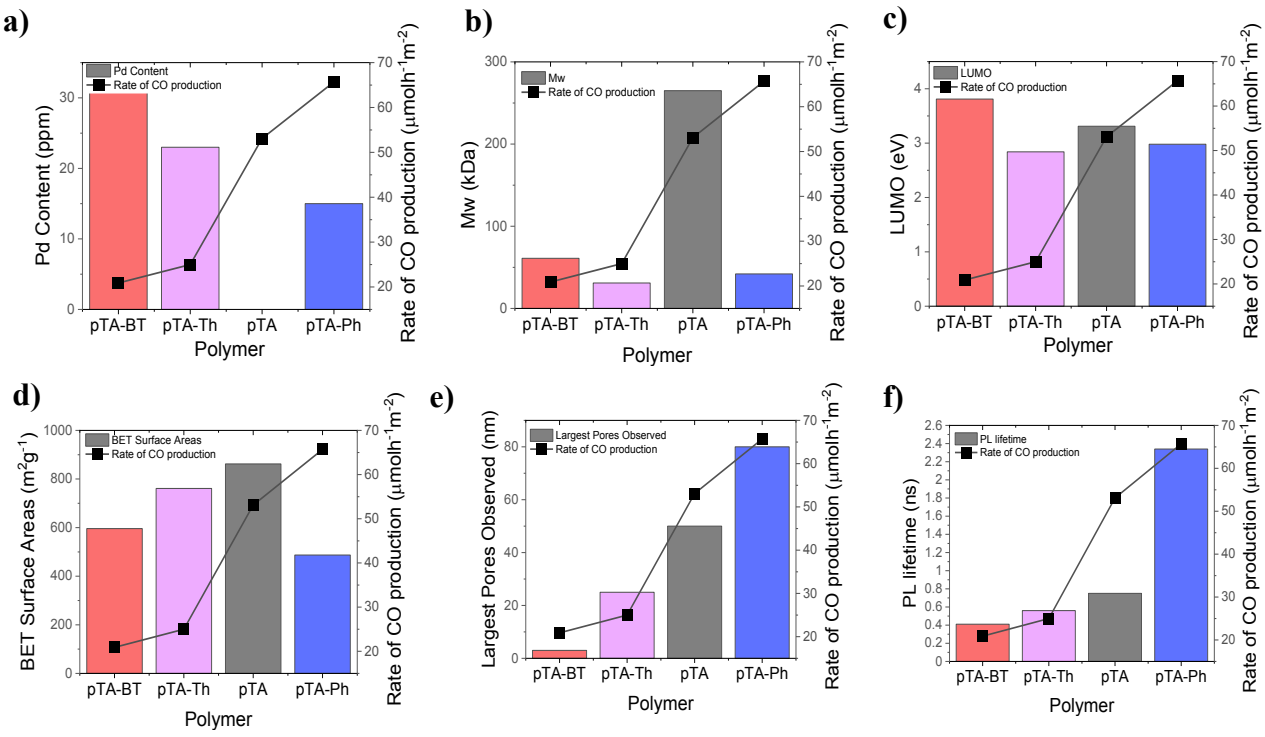


Figure 4.11 Graphs illustrating trends comparing polymer reduction rate to specific factors. For each graph, the secondary y-axis highlights the rate of CO production, and the polymers are ordered in order of highest rate. a) palladium content over rate trend shows surface area against rate trend b) BET surface areas over rate trend c) Shows the number of the largest peak in the pore distribution seen over rate trend d) LUMO level over rate trend. e) molecular weight over rate trend f) Photoluminescence lifetimes over rate trend

Factors that could influence photocatalysis were evaluated, to see if any had a linear correlation with an increase in rate, which is shown in **Figure 4.11**. Residual palladium content was investigated as mentioned in sections 4.3.1.3 and 4.3.2.2. A decrease in rate with an addition of 50 ppm of palladium was found, suggesting that the presence of palladium is not favourable

in the photoreduction conditions chosen in this study and it was noted that the slightly larger amount of palladium in **pTA-BT** could contribute to the decrease in rate. However, since the trend was not found to be scalable or linear, the overall maximum decrease in rate was less than 20 % with 50 ppm of palladium and the addition of around 25 ppm of palladium to **pTA** (which is similar to the amount found in the remaining polymers by ICP-MS) was within error and had little effect on rate (**Figure 4.11a**). It was therefore ruled that, although it should be taken into consideration, the amount of palladium was not the most important factor contributing to carbon monoxide formation.

Molecular weight also did not follow a specific trend, as shown in **Figure 4.11b)**. Energy levels were thought to affect the driving force of the reaction, but was not the most important factor affecting product evolution, since the control polymer had the largest bandgap and shallowest LUMO, but was the worst performing **Figure 4.11c)**. The surface area calculated from the BET isotherms, **Figure 4.11d),** also did not follow the trend of product evolution, after a certain surface area was achieved. It should be noted that all these factors likely have some effect, and it is a combination of these which can together determine the overall rate. However, it was found that two factors mirrored the product evolution trend convincingly. The distribution of pores showed a close correlation, with polymers exhibiting larger pore distributions performing better in CO_2 photoreduction. The larger pore sizes observed in the polymers were summarised in **Figure 4.11e),** and there does appear to be some correlation with increased rate and larger pores. Open porous structures, have shown to be advantageous for uninterrupted gas flow over microporous structures. This is because larger pores could increase movement of reactant gas into active sites, decrease the blocking of pores due to product or intermediate build up, and therefore could be a factor affecting the overall reaction rate.[53,54] Another important factor seen to correlate in **Figure 4.11f)** was the photoluminescence lifetime decay kinetics. This measurement provides information on how long it takes for excited states to recombine. The trend in rate of CO production was seen to match the trend of increasing PL decay lifetimes for the polymers. A charge that is longer lived is more likely to travel to the active sites and take part in reactions and is less likely to recombine more quickly. [55] It should be noted, that PLQY might have also followed the rate trend. An anomaly is observed for **pTA-Ph**, but this is likely due to the measurement being too close to the detection limit of the machine used. A higher PLQY would suggest that there is a decrease in non-radiative decay, which indicates a decrease in recombination, which also has a positive impact on photocatalysis rate as more charges are likely to take part in chemistry. It should not be ruled out that pore sizes formed due to rigid

structures might not have a direct effect on the PLQY or general photoluminescence of materials.[56–62] The incorporation of rigid structures has been used in OLED literature before showing good emissive behaviour, and more rigid structures could potentially display a decrease in non-radiative decay.[63] Micropores could provide sites of charge trapping, which decrease overall recombination, therefore the two main factors affecting CO production rate could be directly related to each other. [64]

4.3.2.4. Hydrogen evolution experiments

Hydrogen evolution experiments were carried out in water, in a home built hydrogen evolution set-up, modelled on a previously reported set-up from KAUST. The results are shown in **Figure 4.12**. The conditions were also chosen to replicate those developed by Kosco *et al*. since these have been optimised for hydrogen evolution using organic materials in the same reactor type. Platinum was used as a co-catalyst in the system, and ascorbic acid was employed as a sacrificial reagent. [33,65]

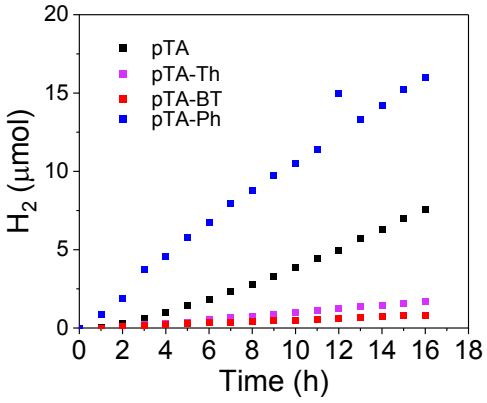


Figure 4.12: Rate of Hydrogen production over time, conditions: 2 mg of polymer, 0.2 mol l^{-1} ascorbic acid (20 ml), pH 2, 5% (10 µg) Pt, 300 W Xe lamp (350 to 800 nm), 160 cm^2 reactor.

The rates of hydrogen evolution mirror, in trend, those shown in carbon dioxide photocatalysis. This is significant because it is likely that surface area and pore sizes have a smaller effect in nanoparticle form on the rate in solution than they do in the gas phase. This suggests that photoluminescence, however, still plays a very large role. It should, however, be noted that **pTA** in the gas phase has a much closer rate to **pTA-Ph**, which suggests that its porosity in the gas phase also largely contributes to the rate but while cementing PL decay kinetics as the most key factor in this series.

4.3.2.5. CO_2 photocatalysis in water

Carbon dioxide photocatalysis in water was also briefly tested as a control experiment in **Figure 4.13**. The conditions used are those optimised in literature. [66]

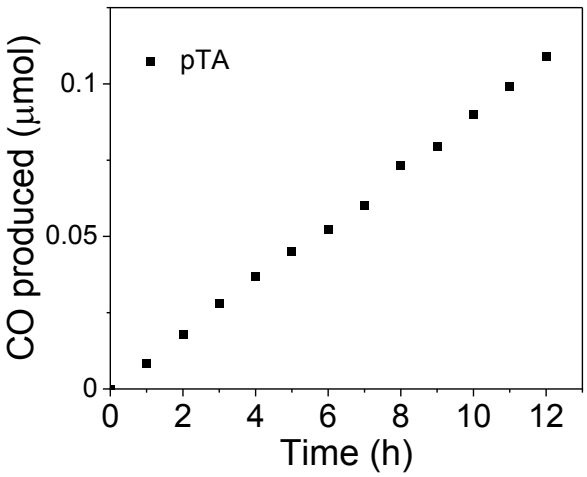


Figure 4.13: CO production over 12 hours by **pTA** in aqueous conditions. Conditions: 5 mg of polymer, 10 mg 2,2′-bipyridine and 5 µmol cobalt(ii) chloride, a mixture of acetonitrile, water and triethanolamine (3 : 1 : 1 vol, 5 mL), were charged to a vial, the suspension was ultrasonicated for 20 minutes. The contents were transferred to the same reactor as that used for gas phase photocatalysis, the solution was purged with CO_2 for 2 hours.

The rate obtained was 0.009 $\mu mol^{-1}h^{-1}$ of CO formation which was half that obtained in the gas phase, further supporting the use of gas phase testing for porous polymers, to fully take advantage of the properties afforded by the polymers.

4.3.3. Copper co-catalyst

Copper, in its various oxidation states, has shown great promise as a co-catalyst for carbon dioxide reduction. It has been shown to strengthen the binding to carbon dioxide and carbon monoxide, and to stabilise C-C coupling reactions, which increases the likelihood to higher hydrocarbons being produced. [67] Copper (II) complexes have been shown to photocatalytically produce CO from CO_2.[68] Copper metal has been established as a good co-catalyst, favouring carbon dioxide photoreduction. [69–71]

In this study, copper iodide (CuI) was chosen as a source of copper as a co-catalyst for carbon dioxide photoreduction. CuI is, in itself, a known co-catalyst for C_{2+} products in electrochemical CO_2 reduction. [72] It has shown promise on graphic carbon nitride for increased light absorption in photocatalytic pollutant removal and as an antibacterial.[73] CuI has moreover shown promise as a transparent hole transporting layer in photovoltaic devices, with high

conductivity.[74] Copper iodide has also been shown to catalyse CO_2 photoreduction by itself. [75] However, in the reactor conditions used for this study, the amount of CuI that would have been present on the polymers was tested and no products were detected, likely due to its absorbance in the UV being cut off by the visible light filter.

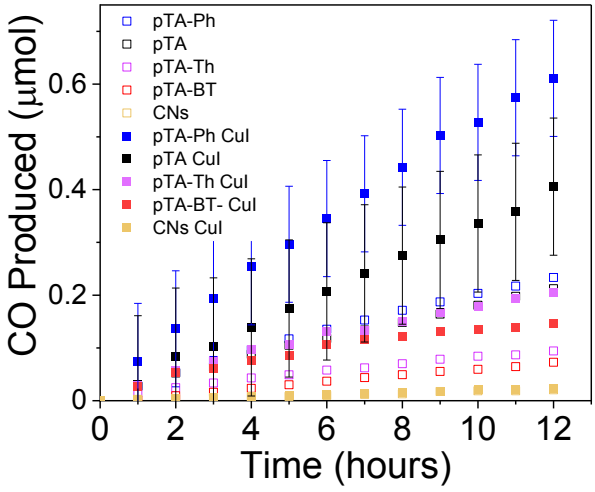


Figure 4.14: CO production including CuI as a co-catalyst and comparing to no added metal catalyst.

When CuI was added to the polymers, a higher rate of product formation was observed. 5 w.t.% of CuI was added to the polymers in solution, the mixture was sonicated for 5 min and the overall solution was drop-cast. **Figure 4.14** shows the performance of the polymers upon addition of a copper iodide co-catalyst. The trend remained the same. As can be seen from the figure, the trend remained the same, and carbon nitride showed minor improvement only. This could be due to CNs being insoluble, and therefore the co-catalyst may not have dispersed well through the structure. The other polymers' rate doubled, with **pTA-Ph** reaching a rate of 175 µmol $h^{-1}m^{-2}$.

Table 4.7: Table summarising rates with copper iodide compared to without

Polymer	Rate with no CuI for ref. (μmol $h^{-1}m^{-2}$)	Selectivity to CO production with CuI (%)*	Rate with CuI (μmol h^{-1})	Rate with CuI (μmol $h^{-1}g^{-1}$)	Rate with CuI (μmol $h^{-1}m^{-2}$)
pTA	53 ± 3	95	0.033 ±0.003	17 ± 1.5	106 ± 10
pTA -Ph	66 ± 4	94	0.05 ±0.01	25 ± 5	175 ± 35
pTA -Th	25 ± 3	95	0.016 ±0.005	8 ± 2.5	55 ± 17
pTA -BT	21 ± 4	98	0.015 ±0.002	6 ± 1	37 ± 6
CNs	5 ± 2	-	0.88 ± 0.2	1 ± 0.3	7 ± 2

As can be seen from **Figure 4.14** and **Table 4.7**, although the rates did increase, it should be noted that the errors associated with the measurements was quite high, especially with **pTA** and **pTA-Ph**. This deviation was calculated by taking an average of at least 4 measurements. It is thought that this difference is due to variation in the dispersion of the catalyst using the drop-casting method.

In order to probe the effect of the iodine specie, Copper Bromide (CuBr) was also tested with **pTA-Ph**, and yielded a rate of 127 μmol $h^{-1}m^{-2}$, this was only slightly lower than when using CuI (175 μmol $h^{-1}m^{-2}$). The similar increase in the rate of reaction when adding CuI or CuBr to **pTA-Ph** compared to the polymer by itself suggested that the copper is the important specie in the reaction, and the effect of the iodine is less significant than that of the copper. Although it was hypothesised that the inclusion of copper iodide could further disrupt packing and therefore lead to increased reduction rate, since the addition of palladium did not have the same effect, it is thought that the copper nanoparticles act as co-catalysts.

Photoluminescence spectra of the polymers containing 5 w.t.% of CuI, after operation, were compared with the PL spectra of the pristine polymer film, with no added co-catalysts, in **Figure 4.15**.

.

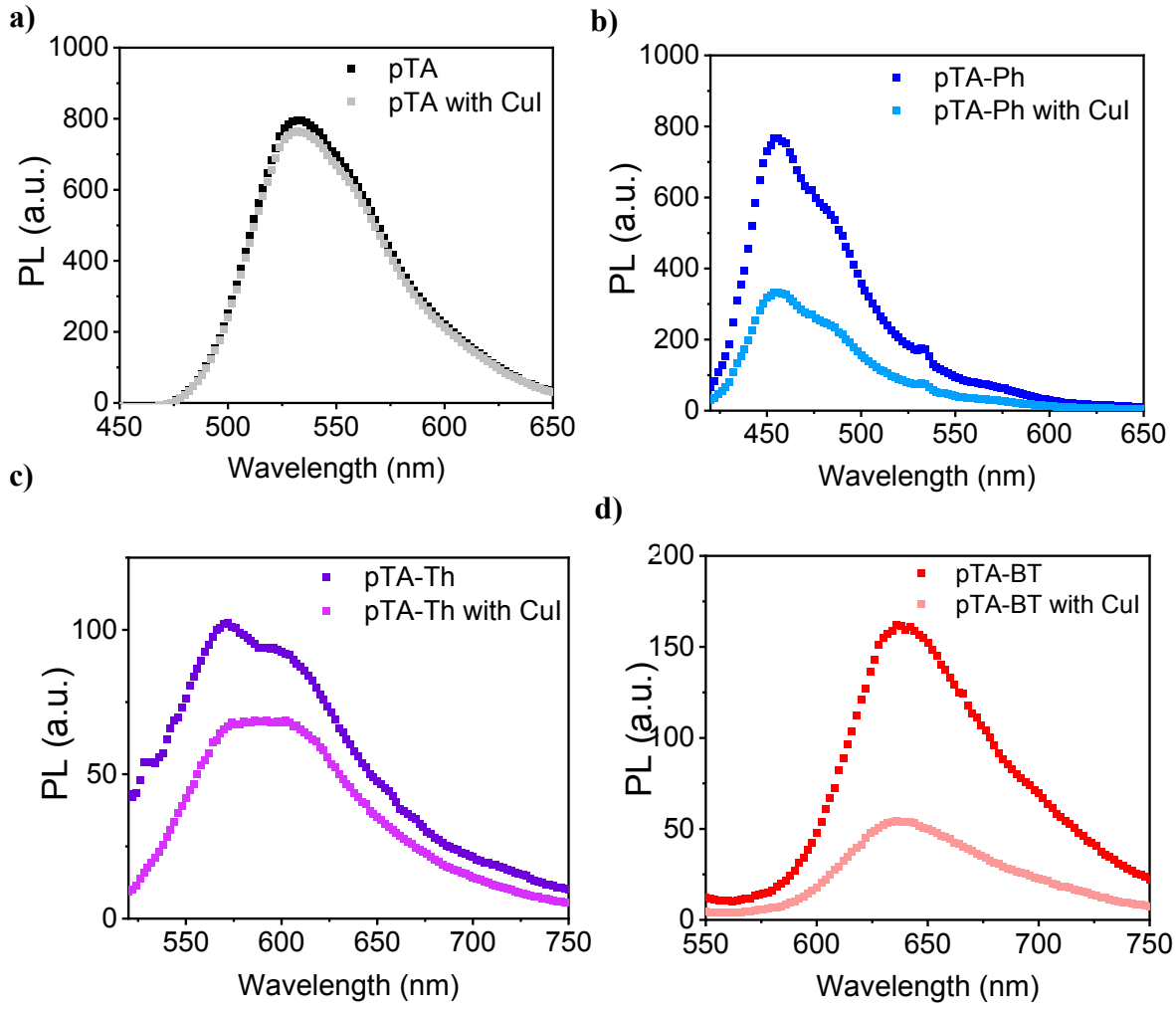


Figure 4.15 a-d: PL e PL spectra of pristine polymers as well as polymers in the presence of CuI, the measurements were carried out in hydrogen to mimic photocatalysis conditions.

The presence of CuI in the films resulted in photoluminescence quenching in polymers **pTA-Ph**, **pTA-Th** and **pTA-BT**, with PLQ of 48%, 35% and 67% respectively of their original copper free value. The quenching supports that charge or energy transfer is taking place from the polymer to the copper iodide co-catalyst. This was not observed in **pTA**, but the rate was indeed seen to improve when CuI was added to the polymer, albeit the increase was smaller relative to **pTA-Ph**. This, coupled with the large error bars exhibited in the graph, suggest some inconsistencies in the addition of copper iodide to the polymers. It is thought that different copper species are forming in the **pTA** microstructure, compared to other polymers which could explain the smaller performance increase. Furthermore, it could be an issue of dispersion, mixing in copper iodide, sonicating, and drop-casting a sample it perhaps not the most reliable

way to achieve uniformity. It would be beneficial in future to investigate ways of ensuring the co-catalyst sits on the active sites and is dispersed evenly in the sample.

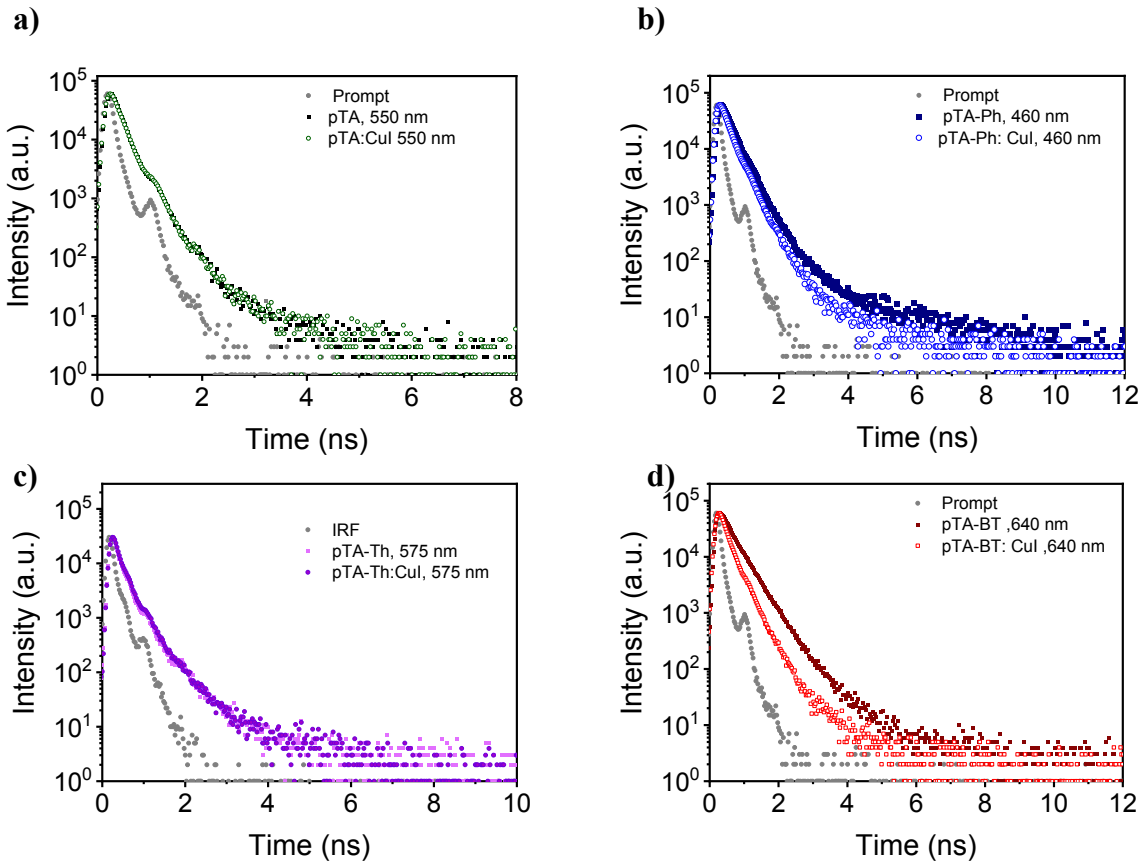


Figure 4.16: Comparison PL decay kinetics of polymer films with/without CuI measured a the maximum PL intensity. Excitation wavelength 404 nm

Analysing the photoluminescence decay kinetics, shown in **Figure 4.16**, supports the idea that there is some inconsistency with the overall way the catalyst is deposited. **pTA-Ph** and **pTA-Th** show a marked decrease in lifetime, which again suggest quenching of energy from the polymer to the co-catalyst. **pTA** and **pTA-Th** show this to a much smaller extent.

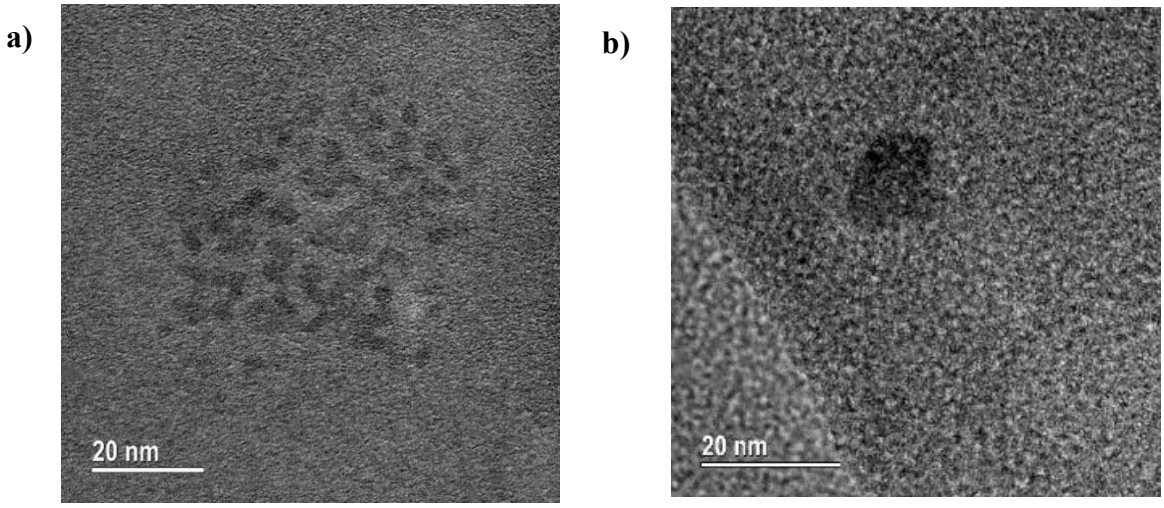


Figure 4.17: TEM images showing copper nanoparticles formed on a **pTA-Ph** polymer film after operation

To image the copper co-catalyst, TEM analysis was carried out on a sample of **pTA-Ph** with 5 w.t.% CuI, after operation. The black clusters in **Figure 4.17a)** which measure around 20 nm, were spread out around the surface of the polymer, showing the distribution was indeed unevenly distributed throughout the polymer film. As can be seen in more detail in the cluster shown in **Figure 4.17b)**, is it likely these nanoparticles are made of copper metal, supporting that during photocatalysis testing, the hydrogen atmosphere and presence of light facilitate the formation of Cu (0) from Cu (I).

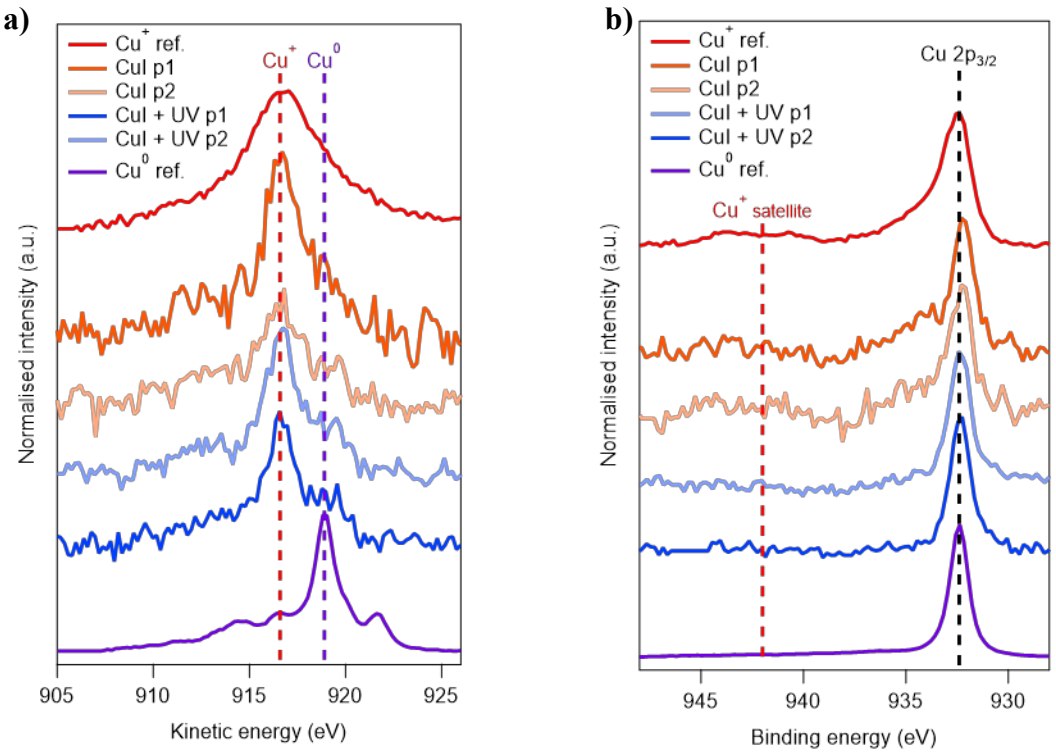


Figure 4.18: XPS data showing CuI with and without exposure to photocatalytic conditions in the reactor and compared to reference materials. Both figures show Cu^0 and Cu^+ as references, p1 and p2 refer to different points on the surface on which the measurement was focused and "UV" highlights the samples which were exposed to light and H_2:CO_2. a) shows the Cu LMM Auger peak, b) shows the Cu $2p_{3/2}$ XPS peak.

XPS of copper iodide was measured on thin film with and without any exposure to hydrogen and light, as seen in **Figure 4.18**. The references for copper(I) was Cu_2O, shown in red, and for copper(0), copper metal was prepared by argon ion etching under UV light and is shown in purple.

In XPS following ionization, an outer shell electron can fill the vacancy created in the lower shell, the energy released in this process can result in the emission of an auger electron. Auger spectra have unique shapes and positions which is useful in identifying the element and its chemical state. Since most copper species share the main Cu LMM Auger peak, the secondary peak was taken into consideration for proving the existence of copper metal.

In **Figure 4.18**a) The orange sample represents copper iodide with no treatment, and it shows as Cu LMM Auger peak at 916.6 eV, due to the presence of Cu(I), likely from formation under photocatalytic conditions.[76] The blue sample represents copper iodide after photocatalysis, whereby it was exposed to hydrogen and UV-light. This sample exhibits a 20% increase in a secondary peak at 919 eV, which is consistent with an increased presence of copper metal, which corresponds to the reference spectrum. The same peak was not observed in samples that were not exposed to photocatalytic conditions. Auger electrons always have the same kinetic

energy resulting from the process of Auger emission, irrespective of the incident X-ray photon energy, so are plotted on a kinetic energy axis.

Figure 4.18b) shows the. Cu $2p_{3/2}$ XPS peak. Each of the samples showed a principal peak at around 932 eV. CuI samples also showed some satellite features around 938 eV. Peak positions and spectral shapes are consistent with XPS literature, for the binding energy referencing used in this work.[77,78] Here the binding energy is plotted, since XPS peaks are always at a fixed binding energy, irrespective of the photon energy. Experimentally, kinetic energy of the photoelectrons is measured, and the binding energy is calculated by using equation 4.1:

$$BE = h\nu + \Phi - KE \qquad (4.1)$$

Whereby BE is the binding energy, Φ is the work function, hν the photon energy and KE the kinetic energy.

Since the samples were quite dilute (5% CuI, as in the photocatalysis measurements), XPS was collected in narrow regions to maximise the counting time.

4.3.3.1. Polymer Blends

Another strategy for increasing carbon dioxide photocatalysis that was employed was the use of polymer blends. This is a common technique that has been successfully used in OPV and in hydrogen evolution. This is because, unlike in inorganic devices, the low dielectric constant of organic materials means it is more difficult for an exciton to dissociate. But it can do so at an interface, with an offset greater than its photon binding energy. This allows the dissociation of the exciton over two materials, and the subsequent transfer of charges to either material.

The blends in this section were made up of 50:50 of each polymer in the blend, unless otherwise stated.

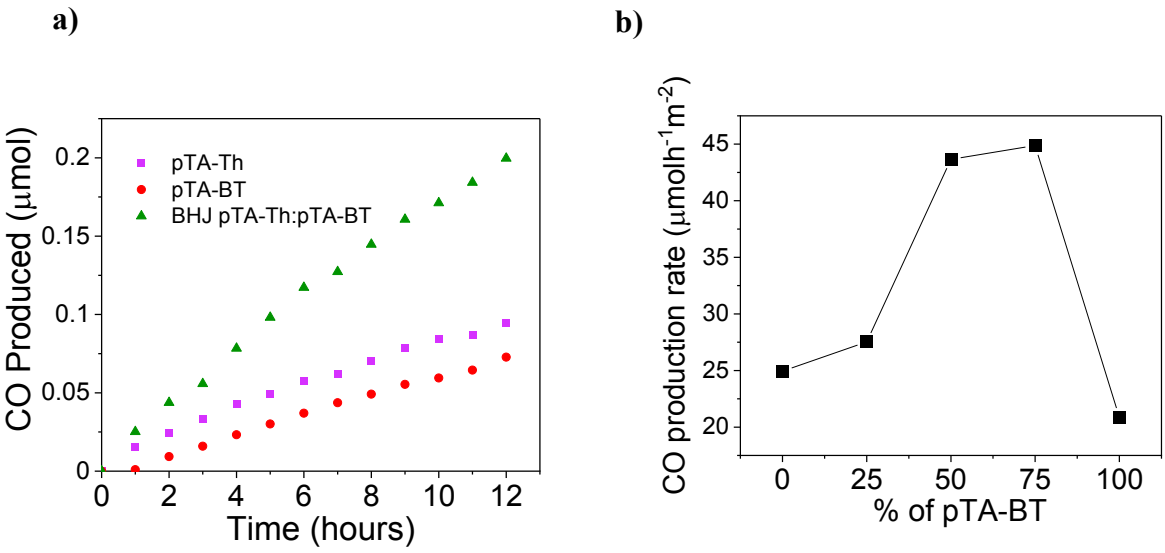


Figure 4.19:a) carbon monoxide production comparison between **pTA-Th** and **pTA-BT** as single component and together as a blend b) rate of carbon monoxide dependent on the ratio of **pTA-Th** and **pTA-BT** polymer blends.

Figure 4.19a) shows the rate obtained from blending **pTA-Th** and **pTA-BT** was over three times that of the single components and higher than the two put together. The blends had the best type two offset of the polymers in this study. The increase in rate suggest that the polymers are working as a heterojunction when blended. **Figure 4.19b)** shows the rates obtained when varying the ratio of the two polymers, with the highest rate obtained when using 75% of **pTA-BT** and 25 % **pTA-Th**.

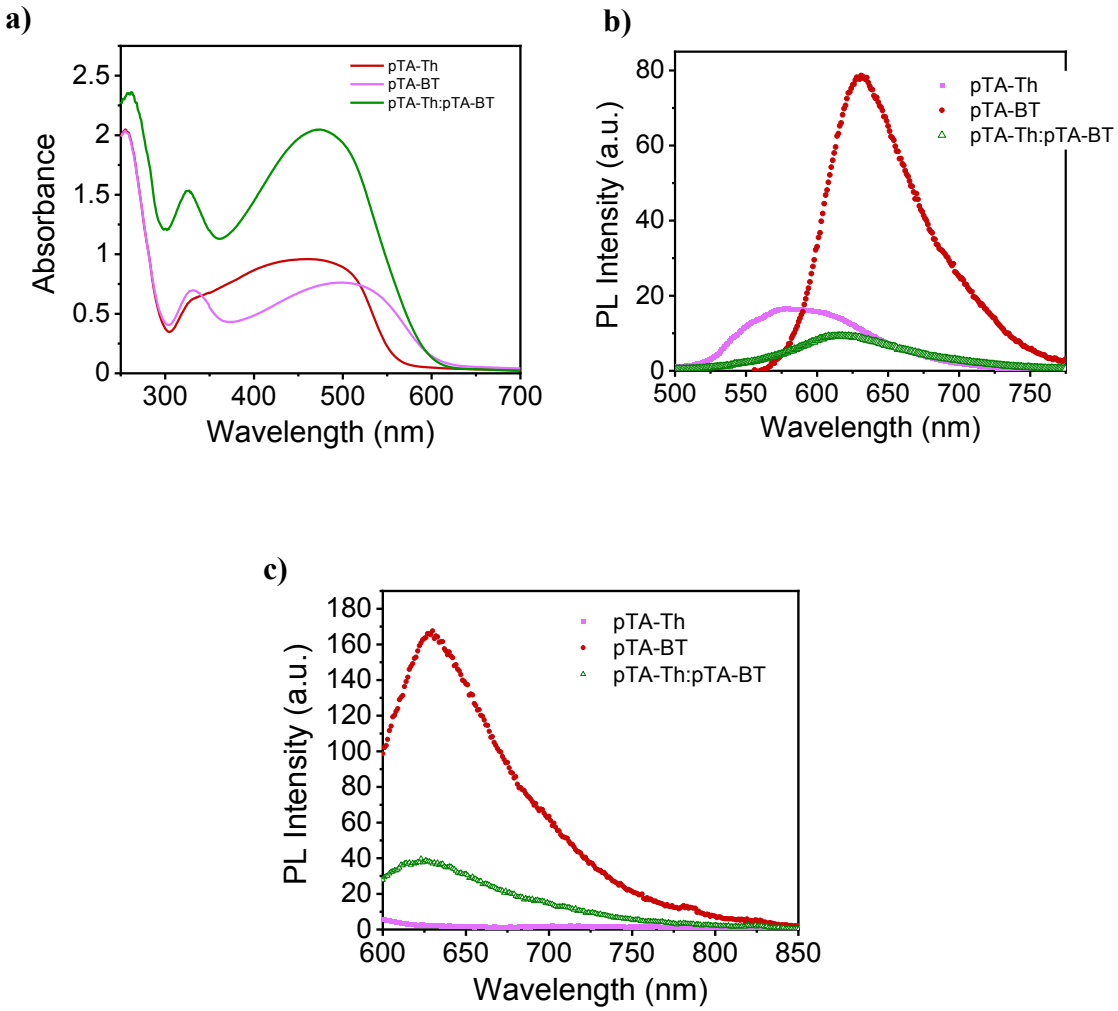


Figure 4.20: Comparison of the a) UV-Vis and b-c) PL spectra of neat polymer films and heterojunction **pTA**:**Th**:**pTA-BT** 1:1. (prepared using 0.25 mg). Excitation wavelength of 400 nm (b) and 575 nm(c).

The PL spectrum of heterojunction **pTA-Th**:**pTA-BT**, shown in **Figure 4.20**, showed an emission band centre at 625 nm upon 400 nm excitation, which corresponds to **pTA-BT** emission. This indicates efficient quenching of the exciton on polymer **pTA-Th** due electron transfer (or energy transfer) from **pTA-Th** to **pTA-BT**. Selective excitation of **pTA**- BT at 575 nm in the heterojunction showed the emission band at 625 nm, in agreement with the emission band assigned to **pTA-BT**, which exhibit a PLQ= 78 %, indicative of less efficient hole transfer from **pTA-BT** to **pTA-Th**.

Interestingly, the other combinations of polymers did not have the same result, the heterojunction was not found to improve more than the best performing polymer, as show in **Figure 4.21**.

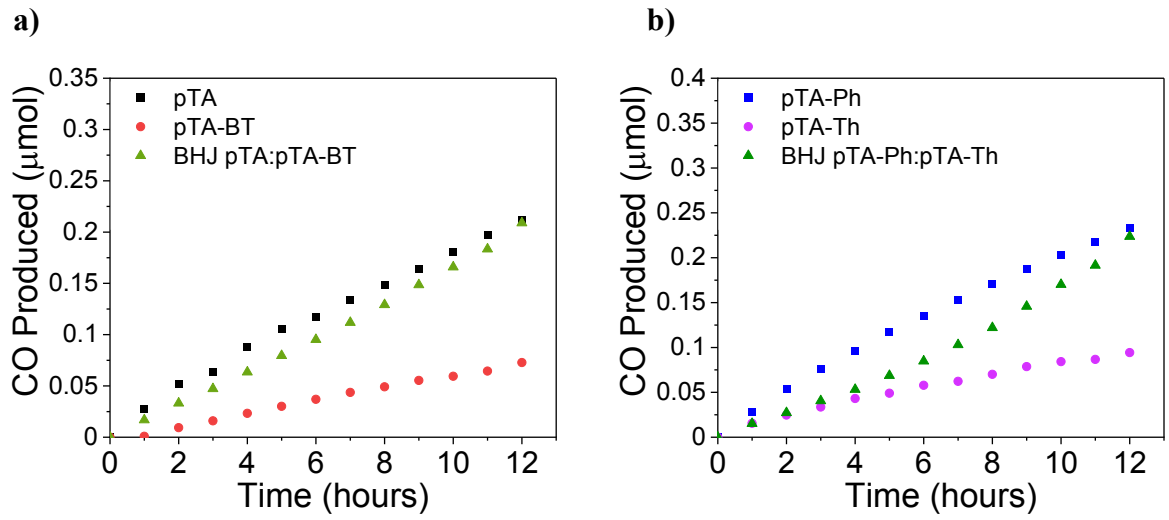


Figure 4.21: Rate of CO produced in blends a) comparing the blend pf pTA and pTA:BT to the single components b) comparing the blend of pTA-Ph and pTA-Th to its single components.

PL of the blends versus single components did not show good quenching, suggesting the polymers did not form effective heterojunctions.

For example, **Figure 4.22** shows the PL spectra of the **pTA-BT** and **pTA** blend. PLQ at 400 nm 86 % for **PTA** and 80 % for **pTA-BT**. Exciting at 550 nm the PLQY is 33 %. This indicating inefficient electron and hole transfer in this system relative to previous heterojunction.

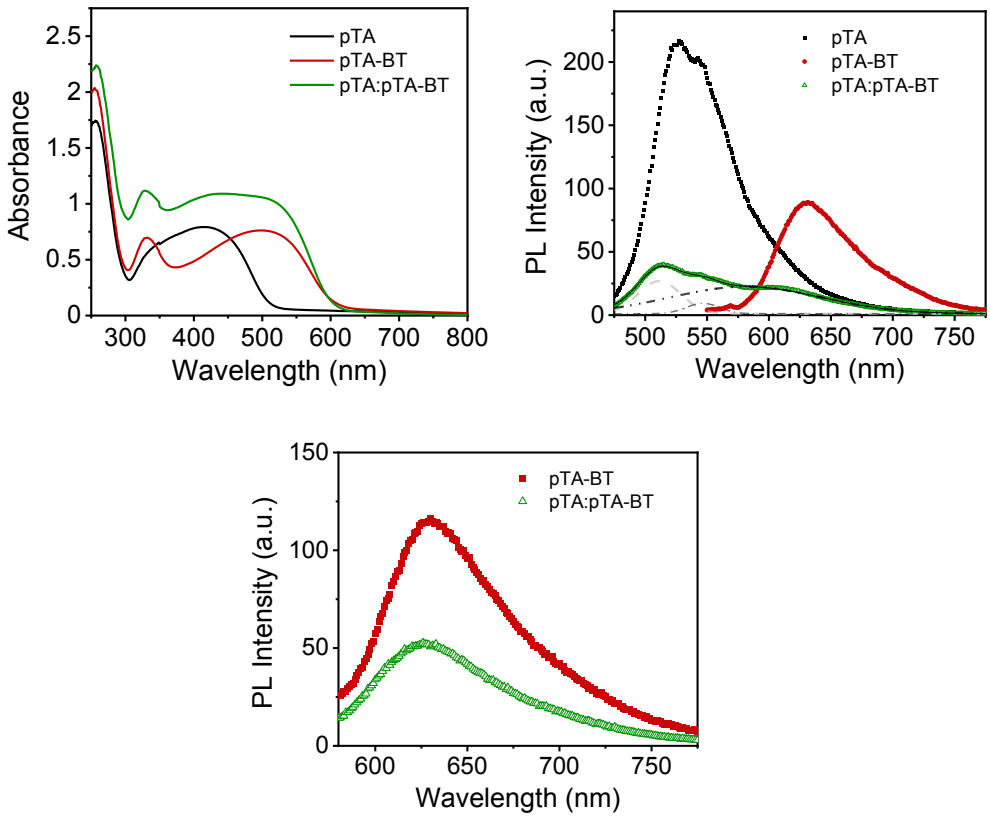


Figure 4.22: Comparison of the a) UV-Vis and b-c) PL spectra of neat polymer films and heterojunction **pTA**:**pTA-BT** 1:1. (prepared using 0.25 mg). Excitation wavelength of 400 nm (b) and 550 nm(c).

It is likely that the other blends are possible not as well mixed, and therefore reduce the amount of quenching and charge transfer possible. Since both polymers are similar in morphology and amorphous, no changes were observed by TEM, and since the difference in elements is so minute, elemental mapping also did not give good evidence of polymer distribution. It could be useful to investigate depositing and forming the blend in more detail, and perhaps utilising more sensitive imaging. It should be noted that exciton diffusion lengths are around 10 nm, therefore, the morphology of the blend is very important, since if the interfaces are significantly further away than the exciton diffusion length, recombination will occur.[79]

It should also be noted, however, that **pTA-Th**: **pTA-BT** had the best type 2 offset, which likely contributed to better charger or energy transfer between the two polymers. In the future, it would be ideal to design a series of porous polymers which would act as acceptors, to investigate effective heterojunctions for porous polymers in carbon dioxide photocatalysis.

4.4. Conclusions and Future Work

A set of donor conjugated polymers with intrinsic microporosity and great solution processibility were synthesised based on the **p3HT** backbone, and were compared to literature standards, and a non-porous control polymer, **pDHT**. The polymers were investigated in the reduction of carbon dioxide photoreduction in the presence of hydrogen.

The porous polymers were found to greatly outperform the non-porous **p3HT** and **pDHT**, and were also found to outperform the carbon nitride and TiO_2 standards. To gain insight into the relationships between polymers properties and rate of product formation, various factors known to affect photocatalysis were considered and investigated. It was found that a high photoluminescence and longer decay kinetics were likely to increase rate of photocatalysis. It was also seen that a higher distribution of larger pores also could cause increase in carbon dioxide photocatalysis, likely due to an ease of gasses moving in and out of the pores more effectively to reach the active sites. The investigation into porous polymers for carbon dioxide photoreduction led to the conclusion that high porosity is indeed an important property to strive towards in gas phase photocatalysis, but once high porosity is achieved, other factors that commonly affect solution phase photocatalysis also play a vital role, such as high PL decay kinetics, and should be taken into consideration.

Charge carrier recombination likely happens quickly in these polymers at 1 sun, however, further work into modelling the recombination dynamics, to further understand the dominating recombination regimes should be carried out, especially if it occurs immediately in a bimolecular process, or if monomolecular mechanisms prevail. This could also aid in better understanding if traps and defects in these polymers are greatly affected by pore size and surface area. As mentioned, PL decay lifetimes can give an idea of a higher or lower non-radiative decay, and can have implication that the excitons are longer lived, but this does not necessarily correlate to a higher diffusion length of the excitons or charges. In order to obtain a clearer picture, exciton mobilities of the materials could be measured. For single component, undoped, wide band gap semiconductors, which normally show low mobilities, techniques such as: space-charge-limited current, impedance spectroscopy or photogenerated charges in carrier extraction by linearly increasing voltage could be used. Using the polymers in organic electrochemical transistors can also be used to obtain mobility values. [80–83] Once longer-lived excitons are achieved, likely using co-catalysts or blends of the polymers further photophysical characterisation and the use of Transient-Absorption Spectroscopy (TAS) and Photo-Induced

Absorption Spectroscopy (PIAS) could provide further information on exciton dissociation and the lifetimes of generated charges. [84]

To increase the rate of product formation two techniques were tested. Firstly, copper iodide was used as a source of copper co-catalyst in the polymers. Mixing the metal salt in the polymer films, under photocatalysis operating conditions, led to the formation of copper metal, which helped to catalyse CO_2 photoreduction, showing an improvement in rate of more than double for the best performing polymer, **pTA-Ph**. Secondly, blends of the polymers were tested to attempt to form a type II heterojunction and increase performance. A blend of **pTA-Th** and **pTA-BT**, two polymers with an idea type II offset in energy levels, showed a vast increase in rate, more than double that of the two polymers by themselves. This investigation paved the way for the use of organic materials in the hydrogenation of carbon dioxide, and in the use of stable and effective, polymers of intrinsic microporosity which retain their processibility. In order to further this investigation, it would be ideal, as a next step, to synthesise a series of acceptor based porous polymers to form heterojunctions with better offsets while also retaining porosity. It could also be interesting to pair a porous polymer with another non-porous specie (for example an NDI polymer or a small molecule), to see if some porosity is maintained, and high rates still possible even if just one of the components is intrinsically porous.

Another interesting investigation for future work would also aim to develop further insights on the mechanism for hydrogenation of carbon dioxide, and to better understand where example the active site would be on the polymers. Understanding this would allow for better design, targeting specific CO_2 adsorption modes, or specific active sites. Computational modelling could be a way to begin addressing this and would be beneficial for the whole community of carbon dioxide photocatalysis. The use of copper iodide was particularly interesting; however, the high error bars suggest a decrease in reproducibility compared to the single component polymers. It would be ideal to find ways to target the copper onto the active sites of the polymers in a more spread out and effective manner rather than just randomly. It should also be noted that the synthesis of polymers of intrinsic porosity with surface areas between 400-860 m^2g^{-1} are amongst the highest ever reported, especially for conjugated polymers. This opens incredible opportunities for other applications for these materials. Currently the author has begun collaborations to form membranes of the materials for use in fuel cells and redox batteries, so although the design of these polymers was thought for CO_2 hydrogenation, their properties make them appropriate for other applications.

4.5. Experimental

4.5.1. Methods and Materials

NMR, Molecular weight analysis, UV-Vis analysis and PESA were carried out as described in Chapter 2.

Sorption Analysis

BET sorption and pore size data were recorded on a Micromeritics 3Flex Surface Characterization Analyzer using multi-point surface area analysis. Surface areas were measured by nitrogen adsorption and desorption at 77.3 K. Samples were degassed for 4 hours at 100 ^{o}C, under vacuum. Surface areas were calculated in the relative pressure (P/P_0) range from 0.1 to 0.6 of the adsorption branches. The pore size distribution was estimated by the desorption isotherm, using the Barrett, Joyner, and Halenda (BJH) method.

Inductively Coupled Plasma Mass Spectrometry

Palladium and Iron contents were determined by ICP-MS using a Perkin Elmer NEXION 2000B. Polymer samples (between 2.5 mg and 5 mg) were digested in nitric acid (2 mL) using a Perkin Elmer Microwave Titan, diluted to 2% nitric acid to water, to a volume of 100 mL. Instrument sensitivity was 1 ppb (0.0000001 wt. %) baseline with respect to the digested sample solution, therefore 'useable' limit is 10 ppm (0.001 wt. %) with respect to the full polymer sample.

Transmission Electron Microscopy (TEM)

TEM was carried out on a JEOL-2100 TEM . Samples were drop-cast onto Cu TEM grids from chloroform solutions after photocatalysis experiments.

X-ray photoelectron spectroscopy (XPS)

Surfaces were formed by spin-coating films on ITO glass and subsequently studied by X-ray photoelectron spectroscopy (XPS) using a water-cooled monochromatic Al Kα source (hν = 1486.6 eV, 15 kV anode voltage, 25 W beam power). Charge compensation with the in-built e^- flood-gun was utilised to prevent peak broadening and position changes induced by charging (1.35 V electron energy, 20 μA beam current). Core level spectra were collected with a pass energy of 55 eV and a step size of 0.1 eV / step (giving a Ag 3d5/2 peak with fwhm of 0.69 eV). The analysis chamber pressure was maintained below 5×10^{-9} mbar during measurement. Data analysis was performed using the CasaXPS software package.

Time-Correlated Single-Photon Counting (TCSPC)

The PL lifetime of polymers thin-films were measured using time-Correlated Single-Photon Counting (TCSPC) setup (Horiba DeltaFlex), equipped with a pulsed LED excitation source (404 nm, Horiba NanoLED series) and a fast rise-time photomultiplier detector (Horiba PPD-650). The instrument response function (IRF) was measured at the excitation wavelength. A suitable long-pass filter was inserted between the sample and detector to block off scattered excitation light in all the measurements.

CO_2 Photocatalysis Measurements

The Photocatalytic Reactor Set-up is described in detail in Chapter 3. 300-W Xe lamp (Asahi Max 303) fitted with an ultraviolet–visible mirror module (350–800 nm) and calibrated to 1 sun using an Ocean Optics USB2000 spectrometer. The amounts of gaseous photoreduction products were recorded by an Agilent 8860 GC system, equipped with TCD and FID detectors. Calibration was carried out using a custom-made reference gas containing 1000 ppm of CO_2, CO and CH_4 (Polymers were drop cast on a glass slide, loaded into the reactor and vacuum was applied for 3 hours. The system was evacuated and refilled 6 times with CO_2 and H_2 gasses in the ratio 3:1 (H_2:CO_2). The pressure in the reactor was allowed to increase to 1.15 bar, after which the system was sealed and simulated sunlight at A.M 1.5 was irradiated on the polymer film. A rotary pump was employed as part of the gas-tight set-up to ensure flow of gasses through the system, and the mixture was injected every hour into a GC flowing in nitrogen, equipped with FID detector and Jetanizer. For stability studies, the chamber was evacuated and refilled with CO_2 and H_2 every 24 hours, the sample was left in the chamber. The illumination area and mass of polymers were kept as constant as possible to allow for close comparison between the polymers.

$^{13}CO_2$ Photocatalysis Measurements

These were done on the set-up of the Eslava Group (Imperial College London), at atmospheric pressure, $^{13}CO_2$ (BOC, >99.9 % atom) was flushed through the reactor with hydrogen, the 35 mL reactor was closed and 1.5 AM sun was shone overnight. The evolved gasses were analysed by a mass spectrometer (Shimadzu MS) equipped with a Q-bond and a MolSieve column with gas sampling valves connected directly to the photoreactor.

H_2 Photocatalysis Measurements

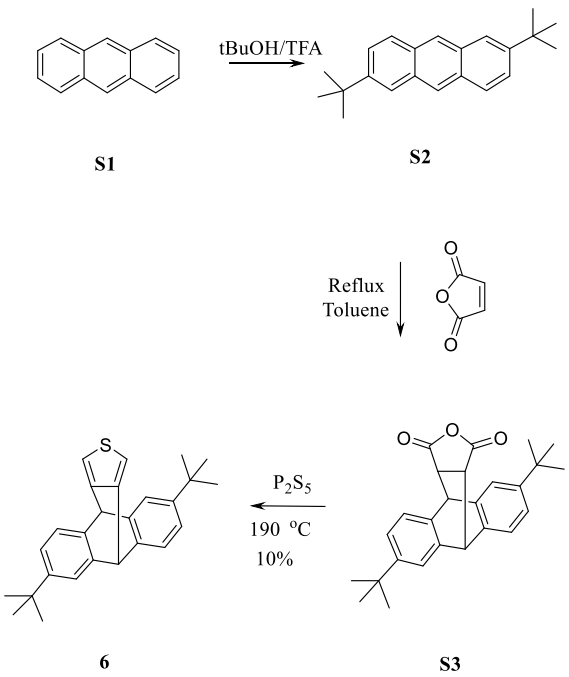
Hydrogen evolution was measured using ascorbic acid as a sacrificial electron donor. 2 mg of polymer, 0.2 mol l^{-1} ascorbic acid (20 ml) was used as a sacrificial reagent, pH 2, 5% (10 μg) Pt was achieved by adding aqueous potassium hexachloroplatinate solution (0.401 mg ml^{-1} Pt). The 16 cm^2 reactor was evacuated and purged with argon five times to remove oxygen, and the pressure was set to 100 Torr. The suspension was stirred and illuminated with a 300-W Xe lamp (Asahi Max 303) fitted with an ultraviolet–visible mirror module (350–800 nm). H_2 evolution was quantified by a gas chromatograph equipped with a thermal conductivity detector.

Materials

Carbon nitride was commercially purchased from Nanoshel and tested as a standard.TiO_2 P25 nanoparticles were purchased from Sigma Aldritch.

4.5.2. Synthesis

Route 1



Scheme 4.4: First synthetic route for monomer **6** Route **1**

2,6-di-tert-butylanthracene (1)

2,6-di-tert-butylanthracene was synthesised using a known procedure.[8] Whereby anthracene (7.1 g, 40 mmol, 1 equiv.), *tert*-butylalcohol (11.8 g, 160 mmol, 4 equiv.) and trifluoroacetic acid (40 g) were added to a 200 mL three-necked flask, and a reaction was conducted at 70° C. for 15 hours. After cooling to room temperature, the resultant was added to an ice water (200 g) over 1 hour, and the precipitate was subjected to filtration. The residue was washed with methanol (71 mL), followed by recrystallization with toluene, so as to obtain intermediate product 2,6-di-tert-butylanthracene (8.4 g, yield=72.7% ^{1}H NMR (400 MHz, Chloroform-d) δ 8.33 (s, 1H), 7.93 (d, J = 8.9 Hz, 1H), 7.87 (d, J = 2.0 Hz, 1H), 7.55 (dd, J = 8.9, 2.0 Hz, 1H), 1.45 (s, 9H)).

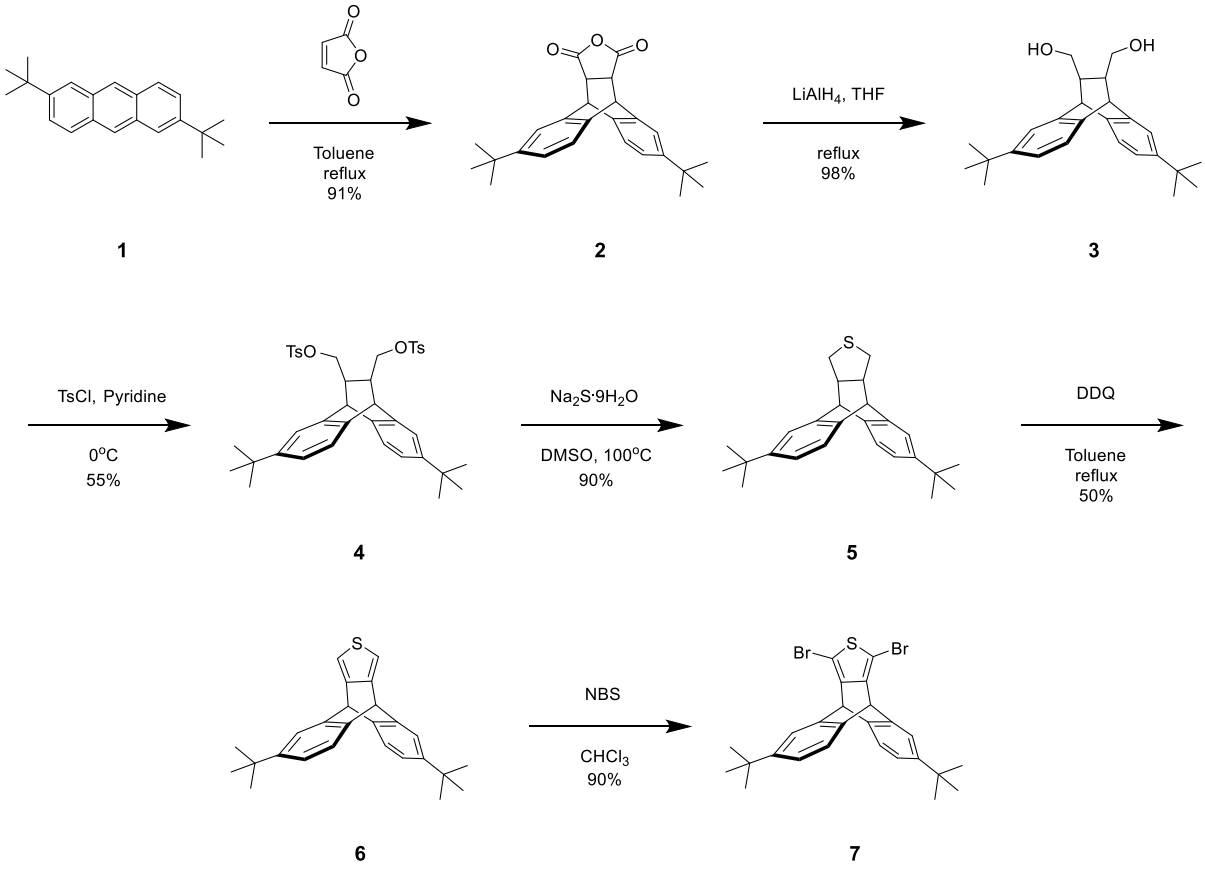
2,6-di-tert-butyl-9,10-dihydro-9,10-[3,4]thiophenoanthracene (2)

Tert-butyl anthracene (0.45 g, 1.55 mmols, 1 equiv.) was dissolved in toluene. Maleic anhydride (0.15 g, 1.55 mmols, 1 equiv.) was added and the mixture was degassed for 20 minutes then heated to reflux overnight. The product was collected by rotary evaporation of the solvent under reduced pressure. Washing with hexane yielded the product, 2,6-di-tert-butyl-9,10-dihydro-9,10-[3,4]thiophenoanthracene (0.4g, 1.1 g, 71 %, ^{1}H NMR (400 MHz, Chloroform-*d*) δ 7.43 (d, *J* = 1.9 Hz, 0H), 7.36 (d, *J* = 1.8 Hz, 1H), 7.34 (s, 0H), 7.28 (d, *J* = 6.2 Hz, 1H), 7.23 (ddd, *J* = 7.8, 4.8, 1.9 Hz, 1H), 4.80 (d, *J* = 2.2 Hz, 1H), 3.66 – 3.44 (m, 1H), 1.31 (d, *J* = 12.8 Hz, 9H)). 13C NMR (126 MHz, CDCl3) δ 170.77, 170.67, 150.89, 150.35, 140.62, 138.04, 137.84, 135.24, 124.66, 124.40, 123.86, 123.72, 122.24, 121.52, 48.32, 48.27, 45.46, 45.44, 34.76, 34.71, 31.47, 31.40.

2 (1 g, 3.6 mmols, 1 equiv.) was dissolved in dichlorobenzene (2 mL) and was added to a solution of P_2S_5 (1 g, 2.2 mmols, 0.6 equiv.) in dichlorobenzene (8 mL). The mixture was heated in a sealed tube at 190 ^{o}C for 16 hours, during which the yellow solution turned dark brown. The solution was then allowed to cool. Vacuum filtration was used to remove the solid residue. The solution was then run through a silica plug, using hexane as the eluent. The product stayed in the silica while impurities were removed (main impurity is anthracene from the reversed Dielz-Alder reaction at Rf 0.4). The desired product was then extracted from the silica using chloroform. The solvent was removed under reduced pressure to give the final product, monomer **6** (0.045 g, 9.8%, ^{1}H NMR (400 MHz, Chloroform-*d*) δ 8.35 (s, 1H), 7.47 (dt, *J* = 7.5, 3.8 Hz, 4H), 7.27 – 7.18 (m, 4H), 5.33 (s, 1H), 1.47 (s, 9H)).

Route 2

Up to compound **2,** the route used stayed the same, the steps outlines will be in place of using P_2S_5.



Scheme 4.5: Synthesis of monomer **7**

(2,6-di-*tert*-butyl-9,10-dihydro-9,10-ethanoanthracene-11,12-diyl)dimethanol (3)

A degassed solution of 2 (22.8 g, 58.7 mmol, 1 equiv.) in THF (100 ml) was added dropwise to a stirred suspension of lithium aluminum hydride (5.57 g, 146.7 mmol, 2.5 equiv.) in THF (100 ml) at 0 °C, under inert atmosphere. The mixture was allowed to come to room temperature and stirred for 30 min. Then heated to reflux overnight. After cooling to room temperature, the suspension was diluted with THF (500 ml) and quenched by addition of water (5.6 ml), followed by NaOH (2.2 g in 5.6 ml of water) and finally water again (5.6 ml). After hydrolysis was complete, the resulting mixture was filtered, the solids washed with THF and the solvent removed in vacuo to give diol 3 in 98% yield (21.5 g).^{1}H NMR (400 MHz, $CDCl_3$) δ 7.33 (d, J = 1.9 Hz, 1H), 7.26 – 7.20 (m, 2H), 7.17 – 7.10 (m, 3H), 4.13 (s, 2H), 3.59 (m, 2H), 3.26 (m, 2H), 2.43 – 2.30 (m, 2H), 1.33 (s, 9H), 1.30 (s, 9H). ^{13}C NMR (101 MHz, $CDCl_3$) δ

148.83, 148.72, 143.33, 140.70, 140.48, 137.87, 124.07, 122.74, 122.42, 122.38, 121.67, 120.46, 64.70, 64.65, 48.07, 47.98, 43.81, 43.65, 34.60, 34.53, 31.61, 31.59.

(2,6-di-*tert*-butyl-9,10-dihydro-9,10-ethanoanthracene-11,12-diyl)bis(methylene) bis(4-methylbenzenesulfonate) (4)

Tosyl chloride (12.6 g, 66 mmol, 2.5 equiv.) was slowly added to a solution of 3 (10 g, 26.4 mmol, 1 equiv.) in dry pyridine (50 mL) at 0 °C. The mixture was then warmed to room temperature and stirred overnight. The reaction mixture was then poured onto 2 M HCl (350 mL) and stirred until the precipitate was no longer sticky. The product was collected via filtration and washed with water. (24 g, 60%). ^{1}H NMR (400 MHz, $CDCl_3$) δ 7.78 (m, 4H), 7.38 (m, 4H), 7.23 (m, 2H), 7.14 (m, 1H), 7.01 (m, 1H), 6.91 (m, 1H), 4.26 (dd, J = 16.7, 1.4 Hz, 2H), 3.74 (m, 2H), 3.38 (m, 2H), 2.51 (s, 3H), 2.48 (s, 3H), 2.42 (m, 2H), 1.3(s, 9H), 1.26(s, 9H). ^{13}C NMR (101 MHz, $CDCl_3$) δ 149.37, 149.29, 145.05, 142.08, 139.42, 139.36, 136.56, 132.76, 132.66, 130.04, 130.01, 129.94, 127.99, 127.86, 127.83, 124.88, 123.20, 122.93, 122.87, 122.66, 120.91, 69.33, 45.46, 45.40, 40.01, 34.63, 34.51, 31.53, 31.44, 21.70.

2,6-di-*tert*-butyl-9,10-dihydro-9,10- [3,4] thiophenoanthracene (5)

To a solution of **4** (7 g, 10.19 mmol, 1 equiv.) in DMSO (40 mL), sodium sulphide nonahydrate (4.9 g, 20.4 mmol, 2 equiv.) in DMSO (30 mL) was added dropwise while stirring at 100 °C, and mixed overnight maintaining 100 ° C. The reaction solution was added to crushed ice and the precipitated product was filtered and washed with water to give the product as a white solid (3.45 g, 90%).^{1}H NMR (500 MHz, $CDCl_3$) δ 7.33 – 7.28 (m, 2H), 7.24 – 7.18 (m, 2H), 7.17 – 7.11 (m, 2H), 4.07 (m, 2H), 2.96 – 2.89 (m, 2H), 2.86 – 2.78 (m, 2H), 2.27 – 2.16 (m, 2H), 1.33 (s, 18H).^{13}C NMR (126 MHz, $CDCl_3$) δ 148.96, 148.71, 143.99, 141.18, 141.17, 138.27, 125.49, 123.18, 123.10, 122.60, 122.31, 120.91, 70.71, 51.03, 48.28, 48.25, 46.94, 46.83, 35.64, 34.61, 34.55, 31.62, 31.60.

2,6-di-tert-butyl-9,10-dihydro-9,10- [3, 4] thiophenoanthracene (6)

To a solution of 5 (1.0 g, 2.65 mmol, 1 equiv.) in 100 ml of degassed toluene at 120 °C was added dropwise a solution of 2,3-dichloro-4,5-dicyanobenzoquinone (1.33 g, 5.84 mmol, 2 equiv.) in toluene (50 mL). After complete addition, the reaction mixture was stirred at 120 °C for 1 h. The reaction was then cooled and filtered through silica gel. The solvent was removed under reduced pressure, and the crude product was further purified by silica gel column chromatography using 5% dichloromethane in hexanes. (0.59 g, 60% yield). ^{1}H NMR (500

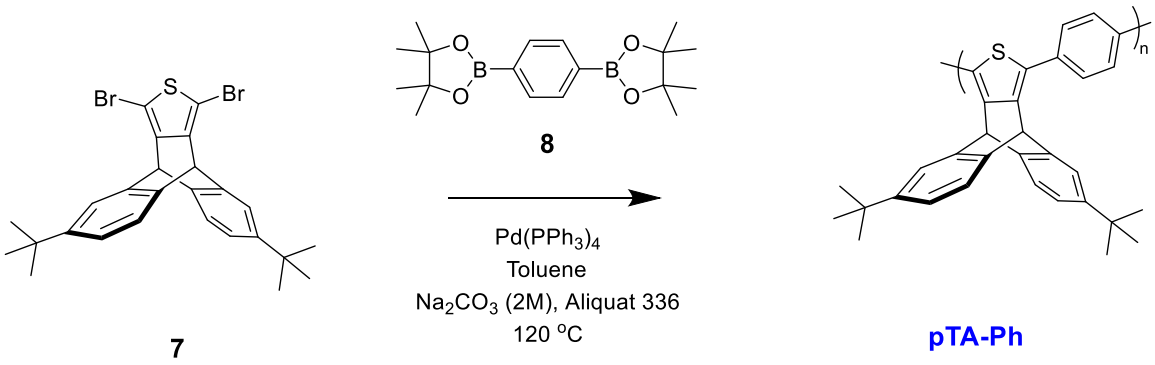
MHz, $CDCl_3$) δ 7.41 (m, 2H), 7.33 – 7.27 (m, 2H), 7.03 (m, 2H), 6.90 (s, 2H), 5.31 (s, 2H), 1.30 (s, 18H). ^{13}C NMR (126 MHz, $CDCl_3$) δ 148.38, 147.65, 145.10, 142.36, 123.12, 122.01, 121.08, 114.03, 49.99, 34.62, 31.55, 21.12, 14.25.

12,14-dibromo-2,6-di-tert-butyl-9,10-dihydro-9,10- [3,4] thiophenoanthracene (7)

6 (1.65 g, 4.43 mmol, 1 equiv.) was dissolved in THF (45 mL) and cooled to 0 °C. N-Bromosuccinimide (1.74 g, 9.74 mmol, 2 equiv.) was added dropwise. After complete addition, the solution was warmed to room temperature overnight. The solvent was removed under vacuum to give the crude product which was purified by silica gel chromatography in hexane (2.1g, 90%). ^1H NMR (500 MHz, $CDCl_3$) δ 7.44 (d, J = 1.9 Hz, 2H), 7.34 (d, J = 7.8 Hz, 2H), 7.11 (dd, J = 7.8, 1.9 Hz, 2H), 5.23 (s, 2H), 1.31 (s, 18H). ^{13}C NMR (126 MHz, $CDCl_3$) δ 149.14, 147.44, 143.72, 140.92, 123.59, 122.56, 121.47, 100.46, 49.20, 34.69, 31.49.

Typical Polymerization Procedures:

pTA-Ph

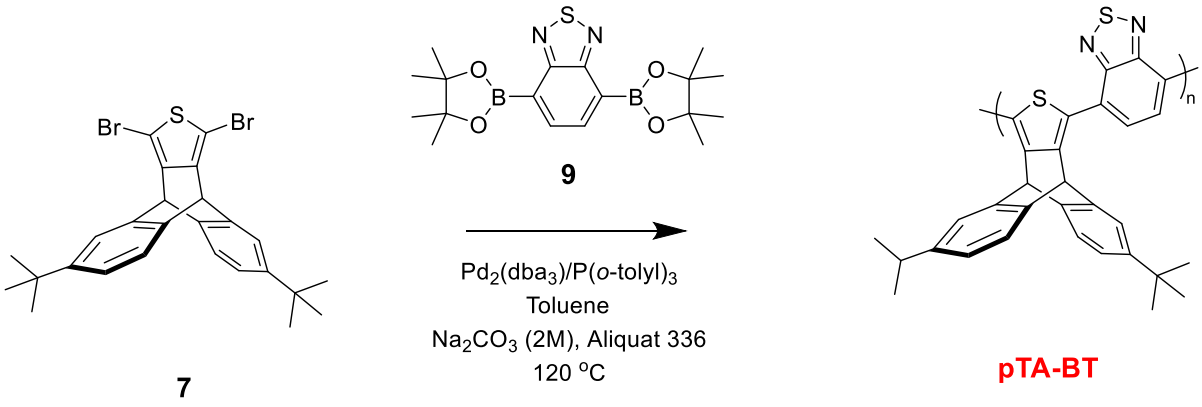


Scheme 4.6: Polymerisation of **pTA-Ph**

To a microwave vial, **7** (200 mg, 0.377 mmol, 1 equiv.), 1,4-bis(4,4,5,5-tetramethyl-1,3,2-dioxaborolan-2-yl)benzene (124.46 mg, 0.377 mmol, 1 equiv.), tetrakis(triphenylphosphine)palladium (22 mg, 5 mol%) and few drops of Aliquat 336 were added. The vial was sealed with septum and was subjected to vacuum followed by nitrogen purge. The process was repeated 3 times and degassed toluene (2mL) was added to the vial. The vial was purged with nitrogen for 10 min. 2ml of degassed 2M Na_2CO_3 aqueous solution was added and purged with nitrogen for 5 min. The vial was heated at 120 °C for 48h. The polymers were end capped by reacting with (0.5 mL) phenylboronic acid for 4h and finally

with bromobenzene (0.5 mL) for 4h. After cooling to room temperature, the reaction mixture was poured into methanol (50 mL) with stirring. The precipitate was filtered and washed with deionized water and methanol. The precipitated solids were subjected to Soxhlet extraction sequentially with methanol, acetone, Petroleum spirit 40 – 60 °C and finally with chloroform. The precipitates were collected by filtration and washed with methanol and dried under vacuum. 110 mg, M_n - 29.4 KDa, M_w - 42 KDa, PDI - 1.43. ^{1}H NMR (500 MHz, $CDCl_3$) δ 7.77 (broad m, 4H), 7.61 – 7.44 (broad m, 4H), 7.23 – 7.15 (broad m, 2H), 5.74 (broad s, 2H), 1.38 (broad s, 18H).

pTA-BT



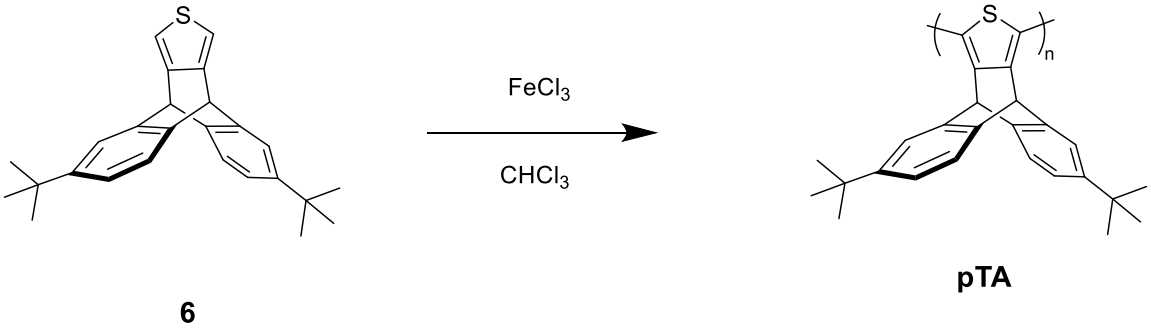
Scheme 4.7: Polymerisation of **pTA-BT**

To a microwave vial was added: **7** (200 mg, 0.377 mmol, 1 equiv.), 4,7-bis(4,4,5,5-tetramethyl-1,3,2-dioxaborolan-2-yl)benzo[c][1,2,5]thiadiazole (146.4 mg, 0.377 mmol, 1 equiv.), Tris(dibenzylideneacetone)dipalladium (7 mg, 2 mol%), Tri(o-tolyl)-phosphine (19 mg, 16 mol%) and few drops of Aliquat 336. The vial was sealed with septum and was subjected to vacuum followed by nitrogen purge. The process was repeated 3 times and degassed toluene (2mL) was added to the vial. The vial was purged with nitrogen for 10 min. 2ml of degassed 2M Na_2CO_3 aqueous solution was added and purged with nitrogen for 5 min. The vial was heated at 120 °C for 48h. The polymers were end capped as described above. After cooling to room temperature, the reaction mixture was poured into methanol (50 mL) with stirring. The precipitate was filtered and washed with water and methanol. The precipitated solids were subjected to Soxhlet extraction sequentially with methanol, acetone, Petroleum spirit 40 – 60 °C and finally with chloroform. The chloroform fraction was concentrated and precipitated in methanol. The precipitates were collected by filtration and washed with methanol and dried

under vacuum. 125 mg, M_n - 37.7 KDa, M_w - 61.7 KDa, PDI - 1.64. ^{1}H NMR (500 MHz, $CDCl_3$) δ 8.02 (broad s, 2H), 7.62 (broad s, 2H), 7.53 (broad d, *J* = 7.8 Hz, 2H), 7.21 (broad d, *J* = 7.8 Hz, 2H), 5.78 (broad s, 2H), 1.40 (broad s, 18H).

pTA

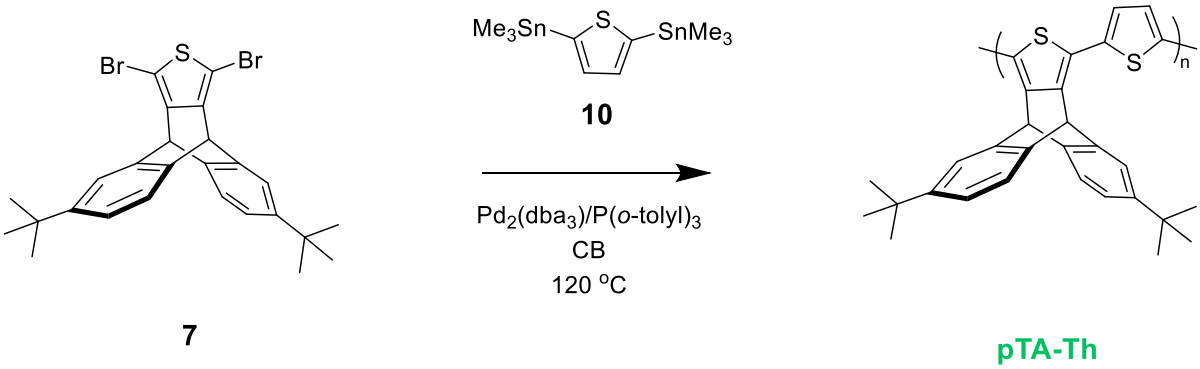
Polymerization of **pTA** using $FeCl_3$ as described by previous literature procedures.[85]



Scheme 4.8: Polymerisation of **pTA**

A microwave vial was charged with Anhydrous $FeCl_3$ (0.14 g, 1.2 mmol, 2.2 equiv.) and **6** (0.3 g, 0.56 mmol, 1 equiv.) was added via a syringe to the suspension. Anhydrous chloroform (1 mL) was injected. The resulting solution was purged with N_2 for 30 min and the reaction was heated to 130°C for 24 hours. The reaction mixture was poured into methanol containing 5% concentration of HCl aq. The precipitate was collected by filtration and washed with methanol then Soxhlet extracted with methanol, acetone, hexane and finally chloroform and the solvent was evaporated to give a bright yellow. Yield: 0.18 g (61%). M_n- 101K. ^{1}H NMR (400 MHz, $CDCl_3$) δ 7.53 (s, 3H), 5.84 (s, 1H), 1.35 (d, *J* = 6.9 Hz, 1H), 1.29 (s, 9H), 1.18 (s, 3H), 1.24 – 1.14 (m, 1H).

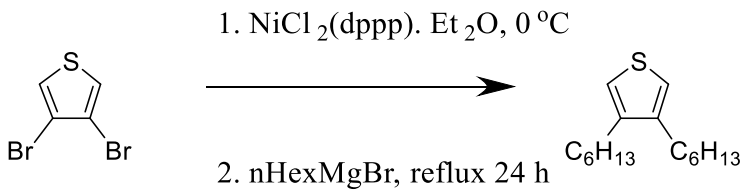
Polymerisation of pTA-Th



Scheme 4.9: Polymerisation of **pTA-Th**

A Mixture of **7** (51.2 mg, 47.89 µmol), 5,5'-bis(trimethylstannyl)-2, thiophene (26.18 mg, 53.23 µmol), $Pd_2(dba)_3$ (0.97 mg, 1.06 µmol) and P(o-tol)3 (1.30 mg, 4.26 µmol) in anhydrous, degassed chlorobenzene (1.2 mL) was degassed under nitrogen for 15 min and heated to 130 °C overnight. After this, a solution of 2-(tributylstannyl)thiophene (0.1 mL) and Pd2(dba)3 (1.50 mg, 1.64 µmol) in anhydrous, degassed chlorobenzene (0.5 mL) were added to the polymerisation mixture which was subsequently stirred for 1 h at 130 °C. 0.1 mL of a solution of 2-bromothiophene (0.1 mL) in anhydrous, degassed chlorobenzene (0.5 mL) was then subsequently added and stirred at 130 °C for a further 1 h. The polymerisation mixture was allowed to cool to room temperature and then precipitated in ethyl acetate (200 mL), followed by the addition of hexane (100 mL). The blue solid was then collected in a thimble and purified via Soxhlet extraction with methanol, acetone, hexane, THF and chloroform. The polymer dissolved in hot chloroform and was then re-precipitated in ethyl acetate (200 mL), with the addition of hexane (100 mL) to give the title polymer (48.1 mg, 86%) as a dark blue solid. ^{1}H NMR (500 MHz, 313 K, chloroform-d) δ 8.83 (s), 7.35 (d), 4.44 (br s), 3.87 – 3.24 (m), 1.53 (br s). GPC (chloroform, 40 °C): Mn - 23.9 kDa, Mw - 48.6 kDa.

pDHT synthesis

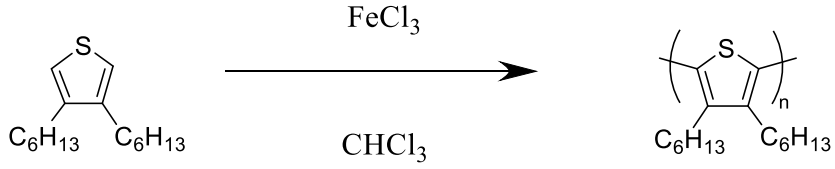


Scheme 4.10: synthesis for 3,4-dihexylthiophene

3,4-dihexylthiophene

To a suspension of $NiCl_2$(dppp) (292 mg, 0.53 mmol, 0.02 equiv.) and 3,4-dibromothiophene (3 ml; 27.1 mmol, 1 equiv.) in Et_2O (70 ml) at 0 °C, was added dropwise a concentrated solution of nHexMgBr in Et_2O, (67.5 ml, 135 mmol, 5 equiv.). At the end of the addition, the mixture was let to reach RT then heated to reflux for 24h. Afterwards, a 1M HCL aqueous solution (10 mL) was added carefully to the mixture under vigorous stirring. After 30 min, the resulting mixture was filtered over celite, and the filtrate evaporated to dryness. The residue was then extracted with DCM. washed with brine, water and dried over $MgSO_4$. The solvent was removed under vacuum. The crude was pre-purified by filtration over a small plug of silica gel (eluent: Petroleum spirit 100%). Purification was achieved by distillation under reduced pressure (150ºC, 9•10-2 mbar) to afford the monomer (5.81 g) in 85% yield as a colourless oil.^{1}H NMR ($CDCl_3$, 400 MHz) δ(ppm): 6.89 (s, 2H), 2.56–2.47 (m, 4H), 1.71–1.56 (m, 4H), 1.43–1.26 (m, 12H), 0.91 (t, 6H).

Polymerization of 3,4-Hexylthiophene with $FeCl_3$



Scheme 4.11: Polymerisation of **pDHT**

A microwave vial was charged with Anhydrous $FeCl_3$ (0.35 g, 2.2 mmol) and 3,4-hexylthiophene (0.25 g, 1.00 mmol) was added via a syringe to the suspension. Anhydrous chloroform (1 mL) was injected. The resulting solution was purged with N_2 for 30 min and the reaction was heated to 130°C for 24 hours. The reaction mixture was poured into methanol containing 5% concentration of HCl aq. The precipitate was collected by filtration and washed with methanol then Soxhlet's extracted with methanol, acetone, hexane and finally chloroform and the solvent was evaporated to give a black product. Yield: 0.17 g (75%). Mn= 24K. ^{1}H NMR (400 MHz, Chloroform-d) δ 2.58 ppm (s), 1.59-1.1 ppm (d), 1.28 ppm (m), 0.89 ppm (t).

Palladium scavenging

The polymers were dissolved in chloroform (100 mg in 100 mL) and added to an equal volume of aqueous solution of sodium diethyldithiocarbamate (1 g in 100 mL). The biphasic mixtures were stirred vigorously for 5 hours at 60 °C. The solutions were then allowed to cool to room temperature. The organic layers were collected and washed three times with deionised

water. This entire process was repeated six times for each polymer. The final chloroform fractions were then filtered through a glass frit packed with Celite®. The resulting solutions were concentrated under reduced pressure, precipitated into methanol, and filtered using a PTFE filter. The polymers were then dried *in vacuo*.

4.6. Chapter 4 Appendix

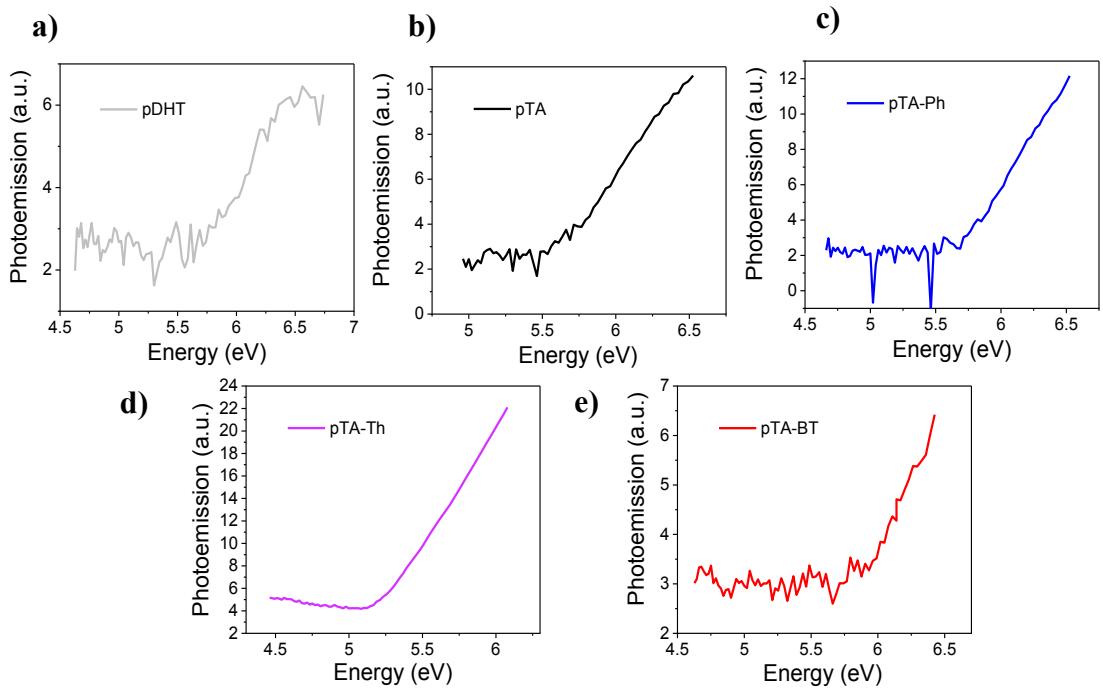


Figure 4.23: PESA of a) **pDHT**, b) **pTA**, c)**pTA-Ph**, d) **pTA-Th**, e) **pTA-BT**

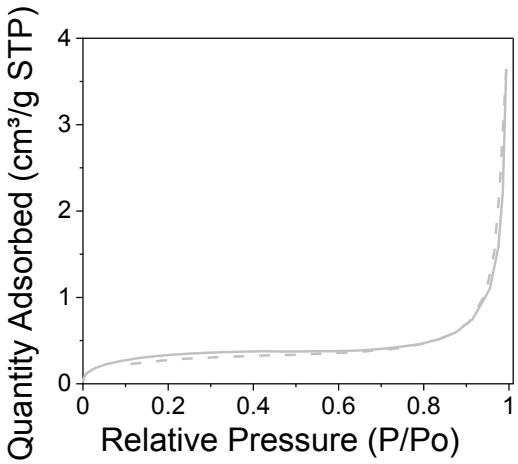


Figure 4.24: BET figure of **pDHT**

Table 4.8: Calculations table for the photoluminescence lifetime of polymers films upon 404 nm excitation wavelength.

Polymer	λ emission (nm)	π_1 (ns)	π_2 (ns)	π_3 (ns)	B_1 (%)	B_2 (%)	B_3 (%)	X	π_{avg}[a]
pTA	550	0.12	0.34		88.3	11.7		1.00	**0.18**
	600	0.21	0.64	2.50	81.5	16.2	2.3	1.02	**0.75**
pTA-Ph	460	0.24	0.46	3.39	76.5	23.0	0.5	0.99	**0.50**
	550	0.30	1.02	4.14	73.8	17.8	8.4	1.19	**2.34**
pTA -Th	550	0.24	0.55		26.8	73.2		1.04	**0.51**
	640	0.28	0.04	0.88	46.4	38.1	15.5	1.04	**0.56**
pTA BT	640	0.27	0.54	65.6	34.4			1.04	**0.41**

[a] *The PL emission decays were adjusted at bi or tri-exponential function. The average lifetime* π_{avg} *was calculated as according to* $t_{avg} = \sum_i B_i \pi_i^2 / \sum_i B_i \pi_i$. *For biexponential decay, the equation : A + B1 exp (I/t) + (-i/t2), taking into account the IRF, was used.*

Table 4.9: Table summarising control experiments on the polymers

Polymer	**N_2:CO_2/ $\mu molh^{-1}m^{-2}$**	**H_2: N_2/ $\mu molh^{-1}m^{-2}$**	**N_2/ $\mu molh^{-1}m^{-2}$**	**No light/ $\mu molh^{-1}m^{-2}$**
pTA	2.4	6.7	3.5	-
pTA-BT	0.9	4.5	2.1	-
pTA-Ph	2.2	3.4	2.3	-
pTA-Th	1.67	4.6	1.4	-



Figure 4.25: Example of **pTA** sample pre-testing

4.7. References

(1) Bandyopadhyay, S.; Anil, A. G.; James, A.; Patra, A. Multifunctional Porous Organic Polymers: Tuning of Porosity, CO_2, and H_2 Storage and Visible-Light-Driven Photocatalysis. *ACS Appl. Mater. Interfaces* **2016**, *8* (41), 27669–27678. https://doi.org/10.1021/acsami.6b08331.

(2) Zhang, G.; Lan, Z. A.; Wang, X. Conjugated Polymers: Catalysts for Photocatalytic Hydrogen Evolution. *Angew. Chemie Int. Ed.* **2016**, *55* (51), 15712–15727. https://doi.org/10.1002/ANIE.201607375.

(3) Senichev, V. Y.; Tereshatov, V. V. SIMPLE SOLVENT CHARACTERISTICS. *Handb. Solvents Second Ed.* **2014**, *1*, 117–149. https://doi.org/10.1016/B978-1-895198-64-5.50006-4.

(4) Chaoui, N.; Trunk, M.; Dawson, R.; Schmidt, J.; Thomas, A. Trends and Challenges for Microporous Polymers. *This J. is Cite this Chem. Soc. Rev* **2017**, *46*, 3302. https://doi.org/10.1039/c7cs00071e.

(5) Mc Keown, N. B.; Budd, P. M. Polymers of Intrinsic Microporosity (PIMs): Organic Materials for Membrane Separations, Heterogeneous Catalysis and Hydrogen Storage. *Chem. Soc. Rev.* **2006**, *35* (8), 675–683. https://doi.org/10.1039/b600349d.

(6) McKeown, N. B. The Synthesis of Polymers of Intrinsic Microporosity (PIMs). *Sci. China Chem.* **2017**, *60* (8), 1023–1032. https://doi.org/10.1007/s11426-017-9058-x.

(7) Tremel, K.; Ludwigs, S. Morphology of P3HT in Thin Films in Relation to Optical and Electrical Properties. *Adv. Polym. Sci.* **2014**, *265*, 39–82. https://doi.org/10.1007/12_2014_288/COVER.

(8) Evoniuk, C. J.; Gomes, G. dos P.; Hill, S. P.; Fujita, S.; Hanson, K.; Alabugin, I. V. Coupling N–H Deprotonation, C–H Activation, and Oxidation: Metal-Free $C(Sp^3)$–H Aminations with Unprotected Anilines. *J. Am. Chem. Soc.* **2017**, *139* (45), 16210–16221. https://doi.org/10.1021/jacs.7b07519.

(9) Jones, S.; Wilson, I. Synthesis of Substituted 3-Furan-2(5H)-Ones via an Anthracene Diels–Alder Sequence. *Tetrahedron Lett.* **2006**, *47* (26), 4377–4380. https://doi.org/10.1016/J.TETLET.2006.04.097.

(10) Vallée, Y.; Khalid, M.; Ripoll, J. L. Generation by Flash Vacuum Thermolysis and Cyclization of Methyl Penta-2,4-Dienedithioate. *Tetrahedron Lett.* **1993**, *34* (16), 2605–2608. https://doi.org/10.1016/S0040-4039(00)77636-2.

(11) Hoffmann, K. J.; Carlsen, P. H.; Hoflinann, K. J.; Carken, P. H. Study of an Efficient and Selective Bromination Reaction of Substituted Thiophenes. *Synth. Commun.* **1999**, *29* (9), 1607–1610. https://doi.org/10.1080/00397919908086142.

(12) Kruse, H.; Grimme, S. A Geometrical Correction for the Inter- and Intra-Molecular Basis Set Superposition Error in Hartree-Fock and Density Functional Theory Calculations for Large Systems. *J. Chem. Phys.* **2012**, *136* (15), 154101. https://doi.org/10.1063/1.3700154.

(13) Kurashige, Y.; Nakajima, T.; Kurashige, S.; Hirao, K.; Nishikitani, Y. Theoretical Investigation of the Excited States of Coumarin Dyes for Dye-Sensitized Solar Cells. *J. Phys. Chem. A* **2007**, *111* (25), 5544–5548. https://doi.org/10.1021/JP0720688/ASSET/IMAGES/LARGE/JP0720688F00002.JPEG.

(14) Babu, N. S. Donor−acceptor−donor (D-A-D) Structural Monomers as Donor Materials in Polymer Solar Cells: A DFT/TDDFT Approach. *https://doi.org/10.1080/15685551.2021.1997178* **2021**, *24* (1), 330–342. https://doi.org/10.1080/15685551.2021.1997178.

(15) El Ghazali, A.; Aboulouard, A.; Zouitina, S.; Atlas, S.; El Idrissi, M.; Tounsi, A. First-Principles Study on Optoelectronic and Photovoltaic Properties in a P3HT/PCBM Complex. *Phys. Chem. Res.* **2023**, *11* (2), 299–313. https://doi.org/10.22036/PCR.2022.339408.2087.

(16) Fortin, P.; Holdcroft, S. Energy Level Alignment and Interfacial Dipole Layer Formation at the P3HT:PCBM-Electrolyte Interface in Organic Photoelectrochemical Cells. *Sol. Energy Mater. Sol. Cells* **2019**, *200*. https://doi.org/10.1016/j.solmat.2019.110009.

(17) Randell, N. M.; Radford, C. L.; Yang, J.; Quinn, J.; Hou, D.; Li, Y.; Kelly, T. L. Effect of Acceptor Unit Length and Planarity on the Optoelectronic Properties of Isoindigo-Thiophene Donor-Acceptor Polymers. *Chem. Mater.* **2018**, *30* (14), 4864–4873. https://doi.org/10.1021/ACS.CHEMMATER.8B02535/SUPPL_FILE/CM8B02535_SI_001.PDF.

(18) Tahir, M. H.; Mubashir, T.; Shah, T. U. H.; Mahmood, A. Impact of Electron-Withdrawing and Electron-Donating Substituents on the Electrochemical and Charge Transport Properties of Indacenodithiophene-Based Small Molecule Acceptors for Organic Solar Cells. *J. Phys. Org. Chem.* **2019**, *32* (3), e3909. https://doi.org/10.1002/POC.3909.

(19) Ravelli, D.; Dondi, D.; Fagnoni, M.; Albini, A. Photocatalysis. A Multi-Faceted Concept for Green Chemistry. *Chem. Soc. Rev.* **2009**, *38* (7), 1999–2011. https://doi.org/10.1039/B714786B.

(20) Kim, J. Y.; Kim, S. H.; Lee, H. H.; Lee, K.; Ma, W.; Gong, X.; Heeger, A. J. New Architecture for High-Efficiency Polymer Photovoltaic Cells Using Solution-Based Titanium Oxide as an Optical Spacer. *Adv. Mater.* **2006**, *18* (5), 572–576. https://doi.org/10.1002/ADMA.200501825.

(21) Becker, W. The Bh TCSPC Handbook Ninth Edition Time-Correlated Single Photon Counting Modules SPC-130EMN, SPC-130EMNX SPC-130IN, SPC-130INX SPC-150N, SPC-150NX, SPC-150NXX SPC-160 SPC-160PCIE SPC-180N, SPC-180NX, SPC-180NXX Detectors, Lasers and Peripheral Devices Simple-Tau Systems Technical Principles TCSPC Applications FLIM Systems Applications in Life Sciences Clinical FLIM Applications SPCM Software SPCImage NG Data Analysis Software.

(22) Nakamura, T. Excitation Energy Transfer Dynamics in a Low-Band-Gap Copolymer: Two-Dimensional Electronic Spectroscopy of PTB7 in Solution. **2020**. https://doi.org/10.1021/acs.macromol.0c01118.

(23) Park, K. H.; Son, S. Y.; Kim, J. O.; Kang, G.; Park, T.; Kim, D. Role of Disorder in the Extent of Interchain Delocalization and Polaron Generation in Polythiophene Crystalline Domains. *J. Phys. Chem. Lett* **2018**, *9*, 3180. https://doi.org/10.1021/acs.jpclett.8b01050.

(24) Bencheikh, F.; Duché, D. D.; Ruiz, C. M.; Simon, J.-J.; Escoubas, L. Study of Optical Properties and Molecular Aggregation of Conjugated Low Band Gap Copolymers: PTB7 and PTB7-Th. **2015**. https://doi.org/10.1021/acs.jpcc.5b07803.

(25) Banerji, N.; Cowan, S.; Vauthey, E.; Heeger, A. J. Ultrafast Relaxation of the Poly(3-Hexylthiophene) Emission Spectrum. *J. Phys. Chem. C* **2011**, *115*, 9726–9739. https://doi.org/10.1021/jp1119348.

(26) Chirvony, V. S.; Sekerbayev, K. S.; Pashaei Adl, H.; Suárez, I.; Taurbayev, Y. T.; Gualdrón-Reyes, A. F.; Mora-Seró, I.; Martínez-Pastor, J. P. Interpretation of the Photoluminescence Decay Kinetics in Metal Halide Perovskite Nanocrystals and Thin Polycrystalline Films. *J. Lumin.* **2020**, *221*, 117092. https://doi.org/10.1016/J.JLUMIN.2020.117092.

(27) Jones, M.; Scholes, G. D. On the Use of Time-Resolved Photoluminescence as a Probe of Nanocrystal Photoexcitation Dynamics. *J. Mater. Chem.* **2010**, *20* (18), 3533–3538. https://doi.org/10.1039/C000165A.

(28) Mikhnenko, O. V.; Kuik, M.; Lin, J.; Van Der Kaap, N.; Nguyen, T. Q.; Blom, P. W. M. Trap-Limited Exciton Diffusion in Organic Semiconductors. *Adv. Mater.* **2014**, *26* (12), 1912–1917. https://doi.org/10.1002/ADMA.201304162.

(29) Fries, F.; Reineke, S. Statistical Treatment of Photoluminescence Quantum Yield Measurements. *Sci. Reports 2019 91* **2019**, *9* (1), 1–6. https://doi.org/10.1038/s41598-019-51718-4.

(30) Kosco, J.; Sachs, M.; Godin, R.; Kirkus, M.; Francas, L.; Bidwell, M.; Qureshi, M.; Anjum, D.; Durrant, J. R.; McCulloch, I. The Effect of Residual Palladium Catalyst Contamination on the Photocatalytic Hydrogen Evolution Activity of Conjugated Polymers. *Adv. Energy Mater.* **2018**, *8* (34), 1802181. https://doi.org/10.1002/aenm.201802181.

(31) Gallagher, W. P.; Vo, A. Dithiocarbamates: Reagents for the Removal of Transition Metals from Organic Reaction Media. *Org. Process Res. Dev.* **2015**, *19* (10), 1369–1373. https://doi.org/10.1021/OP500336H/SUPPL_FILE/OP500336H_SI_001.PDF.

(32) Li, Z.; Meng, X. Recent Development on Palladium Enhanced Photocatalytic Activity: A Review. *J. Alloys Compd.* **2020**, *830*, 154669. https://doi.org/10.1016/J.JALLCOM.2020.154669.

(33) Kosco, J.; Sachs, M.; Godin, R.; Kirkus, M.; Francas, L.; Bidwell, M.; Qureshi, M.; Anjum, D.; Durrant, J. R.; McCulloch, I. The Effect of Residual Palladium Catalyst Contamination on the Photocatalytic Hydrogen Evolution Activity of Conjugated Polymers. *Adv. Energy Mater.* **2018**, *8* (34), 1802181. https://doi.org/10.1002/aenm.201802181.

(34) Sachs, M.; Cha, H.; Kosco, J.; Aitchison, C. M.; Francà, L.; Corby, S.; Chiang, C.-L.; Wilson, A. A.; Godin, R.; Fahey-Williams, A.; Cooper, A. I.; Sprick, S.; Mcculloch, I.; Durrant, J. R. Tracking Charge Transfer to Residual Metal Clusters in Conjugated Polymers for Photocatalytic Hydrogen Evolution. *Cite This J. Am. Chem. Soc* **2020**, *142*, 14574–14587. https://doi.org/10.1021/jacs.0c06104.

(35) Cao, S.; Li, Y.; Zhu, B.; Jaroniec, M.; Yu, J. Facet Effect of Pd Cocatalyst on Photocatalytic CO2 Reduction over G-C3N4. *J. Catal.* **2017**, *349*, 208–217. https://doi.org/10.1016/J.JCAT.2017.02.005.

(36) Camarillo, R.; Tostón, S.; Martínez, F.; Jiménez, C.; Rincón, J. Enhancing the Photocatalytic Reduction of CO2 through Engineering of Catalysts with High Pressure Technology: Pd/TiO2 Photocatalysts. *J. Supercrit. Fluids* **2017**, *123*, 18–27. https://doi.org/10.1016/J.SUPFLU.2016.12.010.

(37) Piera, E.; Tejedor-Tejedor, M. I.; Zorn, M. E.; Anderson, M. A. Relationship Concerning the Nature and Concentration of Fe(III) Species on the Surface of TiO2 Particles and Photocatalytic Activity of the Catalyst. *Appl. Catal. B Environ.* **2003**, *46* (4), 671–685. https://doi.org/10.1016/S0926-3373(03)00288-1.

(38) Cherevan, A.; Gebhardt, P.; Kunzmann, A.; Costa, R. D.; Eder, D. Beware of Doping: Ta2O5 Nanotube Photocatalyst Using CNTs as Hard Templates. *ACS Appl. Energy Mater.* **2018**, *1* (3), 1259–1267. https://doi.org/10.1021/ACSAEM.8B00006/SUPPL_FILE/AE8B00006_SI_001.PDF.

(39) Colmenares, J. C.; Aramendía, M. A.; Marinas, A.; Marinas, J. M.; Urbano, F. J. Synthesis, Characterization and Photocatalytic Activity of Different Metal-Doped Titania Systems. *Appl. Catal. A Gen.* **2006**, *306*, 120–127. https://doi.org/10.1016/J.APCATA.2006.03.046.

(40) Li, L.; Lo, W. Y.; Cai, Z.; Zhang, N.; Yu, L. Donor-Acceptor Porous Conjugated Polymers for Photocatalytic Hydrogen Production: The Importance of Acceptor Comonomer. *Macromolecules* **2016**, *49* (18), 6903–6909. https://doi.org/10.1021/ACS.MACROMOL.6B01764/SUPPL_FILE/MA6B01764_SI_001.PDF.

(41) Wang, Y.; Vogel, A.; Sachs, M.; Sprick, R. S.; Wilbraham, L.; Moniz, S. J. A.; Godin, R.; Zwijnenburg, M. A.; Durrant, J. R.; Cooper, A. I.; Tang, J. Current Understanding and Challenges of Solar-Driven Hydrogen Generation Using Polymeric Photocatalysts. *Nat. Energy 2019 49* **2019**, *4* (9), 746–760. https://doi.org/10.1038/s41560-019-0456-5.

(42) Gao, H. Synthesis of Linear Polymers in High Molecular Weights via Reaction-Enhanced Reactivity of Intermediates Using Friedel-Crafts Polycondensation. *ACS Omega* **2021**, *6* (7), 4527–4533. https://doi.org/10.1021/ACSOMEGA.0C06085/ASSET/IMAGES/ACSOMEGA.0C06085.SOCIAL.JPEG_V03.

(43) Naderi, M. Surface Area: Brunauer–Emmett–Teller (BET). *Prog. Filtr. Sep.* **2015**, 585–608. https://doi.org/10.1016/B978-0-12-384746-1.00014-8.

(44) Stangeland, K.; Li, H.; Yu, Z. CO2 Hydrogenation to Methanol: The Structure–Activity Relationships of Different Catalyst Systems. *Energy, Ecol. Environ.* **2020**, *5* (4), 272–285. https://doi.org/10.1007/S40974-020-00156-4/TABLES/4.

(45) Kosco, J.; Moruzzi, F.; Willner, B.; McCulloch, I. Photocatalysts Based on Organic Semiconductors with Tunable Energy Levels for Solar Fuel Applications. *Adv. Energy Mater.* **2020**, *10* (39), 2001935. https://doi.org/10.1002/aenm.202001935.

(46) Ali, S.; Flores, M. C.; Razzaq, A.; Sorcar, S.; Hiragond, C. B.; Kim, H. R.; Park, Y. H.; Hwang, Y.; Kim, H. S.; Kim, H.; Gong, E. H.; Lee, J.; Kim, D.; In, S.-I. Gas Phase Photocatalytic CO2 Reduction, "A Brief Overview for Benchmarking." *Catalysts* **2019**, *9* (9), 727. https://doi.org/10.3390/catal9090727.

(47) Su, T. ming; Qin, Z. zeng; Ji, H. bing; Jiang, Y. xiu; Huang, G. Recent Advances in the Photocatalytic Reduction of Carbon Dioxide. *Environ. Chem. Lett.* **2016**, *14* (1), 99–112. https://doi.org/10.1007/s10311-015-0528-0.

(48) Lo, C. C.; Hung, C. H.; Yuan, C. S.; Wu, J. F. Photoreduction of Carbon Dioxide with H2 and H2O over TiO2 and ZrO2 in a Circulated Photocatalytic Reactor. *Sol. Energy Mater. Sol. Cells* **2007**, *91* (19), 1765–1774. https://doi.org/10.1016/j.solmat.2007.06.003.

(49) Fang, Y.; Wang, X. Photocatalytic CO2 Conversion by Polymeric Carbon Nitrides. *Chem. Commun.* **2018**, *54* (45), 5674–5687. https://doi.org/10.1039/c8cc02046a.

(50) Wang, K.; Li, Q.; Liu, B.; Cheng, B.; Ho, W.; Yu, J. Sulfur-Doped g-C3N4 with Enhanced Photocatalytic CO2-Reduction Performance. *Appl. Catal. B Environ.* **2015**, *176–177*, 44–52. https://doi.org/10.1016/j.apcatb.2015.03.045.

(51) Jeyalakshmi, V.; Mahalakshmy, R.; Krishnamurthy, K. R.; Viswanathan, B. Photocatalytic Reduction of Carbon Dioxide by Water: A Step towards Sustainable Fuels and Chemicals. *Mater. Sci. Forum* **2013**, *734*, 1–62. https://doi.org/10.4028/WWW.SCIENTIFIC.NET/MSF.734.1.

(52) Hong, J.; Zhang, W.; Ren, J.; Xu, R. Photocatalytic Reduction of CO2: A Brief Review on Product Analysis and Systematic Methods. *Anal. Methods* **2013**, *5* (5), 1086–1097. https://doi.org/10.1039/c2ay26270c.

(53) Schreck, M.; Niederberger, M. Photocatalytic Gas Phase Reactions. *Chem. Mater.* **2019**, *31* (3), 597–618. https://doi.org/10.1021/ACS.CHEMMATER.8B04444/ASSET/IMAGES/MEDIUM/CM-2018-04444Y_0015.GIF.

(54) Yu, J.; Su, Y.; Cheng, B. Template-Free Fabrication and Enhanced Photocatalytic Activity of Hierarchical Macro-/Mesoporous Titania. *Adv. Funct. Mater.* **2007**, *17* (12), 1984–1990. https://doi.org/10.1002/ADFM.200600933.

(55) Kochergin, Y. S.; Noda, Y.; Kulkarni, R.; Škodáková, K.; Tarábek, J.; Schmidt, J.; Bojdys, M. J. Sulfur-And Nitrogen-Containing Porous Donor-Acceptor Polymers as Real-Time Optical and Chemical Sensors. *Macromolecules* **2019**, *52* (20), 7696–7703. https://doi.org/10.1021/ACS.MACROMOL.9B01643/ASSET/IMAGES/LARGE/MA9B01643_0003.JPEG.

(56) Weber, J.; Thomas, A. Toward Stable Interfaces in Conjugated Polymers: Microporous Poly(p-Phenylene) and Poly(Phenyleneethynylene) Based on a Spirobifluorene Building Block. *J. Am. Chem. Soc.* **2008**, *130* (20), 6334–6335. https://doi.org/10.1021/JA801691X/SUPPL_FILE/JA801691X-FILE002.PDF.

(57) Liu, C. L.; Chen, Y.; Shelar, D. P.; Li, C.; Cheng, G.; Fu, W. F. Bodipy Dyes Bearing Oligo(Ethylene Glycol) Groups on the Meso -Phenyl Ring: Tuneable Solid-State Photoluminescence and Highly Efficient OLEDs. *J. Mater. Chem. C* **2014**, *2* (28), 5471–5478. https://doi.org/10.1039/C4TC00720D.

(58) Lee, J. S. M.; Cooper, A. I. Advances in Conjugated Microporous Polymers. *Chem. Rev.* **2020**, *120* (4), 2171–2214. https://doi.org/10.1021/ACS.CHEMREV.9B00399/ASSET/IMAGES/LARGE/CR9B00399_0041.JPEG.

(59) Hong, G.; Gan, X.; Leonhardt, C.; Zhang, Z.; Seibert, J.; Busch, J. M.; Bräse, S.; Hong, G.; Gan, X.; Leonhardt, C.; Zhang, Z.; Seibert, J.; Busch, J. M.; Bräse, S. A Brief History of OLEDs—Emitter Development and Industry Milestones. *Adv. Mater.* **2021**, *33* (9), 2005630. https://doi.org/10.1002/ADMA.202005630.

(60) Bronstein, H.; Nielsen, C. B.; Schroeder, B. C.; McCulloch, I. The Role of Chemical Design in the Performance of Organic Semiconductors. *Nat. Rev. Chem. 2020 42* **2020**, *4* (2), 66–77. https://doi.org/10.1038/s41570-019-0152-9.

(61) Gettinger, C. L.; Heeger, A. J.; Drake, J. M.; Pine, D. J. THE EFFECT OF INTRINSIC RIGIDITY ON THE OPTICAL PROPERTIES OF PPV DERIVATIVES. *Mol. Cryst. Liq. C y s t* **1994**, *256*, 507–512.

(62) Nuyken, O.; Jungermann, S.; Wiederhirn, V.; Bacher, E.; Meerholz, K. Modern Trends in Organic Light-Emitting Devices (OLEDs). *Monatshefte fur Chemie* **2006**, *137* (7), 811–824. https://doi.org/10.1007/S00706-006-0490-4/METRICS.

(63) Wang, Y.; Neumann, C.; Hußmann, M.; Cao, Q.; Hu, Y.; Garrity, O.; Kusch, P.; Turchanin, A.; Eigler, S. Synthesis of Wet-Chemically Prepared Porous-Graphene Single Layers on Si/SiO2 Substrate Increasing the Photoluminescence of MoS2 in Heterostructures. *Adv. Mater. Interfaces* **2021**, *8* (17), 2100783. https://doi.org/10.1002/ADMI.202100783.

(64) Goel, M. Electric Sensors, Filters and MEMS Devices: New Challenges in Materials Research. *Curr. Sci.* **2003**, *85* (4), 443–453.

(65) Kosco, J.; Bidwell, M.; Cha, H.; Martin, T.; Howells, C. T.; Sachs, M.; Anjum, D. H.; Gonzalez Lopez,

S.; Zou, L.; Wadsworth, A.; Zhang, W.; Zhang, L.; Tellam, J.; Sougrat, R.; Laquai, F.; DeLongchamp, D. M.; Durrant, J. R.; McCulloch, I. Enhanced Photocatalytic Hydrogen Evolution from Organic Semiconductor Heterojunction Nanoparticles. *Nat. Mater.* **2020**, *19* (5), 559–565. https://doi.org/10.1038/s41563-019-0591-1.

(66) Fu, Z.; Vogel, A.; Zwijnenburg, M. A.; Cooper, A. I.; Sprick, S. Photocatalytic Syngas Production Using Conjugated Organic Polymers †. **2021**. https://doi.org/10.1039/d0ta09613j.

(67) Wang, W.; Deng, C.; Xie, S.; Li, Y.; Zhang, W.; Sheng, H.; Chen, C.; Zhao, J. Photocatalytic C-C Coupling from Carbon Dioxide Reduction on Copper Oxide with Mixed-Valence Copper(I)/Copper(II). *J. Am. Chem. Soc.* **2021**, *143* (7), 2984–2993. https://doi.org/10.1021/JACS.1C00206/ASSET/IMAGES/LARGE/JA1C00206_0007.JPEG.

(68) Guo, Z.; Yu, F.; Yang, Y.; Leung, C. F.; Ng, S. M.; Ko, C. C.; Cometto, C.; Lau, T. C.; Robert, M. Photocatalytic Conversion of CO2 to CO by a Copper(II) Quaterpyridine Complex. *ChemSusChem* **2017**, *10* (20), 4009–4013. https://doi.org/10.1002/CSSC.201701354.

(69) Li, L.; Hasan, I. M. ul; Qiao, J.; He, R.; Peng, L.; Xu, N.; Niazi, N. K.; Zhang, J.-N.; Farwa, F. Copper as a Single Metal Atom Based Photo-, Electro-, and Photoelectrochemical Catalyst Decorated on Carbon Nitride Surface for Efficient CO_2 Reduction: A Review. *Nano Res. Energy* **2022**, *1* (2), e9120015. https://doi.org/10.26599/NRE.2022.9120015.

(70) Shown, I.; Hsu, H.-C.; Chang, Y.-C.; Lin, C.-H.; Roy, P. K.; Ganguly, A.; Wang, C.-H.; Chang, J.-K.; Wu, C.-I.; Chen, L.-C.; Chen, K.-H. Highly Efficient Visible Light Photocatalytic Reduction of CO_2 to Hydrocarbon Fuels by Cu-Nanoparticle Decorated Graphene Oxide. *Nano Lett.* **2014**, *14* (11), 6097–6103. https://doi.org/10.1021/nl503609v.

(71) Guo, J.; Duchesne, P. N.; Wang, L.; Song, R.; Xia, M.; Ulmer, U.; Sun, W.; Dong, Y.; Loh, J. Y. Y.; Kherani, N. P.; Du, J.; Zhu, B.; Huang, W.; Zhang, S.; Ozin, G. A. High-Performance, Scalable, and Low-Cost Copper Hydroxyapatite for Photothermal CO2 Reduction. *ACS Catal.* **2020**, *10* (22), 13668–13681. https://doi.org/10.1021/ACSCATAL.0C03806/SUPPL_FILE/CS0C03806_SI_001.PDF.

(72) Li, H.; Liu, T.; Wei, P.; Lin, L.; Gao, D.; Wang, G.; Bao, X. High-Rate CO2 Electroreduction to C2+ Products over a Copper-Copper Iodide Catalyst. *Angew. Chemie Int. Ed.* **2021**, *60* (26), 14329–14333. https://doi.org/10.1002/ANIE.202102657.

(73) Ghanbari, M.; Salavati-Niasari, M. Copper Iodide Decorated Graphitic Carbon Nitride Sheets with Enhanced Visible-Light Response for Photocatalytic Organic Pollutant Removal and Antibacterial Activities. *Ecotoxicol. Environ. Saf.* **2021**, *208*, 111712. https://doi.org/10.1016/J.ECOENV.2020.111712.

(74) Sun, W.; Peng, H.; Li, Y.; Yan, W.; Liu, Z.; Bian, Z.; Huang, C. Solution-Processed Copper Iodide as an Inexpensive and Effective Anode Buffer Layer for Polymer Solar Cells. *J. Phys. Chem. C* **2014**, *118* (30), 16806–16812. https://doi.org/10.1021/JP412784Q/SUPPL_FILE/JP412784Q_SI_001.PDF.

(75) Baran, T.; Wojtyła, S.; Dibenedetto, A.; Aresta, M.; Macyk, W. Photocatalytic Carbon Dioxide Reduction at P-Type Copper(I) Iodide. *ChemSusChem* **2016**, *9* (20), 2933–2938. https://doi.org/10.1002/CSSC.201600289.

(76) Yano, T.; Ebizuka, M.; Shibata, S.; Yamane, M. Anomalous Chemical Shifts of Cu 2p and Cu LMM Auger Spectra of Silicate Glasses. *J. Electron Spectros. Relat. Phenomena* **2003**, *131–132*, 133–144. https://doi.org/10.1016/S0368-2048(03)00126-9.

(77) Pauly, N.; Tougaard, S.; Yubero, F. Determination of the Cu 2p Primary Excitation Spectra for Cu, Cu2O and CuO. *Surf. Sci.* **2014**, *620*, 17–22. https://doi.org/10.1016/J.SUSC.2013.10.009.

(78) Biesinger, M. C. Advanced Analysis of Copper X-Ray Photoelectron Spectra. **2017**. https://doi.org/10.1002/sia.6239.

(79) Sajjad, M. T.; Ruseckas, A.; Samuel, I. D. W. Enhancing Exciton Diffusion Length Provides New Opportunities for Organic Photovoltaics. *Matter* **2020**, *3* (2), 341–354. https://doi.org/10.1016/J.MATT.2020.06.028.

(80) Kokil, A.; Yang, K.; Kumar, J. Techniques for Characterization of Charge Carrier Mobility in Organic Semiconductors. *J. Polym. Sci. Part B Polym. Phys.* **2012**, *50* (15), 1130–1144.

https://doi.org/10.1002/POLB.23103.

(81) Felter, K. M.; Caselli, V. M.; Günbaş, D. D.; Savenije, T. J.; Grozema, F. C. Interplay between Charge Carrier Mobility, Exciton Diffusion, Crystal Packing, and Charge Separation in Perylene Diimide-Based Heterojunctions. *ACS Appl. Energy Mater.* **2019**. https://doi.org/10.1021/ACSAEM.9B01490/ASSET/IMAGES/LARGE/AE9B01490_0009.JPEG.

(82) Griggs, S.; Marks, A.; Bristow, H.; McCulloch, I. N-Type Organic Semiconducting Polymers: Stability Limitations, Design Considerations and Applications. *J. Mater. Chem. C* **2021**, *9* (26), 8099–8128. https://doi.org/10.1039/D1TC02048J.

(83) Ohayon, D.; Druet, V.; Inal, S. A Guide for the Characterization of Organic Electrochemical Transistors and Channel Materials. *Chem. Soc. Rev.* **2023**, *52* (3), 1001–1023. https://doi.org/10.1039/D2CS00920J.

(84) Kosco, J.; Gonzalez-Carrero, S.; Howells, C. T.; Fei, T.; Dong, Y.; Sougrat, R.; Harrison, G. T.; Firdaus, Y.; Sheelamanthula, R.; Purushothaman, B.; Moruzzi, F.; Xu, W.; Zhao, L.; Basu, A.; De Wolf, S.; Anthopoulos, T. D.; Durrant, J. R.; McCulloch, I. Generation of Long-Lived Charges in Organic Semiconductor Heterojunction Nanoparticles for Efficient Photocatalytic Hydrogen Evolution. *Nat. Energy* **2022**. https://doi.org/10.1038/S41560-022-00990-2.

(85) Amou, S.; Haba, O.; Shirato, K.; Hayakawa, T.; Ueda, M.; Takeuchi, K.; Asai, M. Head-to-Tail Regioregularity of Poly(3-Hexylthiophene) in Oxidative Coupling Polymerization with FeCl 3. *J Polym Sci A Polym Chem* **1999**, *37*, 1943–1948. https://doi.org/10.1002/(SICI)1099-0518(19990701)37:13.

5. Spiro Based PIMs for Applications in Solar Fuels with Copper Cocatalysts.

Contents

5. SPIRO BASED PIMS FOR APPLICATIONS IN SOLAR FUELS WITH COPPER COCATALYSTS 195

5.1. General Information and Attributions 199

5.2. Introduction 199

5.2.1. "Spiro" polymers 199

5.3. Results and Discussion 201

5.3.1. Spiro Polymer Synthesis and Characterisation 201

5.3.1.1. Polymer Structures and Synthesis 201

5.3.1.2. Optoelectronic Properties 203

5.3.1.3. Palladium Content 205

5.3.1.4. Porosity 205

5.3.2. Photoreduction using the Spirobifluorene Series 207

5.3.2.1. Single components 207

5.3.2.2. Co-catalysts 208

5.3.2.3. Comparison to Iptycene series 210

5.4. Conclusion and Future Work 211

5.5. Experimental 212

5.6. Appendix 215

5.7. References 217

List of Figures

Figure 5.1: 3D representation of the spiro repeat unit. 200
Figure 5.2: a) UV-Vis spectra of polymers on thin film, normalised. b) energy level diagram for the polymers presented.....203
Figure 5.3: BET isotherm plots, with embedded pore distribution plots. a) of **p(Sp),** b) **p(Sp-Ph),** c**) p(Sp-BPh)** d) **p(Sp-NBPh)** 206
Figure 5.4: Single component performance for the polymers over a 12 hour period. 207
Figure 5.5: Performance of a) **p(Sp-Ph)** with copper co-catalysts. b) **p(Sp-NBPh)** with different co-catalysts. 209
Figure 5.6: PESA spectra of a) of **p(Sp),** b) **p(Sp-Ph),** c**) p(Sp-BPh)** d) **p(Sp-NBPh)**.....215
Figure 5.7: PL of the polymers, excited at 380 nm, dissolved in chloroform to 1mgml^{-1} and drop-cast after 15 min of sonication. Emission peaks at 520 nm and 450 nm were an artifact of the instrument lamp.....215
Figure 5.8: Control experiments performed on the polymers. 216
Figure 5.9: UV-Vis data with tangents drawn 216

List of Tables

Table 5.1: Table showing the combinations of monomers that result in each polymer. 202

Table 5.2 - Molecular weight information of the synthesised polymers collected from the GPC 202

Table 5.3 - Tabulated energetic values measured for each polymer. 204

Table 5.4: ICP-MS data showing palladium content in the polymers after palladium scavenging. 205

Table 5.5: Table showing the surface areas obtained from the BET isotherms for the polymers. 205

Table 5.6: Table summarising single components rates of CO production 208

Table 5.7: Table summarising rates of the polymer against the co-catalysts tested. 209

5.1. General Information and Attributions

This work was carried out along with Mr Matt Rosenfeld, whom the author co-supervised with Mr Benjamin Willner, as part of his Part II thesis, and with Miss Angela Xu, who the author supervised as a summer student in 2022. PL data was provided by Teng Fei (Durrant Group, Imperial College London), under the supervision of Dr Sora Gonzalez-Carrero (Durrant Group, Imperial College London).

5.2. Introduction

This Chapter outlines a study done to build upon work outlined in **Chapter 4.** The iptycene study of **Chapter 4** outlined a new class of porous, conjugated and solution processable polymers which were successful for the photocatalytic production of carbon monoxide from carbon dioxide and hydrogen. An increase in pore size, coupled with an increase in photoluminescence lifetimes, were believed to aid an increased rate of product formation. Since this series was covering the aim of the overall thesis, of making new organic materials, testing them for solar fuels production, and begin the moving towards intelligent synthetic design, the study presented in this Chapter aimed to further build upon the previous series. Although the materials shown in **Chapter 4** were successful, the synthesis to obtain the rigid structure required multiple steps, some quite low yielding. It was hoped that if utilising a different rigid structure, would maintain some of the important properties, such as solution processability and porosity, while also aiding the ease of synthesis for an overall more scalable process, so that in the long run, further experimentation could be done with more ease. The polymers of this study should retain (1) high intrinsic porosity from a rigid structure, (2) solution processibility and (3) good conjugation and (4) stability. But to attempt to improve upon the previous series, the polymers should (1) incorporate a known fluorescent specie, (2) integrating an easier synthetic procedure, with higher yields, (3) the series of polymers should be as optically similar and be carried out with the same polymerisation technique. The point of this was to further minimise any minor, residual effect from polymerisation or difference in energy levels, so that properties such as fluorescence and pore sizes could be targeted, by changing the length and type of co-monomer.

5.2.1. "Spiro" polymers

PIMs based on spirocyclic compounds have drawn a lot of interest in both the field of membranes and gas separation, and the field of organic optoelectronics.[1,2] The spiro structure is characterised by two bi-fluorene cores, in a perpendicular arrangement. This enables the

structure to maintain good rigidity, it increases the likelihood of the structure to be soluble and is ideal for fluorescent emitters.[3] Spiro based compounds have also been shown to be highly stable to reversible oxidation and reduction reactions, they have sported good thermal stability, high mobility and have been used as successful charge transporting layers.[4,5]

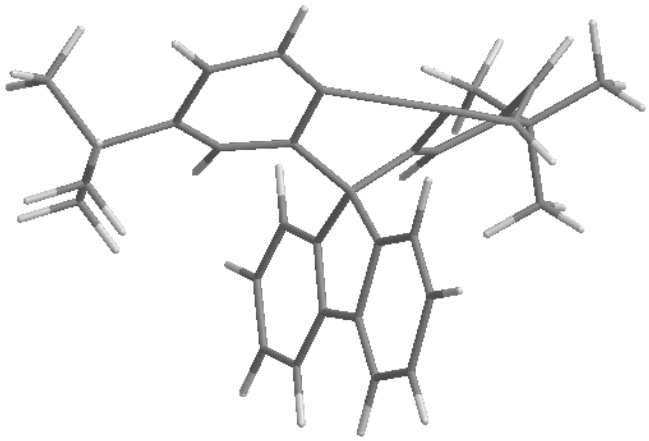


Figure 5.1: 3D representation of the spiro repeat unit.

The orthogonal nature of the spiro groups is illustrated in 3D space in **Figure 5.1**. It was hypothesised that spirocyclic compounds would have great potential, especially due to the fluorescent nature normally given by spiro unit, which complemented the relationship with high PL lifetimes and high rates in the triptycene series. Importantly, as mentioned, ease of synthesis was very sought after since the previous series required many stages. The spiro unit is more researched and common and the rigid monomer can be reached in fewer, simpler, high yielding synthetic steps. As co-monomers, the highest performing co-monomer was chosen from **Chapter 4** and polymerised with a spiro unit. Subsequently, a further phenyl group was added, to see if an increased co-monomer length would have a positive effect on photoluminescence.[6–8] Bipyridine (bipy) was also chosen as a monomer in this series. The two amine groups present, both are able to donate a lone pair, which does not take part in the aromaticity of the molecule, and as a result is a well-known bidentate chelating ligand. It was used in this study to begin a primary investigation into whether such functional groups would increase product formation in photoreduction, either by an increased interaction with carbon dioxide, or by binding more successfully to a potential co-catalyst. [9,10] A further advantage that was sought in this study was that each polymer would be synthesised by Suzuki polymerisation, instead of using 3 different polymerisation techniques, and the energy levels were very similar, to ensure the best comparison possible within the series. A more straight forward and scalable

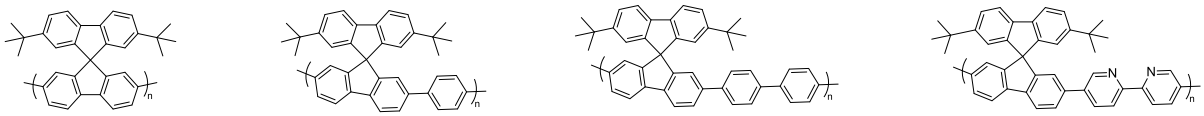
synthesis does decrease the time required for the polymers to be synthesised, which in turn means more co-catalyst studies could be carried out faster on this series. To kick off the process, since copper had shown such promise in the iptycene series outlined in **Chapter 4,** copper as a co-catalyst was compared in different forms, including copper iodide, copper metal and copper metal nanoparticles. Then, to take advantage of the presence of the bipy ligand, a nickel source and a cobalt source were chosen. Hybrid nickel-organic complexes have shown some success in CO_2 photoreduction to CO, and cobalt has been used as a common co-catalyst for CO_2 photocatalysis in water. Both complexes are also able to bind in a square planar arrangement which was thought to be favourable with the bipy ligands.[11–15]

5.3. Results and Discussion

5.3.1. Spiro Polymer Synthesis and Characterisation

5.3.1.1. Polymer Structures and Synthesis

The four polymers presented in this series are shown in **Scheme 5.1**.

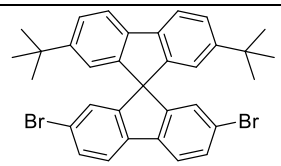
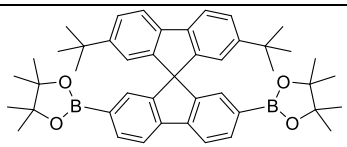
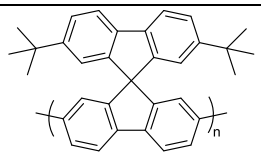
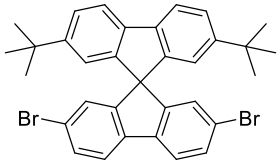
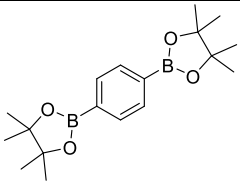
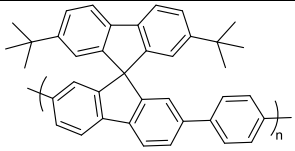
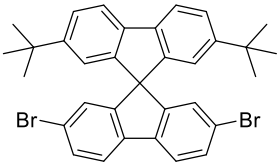
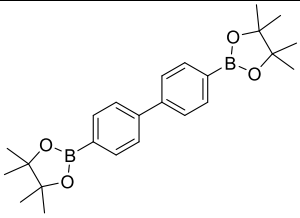
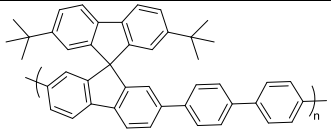
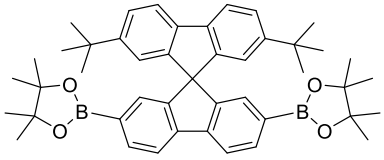
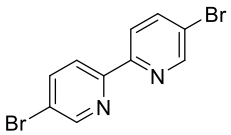
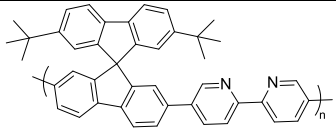


Scheme 5.1: Illustration of the polymers presented in this study.

The *tert*-butyl groups were incorporated to the fluorene spiro monomer to maintain solubility. The analogue without *tert*-butyl groups, 2,7-dibromo-9,9'-spirobi[fluorene], has been previously reported in literature.[16–18] A lithiation was carried out on the mono-brominated product, and subsequent reaction with 2,7-dibromofluorenone. Acidification of the intermediate led to the title monomer, 2',7'-dibromo-2,7-ditert-butyl-9,9'-spirobi[fluorene].

The use of Suzuki-Miyaura coupling for each of the polymerisations ensured the same conditions and metal catalysts were used in the formation of each polymer.[19] **Table 5.1** highlights which monomer was the boronic ester in the polymerisation and which was di-brominated. It should be noted that, in this study, the homopolymer p(Sp) was also polymerised using Suzuki coupling, after converting some of the 2',7'-dibromo-2,7-ditert-butyl-9,9'-spirobi[fluorene] monomer into its boronic ester equivalent.

Table 5.1: Table showing the combinations of monomers that result in each polymer.

Monomer 1	Monomer 2	Polymer
		 p(Sp)
		 p(Sp-Ph)
		 p(Sp-BPh)
		 p(Sp-NBPh)

The molecular weight of the polymers ranged between 10 and 85 kDa, as summarised in **Table 5.2**. **p(Sp-NBPh)** obtained the largest molecular weight, even with decreased reaction times, due to this, it was the least soluble of the polymers, requiring gentle heating to solubilise and process in chloroform, a high PDI of 4.43 was observed, which shows a wide spread of polymer chains lengths in the polymer. The other polymers had PDIs of 2 or lower, which is more in line with standard polymers.

Table 5.2 - Molecular weight information of the synthesised polymers collected from the GPC

Polymer	Mw /Da	Mn /Da	PDI
p(Sp)	15462	7988	1.94
p(Sp-Ph)	10594	5820	1.82
p(Sp-BPh)	24595	12115	2.03
p(Sp-NBPh)	84986	19185	4.43

Soxhlet extraction was utilised to purify each polymer, followed by precipitation in EA, then in methanol.

5.3.1.2. Optoelectronic Properties

The optoelectronic techniques used in this Chapter are explained in **Chapter 4.** The UV-Vis spectra of the polymers are show in **Figure 5.2**: a) UV-Vis spectra of polymers on thin film, normalised. b) energy level diagram for the polymers presented**Figure 5.2** and summarised in **Table 5.3**. The techniques explained in section 1.4.1.1. were utilised to calculate the bandgap of the polymers and PESA was again utilised to obtain the HOMO of the polymers, as shown in appendix **Figure 5.6** and summarised in **Table 5.3**.

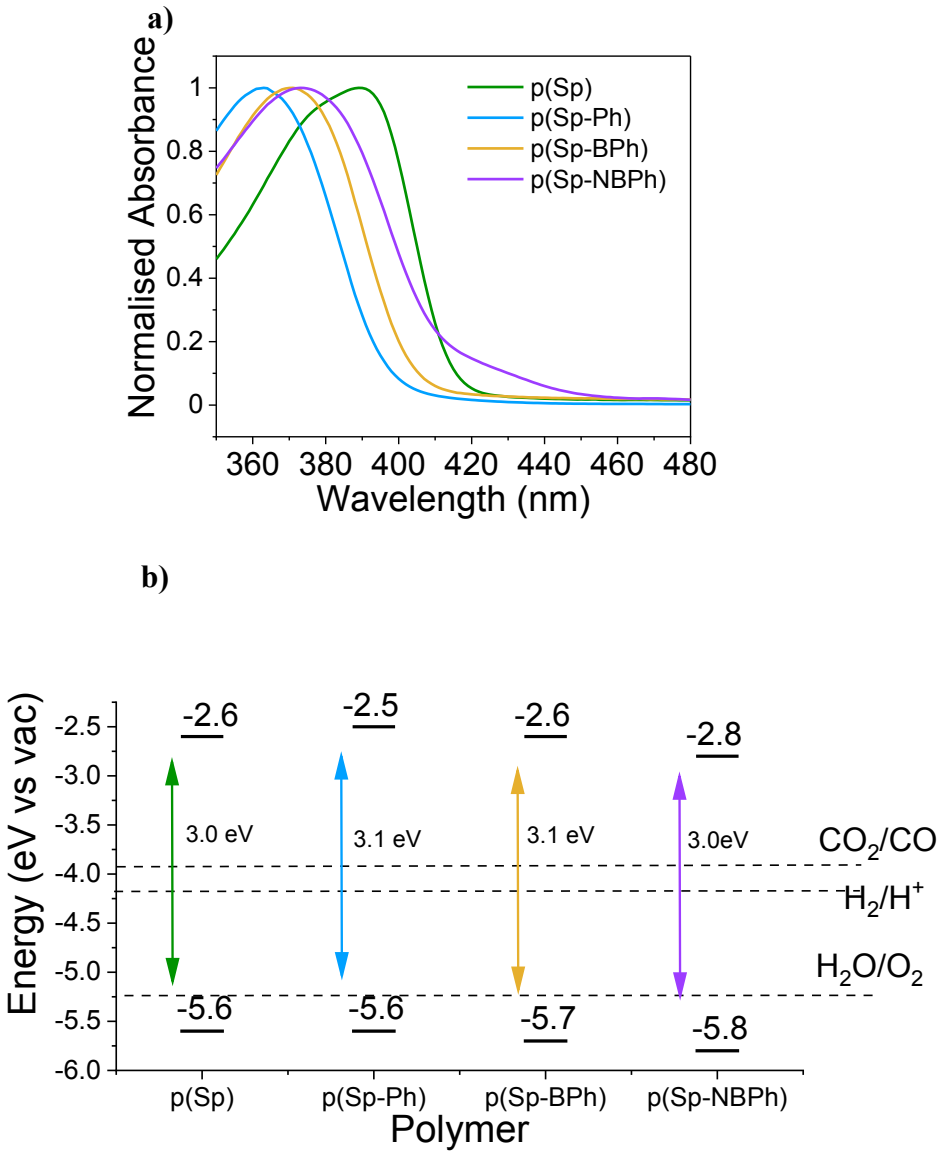


Figure 5.2: a) UV-Vis spectra of polymers on thin film, normalised. b) energy level diagram for the polymers presented

The UV-Vis data shown in **Figure 5.2a),** highlights the absorption maxima of each polymer in the visible region. The curve edge was used for each of the polymers to obtain the bandgap. **p(Sp-BPh)** and **p(Sp-Ph)** both exhibited badgaps of 3.1 eV while **p(Sp)** and **p(Sp-NBPh)** had calculated bandgaps of 3.0 eV. Tangents to the UV-Vis data are shown in **Figure 5.9**. HOMO levels were calculated from PESA, to be -5.6, -5.7, -5.6 and -5.8 eV for **p(Sp)**, **p(Sp-Ph)** , **p(Sp-BPh)** and **p(Sp-NBPh)** respectively. This data was used to plot the energy diagram shown in **Figure 5.2b).** These values straddle the potentials of carbon dioxide photoreduction using hydrogen as a co-oxidant and were therefore deemed suitable for testing. The polymers had very similar energy levels and bandgaps, likely due to the similarity in aromaticity and bond angles of the co-monomers. The co-monomers were chosen to not exhibit particular destabilising or stabilising interactions. Although heteroatoms (2 nitrogen atoms) are present in **p(Sp-NBPh)**, since the lone pair on the nitrogen does not contribute to the aromaticity of the monomer, the heteroatom does not appear to exhibit particularly electron donating effects.

Table 5.3 - Tabulated energetic values measured for each polymer.

Polymer	HOMO	Bandgap		LUMO
	/eV	/nm	/eV	/eV
p(Sp)	-5.6	412	3.0	-2.5
p(Sp-Ph)	-5.7	398	3.1	-2.7
p(Sp-BPh)	-5.6	402	3.1	-2.6
p(Sp-NBPh)	-5.8	410	3.0	-2.8

Unfortunately, unlike the iptycene series and despite the normally high emissive nature of spiro containing polymers, the thin films were not found to have particularly high photoluminescence, as can be seen in **Figure 5.7**. The materials were excited at 380 nm in order to measure PL and the spectrum of **pTA-Ph** was added for comparison. It should be noted that the polymers were sonicated for over 15 minutes prior to spin-coating, which could have potentially impacted their structures. Only **p(Sp-BPh)** showed a convincing emission peak at around 500 nm, suggesting that PL was improved by the addition of a further phenyl group.

5.3.1.3. Palladium Content

Palladium content, after scavenging, was determined using ICP-MS. The results obtained are shown in **Table 5.4**.

Table 5.4: ICP-MS data showing palladium content in the polymers after palladium scavenging.

Polymer	Pd (ppm)
p(Sp)	11
p(Sp-Ph)	13
p(Sp-BPh)	11
p(Sp-NBPh)	17

The palladium content ranged from 11 to 17 ppm. It is interesting that residual palladium is decreased in this series compared to the iptycene series, it is hypothesized that since the iptycene series is a more porous one and contained extra heteroatoms, it was more difficult to remove the residual metal from polymerization. **p(Sp-NBPh)** contained the highest amount of residual palladium, likely due to the chelating nature of the nitrogen lone pairs on the bipy unit, which could be more likely to cling to the residual metal. The numbers were, however, deemed low enough and similar enough to proceed with testing, in the likelihood that any palladium effects were minimised.

5.3.1.4. Porosity

The nitrogen BET isotherms of the polymers are shown in **Figure 5.3** with embedded graphs showing the distribution of pore volumes. The absorption is shown as a coloured line, while the desorption is shown as a dotted line. The surface areas obtained are summarised in **Table 5.5.**

Table 5.5: Table showing the surface areas obtained from the BET isotherms for the polymers.

Polymer	Bet surface area (m^2g^{-1})	Average pore size (nm)	Largest pore size distribution (nm)
p(Sp)	680	~5	~50
p(Sp-Ph)	481	~5	~45
p(Sp-BPh)	67.2	~17	~60
p(Sp-NBPh)	52.0	~20	~65

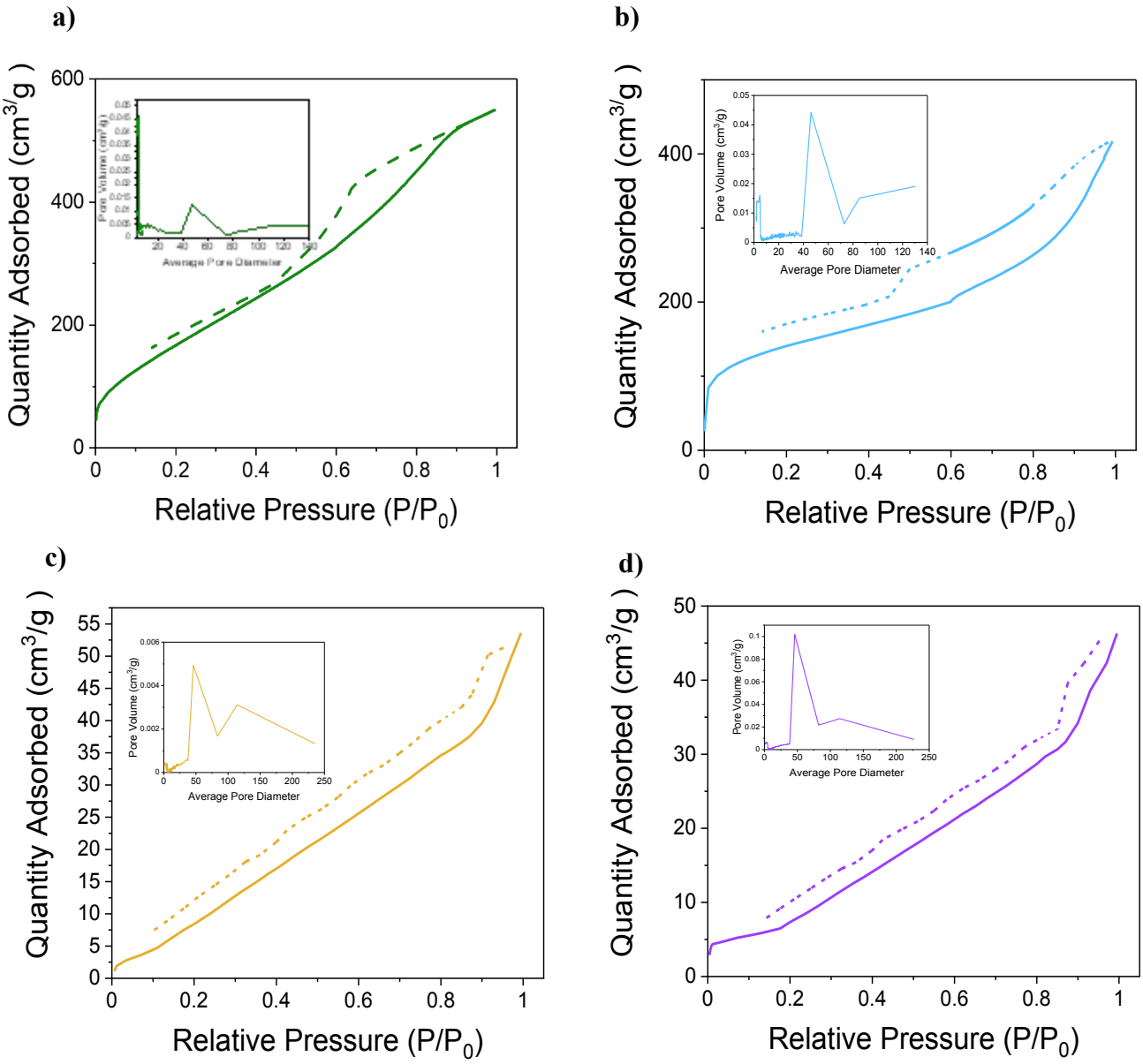


Figure 5.3: BET isotherm plots, with embedded pore distribution plots. a) of **p(Sp),** b) **p(Sp-Ph),** c) **p(Sp-BPh)** d) **p(Sp-NBPh)**

The BET graph shapes of **p(Sp)** and **p(Sp-Ph)** convincingly show the presence of microporosity, shown by the sharp increase at around 0-0.3 P/P_0. The surface areas were calculated to be 680 m^2g^{-1} and 481 m^2g^{-1} respectively. It was expected that **p(Sp)** would display a much higher surface area than its phenyl co-polymerised counterpart, since it contained a higher number per repeat unit of the rigid structure. Both graphs show hysteresis consistent with mesopores as well as micropores, consistent with a type IV isotherm. The pore distribution graph shows a peak between 40-50 nm, further supporting this, for **p(Sp-Ph)** similarly, **p(Sp)** shows a peak at 5 nm and another at 45 nm, also consistent with the presence of mesopores and micropores. It is likely **p(Sp-Ph)** shows a reduction in surface area compared to **p(Sp)**, due to

the incorporation of a phenyl monomer, which does not contain a rigid unit, and therefore increases somewhat the planarization of the polymer. The area is still above that of a non-spiro containing linear polymer, which normally exhibit surface areas below 20 m^2g^{-1}.

Interestingly, **p(Sp-BPh)** and **p(Sp-NBPh)** show markedly lower surface areas than the other two polymers. With a total of 67 and 52 m^2g^{-1} respectively. Although both are above that of standard linear polymers, both appear to be of minimal porosity. The shapes also show minimal microporous or mesoporous characteristics since the sharp incline at the start is quite marginal and little hysteresis can be observed. This could be due to the increased linker chain length, which overall decreases the presence of the rigid unit in the system, and likely leads to an increased packing of the polymer chains, and thus a decrease in the presence of micropores.

5.3.2. Photoreduction using the Spirobifluorene Series

5.3.2.1. Single components

The polymers were first tested with no added co-catalysts, as single components in the photoreduction of carbon dioxide in the presence of hydrogen. Carbon monoxide was formed almost exclusively with minute amounts of methane produced too. No other products were detected by GC.

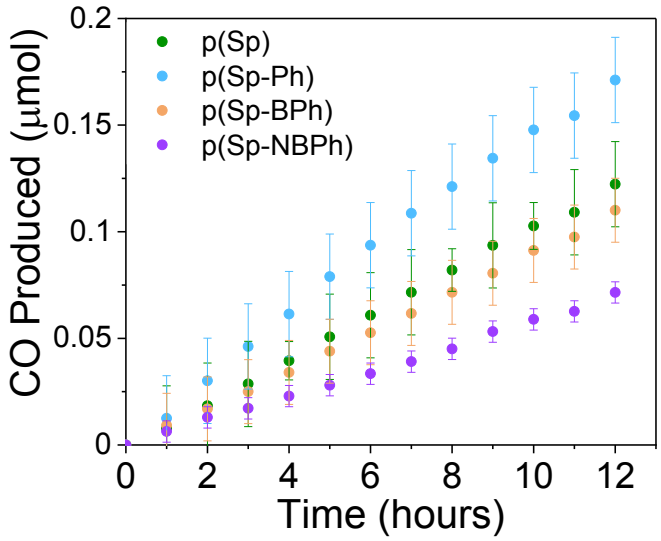


Figure 5.4: Single component performance for the polymers over a 12 hour period.

The raw amount of CO produced is plotted over 12 hour runs, and the polymers kinetic slopes were plotted against each other in **Figure 5.4**, with the rates and selectivity tabulated in **Table 5.6**

Table 5.6: Table summarising single components rates of CO production

Polymer	Rate (μmol h^{-1})	Selectivity to CO production (%)	Rate (μmol $h^{-1}g^{-1}$)	Rate (μmol $h^{-1}m^{-2}$)
p(Sp)	0.010 ± 0.001	98	4.9 ± 0.5	35 ± 4
p(Sp-Ph)	0.015 ± 0.002	97	7.2 ± 0.9	55 ± 7
p(Sp-BPh)	0.009 ± 0.002	98	4.7 ± 0.6	32 ± 5
p(Sp-NBPh)	0.006 ± 0.001	99	2.5 ± 0.5	22 ± 4

The rates obtained were in an atmosphere of H_2:CO_2 in the ratio 3:1, at 1 sun illumination, with UV cut off filter, and at a pressure of 1.15 bar. The highest rate was afforded by **p(Sp-Ph)**, which formed 55 μmol $h^{-1}m^{-2}$ of CO. **p(Sp-BPh)** and **p(Sp)** yielded quite similar rates of 32 and 35 μmol $h^{-1}m^{-2}$ of CO respectively. **p(Sp-NBPh)** afforded the lowest rate with 22 μmol $h^{-1}m^{-2}$ of CO produced. This trend could suggest a trade-off between surface area and pores and some photoluminescence, since **p(SP-BPh)** was not found to be porous, but was found to be emissive, while the similar rate obtained by **p(Sp)** could be due to low emission, but high surface area.

As in **Chapter 4**, control experiments were carried out and outlined in **Figure 5.8** (Appendix). Firstly, the polymers were tested with 1:3 CO_2:H_2 gas ratio with no light present, with no carbonaceous products detected at all. Subsequently, under light the polymers were tested in CO_2:N_2 in a 1:3 ratio, N_2 only, N_2:H_2 also in a 1:3 ratio. These controls yielded small amounts of CO products, but significantly lower than under photocatalytic CO_2 reduction conditions, highlighting the obtained CO is formed primarily from photoreduction of CO_2.

5.3.2.2. Co-catalysts

The best performing polymer **p(Sp-Ph)** was chosen to study the effects of adding a copper-based co-catalyst in different forms. Copper iodide was chosen since it was successfully used as a co-catalyst in the iptycene series. Copper metal nanoparticles were chosen also, since it was shown in **Chapter 4** that the catalysing specie was likely copper metal. These were loaded in a glovebox, transported under inert atmosphere and loaded into the reactor under a flow of nitrogen in order to minimise any oxidation of the copper(0).

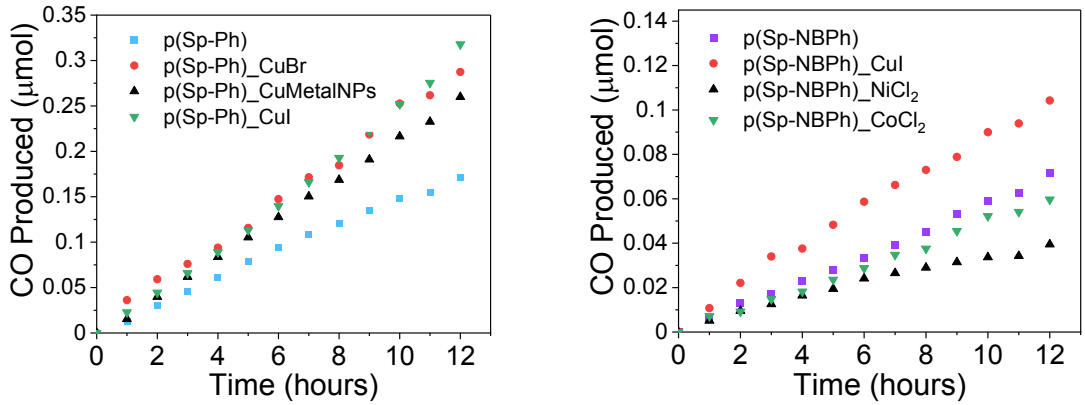


Figure 5.5: Performance of a) **p(Sp-Ph)** with copper co-catalysts. b) **p(Sp-NBPh)** with different co-catalysts.

The mixtures of polymer and 5 w.t% co-catalyst were compared against the single component polymer performance with no added co-catalysts. The copper-based co-catalysts all outperformed the polymer alone when used with **p(Sp-Ph).** CuI showed the largest rate increase from 56 to 93 µmol $h^{-1}m^{-2}$. CuBr also showed an increase in rate to 74 µmol $h^{-1}m^{-2}$. Copper metal nanoparticles showed a slightly lower increase in rate, which could be due to a decreased distribution of particles in the polymer due to the loading method, nonetheless, an increase in rate was still observed at 68 µmol $h^{-1}m^{-2}$. The rate kinetics can be observed in **Figure 5.5** and the rates obtained are tabulated in **Table 5.7**. These further validate that copper is a promising co-catalyst in carbon dioxide photoreduction.

Table 5.7: Table summarising rates of the polymer against the co-catalysts tested.

Polymer	Co-catalyst	Rate (µmol h^{-1})	Rate (µmol $h^{-1}g^{-1}$)	Rate (µmol $h^{-1}m^{-2}$)
p(Sp-Ph)	-	0.015 ±0.002	7.2 ± 0.9	55 ± 7
p(Sp-Ph)	CuBr	0.023 ± 0.005	10.3 ± 4	74 ± 28
p(Sp-Ph)	Cu NPs	0.022 ± 0.004	9.4 ± 2	68 ± 13
p(Sp-Ph)	CuI	0.026 ± 0.005	13.7 ± 3	93 ± 20
p(Sp-NBPh)	-	0.006 ± 0.001	2.9 ± 0.5	22 ± 4
p(Sp-NBPh)	CuI	0.008 ± 0.002	4.7 ± 1	28 ± 6
p(Sp-NBPh)	$NiCl_2$	0.003 ± 0.001	1.6 ± 0.5	11 ± 4
p(Sp-NBPh)	$CoCl_2$	0.005 ± 0.001	2.3 ± 0.5	16 ± 4

p(Sp-NBPh) was also tested with various co-catalysts to begin experimentation towards utilising the chelating bipy ligand. Copper iodide showed a minor increase in rate from 22 to 28 $\mu molh^{-1}m^{-2}$. Cobalt chloride has been used as a CO_2 reduction catalyst and was therefore tested with the polymer. Unfortunately, a decrease in catalytic activity was observed, which a rate of 16 $\mu molh^{-1}m^{-2}$. Similarly, $NiCl_2$ was chosen due to its ability to form a square planar complex, which was thought could successfully chelate to the polymer, however again a decrease in rate was observed at 11 $\mu molh^{-1}m^{-2}$. It is thought that this is an interesting first step in the usage of metals and linear porous polymers, but the decrease in rate observed highlights that further work would need to be carried out to further this process, which is an interesting prospect for future work. It is possible that the distribution process would need to be altered for the metal centres to actually be bound to the bipy unit. It is also possible that experiments with lower loadings of catalyst would be required to move forward, since it is possible that parasitic light absorption is occurring, thus decreasing the overall reaction rate. Another possible explanation could be an energy level mismatch, and potential recombination centres offered by the presence of $CoCl_2$ and $NiCl_2$.

5.3.2.3. Comparison to Iptycene series

This series attempted to build upon knowledge gained from the iptycene series. The investigation focused on increasing the linker size of the non-rigid monomer, going from no co-monomer **p(Sp)** to one phenyl group **p(Sp-Ph)** to two phenyl groups **p(Sp-BPh).** This was done to probe if the photoluminescence of the materials as well as an increase in pore sizes could be achieved, to improve on CO production. The series based on spirobifluorene was synthesised with the aim of having similar energy levels, and the same polymerisation techniques, which are possible factors that could affect carbon dioxide photoreduction. Having taken these considerations into account, it was hoped that the differences in rate would come prevalently from the increase of the non-rigid unit and co-monomer modifications. The best performing polymer, **pTA-Ph** in **Chapter 4**, achieved a CO production rate of 66 $\mu mol\ h^{-1}m^{-2}$, the highest performing in this series, **p(Sp-Ph)** was 55 $\mu mol\ h^{-1}m^{-2}$. These rates are quite comparable, but it is possible the higher rate seen in **pTA-Ph** is due to an increased dihedral angle in the iptycene unit, which further inhibits packing, and possibly gives rise to slightly larger pores, as well as the high PL decay lifetimes observed in **pTA-Ph** that could not be observed in its spiro counterpart due to low photoluminescence. It should also be noted that **p(Sp-Ph)** and **p(Sp)** also had comparable BET surface areas and isotherm shapes to the two best performing polymers in the iptycene series. Although performance was not matched, or

overtaken, the series was useful for comparing monomer size, the importance of a higher yielding, much faster synthesis should also not be understated. Overall, the iptycene series was indeed used for intelligent synthetic design in this new series, and although the increased monomer length decreased surface area too much for the series to be successful in improving the rate of CO production, **p(Sp)** and **p(Sp-Ph)** performed similarly to **pTA** and **pTA-Ph** but took half the number of steps to make.

5.4. Conclusion and Future Work

This chapter explores a series of solution processable polymers of intrinsic microporosity, based on a spirobifluorene rigid unit. The spirobifluorene unit was used to form a homopolymer, co-polymerised with a phenyl group and a biphenyl group, in order to investigate the influence of increasing molecular length of the co-monomer and monitor its effects on surface area and performance. It was thought the bifluorene unit would increase the photoluminescence of the polymers and perhaps even aid with the formation of larger mesopores in the structure. Although **p(Sp-BPh)** was indeed seen to have a possible increased pore size, it could be just likely due to general amorphous polymer behavior in 3D space, and it was found that the longer monomer caused a large decrease in overall surface area. This is likely due to increased packing between polymer chains, specifically due to a longer unit since this decreases the contribution of the rigid unit per repeat unit. So, although the polymer did show an increased photoluminescence, the overall decrease in area was likely responsible for the low performance of the polymer. A bipy based polymer was also synthesized with the aim of using the monomer unit for chelation to possible metal centers, such as nickel or cobalt. **p(Sp-NBPh)** was structurally similar to **p(Sp-BPh),** therefore, unsurprisingly the surface area was found to be comparable, and much lower than that of **p(Sp)** and **p(Sp-Ph).** The polymers were tested as single component and the rates were seen to follow the trend of **p(Sp-Ph)** outperforming **p(Sp)** and **p(Sp-BPh)** which performed very similarly, and in turn all outperformed **p(Sp-NBPh).**

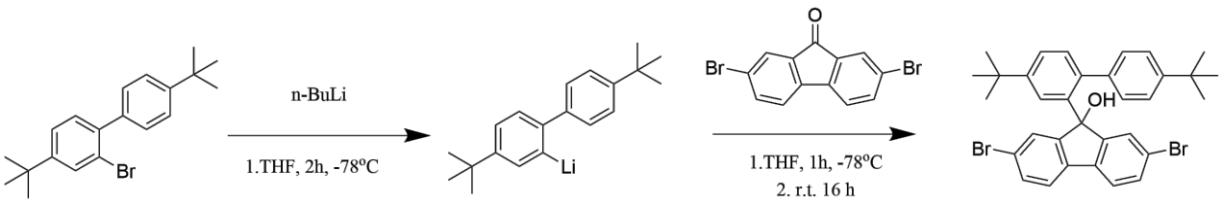
Since **p(Sp-Ph)** was the best performing polymer, it was used to further investigate the incorporation of copper as a co-catalyst in CO_2 photoreduction to CO. One technique for the incorporation of copper in the system was to utilize different copper sources. CuI, CuBr and Cu metal nanoparticles were each mixed in with the polymer, to investigate if the different sources made a difference to CO production rates. Copper iodide yielded the highest rate, and it is thought this could be due to a better photo-deposition of the copper species. An interesting avenue for further work would involve monitoring more closely the incorporation of copper

into the active sites of the polymers and investigating various loading amounts. The chelating nature of **p(Sp-NBPh)** made this an interesting polymer to begin testing with different co-catalysts. Initially sources of cobalt, nickel and copper were loaded in with the polymer. Cobalt chloride and nickel chloride both showed a decrease in overall rate in these preliminary tests. Once again, a further investigation into loading amounts and methods could better ensure chelation is occurring and would allow better monitoring of the effects, so that these could be used as co-catalysts effectively. Overall, this preliminary study into a new spirobifluorene based polymer series, shows the benefits of intelligent synthetic designs, that can be applied from one polymer series to another. This study was useful in providing a new series of solution processable polymers of intrinsic microporosity. The rigid unit was achieved with a straight-forward 3 step synthesis, followed by polymerisation. Although the coveted high photoluminescence was not achieved, the polymers did still show promise. Their properties of processability, porosity and conjugation make them candidates not just for photocatalysis but for other applications such as redox batteries or membranes.

5.5. Experimental

Synthesis of monomers:

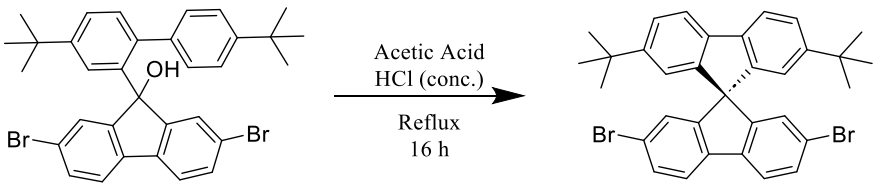
Lithiation and Functionalisation of 2-bromo-4,4'-di-tert-butylbiphenyl



Scheme 5.2 - Lithiation and Functionalisation of 2-bromo-4,4'-di-tert-butylbiphenyl

2-bromo-4,4',di-tert-butylbiphenyl (7.5 g, 21.7 mmol, 1.50 eq.) was dried under high vacuum for 20 minutes then dissolved in dry THF (300 mL). The mixture was cooled to -78 °C followed by dropwise addition of n-butyl lithium (10 mL, 25 mmol, 1.7 eq., 2.5 M), and stirring for 2 hours. 2,7-dibromo-9-fluorenone (4.9 g, 14.6 mmol, 1.00 eq.) was degassed for 20 min then added into the reaction mixture, which was then allowed to warm to room temperature and stirred overnight. The reaction was quenched with sodium hydrogen carbonate (aq) and the product extracted with dichloromethane. The combined organic layers were then washed with water then dried using brine and further dried with anhydrous magnesium sulphate. The solution was filtered then dried under reduced pressure to yield the crude tertiary alcohol intermediate, which was then used immediately without purification. ^{1}H NMR (400 MHz, $CDCl_3$) δ 7.74 – 7.65 (m, 2H), 7.49 (dd, *J* = 8.2, 1.8 Hz, 1H), 7.42 (dd, *J* = 8.1, 1.8 Hz, 1H), 6.84 (d, *J* = 1.7 Hz, 1H), 6.62 (dd, *J* = 1.8, 0.6 Hz, 1H), 1.18 (s, 8H).

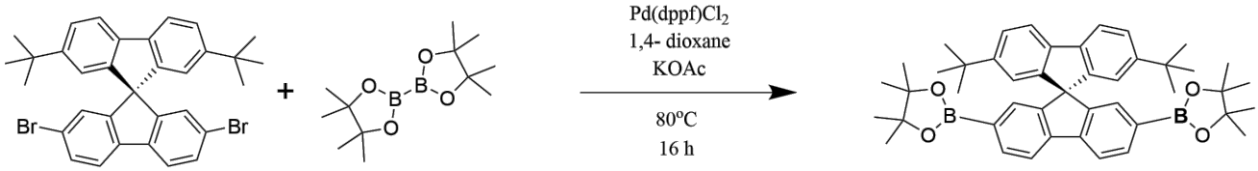
Dehydration to target Monomer



Scheme 5.3 - Dehydration of crude tertiary alcohol to yield the desired spiro centre-containing monomer, 2,7-dibromo-2',7'-ditert-butyl-9,9'-spirobi[fluorene]

Acetic acid (44 mL) was added dropwise to the crude tertiary alcohol intermediate, followed by concentrated hydrochloric acid (15 drops). The reaction mixture was heated to reflux and stirred overnight, then allowed to cool to room temperature. Water was added, and the product extracted using DCM. The combined organic layers were dried with brine and anhydrous magnesium sulphate. The washed solution was then filtered, and the solvent was removed under reduced pressure. Hexane and then ethanol were used to remove any soluble impurities, the monomer was recrystallised from hexane. The solid product was collected, washed with hexane again, and dried *in vacuo* to afford 2',7'-dibromo-2,7-ditert-butyl-9,9'-spirobi[fluorene] (4.1 g, 48% yield): ^{1}H NMR (400 MHz, $CDCl_3$) δ 7.71 (d, J = 8.1 Hz, 2H), 7.68 (d, J = 8.1 Hz, 2H), 7.49 (dd, J = 8.1, 1.8 Hz, 2H), 7.41 (dd, J = 8.1, 1.8 Hz, 2H), 6.84 (d, J = 1.8 Hz, 2H), 6.62 (d, J = 1.7 Hz, 2H), 1.18 (s, 18H).

Borylation of Spirobiflurorene

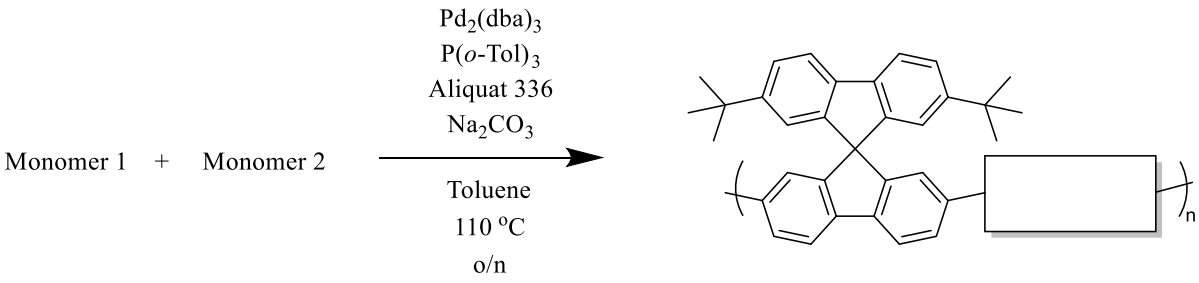


Scheme 5.4 – Borylation of spirobifluorene to yield 2,2'-(2',7'-di-tert-butyl-9,9'-spirobi[fluorene]-2,7-diyl)bis(4,4,5,5-tetramethyl-1,3,2,dioxaborolane

2,7-dibromo-2',7'-di-tert-butyl-9,9'sprobi[fluorene] (1.0 g, 1.7 mmol, 1 eq.), bis(pinacolato)diboron (1.0 g, 3.9 mmol, 2.3 eq.), potassium acetate (10.0 g, 102 mmol, 60 eq.), and $Pd(dppf)Cl_2$ (0.062g, 0.085 mmol, 0.05 eq.) were dried for 30 min. The dried reactants were then added to dry 1,4-dioxane (70 mL), heated to 80 °C and left to stir under an inert atmosphere overnight. Once the reaction had gone to

completion (checked using TLC with a 3:1 hexane:dichloromethane eluent) the organic layer was extracted with ethyl acetate before being washed with deionised water and brine. The combined organic layers were then dried with anhydrous magnesium sulfate, filtered, and dried under reduced pressure. The product was purified using column chromatography (silica, DCM:Hexane 1:3) to yield the borylated monomer as a white solid. 0.74 g, 64%, ^{1}H NMR (400 MHz, $CDCl_3$) δ 7.99 – 7.75 (m, 2H), 7.61 (d, *J* = 8.1 Hz, 1H), 7.36 (dd, *J* = 8.0, 1.8 Hz, 1H), 7.24 (s, 1H), 7.14 (d, *J* = 1.1 Hz, 1H), 1.42 (s, 9H), 1.20 (s, 12H).

General procedure for Suzuki–Miyaura Polymerisations:



Scheme 5.5 - General Suzuki Polymerisation Procedure

Polymerisations were carried out as explained in **Chapter 4**, including palladium scavenging and purification, to yield the final 4 polymers presented in this chapter.

p(Sp): pale yellow solid 72 mg, 48%, ^{1}H NMR (400 MHz, $CDCl_3$) δ 7.65 (d, *J* = 8.3 Hz, 2H), 7.32 (d, *J* = 8.1 Hz, 2H), 7.26 (s, 1H), 6.77 (s, 1H), 6.67 (d, *J* = 8.3 Hz, 1H), 6.58 (d, *J* = 8.1 Hz, 1H), 1.14 (s, 9H)

p(Sp-Ph): pale yellow solid, 47 mg, 55%, ^{1}H NMR (400 MHz, $CDCl_3$) δ 7.81 (d, *J* = 8.4 Hz, 2H), 7.61 (d, *J* = 8.1 Hz, 2H), 7.51 (d, *J* = 7.8 Hz, 2H), 7.40 – 7.24 (m, 8H), 6.81 (s, 1H), 6.60 (s, 1H), 1.03 (s, 18H);

p(Sp-BPh): pale green solid, 36 mg, 23%, ^{1}H NMR (400 MHz, CDCl3) δ 7.89 (d, J = 11.2 Hz, 2H), 7.81 (d, J = 8.4 Hz, 1H), 7.72 (d, J = 8.4 Hz, 2H), 7.69 (d, J = 11.2, 2H), 7.58 (d, J = 11.0 Hz, 1H), 7.51 (s, 2H), 7.49 (d, J=11.0 Hz, 1H) 7.40 – 7.31 (m, 3H), 7.26 (s, 4H), 6.88 (s, 1H), 6.75 – 6.65 (m, 4H), 1.10 (s, 18H).

p(Sp-NBPh): pale grey solid, 48 mg, 31%, ^{1}H NMR (400 MHz, $CDCl_3$) δ 8.71 (s, 1H), 8.31 (s, 1H), 8.00 (m, 2H), 7.84 (d, *J* = 8.6 Hz, 2H), 7.79 – 7.67 (m, 5H), 7.41 (d, *J* = 8.5 Hz, 2H), 6.99 (s, 2H), 6.73 (s, 1H), 6.59 (s,1H), 6.00 (s, 1H), 1.15 (s, 18H).

5.6. Appendix

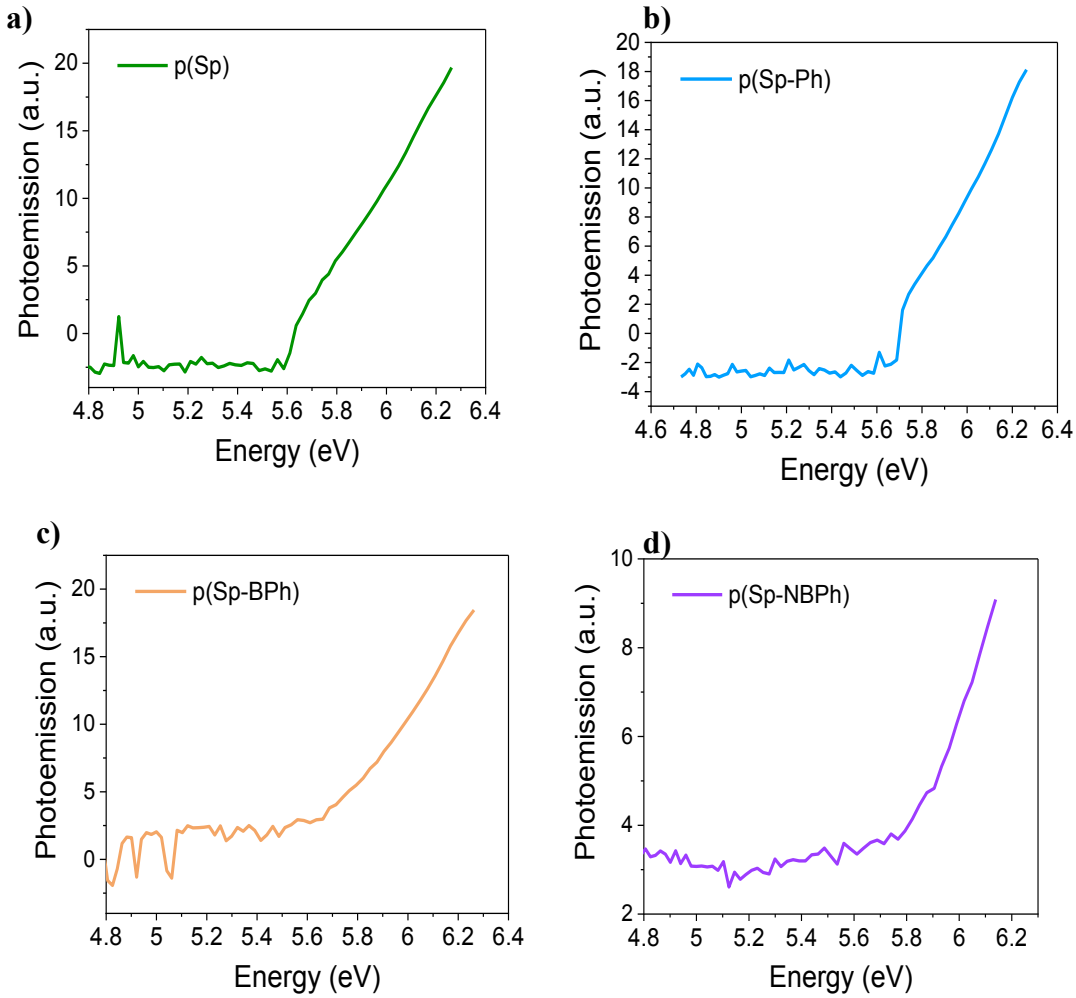


Figure 5.6: PESA spectra of a) of **p(Sp),** b) **p(Sp-Ph),** c) **p(Sp-BPh)** d) **p(Sp-NBPh)**

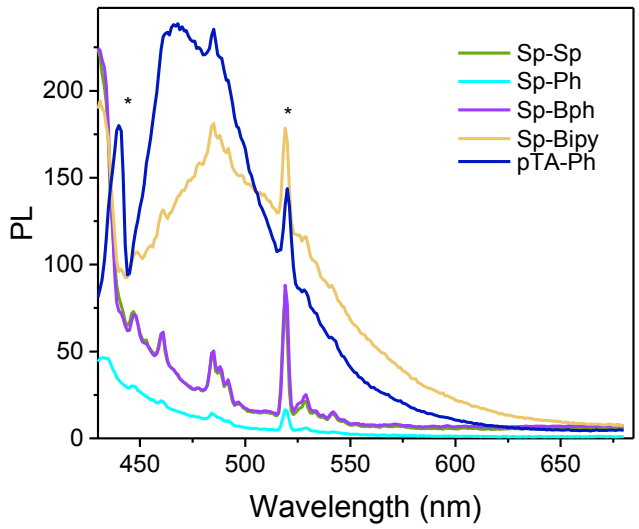


Figure 5.7: PL of the polymers, excited at 380 nm, dissolved in chloroform to 1mgml^{-1} and drop-cast after 15 min of sonication. Emission peaks at 520 nm and 450 nm were an artifact of the instrument lamp.

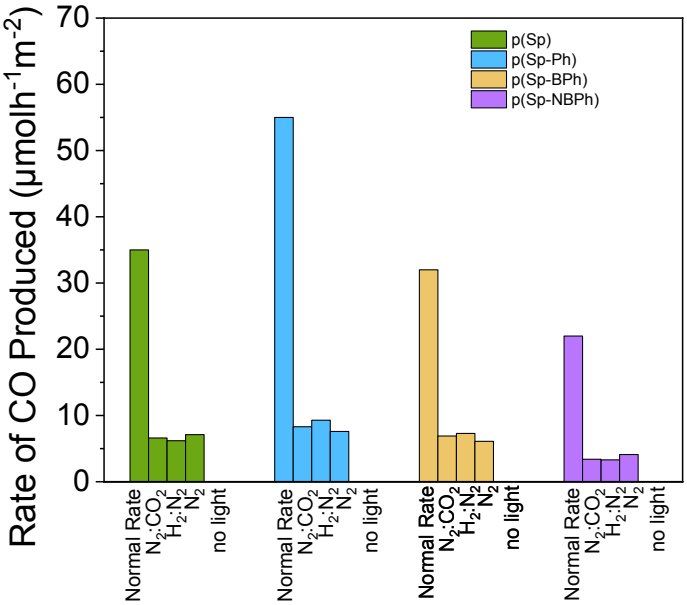


Figure 5.8: Control experiments performed on the polymers.

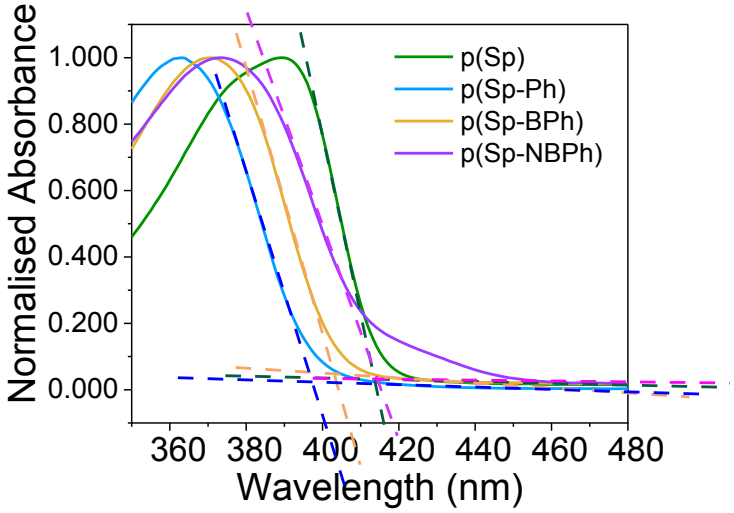


Figure 5.9: UV-Vis data with tangents drawn

5.7. References

(1) Bezzu, C. G.; Fuoco, A.; Esposito, E.; Monteleone, M.; Longo, M.; Carolus Jansen, J.; Nichol, G. S.; Mckeown, N. B.; Bezzu, C. G.; Nichol, G. S.; Mckeown, B.; Fuoco, A.; Esposito, E.; Monteleone, M.; Longo, M.; Jansen, J. C. Ultrapermeable Polymers of Intrinsic Microporosity Containing Spirocyclic Units with Fused Triptycenes. *Adv. Funct. Mater.* **2021**, *31* (37), 2104474. https://doi.org/10.1002/ADFM.202104474.

(2) Thompson, K. A.; Mathias, R.; Kim, D.; Kim, J.; Rangnekar, N.; Johnson, J. R.; Hoy, S. J.; Bechis, I.; Tarzia, A.; Jelfs, K. E.; McCool, B. A.; Livingston, A. G.; Lively, R. P.; Finn, M. G. N-Aryl–Linked Spirocyclic Polymers for Membrane Separations of Complex Hydrocarbon Mixtures. *Science (80-.).* **2020**, *369* (6501), 310–315. https://doi.org/10.1126/SCIENCE.ABA9806/SUPPL_FILE/ABA9806_THOMPSON_SM.PDF.

(3) Saragi, T. P. I.; Spehr, T.; Siebert, A.; Fuhrmann-Lieker, T.; Salbeck, J. Spiro Compounds for Organic Optoelectronics. *Chem. Rev.* **2007**, *107* (4), 1011–1065. https://doi.org/10.1021/CR0501341/ASSET/CR0501341.FP.PNG_V03.

(4) Huang, Z.; Bin, Z.; Su, R.; Yang, F.; Lan, J.; You, J. Molecular Design of Non-Doped OLEDs Based on a Twisted Heptagonal Acceptor: A Delicate Balance between Rigidity and Rotatability. *Angew. Chemie* **2020**, *132* (25), 10078–10082. https://doi.org/10.1002/ANGE.201915397.

(5) Wu, C. chih; Liu, T. L.; Hung, W. Y.; Lin, Y. T.; Wong, K. T.; Chen, R. T.; Chen, Y. M.; Chien, Y. Y. Unusual Nondispersive Ambipolar Carrier Transport and High Electron Mobility in Amorphous Ter(9,9-Diarylfluorene)S. *J. Am. Chem. Soc.* **2003**, *125* (13), 3710–3711. https://doi.org/10.1021/JA029630M/SUPPL_FILE/JA029630MSI20030208_103801.PDF.

(6) Li, S. Y.; Hui, Y. J.; Sun, Z. B.; Zhao, C. H. A Triarylborane-Based Biphenyl Exhibiting Abrupt Fluorescence Enhancement at a Specific High Temperature. *Chem. Commun.* **2017**, *53* (24), 3446–3449. https://doi.org/10.1039/C6CC10088K.

(7) Xiong, K.; Wang, Y.; Zhang, F.; Li, X.; Lang, X. Linker Length-Dependent Photocatalytic Activity of β-Ketoenamine Covalent Organic Frameworks. *Appl. Catal. B Environ.* **2023**, *322*, 122135. https://doi.org/10.1016/J.APCATB.2022.122135.

(8) Costero, A. M.; Gil, S.; Sanchis, J.; Peransí, S.; Sanz, V.; Gareth Williams, J. A. Conformationally Regulated Fluorescent Sensors. Study of the Selectivity in Zn2+ versus Cd2+ Sensing. *Tetrahedron* **2004**, *60* (30), 6327–6334. https://doi.org/10.1016/J.TET.2004.05.075.

(9) Kaes, C.; Katz, A.; Hosseini, M. W. Bipyridine: The Most Widely Used Ligand. A Review of Molecules Comprising at Least Two 2,2′-Bipyridine Units. *Chem. Rev.* **2000**, *100* (10), 3553–3590. https://doi.org/10.1021/CR990376Z.

(10) Constable, E. C.; Housecroft, C. E. The Early Years of 2,2′-Bipyridine—A Ligand in Its Own Lifetime. *Molecules* **2019**, *24* (21). https://doi.org/10.3390/MOLECULES24213951.

(11) Mo, Z.; Li, Y.; Lee, H. K.; Deng, L. Square-Planar Cobalt Complexes with Monodentate N-Heterocyclic Carbene Ligation: Synthesis, Structure, and Catalytic Application. *Organometallics* **2011**, *30* (17), 4687–4694. https://doi.org/10.1021/OM200527Y/SUPPL_FILE/OM200527Y_SI_002.PDF.

(12) Huang, P.; Pantovich, S. A.; Okolie, N. O.; Deskins, N. A.; Li, G. Hybrid Carbon Dioxide Reduction Photocatalysts Consisting of Macrocyclic Cobalt(III) Complexes Deposited on Semiconductor Surfaces. *ChemPhotoChem* **2020**, *4* (6), 420–426. https://doi.org/10.1002/CPTC.201900282.

(13) Lei, K.; Wang, D.; Ye, L.; Kou, M.; Deng, Y.; Ma, Z.; Wang, L.; Kong, Y. A Metal-Free Donor–Acceptor Covalent Organic Framework Photocatalyst for Visible-Light-Driven Reduction of CO2 with H2O. *ChemSusChem* **2020**, *13* (7), 1725–1729. https://doi.org/10.1002/CSSC.201903545.

(14) Kojima, T. Photocatalytic Carbon Dioxide Reduction Using Nickel Complexes as Catalysts. *ChemPhotoChem* **2021**, *5* (6), 512–520. https://doi.org/10.1002/CPTC.202000263.

(15) Bueno-Alejo, C. J.; Arca-Ramos, A.; Hueso, J. L.; Santamaria, J. LED-Driven Continuous Flow Carbon Dioxide Hydrogenation on a Nickel-Based Catalyst. *Catal. Today* **2020**, *355*, 678–684. https://doi.org/10.1016/J.CATTOD.2019.06.022.

(16) Zhang, W.; He, Z.; Pang, H.; Wang, Y.; Zhao, S.; Zhang, W.; He, Z.; Pang, H.; Wang, Y.; Zhao, S. Spirobifluorene and Biphenylaminophenyl Fluorene with Dimesitylboron as Multifunctional Electroluminescent Materials. *OptMa* **2015**, *50*, 154–161. https://doi.org/10.1016/J.OPTMAT.2015.10.015.

(17) Thiery, S.; Tondelier, D.; Declairieux, C.; Seo, G.; Geffroy, B.; Jeannin, O.; Rault-Berthelot, J.; Métivier, R.; Poriel, C. 9,9′-Spirobifluorene and 4-Phenyl-9,9′-Spirobifluorene: Pure Hydrocarbon Small Molecules as Hosts for Efficient Green and Blue PhOLEDs. *J. Mater. Chem. C* **2014**, *2* (21), 4156–4166. https://doi.org/10.1039/C4TC00171K.

(18) Olah, G. A.; Kuhn, S. J.; Flood, S. H.; Hardie, B. A. Aromatic Substitution. XIV.1 Ferric Chloride Catalyzed Bromination of Benzene and Alkylbenzenes with Bromine in Nitromethane Solution. *J. Am. Chem. Soc.* **1964**, *86* (6), 1039–1044. https://doi.org/10.1021/JA01060A014/ASSET/JA01060A014.FP.PNG_V03.

(19) Miyaura, N.; Yanagi, T.; Suzuki, A. The Palladium-Catalyzed Cross-Coupling Reaction Of Phenylboronic Acid With Haloarenes In The Presence Of Bases. *Synth. Commun.* **1981**, *11* (7), 513–519. https://doi.org/10.1080/00397918108063618.

6. Conclusions and Future Work

This chapter aims to summarise the conclusions and future work outlined in the other chapters, and comment on the future of the field. The overall aim of this project was to investigate the use of organic semiconductors in solar fuels applications. The main aim was to achieve photochemical reduction of carbon dioxide. Initially, photoelectrochemistry for hydrogen evolution was attempted. The general theory was utilised to direct functionalisation of the materials and considerations in testing towards gas phase CO_2 photoreduction. To do this, porous polymers were designed, and testing equipment and methods were developed.

When first looking at organic polymers in photoelectrochemistry, **Chapter 2** outlined the potential of functionalising polymers to achieve increased adhesion and improve stability in organic photocathodes. The blend **PCE12**:**N2200** was investigated firstly in OPV, followed by photocathode fabrication. It was found that the inclusion of glycol side chains and a 10% substituted phosphate anchor group on the **N2200** and insertion of this polymer as an overlayer increased the relative coverage of titania at low ALD cycle numbers. This in turned showed an increased operational stability compared to the version of the photocathode which did not include the overlayer. This study showed the potential of functionalities incorporated in polymers to tackle the issue of bad adhesion in photoelectrodes. As mentioned in the chapter, further work in this area should focus on firstly optimising the photocathode structure itself, followed by further research into different types of anchor groups. Further imaging should also be carried out to compare which group can aid adhesion between layers while still maintaining polymer properties, or how an overlayer with anchor groups can be effectively incorporated, as in this study, so that only a very thin film of ALD layer is required for a pin-hole free organic photocathode. **Figure 6.1** shows two more potential anchor groups that could be attempted for an overlayer. A carboxyl group could be incorporated via an S_N2 reaction using a carboxyl salt, either as a carboxylic acid, or as a spacer. A carboxylic acid group could also be formed via hydrolysation of a cyano group, also added via S_N2 to replace the bromine. A carboxylic acid could also be converted to a hydroxamate directly.[1] Hydroxamate groups have been also shown to link very effectively to titania and it could therefore be interesting to compare this to phosphonates.[2,3] The inclusion of anchor groups is a promising direction for the field of organic photocathodes to take, in order to achieve the high operational stabilities required to make the process economically viable.

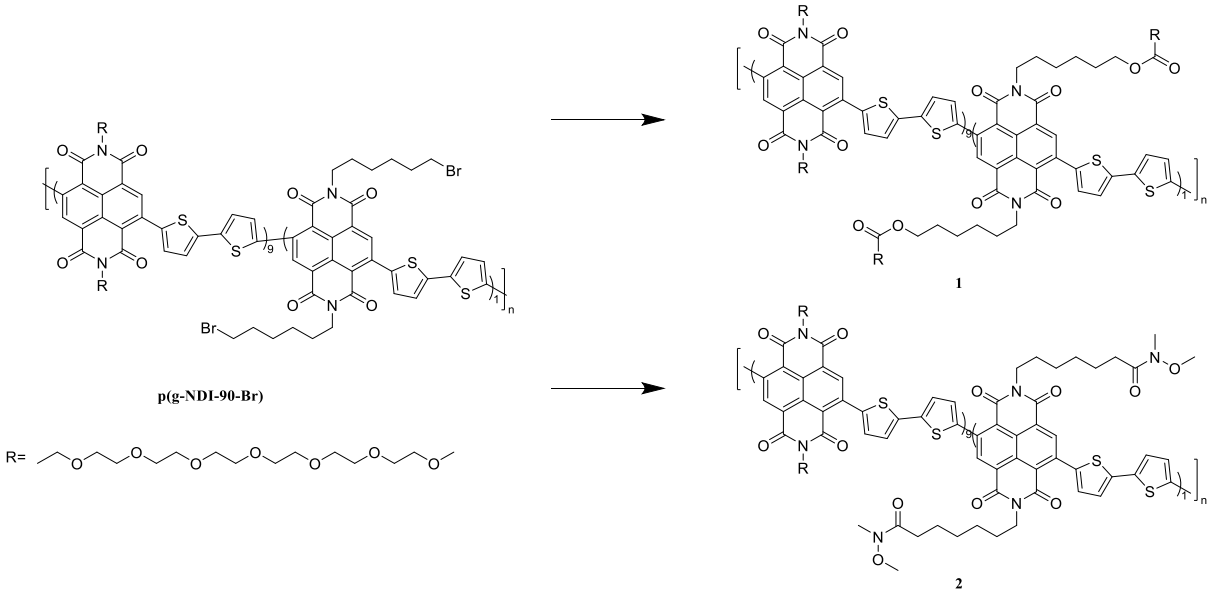


Figure 6.1: Potential anchor groups that could be used in photocathode studies.

Leaning on theoretical knowledge gained in photoelectrochemistry for hydrogen evolution, the author moved into adapting similar principles in the design of testing and materials for carbon dioxide unassisted photoreduction. **Chapter 3** outlined the design of the set-up built for CO_2 photoreduction testing. The primary focus of the system was for gas phase photocatalysis, but the set-up was built with flexibility in mind for water vapour, solution-based reactions, as well as the potential to insert a photochemical cell with a potentiostat, for possible photoelectrochemistry measurements. To improve the set-up itself, the addition of a MS would mean being able to run isotope labelling experiments. Furthermore, inserting a trap and septum would be ideal for future experiments if using solution phase more often, or if forming liquid products. The chapter outlined the challenge of potential degradation of organic materials under strong light exposure in a hydrogen atmosphere, and shed light on the issue of carbonaceous impurities found either in set-ups or within materials due to fabrication and processing of the device or due to synthesis. It was important to outline the significance of control reactions to ensure the CO rates from CO_2 photocatalysis were not inflated. Another challenge outlined in the chapter was that of standardisation in the field. The difficulty in comparing various literature materials due to the differences in set-ups and testing conditions cannot be understated. Future literature in the field would benefit from outlining testing and standardisation benchmarks. Currently, due to the variety of testing methods available, benchmarking by using known commercially available standards as comparisons is useful, and clearly explaining conditions is critical. Gas phase carbon dioxide photoreduction is still far

from being ready for commercialisation, due to the low efficiencies of materials, as a result, equipment that is able to effectively screen materials is valuable.

Using the testing equipment built it was then possible to address the main aim of the thesis in understanding how structural features of organic materials could affect the rates of production in carbon dioxide photoreduction. **Chapter 4** presented a series of iptycene based, solution processable porous polymers which exhibited high porosity and were able to catalyse the photoreduction of carbon dioxide into carbon monoxide in the presence of hydrogen. The study attempted to look into a structure-rate correlation, focusing on factors such as the polymers' molecular weight, residual polymerisation metal, energy levels and porosity. Ultimately a link between good performance, large pore sizes and high PL decay lifetimes was highlighted. Although material design is very important, organic materials are known to suffer from high recombination rates. Splitting charges is therefore critical for effective photocatalysis. The techniques attempted were firstly the inclusion of a source of copper to act as a co-catalyst. The hypothesis was that this would aid charge separation and offer an active site of lower activation energy for photocatalysis to occur. Copper was introduced from CuI salt and showed a two-fold increase in rate of CO formation. An alternative approach to improve charge separation was the incorporation of a heterojunction. The two polymers with the best Type II offset showed a promising increase in rate. Further research in optimising mixing and heterojunction structure should be carried out for this technique to function to its theoretical potential. A possible example would be to couple the thiophene unit with an acceptor-type co-monomer, to perhaps obtain a better energy level offset for a heterojunction. Another technique could be to couple the porous polymers with a small molecule to see if porosity is maintained while charge separation is increased.

Testing the polymers with different conditions, and techniques was important for taking these materials further, but the synthesis of the rigid iptycene monomer unit presented in **Chapter 4** was quite time consuming and low yielding. A spirocyclic rigid unit was proposed instead as an alternative, and a new series based on the spiro unit was presented in **Chapter 5.** It was thought that increasing the length of the non-rigid co-monomer may aid with an increase in pore size, which had been seen in the previous series to be beneficial to higher performance. Ultimately this was not found to be the case, since the longer linker unit decreased the overall percentage of the rigid unit and overall decreased the porosity of the materials, as well as making them less soluble in chloroform (heating was required for good solubility). However, the homopolymer and the rigid unit polymerised with a single phenyl group showed good

promise. The PL of the polymers was lower than that of the iptycene polymers, but the surface area was maintained high, which could in turn be credited for a nearly comparable performance. The incorporation of copper was further investigated in this series, by adding it via different sources. Each was still found to increase the rate of reaction. Other co-catalysts did not have the same effect. It is thought this would merit further research, with the aim to better understand catalyst loadings and loading techniques available which could help achieve higher product rates. These two chapters outline the potential of solution processable polymers yielding high porosity, while maintaining conjugation and light absorbing properties. These exciting materials could have a multitude of applications not just in photocatalysis, but as membranes, as gas diffusion layers in fuel cells or electrochemical cells, due to their combined porosity and redox capabilities.[4]

This research paves the way for the use of organic solution processable, porous materials in carbon dioxide photoreduction. The thesis introduced series of materials which show high intrinsic porosity, can form a film, and can, as single components catalyse the photoreduction of carbon dioxide into carbon monoxide in the presence of light. Although the studies presented in this thesis prove the concept and make a strong case for the advantages of using these materials, challenges still need to be overcome. Much like at the start of the field of OPV, we are still at the start of the organic photocatalysis field for CO_2. Currently, photocatalysis cannot compete in terms of efficiencies, and economic value with OPV + electrolysis, but the field has the potential to meet this goal, and with high efficiencies, and sustainable syntheses and engineering, could benefit over PV + electrolysis in its "one-pot" nature.

In order to tackle these challenges, future areas of research should focus on: (1) using classes of PIMs for this application, but improving overall efficiencies, by introducing better heterojunctions, co-catalysts and activating groups. (2) Improving mechanistic insights into the process, by modelling and via experiments, further understanding the active sites, charge transport and mobilities and recombination. (3) moving towards different reaction products and input streams to improve the overall value of the process. These areas are intrinsically tied together. By elucidating more relationships between functionalities and factors effecting photocatalysis, and taking into account those found in this thesis, a better intelligent synthetic design for materials would ensure an application driven approach to material synthesis. In regards to point (1), materials which can form good heterojunctions should be tested and better understood, with the aim to decrease charge recombination in photocatalysis and obtain higher efficiencies, in much the same detail as they have been for photovoltaic systems.[6] This thesis

touched upon type II heterojunctions, which should be better investigated, however, artificial photosynthesis is based on nature, which uses a Z-scheme type structure. The research and incorporation of a Z-scheme type system might allow the high efficiencies sough for commercialisation of carbon dioxide derived solar fuels.[7] Similarly, further co-catalyst studies, focused on the placement of the co-catalyst and on elucidating more information on the mechanisms would be greatly beneficial, and a good co-catalyst would aid in lowering the activation energy required for photocatalysis as well as aiding with charge separation. This nicely ties in with point (2), understanding more of the mechanistic insights and elucidating information about the active sites would provide useful information and support intelligent synthetic design for these applications. Furthermore, the ideal usage of gas-phase carbon dioxide photoreduction would be from waste gas from industrial processes. Currently efficiencies are too low for this process to be viable. Materials focused on activating and capturing functionalities for carbon dioxide could be at the forefront of research, to obtain materials which can photoreduce carbon dioxide in low quantities, and oxidise water vapour in low quantities.[5] An advantage of organic materials is the possibility to incorporate functionalities such as amines or glycol chains which might help address this challenge by interacting with carbon dioxide or the reaction intermediates more effectively. This technique is much like that of adding anchor groups to polymers for photocathodes. Although the bipy unit shown in **Chapter 5** did not have the desired effect of increasing either reaction rate or the inclusion of co-catalysts, further research is merited. Understanding how these functionalities would help mechanistically, and experimenting by introducing these functionalities to PIMs could be a step towards achieving this value-added application, as mentioned in point (3). Equally, this thesis achieved CO formation as the primary product of CO_2 photoreduction. Conceptually, this is a good first step since it is a coveted intermediate for products such as methanol. However, achieving selectivity for different products, with an increased value would truly set these apart and take us a step closer to decarbonisation.

Overall, this study outlined a new class of porous materials for gas phase carbon dioxide photocatalysis, it showed the importance of functionalisation on photocatalysis properties, and in photoelectrochemistry of organic polymers too. The thesis also outlined the need for better standardisation in the field, which will be paramount as the field continues to expand. Finally, the author would like to highlight the need to use a multidisciplinary approach when tackling the application of solar fuels in general. A way of thinking which incorporates the engineering and usage of the materials combined with the materials themselves and the architectures of the

devices obtained using the materials is critical. The ability to think outside the box and to link different fields, taking lessons from each one should be championed in research in this field that has such promise for tackling global warming, and allowing us to abundantly make use of such an exciting energy source, the sun.

6.1. References

(1) Niu, T.; Wang, K. H.; Huang, D.; Xu, C.; Su, Y.; Hu, Y.; Fu, Y. One-Pot Transition-Metal-Free Synthesis of Weinreb Amides Directly from Carboxylic Acids. *Synthesis (Stuttg).* **2014**, *46* (03), 320–330. https://doi.org/10.1055/S-0033-1340317.

(2) Zhang, L.; Cole, J. M. Anchoring Groups for Dye-Sensitized Solar Cells. *ACS Appl. Mater. Interfaces* **2015**, *7* (6), 3427–3455. https://doi.org/10.1021/AM507334M/ASSET/IMAGES/LARGE/AM-2014-07334M_0006.JPEG.

(3) Padial, N. M.; Castells-Gil, J.; Almora-Barrios, N.; Romero-Angel, M.; Da Silva, I.; Barawi, M.; García-Sánchez, A.; De La Peña O'Shea, V. A.; Martí-Gastaldo, C. Hydroxamate Titanium-Organic Frameworks and the Effect of Siderophore-Type Linkers over Their Photocatalytic Activity. *J. Am. Chem. Soc.* **2019**, *141* (33), 13124–13133. https://doi.org/10.1021/JACS.9B04915/SUPPL_FILE/JA9B04915_SI_002.CIF.

(4) Liu, R. Y.; Guo, S.; Luo, S. X. L.; Swager, T. M. Solution-Processable Microporous Polymer Platform for Heterogenization of Diverse Photoredox Catalysts. *Nat. Commun. 2022 131* **2022**, *13* (1), 1–8. https://doi.org/10.1038/s41467-022-29811-6.

(5) Ma, Y.; Wang, S.; Duan, X. Recent Advances in Direct Gas–Solid-Phase Photocatalytic Conversion of CO2 for Porous Photocatalysts under Different CO2 Atmospheres. *Chem. Eng. J.* **2023**, *455*, 140654. https://doi.org/10.1016/J.CEJ.2022.140654.

(6) Saravanan, R.; Gracia, F.; Stephen, A. Basic Principles, Mechanism, and Challenges of Photocatalysis; Springer, Cham, 2017; pp 19–40. https://doi.org/10.1007/978-3-319-62446-4_2.

(7) Yoshino, S.; Iwase, A.; Yamaguchi, Y.; Suzuki, T. M.; Morikawa, T.; Kudo, A. Photocatalytic CO2Reduction Using Water as an Electron Donor under Visible Light Irradiation by Z-Scheme and Photoelectrochemical Systems over (CuGa)0.5ZnS2in the Presence of Basic Additives. *J. Am. Chem. Soc.* **2022**, *144* (5), 2323–2332. https://doi.org/10.1021/JACS.1C12636/ASSET/IMAGES/LARGE/JA1C12636_0009.JPEG.